General Disclaimer

One or more of the Following Statements may affect this Document

- This document has been reproduced from the best copy furnished by the organizational source. It is being released in the interest of making available as much information as possible.

- This document may contain data, which exceeds the sheet parameters. It was furnished in this condition by the organizational source and is the best copy available.

- This document may contain tone-on-tone or color graphs, charts and/or pictures, which have been reproduced in black and white.

- This document is paginated as submitted by the original source.

- Portions of this document are not fully legible due to the historical nature of some of the material. However, it is the best reproduction available from the original submission.

STUDY OF SHUTTLE IMAGING MICROWAVE SYSTEM ANTENNA

VOLUME I
CONCEPTUAL DESIGN
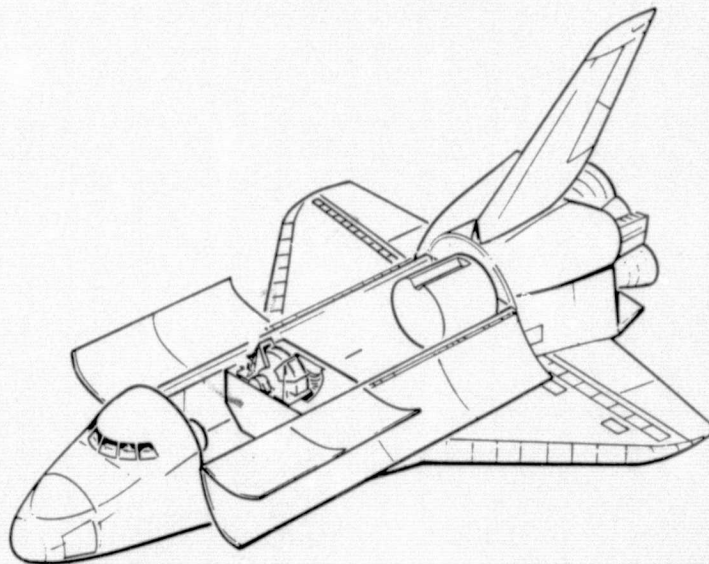
Rockwell International

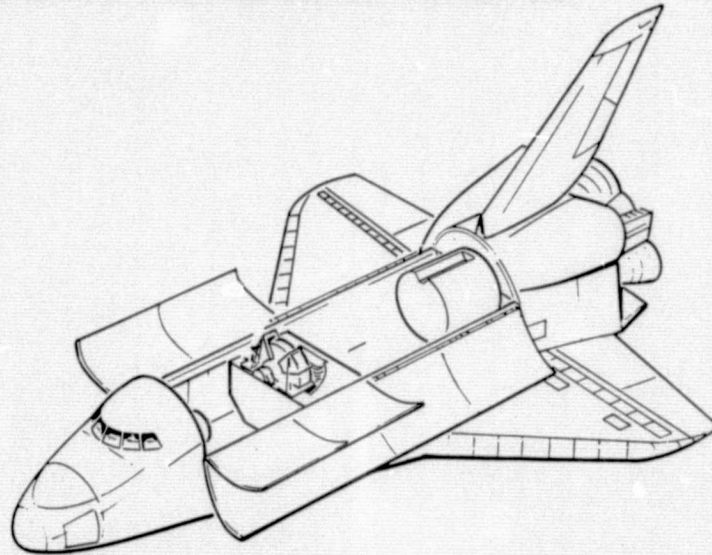# STUDY OF SHUTTLE IMAGING MICROWAVE SYSTEM ANTENNA

VOLUME I
CONCEPTUAL DESIGN

21 November 1975

Prepared by:

R. W. Wesley, D. K. Waineo, C. R. Barton, A. W. Love

JPL Contract No. 954253

Rockwell International

Missile Systems Division
3370 Miraloma Avenue
Anaheim, California 92803

ABSTRACT

This report gives a detailed preliminary design and complete performance evaluation of an 11-channel large aperture scanning radiometer antenna for the Shuttle Imaging Microwave System (SIMS) Program. Provisions for interfacing the antenna with the Space Shuttle Orbiter are presented and discussed. A program plan for hardware development and a rough order of magnitude (ROM) cost are also included.

The conceptual design of the antenna is first presented. It consists of a four-meter diameter parabolic torus main reflector, which is a graphite/epoxy shell supported by a graphite/epoxy truss. A rotating feed wheel assembly supports six Gregorian subreflectors covering the upper eight frequency channels from 6.6 GHz through 118.7 GHz, and two three-channel prime forms feed assemblies for 0.6, 1.4, and 2.7 GHz. The feed wheel assembly also holds the radiometers and power supplies, and a drive system using a 400 Hz synchronous motor is described.

The RF analysis of the antenna is performed using physical optics procedures for both the dual reflector Gregorian concept and the single reflector prime focus concept. A unique aberration correcting feed for 2.7 GHz is analyzed. A structural analysis is also included. The analyses indicate that the antenna will meet system requirements.

FOREWORD

This report describes the results of work conducted under JPL Contract 954253 "Study of the Antenna Subsystem for the Shuttle Imaging Microwave System (SIMS) directed by Dr. J. W. Waters.

"This work was performed for the Jet Propulsion Laboratory, California Institute of Technology sponsored by the National Aeronautics and Space Administration under Contract NAS7-100."

The primary program effort was performed by the Antenna Systems Group within Missile Systems Division of Rockwell International, during the period 16 June, 1975 through 15 November 1975. The Project Engineer was R. W. Wesley. The key Electrical Research Engineer was D. K. Waineo and the key Mechanical Research Engineer was C. R. Barton. The report was prepared and submitted in November, 1975.

ACKNOWLEDGMENT

CONTENTS

CONTENTS (Cont)

ILLUSTRATIONS

ILLUSTRATIONS (Cont)

ILLUSTRATIONS (Cont)

TABLES

1. INTRODUCTION

The Shuttle Imaging Microwave System (SIMS) is a multi-channel, high resolution, passive radiometer for observations of thermal emission from the Earth's atmosphere and surface. It is being designed to fit within the Space Shuttle payload. The Shuttle will be in an earth viewing orbit with its axis in the direction of flight. The SIMS antenna beam will be scanned in a plane normal to the flight vector while orbital motion will provide scanning in the orthogonal direction. The large payload of the Shuttle allows a much larger antenna than possible on previous space vehicles. This larger antenna structure will provide increased resolution and in addition will make possible the use of longer wavelengths not previously used for earth observations.

The purpose of this study was to study, investigate and recommend a suitable antenna concept which will be referred to as SIMS-A. This conceptual design must provide simultaneous operation at eleven frequencies from 0.610 GHz to 118.7 GHz. In addition, it was desirable that the primary collimator be capable of operating at frequencies up to 300 GHz. The 11 channelized frequencies for this concept – SIMS-A (Alternative 1) are:

Channel	Frequency (GHz)
1	0.610
2	1.413
3	2.695
4	6.6
5	10.69
6	20.0
7	22.0
8	37.0
9	53.0
10	94.0
11	118.7

It was also desirable that a five-channel system (4, 5, 7, 8 and 10) be considered. This system, referred to as SIMS-A (Alternative 2) must have growth capability to Alternative 1.

The frequency spectrum requirements imply a true time delay optical type collimating system. Each channel is relatively narrow band so that a multiplicity of channelized feeds will adequately provide the desired frequency coverage. For these reasons the prime candidate solution to the SIMS-A requirements was a parabolic torus reflector with a rotating feed wheel containing Gregorian sub-reflector feeds for the high frequency channels and point source focal plane feeds for the lower frequency channels. It was a requirement to perform a design study and performance analysis of this prime candidate and any suitable alternative concept approved by JPL.

Primary emphasis of the design study was to achieve a conceptual design with the following properties:

- Maximum main beam efficiency > 90 percent

- Minimum insertion loss

- Simplicity of mechanical construction (consistent with performance requirements)

- Minimal cost

- Space Shuttle payload compatibility

Significant output requirements of the study were to include: discussions of results of all analyses; specifications, drawings and description of the recommended antenna system; and a rough order of magnitude (ROM) cost estimate for each alternative.

Volume I contains all of the technical results while Volume II presents a recommended program plan, schedule and ROM cost estimate. Section 2 of Volume I gives a detailed description of the antenna, its performance characteristics, and the Shuttle/SIMS interface characteristics and considerations. Section 3 presents the design approach and all analyses upon which the conceptual design is based. Section 4 is a discussion of considerations which will be significant in developing a test program for an antenna of this size and frequency bandwidth with an intended use in the Space Shuttle. Conclusions and recommendations which have resulted from this study are found in Sections 5 and 6 respectively.

2. ANTENNA CONCEPTUAL DESIGN SPECIFICATIONS

2.1 INTRODUCTION

This specification describes an antenna which meets all of the functional requirements of Exhibit I entitled "SIMS-A Antenna Study Requirements" dated January 7, 1975, and conforms to JSC 07700, Volume XIV, Revision C, Change No. 11, entitled Space Shuttle System Payload Accommodations.[1]* Section 2.2 presents a description of the antenna and Section 2.3 provides the performance characteristics of the baseline antenna.

---

*For convenience, reference to this document will be identified simply as JSC 07700.

2.2 ANTENNA DESCRIPTION

2.2.1 Electrical (RF) Specifications

2.2.1.1 General

The antenna operates on eleven frequency channels from 0.61 GHz to 118.7 GHz. It is composed of an offset-fed parabolic torus reflector fed by a number of abberation correcting feeds spaced around a rotating feed wheel. In operation, continuous rotation of the feed wheel scans the antenna beams in the cross-track direction, called azimuth for simplicity. The along-track direction is called elevation. During the portion of the scan when the feeds are not illuminating the reflector, the entire feed assembly passes through a three-sided enclosure which gives reference temperatures for calibration purposes.

2.2.1.2 Specific Item Descriptions

Main Reflector

The main reflector is a parabolic torus with a diameter of 4m and a height of 2m. The bottom of the reflector corresponds to the vertex of the parabola, which has a focal length of 1m. The reflector subtends 180 deg. in azimuth from its center.

Feed Systems

The rotating feed wheel contains a number of feed positions in its circumference. The predominant feed concept is a Gregorian subreflector with a horn primary feed. Dual concentric primary feeds are used in those cases where two bands share the same subreflector, and each feed is dual polarized. The primary feed in all cases can be a rectangular corrugated horn 2.6λ high and 1.5λ wide. A small flare angle is used to maintain less than 0.1λ path length error in the horn aperture. The various parameters (feed size, feed location, subreflector location, and surface contour) have been optimized as discussed in Paragraph 3.1.

The Gregorian approach is used at all frequencies for which overall performance is acceptable. Analysis indicates that for the lowest three frequencies another approach is required, and feeds located near the paraxial focus which directly illuminate the parabolic torus are utilized. These are called prime focus feeds. For the lowest frequency (0.61 GHz), a very simple feed with four dipoles spaced 0.63λ apart in a square lattice is used. For the second frequency (1.413 GHz), a narrower feed pattern is needed to minimize the effects of reflector abberation. A seven element dipole array (a central dipole surrounded by six dipoles located on a circle of radius 0.683λ) is used. The outer six dipoles are fed in phase and 6 dB lower in amplitude relative to the center one.

The effects of the relatively poor collimation of the parabolic torus are severe enough at 2.695 GHz that a relatively complex feed is required. The feed for that frequency is a 19-element slot array with the elements located on a triangular lattice and forming a hexagonal aperture. The amplitude and phase of the 19 slots have been optimized for best overall performance, as discussed in Paragraph 3.1.2.3.

Vertically polarized dipole arrays for 0.61 Ghz and 1.413 GHz integrate well with a horizontally polarized slot array for 2.695 GHz, with the slot array forming the ground plane for the dipole arrays. The slot array, being cross polarized relative to the dipoles, can "look through" the dipoles with little degradation. A feed array with the opposite polarizations (0.61-H, 1.413-H, and 2.695-V) is located diametrically opposite on the feed wheel to give dual polarized operation.

The baseline configuration of all feeds on the feed wheel is shown in Figure 2-1. Eight locations spaced 45 deg. apart on the feed wheel are used. All feeds are dual frequency and dual polarized except for the lowest three bands, which have three frequencies with one polarization each.

For each dual frequency feed, the presence of the higher frequency aperture in the center of the lower frequency aperture will cause degradation of main beam efficiency at the lower frequency. The patterns of the primary feed will narrow and the sidelobe levels will increase due to the aperture blockage, causing primarily an increase in spillover past the subreflector. A suitable dual frequency concentric feed must be developed and the magnitude of this degradation would be determined at that time. All of the drawings, designs, and analyses in this report deal with this baseline feed layout, but the analysis does not include the blockage effects.
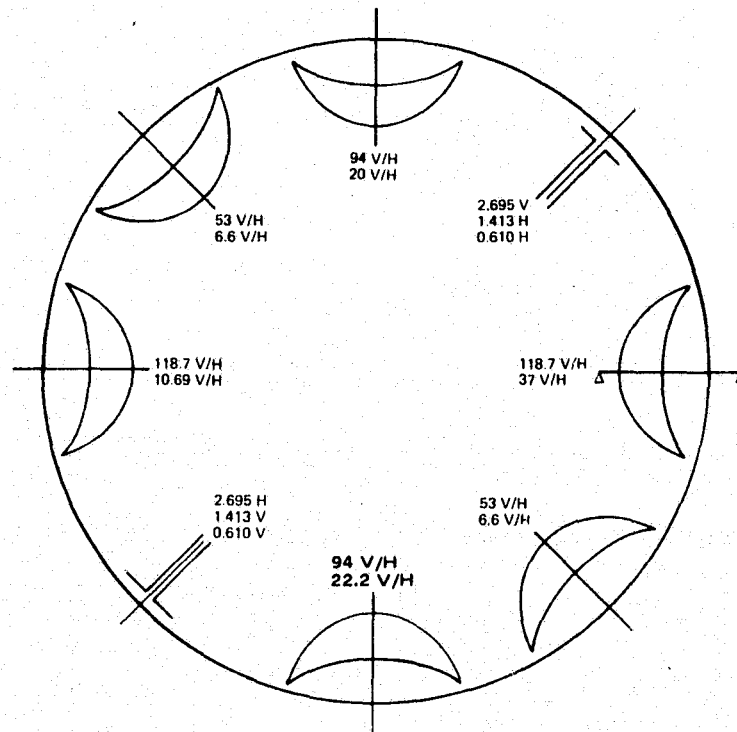
Figure 2-1. Baseline Feed Layout

An optional alternative feed layout is shown in Figure 2-2. Here 10 feed positions spaced 36 deg. apart are used. The primary advantage of this layout is that only two dual concentric feeds are used, 6.6/94 and 10.69/118.7 GHz. The frequency separation here is more than 10:1 so the blockage degradation effect will be minimal. There are several disadvantages, however, so the alternate configuration should only be used if the baseline proves to have too much blockage. The disadvantages are:

1. More subreflectors (eight rather than six).

2. Less room for flanges around the subreflectors. These flanges would be used to direct the spillover energy to areas where it will be absorbed, hence improving beam efficiency and enhancing coupling to the calibration cavity.

3. A filter is required to separate 20 and 22 GHz, which share a common horn aperture. This will increase losses in these two channels.

This optional configuration will not be considered further in this report.
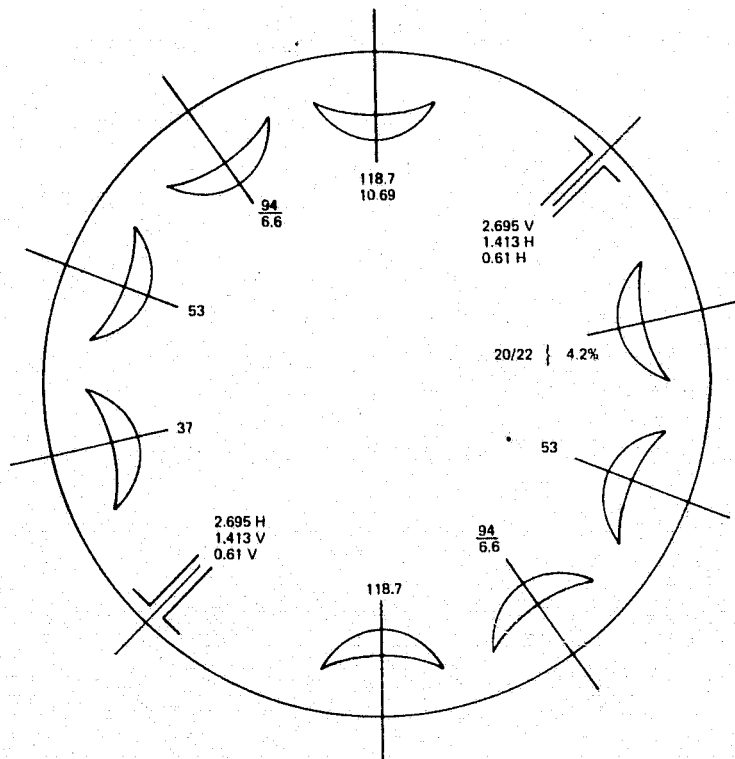
Figure 2-2. Optional Layout with 10 Feed Locations

Figure 2-3 shows the feed layout for Alternative 2. Eight feed locations with only one dual concentric feed (6.6/94 GHz) would be used. Because four feeds are included for the highest frequency, the rotation speed required to give contignous coverage on the earth will be only 2.1 rps rather than the 5.4 rps required for two feeds at 118.7 GHz.

Calibration Loads

As each feed rotates, it will pass through a warm and a cold calibration enclosure. These enclosures consist of a plane of absorber above the feeds in the vertex plane of the reflector, a plane of absorber below the feeds, and a cylindrical section of absorber on the outside of them. Thermal emission from external sources will have to reflect off at least two absorber surfaces in order to reach the feed, so the effective absorbtivity of the calibration load is correspondingly better than that of the absorber surface itself. Consequently, a thin and broadband free space absorber with -20 dB reflectivity can be effectively used.

The calibration targets require keeping all feed assemblies below the vertex plane in order to avoid mechanical interference. The feed assembly for the lowest three bands is centered 17.08 cm below the vertex plane to ensure this. As a result the antenna beams are elevated above the horizontal plane in these three bands.
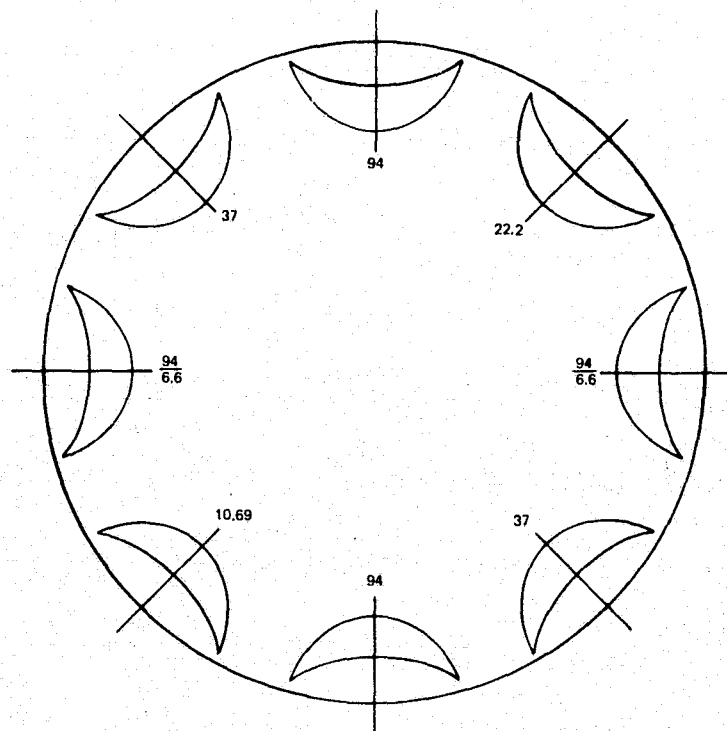
Figure 2-3. Feed Configuration for Alternative 2 Frequencies

Radiometers

The specific design of the radiometers is not covered in this report. However, the radiometer block diagram is shown in Figure 2-4. The radiometer can be packaged in two parts as shown. This allows placing Package A, which can be quite small, very close to the feed. Package B would then be placed in its normal location closer to the center of the feed wheel. This split packaging concept would be used in the highest frequency channels to avoid the losses of long millimeter waveguide runs. In addition, because Package B is connected with coax its position can be adjusted to balance the feed wheel.

Power Supplies

Power is transmitted to the feed wheel using non-contacting inductive coupling. This power is rectified, filtered, and regulated in power supplies which are located on the feed wheel.

Data Link

The video data will be multiplexed onto a Ku-band carrier and transmitted off the feed wheel using a non-contacting "data link". This requires a Ku-band transmitter and modulator on the feed wheel.

2.2.2 Mechanical Design

2.2.2.1 General/Overall Description

The SIMS-A conceptual design antenna to which this specification applies is shown positioned in the Space Shuttle Orbiter payload bay in Figure 2-5. The antenna is provided with three retention trunnions which are latched by three non-deployable (bolt-down) load retention fittings along the payload bay door longerons and one fitting which is captured by a payload bay keel fitting. All Orbiter fittings and fitting locations are standard and no special components are required. Except
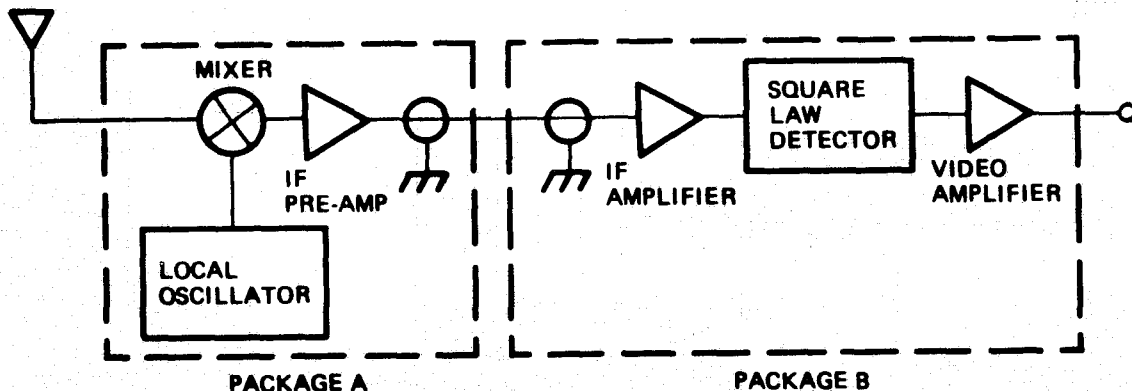
Figure 2-4. Radiometer Block Diagram
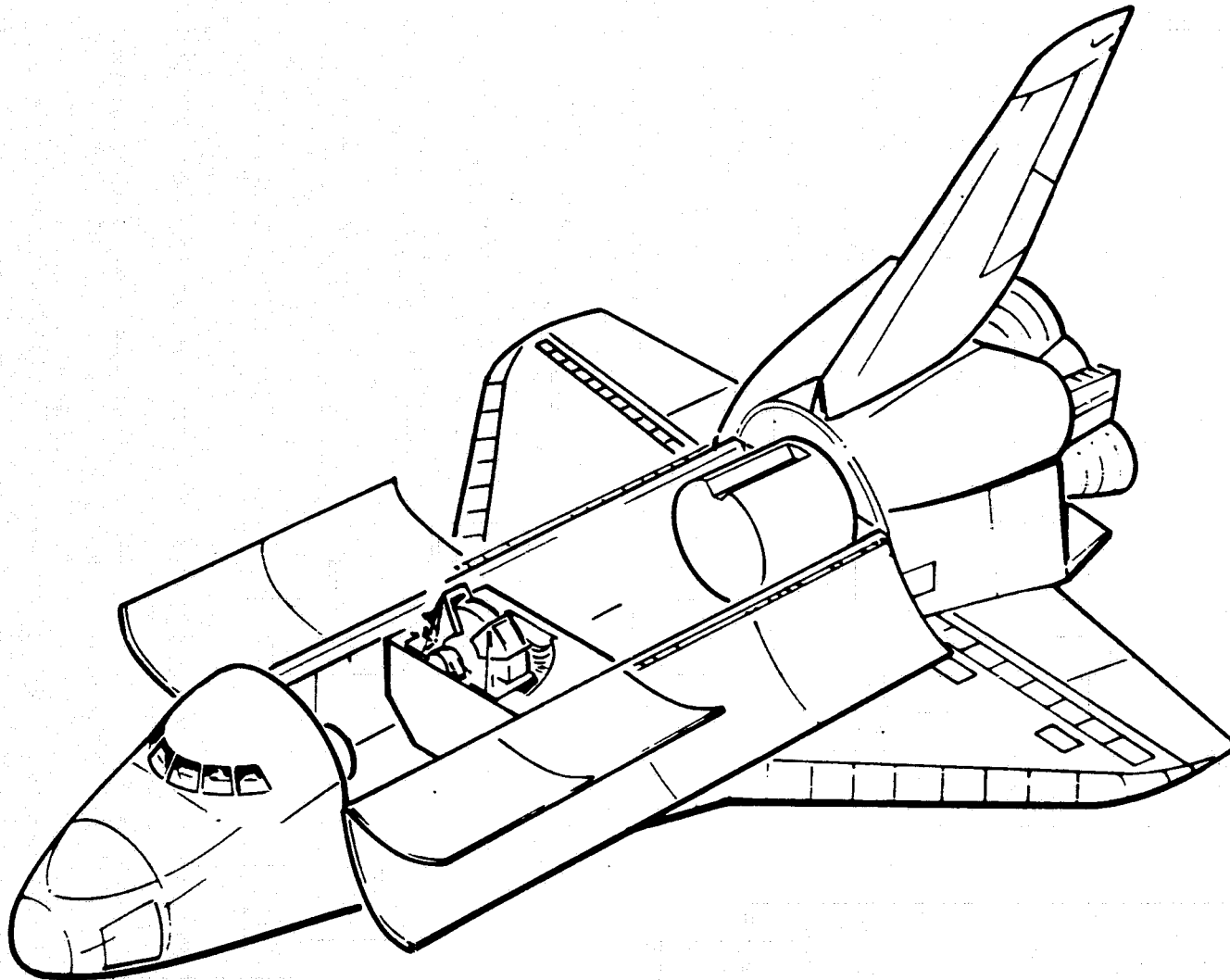
Figure 2-5. Orbiter with SIMS-A Antenna

for electrical connections, there are no other physical interfaces between SIMS-A and the Orbiter. However, there are antenna performance parameters which may be considered as Orbiter/payload interface items. These are discussed in Para. 2.3.2.1.

Figure 2-6 is a perspective sketch of the antenna alone and Figures 2-7 and 2-8 comprise a three view drawing (CRB751101) which identifies all antenna sub-assemblies and major components. The antenna main frame is a truss structure which provides load paths from all areas of the antenna to the retention trunnions. The trunnions are capable of transfering all antenna loads into the orbiter retention fittings without failure. The truss structure also provides nodal points which support the parabolic torus primary reflector surface. Additionally, the main frame provides a truss wall for support of the feed wheel drive mechanism and the radio-meter calibration target housings. The drive mechanism assembly contains the drive motor, gears, bearings and drive shaft required to drive the rotating feed wheel at its required speed. The rotating feed wheel, keyed to the drive shaft, con-tains the sub-reflectors, feed horns, feed arrays, waveguides, radiometers, data link and power supplies which are required to achieve the RF performance require-ments. Radiometer calibration targets wrap around the feed wheel in areas outside the main beam scan area. The housings are attached to the antenna main frame. The speed control is accomplished by using an AC synchronous motor synchronized to a 400 Hz power source. An encoder keyed to the drive shaft indicates shaft position with a digital output.

2.2.2.2 Detailed Descriptions

Rotating Feed Wheel

Figure 2-9 (2 sheets) is a drawing of the feed wheel (CRB 751007). The wheel is made from two honeycomb sandwich discs spaced about six inches apart by eight radial honeycomb sandwich ribs and eight honeycomb sandwich circular ring segments. The ribs are continuous from hub to outer end, while the circular ring segments fit between the ribs. Spokes on the hub are bonded between the face sheets of the rib-panels. The arrangement of these components forms eight approximately trapezoidal compartments between the hub wall, circular ring seg-ments and ribs. Access to these compartments is provided by making the section of the outboard (away from the drive shaft) disc between the hub and circular ring into a removable door. The door is shear pinned to the ribs so that the door participates in resisting bending of the wheel assembly. All electronic hardware except power supplies, radiometers and feed components are installed in the compartments. There are provisions for mounting 32 radiometers and 32 power supplies on the wheel although only 30 of each are required. The extra locations may be used to distribute balance weights as required. The outboard disc has attached to its inner (between discs) side 16 radiometers and to its outer side all of the power supplies. The 16 remaining radiometer locations are on the outer side of the inboard (drive shaft side) disc and these radiometers are for the high frequency feed at each of the subreflector locations. The high frequency feeds are connected to their respective
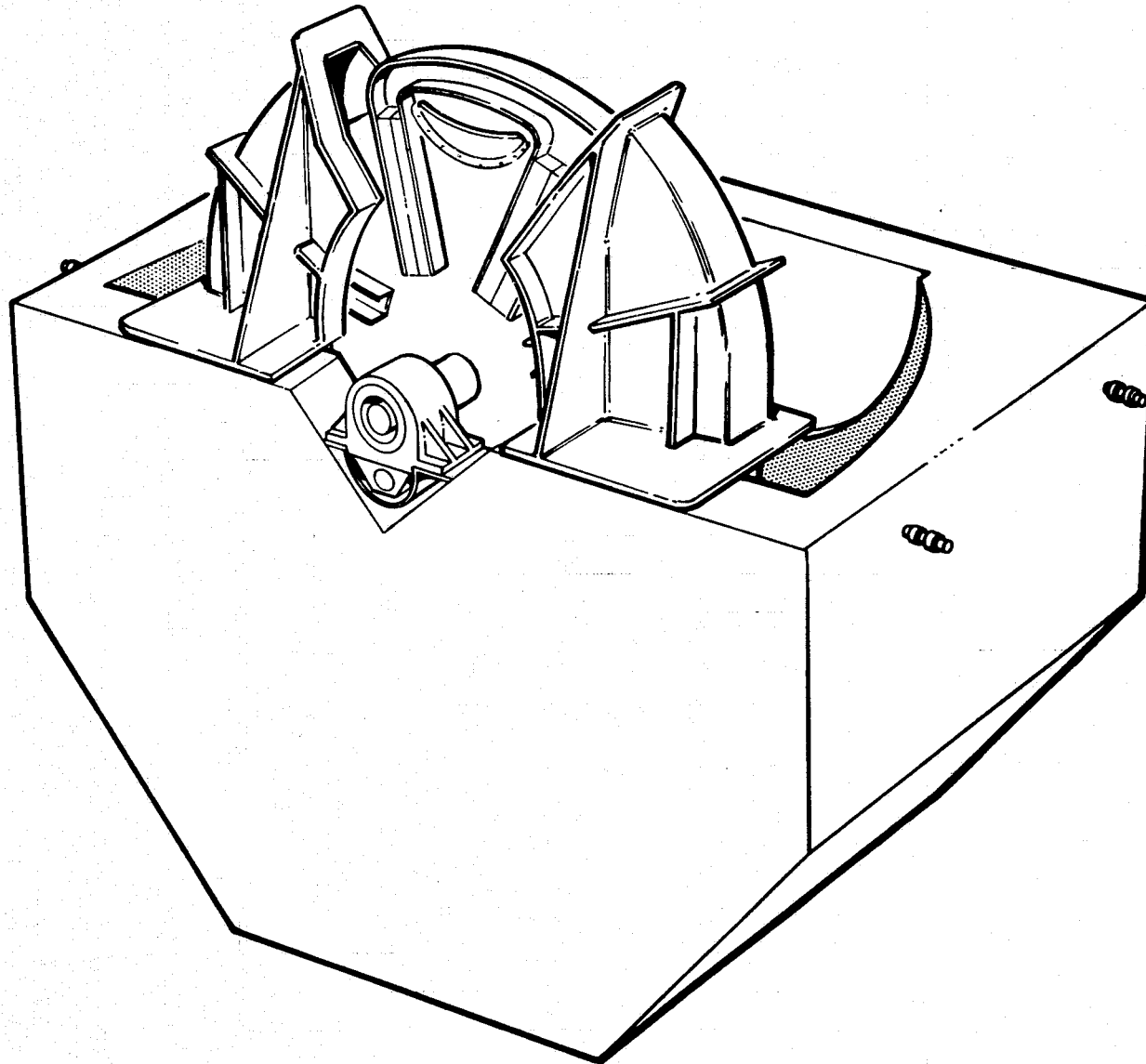
Figure 2-6. Antenna Perspective View

radiometers by coaxial lines, therefore the radiometers for those feeds can be adjustable with respect to radial distance from the hub and this feature may be used to obtain fine adjustments in dynamic balance of the wheel. There are six subreflectors fed by dual frequency concentric horns and two triple frequency arrays spaced at equal angles around the periphery of the wheel. The low frequency section of each concentric horn is connected to a turnstile junction which distributes the two polarizations through waveguides to the correct radiometer. The high frequency horn section is inside the lower frequency horn section and its waveguide is brought through the wall of the larger waveguide and connected to an orthomode transducer. Each output from the orthomode transducer is combined in a separate mixer assembly with the output from a local oscillator. The signal from the mixer is pre-amplified near the horn/transducer/mixer assembly and connected by coaxial cable to the correct radiometer. There are two feed support channels diametrically opposite each other on the wheel perimeter. Each channel supports the feed horns, waveguides, transducers, mixers, local oscillators and pre-amplifiers associated with three dual-frequency feeds.

Reflector/Main Frame

The reflector/main frame assembly shown in Figures 2-10 and 2-11 is a space truss structure composed of many tubular graphite-epoxy elements of 1.00 in. O.D and 0.125 in. wall thickness. In the aperture area the elements form nodes at approximately 15.00 in. spacing in orthogonal directions along the reflector contour. A 0.030 in. thick graphite-epoxy laminate shell (parabolic torus) is bonded to the nodes of the back-up structure. Three trunnion fittings and one tongue fitting conforming to Rockwell International Space Division's Drawing VC70-004105, Rev. A (See Appendix B) are built into the truss structure. These four fittings form the determinant four-point retention system used to mount SIMS-A in the Shuttle Orbiter payload bay. With the keel fitting and the two longeron fittings in the plane of the system center of gravity as shown on the drawing there are 63 candidate mounting locations using standard Orbiter hardware. Two trussed walls close out the ends of the structure and the one spanning the parabola axis side of the aperture has provisions for mounting the drive mechanism and the radiometer calibration targets. The aperture shell is made reflective by electro-deposited nickel.

Drive and Shaft Position Pickoff System

The drive mechanism for the rotating feed wheel is shown in schematic form in Figure 2-12 and as an assembly drawing in Figure 2-13 (2 sheets). The mechanism is an independent module attached to the trussed wall spanning the main frame assembly. Within its housing an AC synchronous motor with power factor correction drives the main shaft through a two stage helical gear train. An encoder, keyed to the shaft, provides shaft position data.

The graphite-epoxy drive shaft is supported in the housing on two 8.00 inch I.D. angular contact bearings. A 12.00 inch pitch diameter helical gear attached to the drive shaft is driven by the output gear of the intermediate shaft which is driven by the motor pinion. Overall reduction is 36.96:1.00. A brake is integrated into the gear train and is released when power is applied to the motor.

118.11 (REF)

37.10

CALIBRATION TARGET 2 REQD

CRB 751024

CRB 751024 1 REQD

CALIBRATION TARGET

SYSTEM CENTER OF GRAVITY

59.00 (REF)

16.00

6.00 (REF)

CRB 751007 1 REQD

111.00 (REF)

90.00 R
PAYLOAD ENVELOPE
(REF)

CRB 751030 1 REQD

A

CRB 751007

57.0 R.

RB 751024

I REQD

TION TARGET

CENTER LINE O
PAYLOAD BAY (RE
$z_0 = 400$

REFLECTOR CONTOUR AT
APERTURE LIMITS (RE

.00 R
D ENVELOPE
REF)

CRB 751030
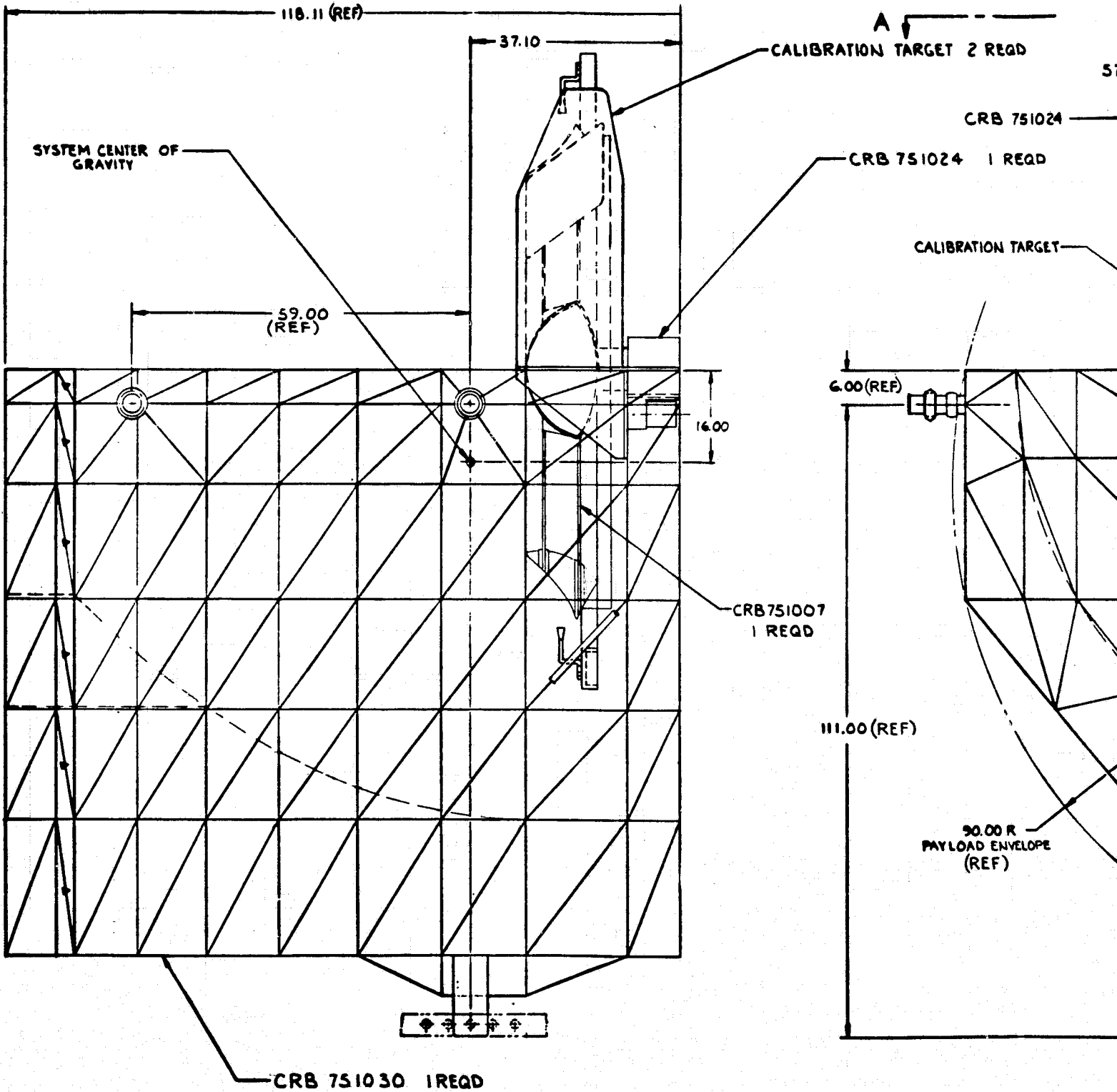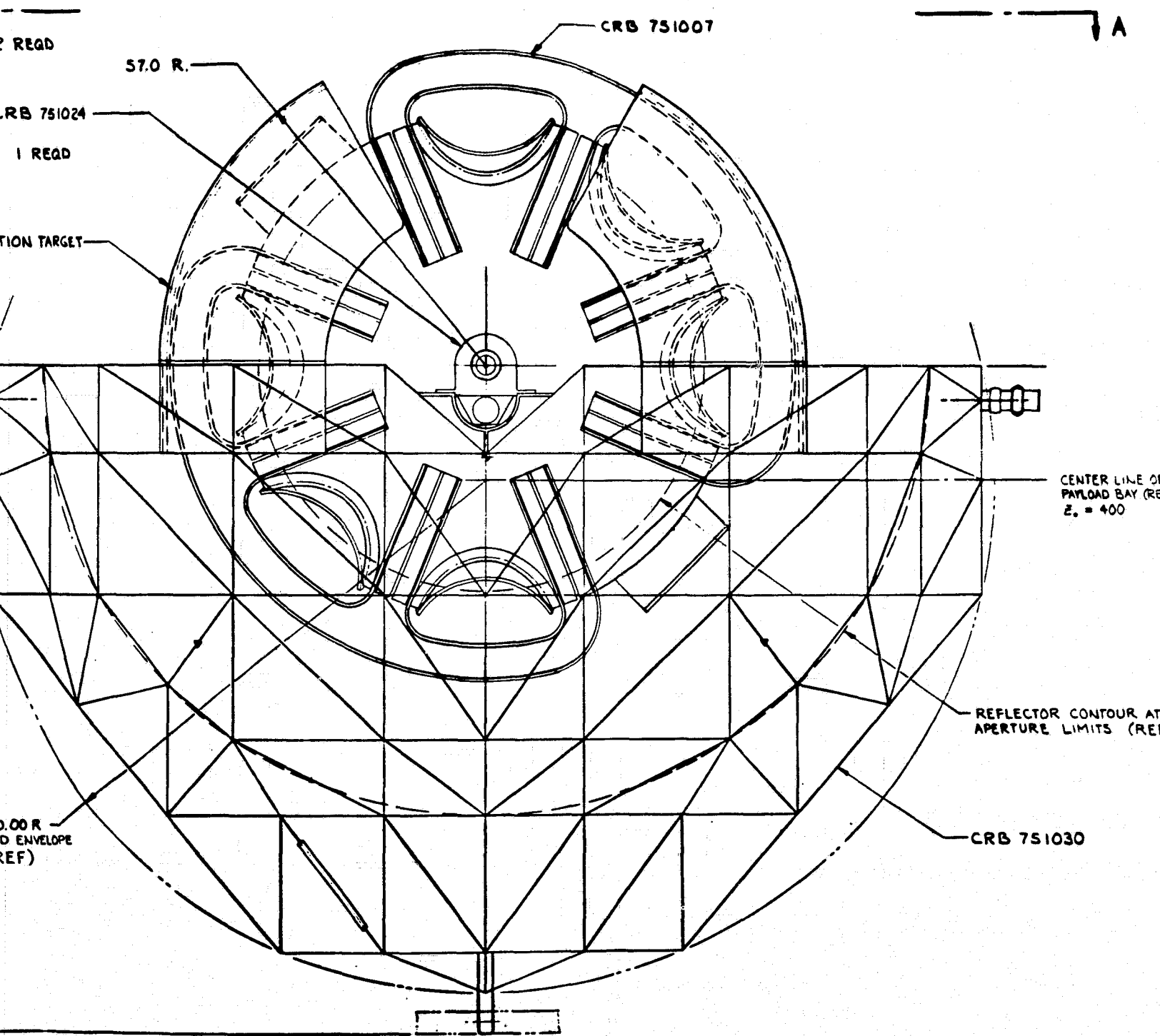
Figure 2-7. Antenna - End and Side Views
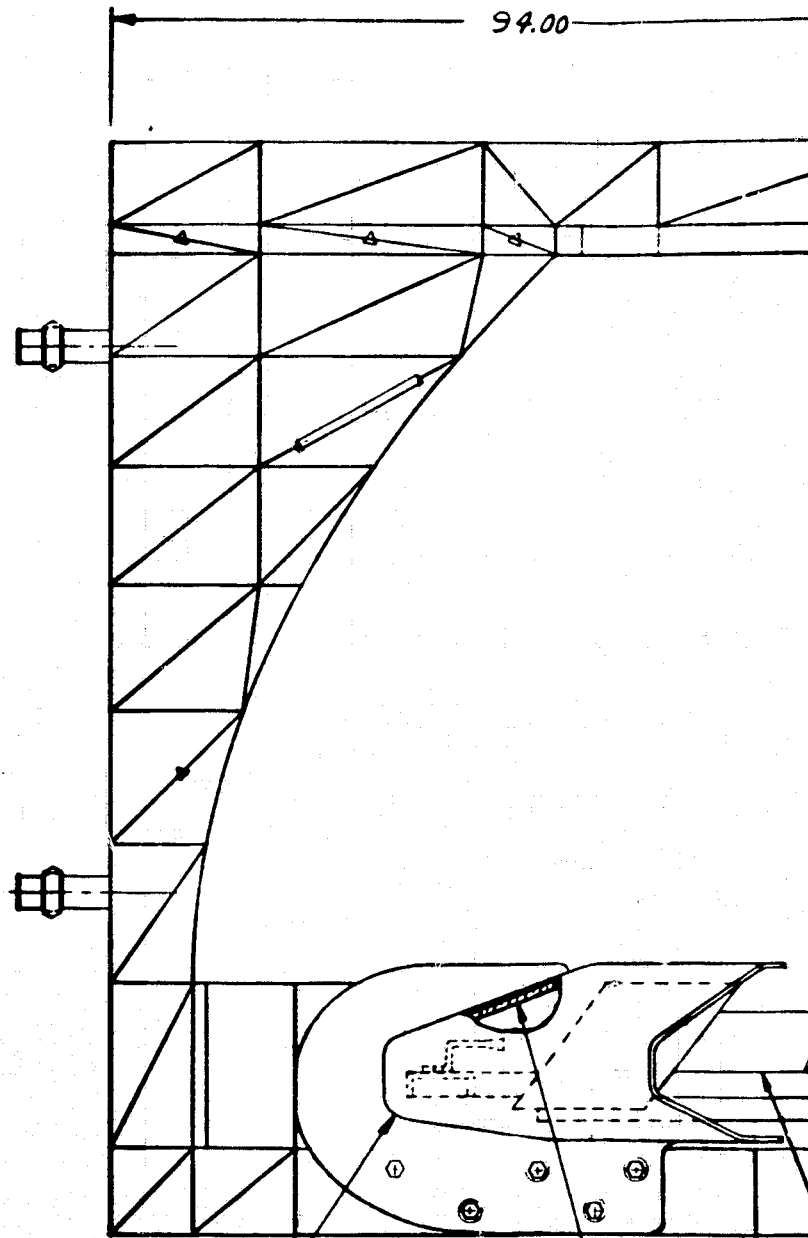
FOLDOUT FRAME

94.00

—TARGET ABS⌐

—CALIBRATION TARGET HOUSING
FIBERGLASS HONEYCOMB SANDWICH

VIE⌐

00 —|— 94.00 —|

CRB 751030

CRB 751007   CRB 751024

TARGET ABSORBING MATERIAL

T HOUSING
COMB SANDWICH
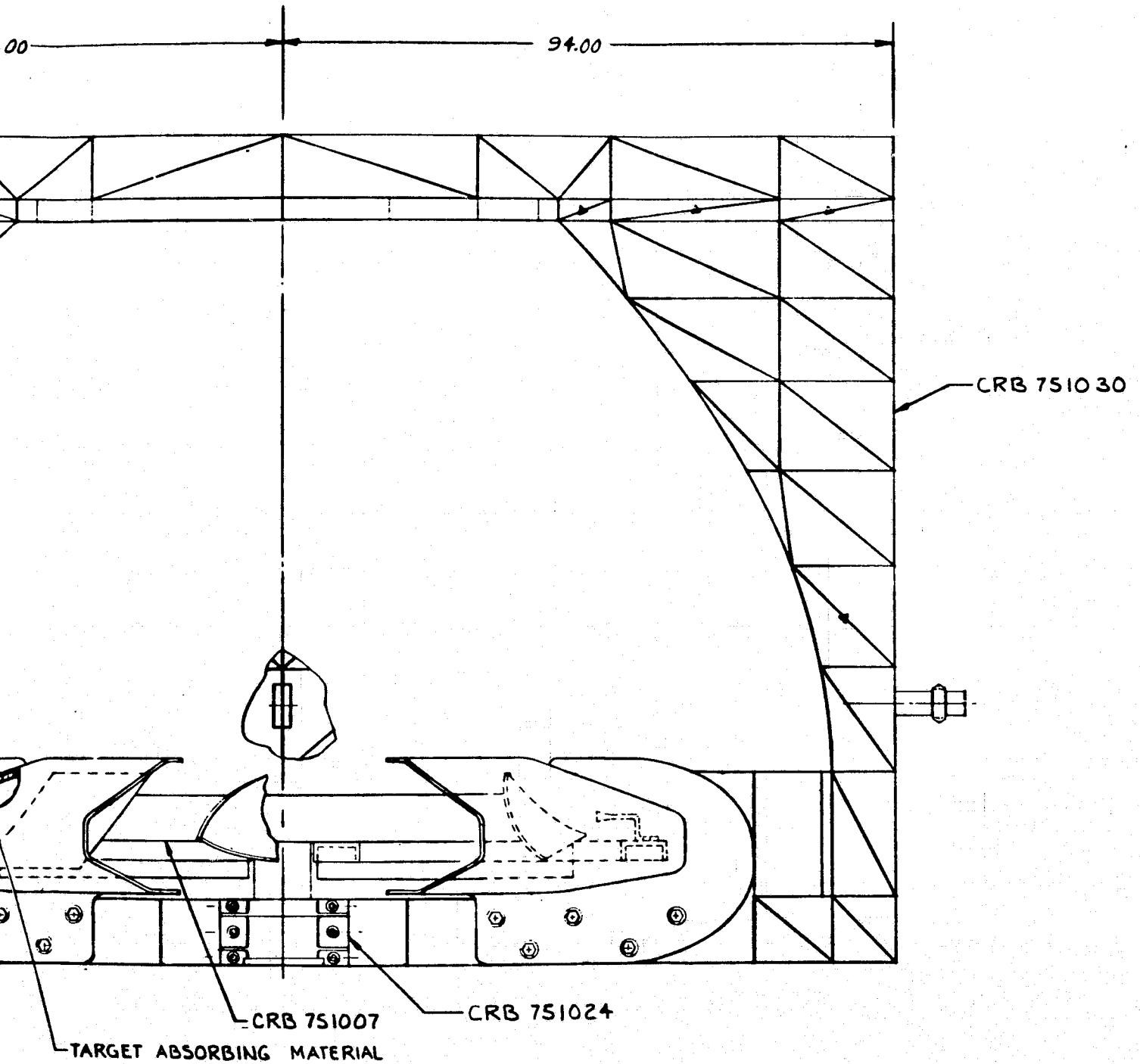
VIEW A-A

Figure 2-8. Antenna Plan View

2-13/2-14

FEED SUPPORT 2 PLACES

LOW FREQUENCY
RADIOMETERS

HIGH FREQUENCY
RADIOMETERS

VIEW A-A

J

J

DUAL FREQUENCY / DUAL POLARIZATION
CONCENTRIC FEED 6 PLACES
OUTER - 20.00 GHz
INNER - 94.00 GHz

GREGORIAN SUB-REFLECTOR 6 PLACES

OUTER - 6.60 GHz
INNER - 53.00 GHz

TRIPLE CHANNEL FEED ARRAY 2 PLAC
0.610 GHz VERT
1.413 GHz VERT.
2.695 GHz HORIZ.

A

TURNSTILE
JUNCTION

D

44.29 R

POWER SUPPLIES

RADIOMETERS

55.50 R

OUTER - 37.00 GHz
INNER - 118.70 GHz

R - 10.69 GHz
R - 118.70 GHz

D

3.00 TYP

G

4.50 TYP

ER SUPPLIES
REQD (32 SHOWN,
RE DUMMY)

2.50 TYP

6.25 TYP

B   B

RADIOMETERS
POWER SUPPLIES

G

C   C

VIEW G - G

0.610 GHz HORIZ
1.413 GHz HORIZ
2.695 GHz VERT.

A

OUTER - 22.00 GHz
INNER - 94.00 GHz

OUTER - 6.60 GHz
INNER - 53.00 GHz

Figure 2-9.   Feed Wheel Drawing (Sheet 1 of 2

2-15/2-16

FOLDOUT FRAME

20.47 TYP

8.00

SECTION J-J FULL SIZE

.50 TYP

7.00

GRAPHITE-EPOXY LAMINATE
.031 THICK BOTH SIDES ALL
PANELS

GRAPHITE-EPOXY- ⅜ CELL
6.0 LB/FT³ HONEYCOMB CORE
.75 THICK IN WEB
.44 THICK IN FLANGES

.812

3.00
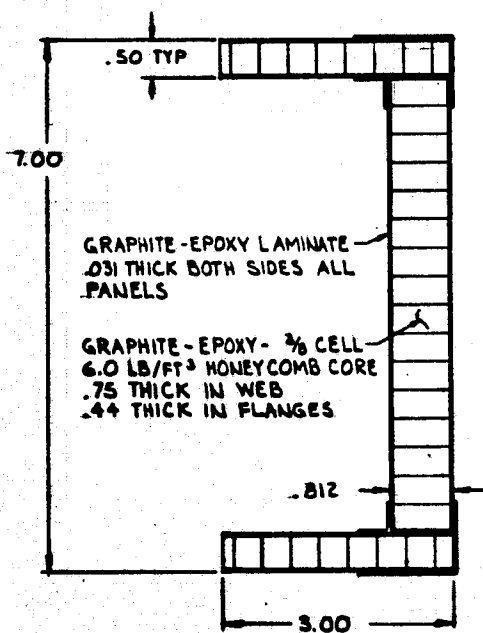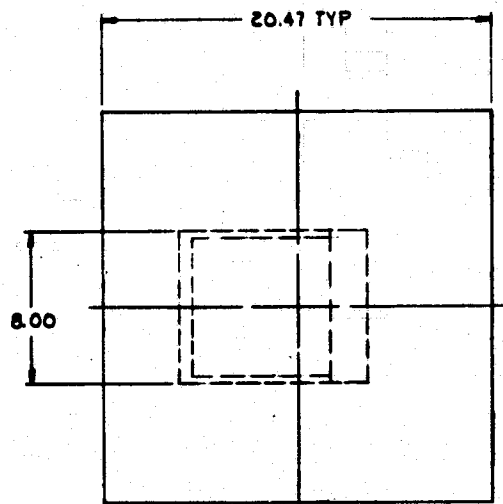
.812 THICK ARRAY
SUPPORT PANEL

GRAPHITE-EPOXY LAMINATE-.031
THICK BOTH SIDES ALL PANELS

GRAPHITE-EPOXY - ⅜ CELL
6.0 LB/FT³ HONEYCOMB
CORE.

.437 THICK BOX
SECTION WALLS

SECTION D-D ¼ SIZE

.031 4

.3
2 P

6.376

GRAPHIT
JOINING

NICKEL PLATING

VIEW E-E   ¼ SIZE

6.000

.188

VIEW C-C   ¼ SIZE

.031 TYP

.75

SECTION H-H

.125

GRAPHITE-FPOXY-
CELL - 6.0 LB/FT²
HONEYCOMB CORE

BOSS AS REQD AT BOLT
& DOWEL LOCATIONS

1.50

1.50

GRAPHITE-EPOXY LAMINATE

GRAPHITE-EPOXY LAMINATE 2 PLACES

.625

.062 2 PLACES

DETAIL F   - FULL SIZE

.031 4 PLACES

.375
2 PLACES

GRAPHITE-EPOXY - ⅜ CELL-
6.0 LB/FT² HONEYCOMB CORE

.75

6.376

H   H

.031 2 PLACES

GRAPHITE-EPOXY
JOINING STRIP

GRAPHITE-EPOXY LAMINATE TYPICAL

.040 TYP

.44 TYP

.28 TYP.
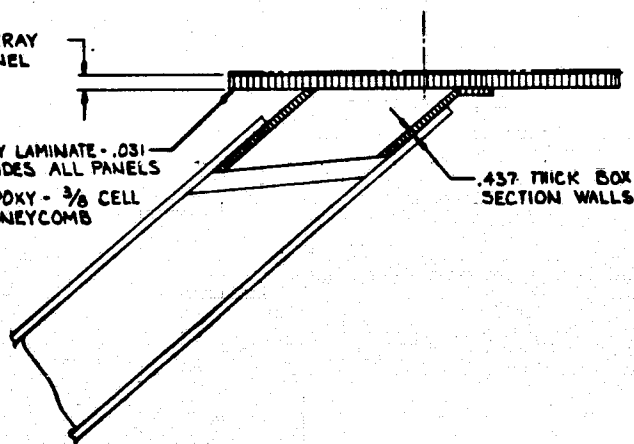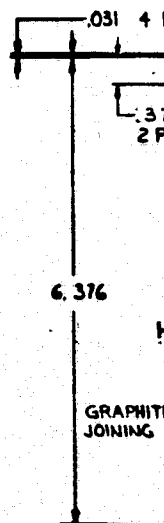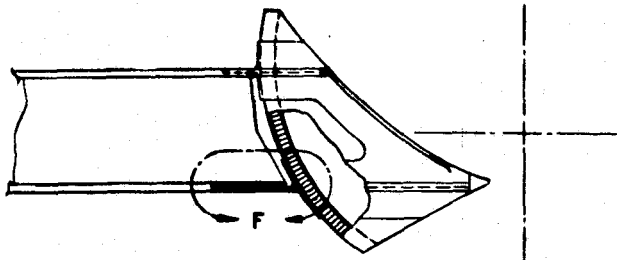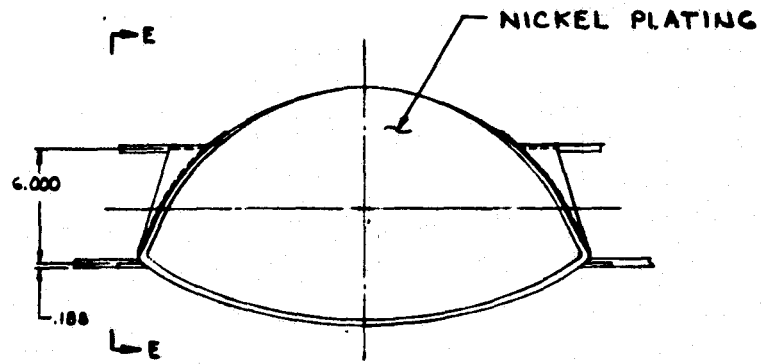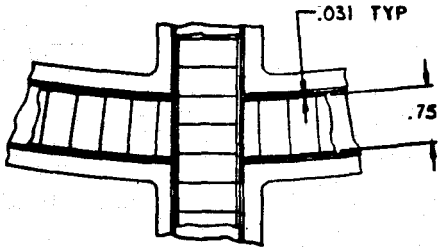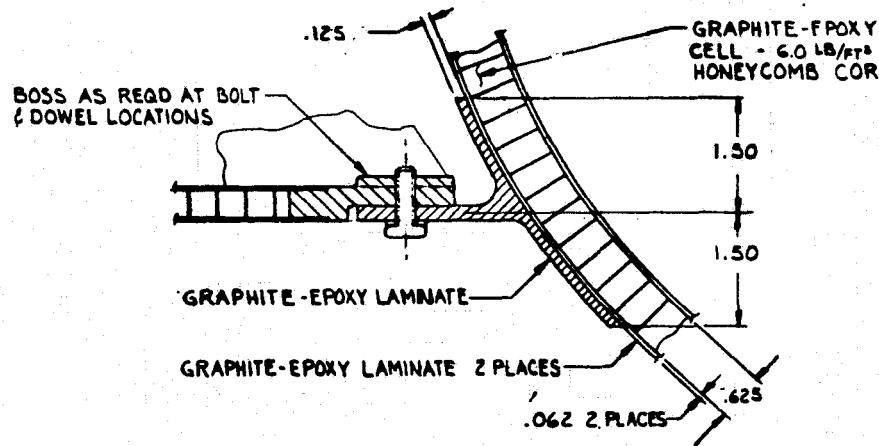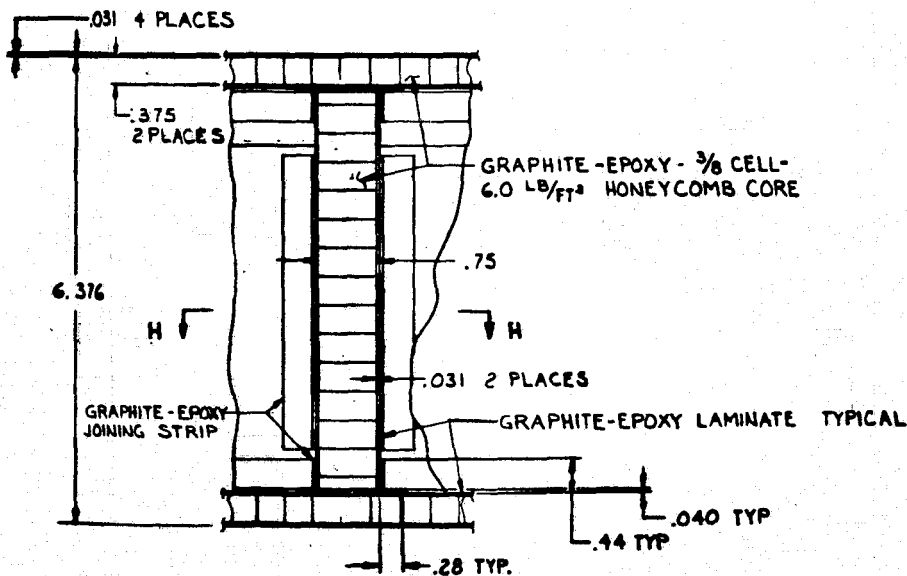
SECTION B-B   FULL SIZE

Figure 2-9.   Feed Wheel Drawing (Sheet 2 o

2-17/2-18

118.11

59.00

37.10

TYPICAL PAYLOAD MOUN
PER ROCKWELL DWG V
ORBITAL FLIGHT CON
CHANGE NO. OF JSC

A

6.00

16.00

78.74

111.00

24.00

PA

REFLECTOR CONTOUR
AT ANTENNA CENTER
LINE

12.00

78.74 (APERTURE)

17.87

9.50
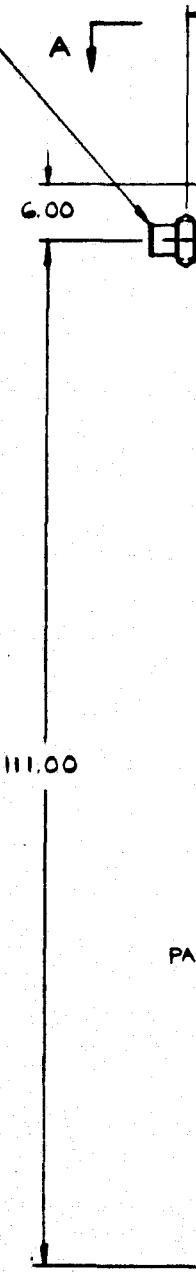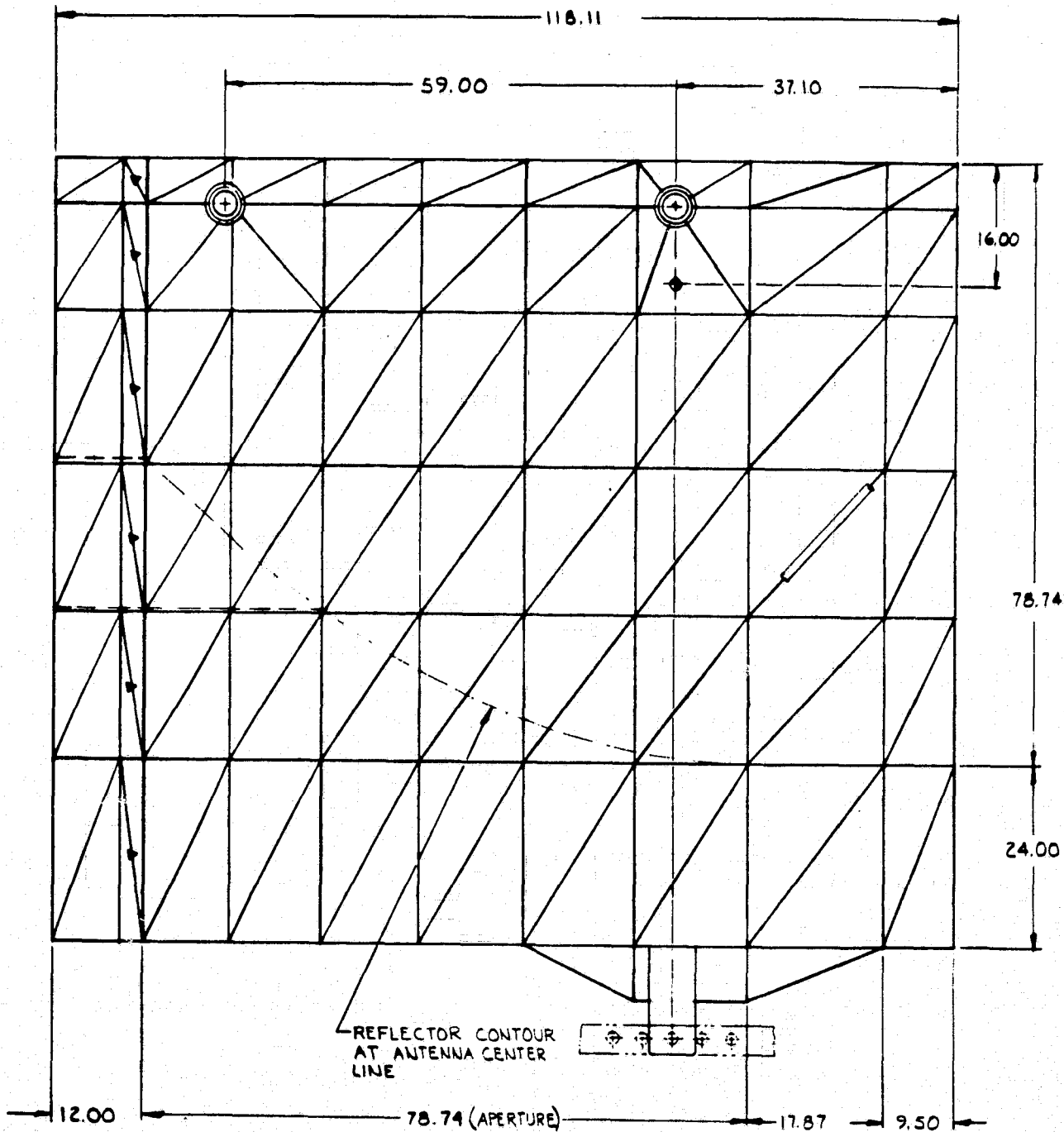
3. ELEMENTS CODED
   SIMULATION
2. THE TRUSS STRU
   ANALYZED USING
   DIMENSIONAL INF
   THE COMPUTER
1. DIMENSIONS ARE
NOTES:

Figure 2-10. Reflector/Main Frame Assembly - Side a[...]

Labels on drawing:

G TRUNNION 3 PLACES
-004105 REV A. FOR
URATION SEE APPROPRIATE
700 VOL. XIV

ANTENNA CENTER LINE
PAYLOAD BAY CENTER LINE

DRIVE MECHANISM (CRB 75102G) REF

DRIVE MECHANISM SUPPORT

94.00 TYPICAL

SYSTEM C.G.

90.00 R
AD ENVELOPE

PAYLOAD KEEL TONGU
PER ROCKWELL DWG \
FOR ORBITAL FLIGHT C(
APPROPRIATE CHANGE N
VOL. XIV
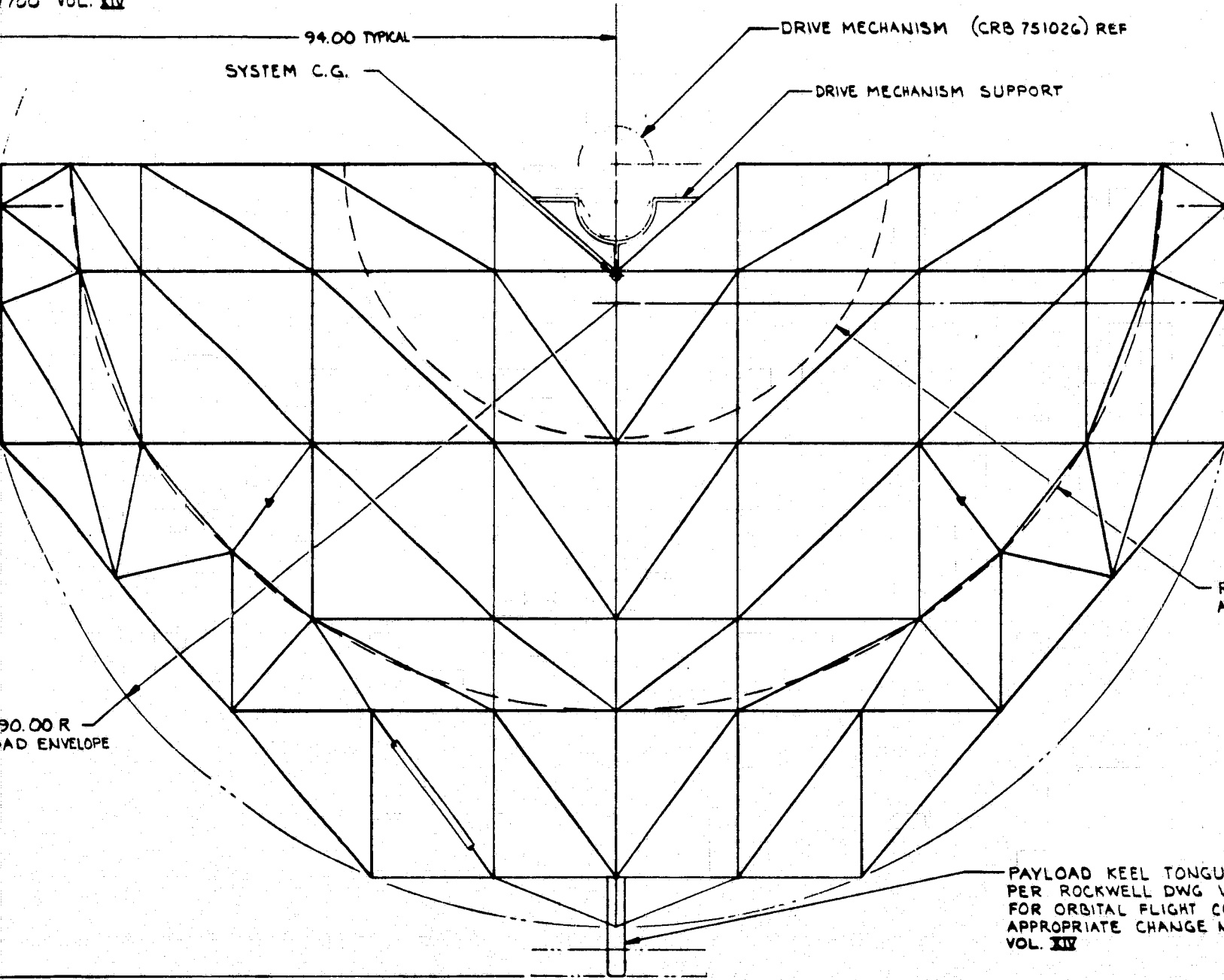
WERE ADDED AFTER COMPUTER

URE SHOWN WAS MODELED AND
HE NASTRANS COMPUTER PROGRAM.
ATION NOT SHOWN IS AVAILABLE IN
TPUT DATA.
N INCHES

2-19/2-20

ANTENNA CENTER LINE
PAYLOAD BAY CENTER LINE

— DRIVE MECHANISM (CRB 751026) REF

O TYPICAL

— DRIVE MECHANISM SUPPORT

A SHEET 2

—20.00

CENTER LINE OF
PAYLOAD BAY (REF)
$Z_o = 400$

— REFLECTOR CONTOUR AT
APERTURE LIMITS

PAYLOAD KEEL TONGUE   I PLACE
PER ROCKWELL DWG VC 70-004105 REV. 'A'
FOR ORBITAL FLIGHT CONFIGURATION SEE
APPROPRIATE CHANGE NO. OF JSC-07700
VOL. XIV
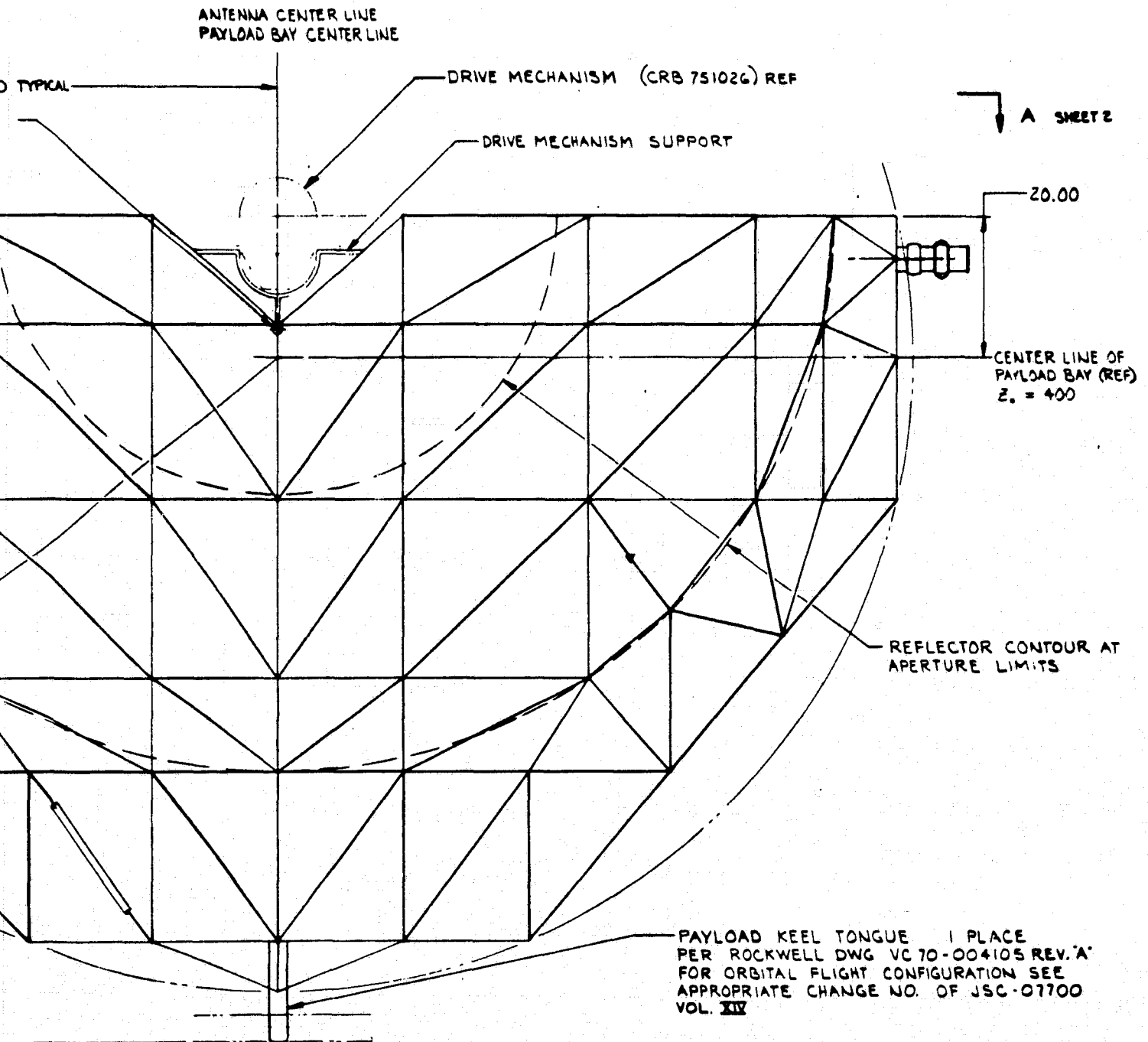
Figure 2-10. Reflector/Main Frame Assembly - Side and End View

CYLINDRICAL TRUSS ELEMENTS
ARE GRAPHITE-EPOXY. FIBER
ORIENTATION IS UNIDIRECTIONAL

1.00

.750

DETAIL B FULL SIZE

REFLECTOR SHELL - .030 GRAPHITE-EPOXY
WITH VAPOR DEPOSITED ALUMINUM REFLECTIVE
COATING

87.72   87.72

B
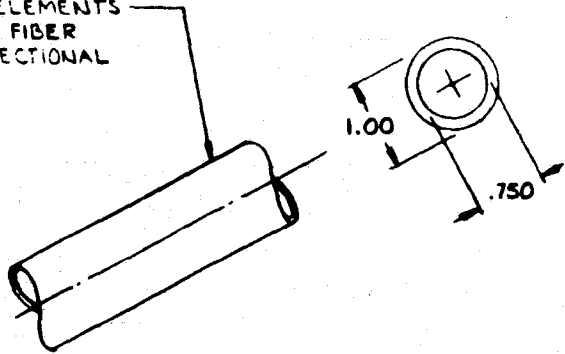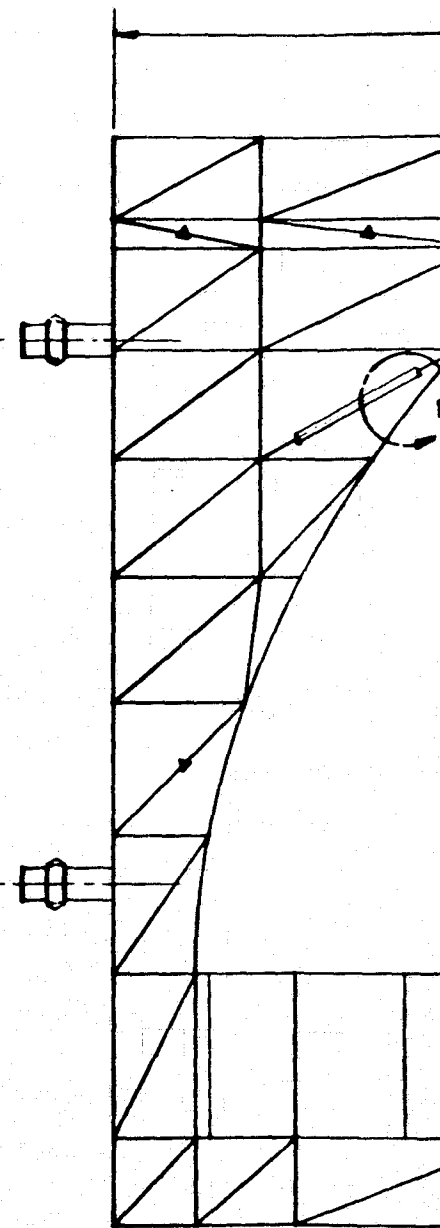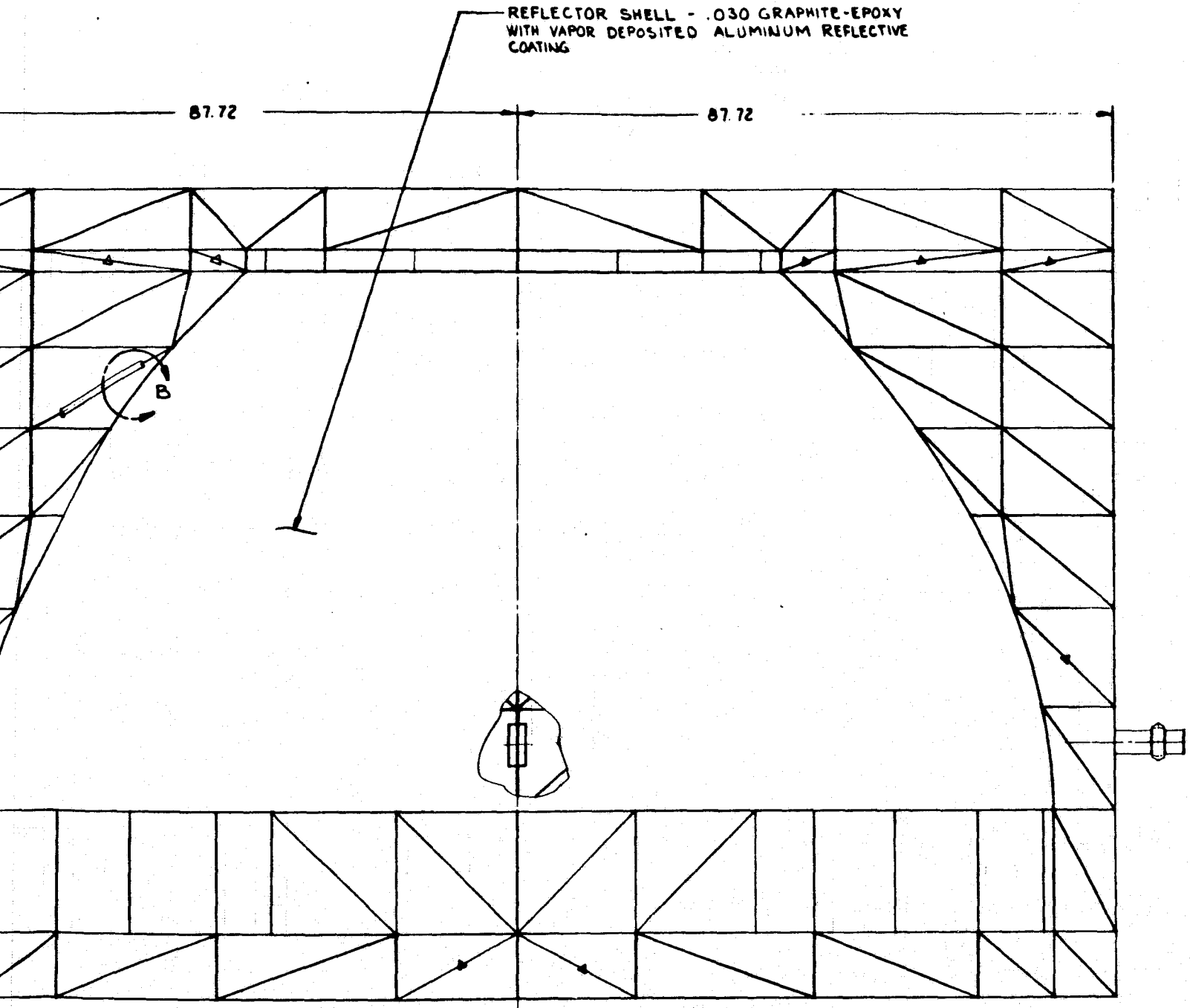
Figure 2-11.   Reflector/Main Frame Assembly - Plan View

2-21/2-22

PRIME POWER
115/200V RMS
3 PH, 400 Hz

MOTOR SYNC SPEED
12,000 RPM

ϕA

ϕB

ϕC

SYNCHRONOUS
MOTOR

RUN PF CORR

NEU.

N

1

$N = 36.962429$

θ

$f_{vis} = N^2 f_m + f_L$

θ SYNC = 324.65398 RPM

APPLY POWER
TO RELEASE

RETURN

BRAKE

θ

LOAD
INERTIA

+6 VDC

-6 VDC

COMMON

/3

13 LINE
SELF-DECODING
NATURAL
BINARY
ENCODER

$\dot{\theta}$

$J_T = N^2 J_m + J_L$

DATA READY

(0.0439°) LSB 1

/13

360° = 8192 COUNTS WITH
22.56 μS DWELL TIME PER
COUNT AT SYNCH SPEED

2

3

4

5

6

7

8

9

10

11

(90°) 12

(180°) MSB 13

$\dot{\theta}$	= ANGULAR VELOCITY
f_{vis}	= TOTAL VISCOUS DAMPING COEFFICIENT
N	= GEARING REDUCTION RATIO
f_M	= VISCOUS DAMPING COEFFICIENT OF MOTOR
f_L	= VISCOUS DAMPING COEFFICIENT OF LOAD (BEARINGS)
J_T	= TOTAL INERTIA
J_M	= INERTIA OF MOTOR
J_L	= INERTIA OF LOAD (WHEEL, SHAFT, ETC)

Figure 2-12.   Drive and Encoder Schematic

SEE SH 2 OP2   B →

MAIN DRIVE GEAR
SEE SH 2 OP2

PILLOW BLOCK HSG.
SEE SH 2 OP2 FOR
ENCODER MTG DETAIL

MAIN BRG MTG FLANGE
P/O PILLOW BLOCK HSG.

MAIN BEARING
SEE SH 2 OP2

MAIN DRIVE SHAFT

DOWEL PI
BOTH SIDES
TO MAINTAIN
ALIGNMENT

CLEARANCE IN MOTOR MTG FLANGE
FOR BORING INTERMEDIATE SHAFT
BEARING SEAT

DRIVE MOTOR
SEE SH 2 OP2

11.00
MTG KEY FOR PILLOW
BLOCK HOUSING

GRAPHITE EPOXY STRUCTURE

B →

A-A

MAIN DRIVE GEAR

TRANSFORMER
PRIMARY MTD TO SHROUD ATTACHED TO PILLOW BLOCK
SECONDARY ATTACHED TO MAIN DRIVE SHAFT

THRUST

THRUST

THRUST

WHEEL MTG FLANGE

MAIN DRIVE SHAFT

FEED WHEEL ASSEMBLY
SEE DWG CRB-751007
(KEYED TO MAIN DRIVE SHAFT

BEARING BOSS FOR INTERMEDIATE GEAR SHAFT
P/O PILLOW BLOCK HOUSING

MOTOR MTG FLANGE
P/O PILLOW BLOCK HSG.

GENERAL NOTES

ALL MOVING PARTS WHICH REQUIRE LUBRICATION
TO BE TREATED WITH "VAC-KOTE" BY BALL
BROTHERS RESEARCH CORP - BOULDER, COLORADO.

MATERIALS TO BE SELECTED FOR MINIMUM
DIFFERENTIAL EXPANSION/CONTRACTION IN
SPACE ENVIRONMENT (-95°C TO +82°C)
OPERATING TEMPERATURE (-95°C TO -37°C)

Figure 2-13. Drive System Drawings (Sheet 1 of 2)

FOLDOUT FRAME

24.25

9.50   0.25

**MAIN DRIVE GEAR - 16 PITCH -
20° HELICAL · 20° PRESSURE ANGLE
11.5625 PITCH DIA · 185 TEETH -**

6.375

**PILLOW BLOCK HOUSING
CONTAINS ALL MTG PROVISIONS
FOR DRIVE MECHANISM ELEMENTS
SEE SH 10P2**

**ANGULAR BEARINGS
KEENE CORP TYPE A
KF080 AHO
8.00 BORE ×.75 WIDE
TYP 2 PLACES**

MAIN DRIVE SHAFT

**BEARING CLAMP
REMOVABLE SHIMS FOR
PRELOAD ADJUSTMENT**

**ENCODER - LITTON IND.
MODEL SNB 35-13L1**

**ENCODER SHAFT SPLINED
INTO BULKHEAD IN ROTATING SHAFT**

**ANGULAR BEARINGS
MPB CORP. - STAR D-17 - .625 BORE ×.25
MTD WITH SHIM ADJ FOR PRELOAD
TYP 2 PLC**

**ENCODER INPUT/OUTPUT
CONNECTOR**

**FIXED CAGE FOR
MOUNTING ENCODER**

**INTERMEDIATE SHAFT
2500 RPM**

**MOTOR PINION
12000 RPM**

**HYSTERESIS SYNCHRONOUS MOTOR
208 V · 3∅ · 400 HZ · 12000 RPM
STARTING TORQUE 80 OZ.IN.
ELECTRIC INDICATOR CO
TYPE 1148 (MODIFIED)**

**ADD PINION GEAR SHAFT AND
THRUST BEARINGS.
ROTATING PARTS TO BE
LUBRICATED WITH "VAC-KOTE"
BY BALL BROS. RESEARCH INC.**

**INTERMEDIATE GEAR - 16 PITCH
20° HELICAL · 20° PRESSURE ANGLE
1.500 PITCH DIA. · 24 TEETH**

**INTERMEDIATE GEAR - 24 PITCH
20° HELICAL · 20° PRESSURE
2.000 PITCH DIA · 48 TEETH**

MOTOR WIRING

27.38

14.00
MAX. WIDTH OF ROTATING

B - B
SEE SH1

**MOTOR PINION - 24 PITCH - L.H.
20° HELICAL · 20° PRESSURE ANGLE
.417 PITCH DIA · 10 TEETH · .50**

AR - 16 PITCH - R.H.
° PRESSURE ANGLE
IA - 185 TEETH - .50 FACE

—— 6.375 ——

FEED WHEEL ASSEMBLY
SEE DWG CRB·751007

8.00 DIA.
MAIN DRIVE SHAFT

ROTATION
(324.324 RPM)
(CLKWSE FACING FWD)

17 - .625 BORE x .25 WIDE
OR PRELOAD

KEY

7.25
BOLT CIRCLE

GEAR - 16 PITCH - L.H.
20° PRESSURE ANGLE
DIA. - 24 TEETH - .50 FACE

TE GEAR - 24 PITCH - R.H.
- 20° PRESSURE ANGLE
DIA - 48 TEETH - .375 FACE

WHEEL MTG FLANGE OMITTED

14.00
OF ROTATING WHEEL

24 PITCH - L.H.
° PRESSURE ANGLE
- 10 TEETH - .50 MIN FACE

Figure 2-13.   Drive System Drawings (Sheet 2 of 2)

The motor is a three-phase, 400 Hz, four-pole hysteresis type having the following characteristics:

Nominal rating	1/4 H. P.
Input	3 phase
frequency	400 Hz
voltage, line-to-line	200 Vrms
full load watts	365 watts
full load amps	3.85 amps
Synchronous speed	12,000 rpm
Torque developed	
starting	80 oz-in.
pull-in	25 oz-in.
pull out	27.2 oz-in.
rated	21 oz-in.

The shaft angle encoder is a self-decoding, natural binary, optical unit. It provides 2^{13} (8192) resolution in 360 deg. The binary word is provided on 13 parallel, TTL compatible, output lines with LSB (least significant bit) value of 0.0439453 deg. (2.6 minutes of arc). Mechanical characteristics are:

Operating speed (max.)	375 rpm
Slewing speed (max.)	3000 rpm
Starting torque req'd.	0.5 oz-in.
Running torque req'd.	0.4 oz-in.

Power factor correction to achieve unity power factor at synchronous speed is accomplished by inserting an estimated capacitance of 2.5 µF between each 400 Hz line and the neutral. The recommended capacitors are:

Qty.	Capacitance	Dimensions
3	1 µF	.75 in. dia. x 2.12 in. long
3	1.5 µF	1.00 in. dia. x 2.12 in. long

Metal case, glass to metal seal with polycarbonate dielectric.

400 VDC	240 V at 400 Hz

Calibration Target Housings

Each target housing is a channel cross-section, 60 deg. annulus shown installed in Figures 2-7 and 2-8. The channel cross-section wraps around the edge of the feed wheel enclosing the subreflector, feed horn, waveguides, and feed support channel. The target materials are attached to the inside of the housing with minimal clearance for the rotating wheel components. The three walls forming the channel are plastic honeycomb sandwich construction. The flat wall on the drive shaft side of the channel is attached to the drive mechanism support wall of the main frame.

2.3 PERFORMANCE OF THE BASELINE ANTENNA SYSTEM

2.3.1 Electrical (RF)

As noted previously, the antenna consists of a parabolic focus main reflector with a combination of Gregorian subreflector feeds and prime focus feeds for the various channels.

2.3.1.1 Gregorian Subreflector

A cross-section of the Gregorian subreflector contour in relation to the main reflector is shown in Figure 2-14. This concept is used for eight channels from 6.6 through 118.7 GHz. A normal Gregorian subreflector for use with a paraboloidal main reflector is an ellipsoid. With a torus, the subreflector surface is easily defined only in the plane X = 0, where the main reflector is exactly a parabola and the subreflector is exactly an ellipse. At all other points, the subreflector surface is chosen to maintain a constant path length between the feed and the aperture plane Y = 0. The analysis of this report defines the subreflector point corresponding to a given ray path. Given the point (X, O, Z) where the ray crosses the aperture plane, the point on the subreflector which connects that ray to the feed is precisely located by a FORTRAN subroutine GEODES given in the appendix, using a procedure outlined by Gustincic.[2] As discussed in Paragraph 3.1.1.1, the location of the feed and subreflector have been optimized for best overall performance. The parameters which define the optimized location are given in Table 2-1.
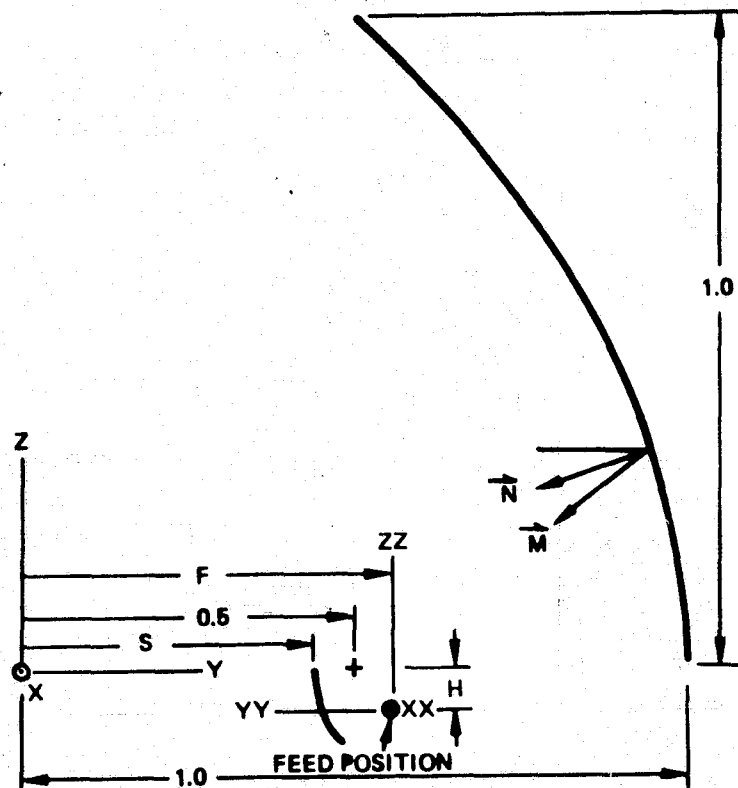
Figure 2-14.   The Antenna Geometry

Table 2-1. Subreflector Design Parameters

R = radius of Main Reflector = 2m

H = 0.0813 R

F = 0.5625 R

S = 0.4000 R

The periphery of the subreflector is also defined numerically. The aperture used is defined in the X-Z plane by two ellipses as shown in Figure 2-15. This aperture shape gives a smooth aperture contour which avoids flats that will degrade the sidelobe level. It also avoids the areas near the upper right and left corners that are not suitable for use due to severe torus phase aberrations in these areas.

An aperture diameter of 1.6 meters in both dimensions is therefore utilized. Projecting this dual ellipse aperture back along the geometric rays to the sub-reflector defines the subreflector contour, which is illustrated in Figure 2-16.

UPPER ELLIPSE SEGMENT

$$\left(\frac{X}{0.4}\right)^2 + \left(\frac{Z-0.3}{0.5}\right)^2 = 1; Z > 0.3$$

LOWER ELLIPSE SEGMENT

$$\left(\frac{X}{0.4}\right)^2 + \left(\frac{0.3-Z}{0.3}\right)^2 = 1; Z < 0.3$$
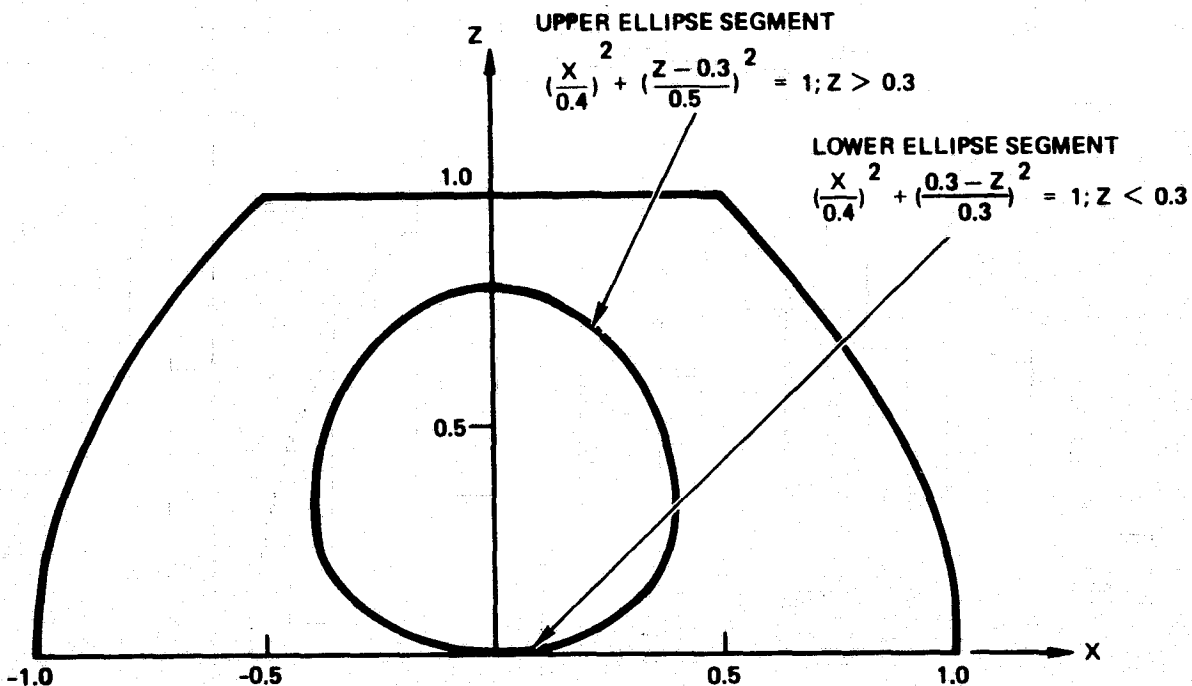
Figure 2-15. Definition of Dual Ellipse Aperture Shape
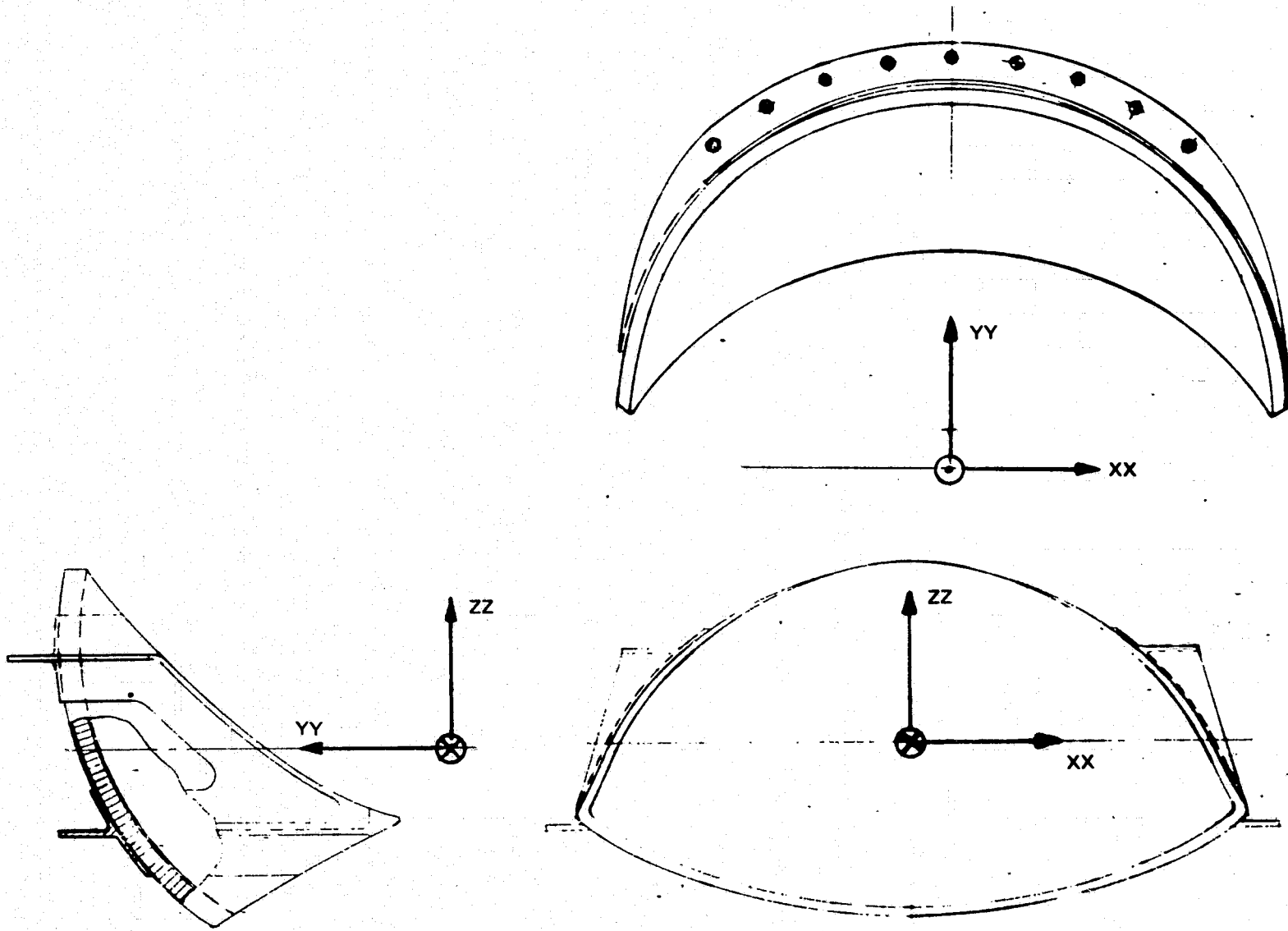
Figure 2-16. Three Views of Subreflector

A flange is required around the periphery of the subreflector. The purpose of this flange is two-fold.

1. To reflect the spillover energy in a downward direction, away from the main reflector. This will keep the spillover from appearing as sidelobes in the far field patterns, which will degrade the main beam efficiency. The corresponding areas below the main reflector will be lined with absorber.

2. When the feed is within the calibration cavity, the flange will also guarantee that virtually all of the feed illumination will be coupled to the cavity. Without the flange, the spillover will illuminate areas outside of the cavity and degrade the calibration accuracy.

Specific design of this flange should be done as part of the detailed design of the subreflector. It is not shown in the sketches for simplicity.

The surface contour of the subreflector must be accurate to 0.0025 cm rms (0.001 in.) to ensure adequate performance at the higher frequencies.

2.3.1.2 Gregorian Feed

The nominal feed characteristics are given in Table 2-2.

These are called nominal characteristics because the overall performance with such a feed has been completely evaluated. The feed was assumed to have a rectangular aperture 2.6λ high by 1.5λ wide with no phase error and a cosine taper in both dimensions, such as would be approximately the case for a rectangular corrugated horn.

A dual concentric feed could be fabricated as shown in Figure 2-17. The high frequency feed passes through the center of the low frequency turnstile junction. Two "Magic Tee" hybrids are required to feed opposite ports of the turnstile, thus giving crossed linear polarization for the low frequency channel. A normal orthomode transducer gives crossed linear polarization in the high frequency channel.

Table 2-2. Nominal Feed Characteristics

Pointing angle (from vertical)	90 deg
Beamwidth (3 dB)	44.1^0 Az x 26.0 deg ± 1
Beamwidth (10 dB)	80.4^0 Az x 45.5 deg ± 1
Sidelobe level	23 dB
Spillover (power outside of active portion of subreflector)	2.62% (-0.115 dB)

LOW BAND TURNSTILE JUNCTION

HIGH BAND CORRUGATED HORN

HIGH BAND ORTHO-MODE TRANSDUCER

LOW BAND CORRUGATED HORN

SEC A-A

VIEW OF APERTURE
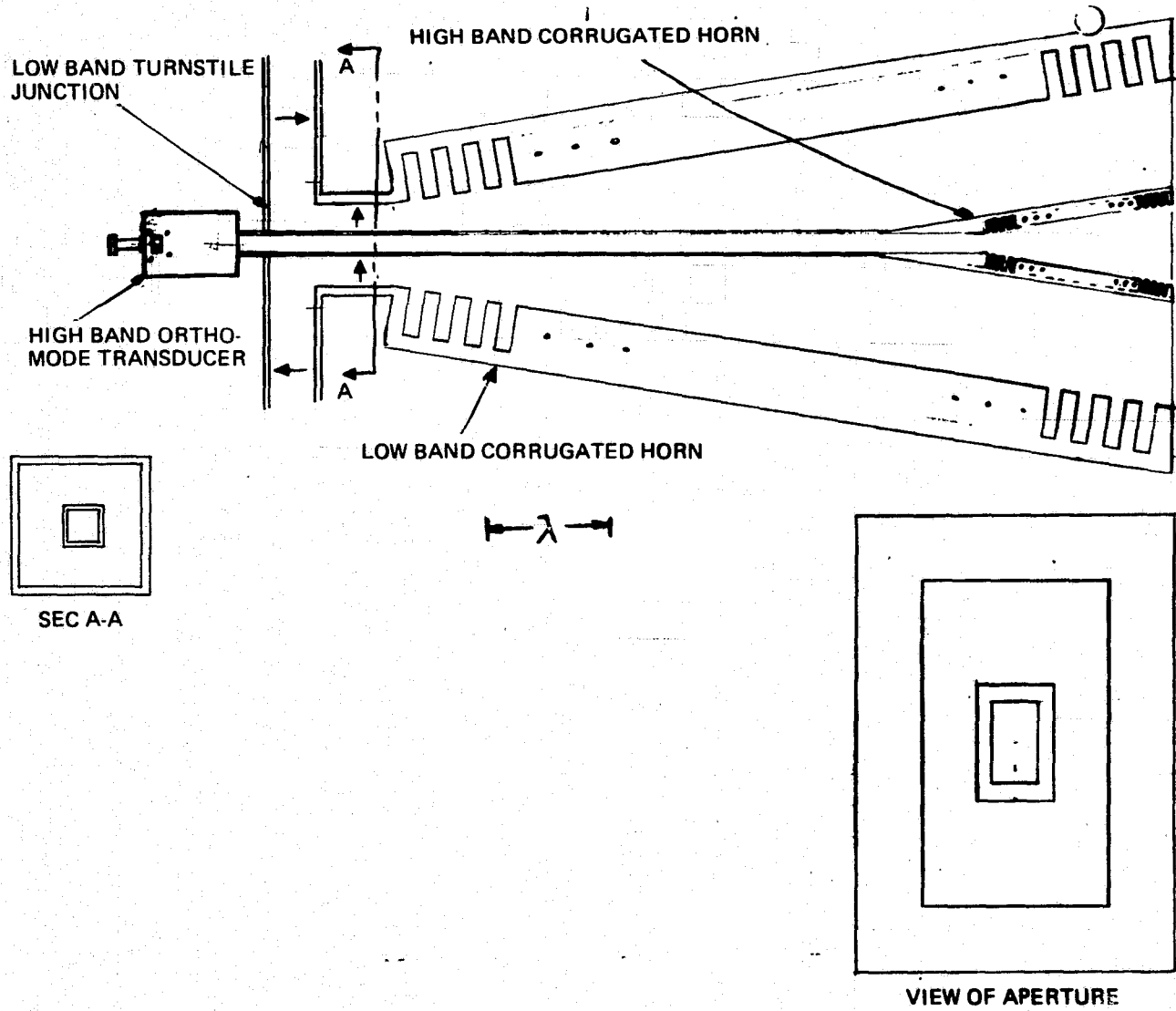
Figure 2-17. Possible Dual Concentric Feed Design

As noted earlier, the amount of degradation in the low frequency channel caused by the presence of the high frequency channel has not been determined because it would have to be done experimentally.

Other horn types, such as an elliptical version of the dual mode conical horn,[3,4] could also be used. The use of such a horn for the high frequency channel in a dual concentric feed would reduce blockage because a dual mode horn would be considerably smaller than a corrugated horn. A dual-mode horn would also be easier to fabricate with sufficient accuracy for the millimeter wavelength channels. Development and experimental evaluation of the elliptical dual mode conical horn is needed to verify its performance.

Still another horn type is a wide-flare-angle ring-loaded corrugated horn.[5] This horn has been investigated experimentally in a round conical configuration (equal beam widths). The use of a large flare angle and large aperture size makes the feed pattern tend to be equal to that of the dominant mode in the conical horn independent of frequency, and the use of ring loaded corrugations gives a bandwidth of 6:1 while maintaining the required capacitive surface impedance, except for a small stop band with inductive reactance which could be located between two channels. Its applicability as a Gregorian feed is questionable for the following reasons:

1. The patterns are not exactly constant over the 6:1 bandwidth, so a complete evaluation of the effect on beam efficiency is needed. Even with well-controlled patterns, the performance margin with respect to main beam efficiency and spillover is very small, making the feed patterns quite critical.

2. The presence of a well-defined phase center which is constant over the band has not been established.

3. Fabrication of the horn in an elliptical shape would be difficult, so a rectangular version should be investigated.

Should these questions be resolved sufficiently, a number of channels could be located at one position on the feed wheel with possible cost and performance advantages over the baseline design. Such an evaluation involves hardware development so it is beyond the scope of this study.

2.3.1.3 Prime Focus Feeds

The prime focus feeds at 0.61, 1.413, and 2.695 GHz are co-located as shown in Figure 2-18.

0.61 GHz

Four dipoles excited with equal amplitude and phase are used. The dipole spacing is 30.962 cm (0.63λ) in both directions. Because of the narrow bandwidth required, the dipoles can be spaced as close as 2.457 cm (0.05λ) above the 2.695 GHz slot array which acts as a ground plane. The beamwidth of this feed will be about 44 deg.
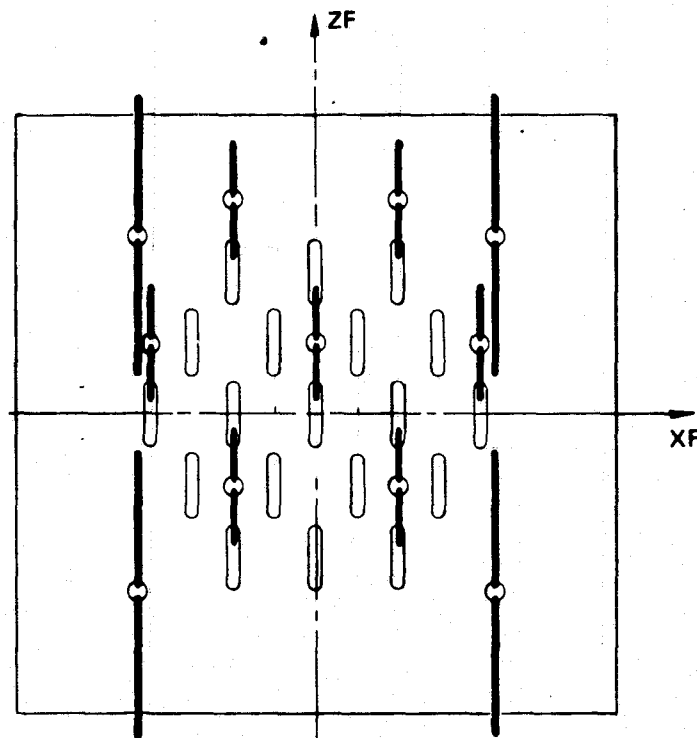
Figure 2-18. Triple Frequency Prime Focus Feed

1.413 GHz

Seven dipoles are used, with the central dipole excited 6 dB stronger than each of the outer six. The positions and amplitudes of the dipoles are summarized in Table 2-3. These dipoles can be spaced somewhat closer to the ground plane than the 0.61 GHz dipoles, or 1.5 cm (0.071λ). The use of seven dipoles reduces the beamwidth to about 34 deg. in order to reduce the degradation caused by the aberrations of the parabolic torus.

Table 2-3. Dipole Array Excitation for 1.413 GHz

Element	X	Y	Amplitude	Phase
1	−7.231	−6.262	0.125	0.0
2	+7.231	−6.262	0.125	0.0
3	−14.461	0.0	0.125	0.0
4	0.0	0.0	0.250	0.0
5	+14.461	0.0	0.125	0.0
6	−7.231	+6.262	0.125	0.0
7	+7.231	+6.262	0.125	0.0

2.695 GHz

The feed for this channel is a 19 slot array with a hexagonal aperture. This feed was optimized for maximum performance by systematically adjusting the amplitude and phase of each slot. The feed pattern then has approximate amplitude symmetry with about a 27 deg. beamwidth at -3 dB and a 55 deg. beamwidth at -10 dB. The phase, however, varies over a 100 deg. range to compensate for the aberrations of the torus. Details of the amplitude and phase distribution on the slots and the primary patterns are given in Paragraph 3.1.2.3.

The slot array can be fed by a stripline corporate feed with variable path lengths to produce the desired phase distribution. Because of variations in the mutual coupling over such a small array, it is expected that several iterations with the actual hardware will be required to achieve the desired slot excitations with sufficient accuracy.

2.3.1.4 Overall Performance

The calculated overall performance is given in detail in Table 2-4. Analyses which support these figures can be found in Section 3.1. Most of the parameters for the Gregorian channels are based on the 6.6 GHz results, so they are pessimistic because the performance of this geometric optics design will improve with increasing frequency due to reduced diffraction losses. Consequently, the slight deficiencies in main beam efficiency at 94 and 118.7 GHz are of no concern because the actual efficiency will be higher.

2.3.2 Mechanical Specifications

2.3.2.1 Shuttle Interface

Baseline Four-point Retention Concept

A four-point retention system, as shown in Figure 2-19 (for a generalized payload), provides a statically determinate mounting. The attachment fittings along the longeron react to loads in either the ±X and ±Z (primary fittings) or the ±Z directions (stabilizing fitting), while the lower keel fittings (auxiliary) react loads in the ±Y direction only. (See Figure 2-20 for a definition of the orbiter coordinate system). The stabilizing fitting may be located on either the left or right side of the antenna. The orbiter supplied interface fittings will minimize Y-loads in the primary fittings, X and Y loads in the stabilizing fittings, and X and Z loads in the keel fittings. The primary (X and Z load) fittings and the auxiliary (Y load) fitting on the antenna are located in a common plane and the stabilizing fitting is located 59.00 inches from this plane.

SIMS-A Attachment Locations in Payload Bay

Eight primary payload structural attachment locations are available for SIMS-A along the payload bay between $X_0 = 715$ and $X_0 = 1128$ as shown in Figure 2-21. Each location consists of three attachment points, one on each longeron ($Z_0 = 414$, $Y_0 = \pm 94$) and one at the keel ($Z_0 = 305$, $Y_0 = 0$). Each set of three attachment points

Table 2-4. Antenna Performance

Channel	1	2	3	4	Units
Frequency (run number)	0.610 72-2	1.413 72-1	2.695 87-2	6.600 41-1	GHz
Polarization	V+H (interlaced)	V+H (interlaced)	V+H (interlaced)	V+H (simultaneous)	
Multiplicity	1	1	1	2	
Temperature Resolution	0.13	0.16	0.55	0.13	°K
Beamwidth – Azimuth	17.29	9.18	4.86	1.98	deg
Elevation	17.41	8.74	5.02	2.15	deg
Elevation Beam Position	+5.34	+4.37	+7.79	−0.04	deg
Effective Aperture 72.6 λ/θ	2.05	1.72	1.63	1.60	meters
Total Power within Main Beam	89.86	94.11	91.53	91.26	percent
Total Power within Pattern	96.86	98.63	97.79	96.11	percent
Tolerance Loss	1.0	2.0	3.0	0.03	percent
Main Beam Efficiency*	91.2	93.2	90.2	94.1	percent
Sidelobe Level	−19	−24	−19	−17	dB
Polarization Purity	−16	−19	−19	−20	dB
VSWR	<1.1:1	<1.1:1	<1.2:1	<1.2:1	
Beam position accuracy	±0.045	±0.045	±0.045	±0.045	deg
Calibration Targets Coupling	NA	NA	99.5	99.5	percent
Gain w/o Ohmic Loss	20.53	26.35	31.61	39.13	dB
Ohmic Loss	0.31	0.25	0.68	0.34	−dB
Net Gain	20.22	26.10	30.93	38.79	+dB
Scan Coverage	TBD	TBD	TBD	±60	degrees

*Assuming 80% of spillover is absorbed.

Table 2-4. Antenna Performance (Cont)

Channel	5	6	7	8	Units
Frequency	10.69	20.0	22.0	37.0	GHz
Polarization (all simultaneous)	V+H	V+H	V+H	V+H	
Multiplicity	1	1	1	1	
Temperature Resolution	0.37	0.59	0.67	0.78	°K
Beamwidth	1.27	0.680	0.618	0.368	deg
Elevation Beam Position	0	0	0	0	deg
Effective Aperture	1.60	1.60	1.60	1.60	meters
Total Power within Main Beam	91.26	91.26	91.26	91.26	percent
Total Power within Pattern	96.11	96.11	96.11	96.11	percent
Tolerance Loss	0.07	0.23	0.28	0.79	percent
Main Beam Efficiency*	94.12	93.97	93.93	93.45	percent
Sidelobe Level	−17.0	−17.0	−17.0	−17.0	dB
Polarization Purity	−20.0	−20.0	−20.0	−20.0	dB
VSWR	<1.2:1	<1.2:1	<1.2:1	<1.2:1	
Beam Position Accuracy	±0.045	±0.045	±0.045	±0.045	deg
Calibration Targets Coupling	99.5	99.5	99.5	99.5	percent
Gain w/o Ohmic Loss (but including tol. loss)	43.31	48.75	49.57	54.07	dB
Ohmic Loss	0.34	0.34	0.34	0.34	−dB
Net Gain	42.97	48.41	49.23	53.73	+dB
Scan Coverage	±60	±60	±60	±60	degrees

*Assuming 80% of spillover is absorbed.

Table 2-4. Antenna Performance (Cont)

Channel	9	10	11		Units
Frequency	53.0	94.0	118.7	300.0	GHz
Polarization (all simultaneous)	V+H	V+H	V+H		
Multiplicity	2	2	2		
Temperature Resolution	1.99	2.63	5.63		°K
Beamwidth	0.257	0.145	0.115		deg
Elevation Beam Position	0	0	0		deg
Effective Aperture	1.60	1.60	1.60		meters
Total Power within Main Beam	91.26	91.26	94.34		percent
Total Power within Pattern	96.11	96.11	96.11		percent
Tolerance Loss	1.63	5.06	7.94	37.9	percent
Main Beam Efficiency*	92.66	89.42	89.64**		percent
Sidelobe Level	−17.0	−17.0	−17.0		dB
Polarization Purity	−20.0	−20.0	−20.0		dB
VSWR	<1.2:1	<1.2:1	<1.2:1		
Beam Position Accuracy	±0.045	±0.045	±0.045		deg
Calibration Targets Coupling	99.5	99.5	99.5		percent
Gain w/o Ohmic Loss (but including tolerance loss)	57.15	61.97	63.87		dB
Ohmic Loss	0.34	0.34	0.34		−dB
Net Gain	56.81	61.63	63.53		+dB
Scan Coverage	±60	±60	±60		degrees

*Assuming 80% of spillover is absorbed.
**Defined relative to the 5⊕ circle for this frequency.

PRIMARY FITTINGS;
REACT LONGITUDINAL &
VERTICAL LOADS
$(F_x \& F_z)$

Z

Y   X

LOWER C_L AUXILIARY FITTING;
REACTS SIDE LOAD (F_y)
SHOULD BE LOCATED UNDER
PAYLOAD CG

STABILIZING FITTING:
REACTS VERTICAL LOAD (F_z)

(OPTIONAL LOCATION, RIGHT
OR LEFT LONGERON)
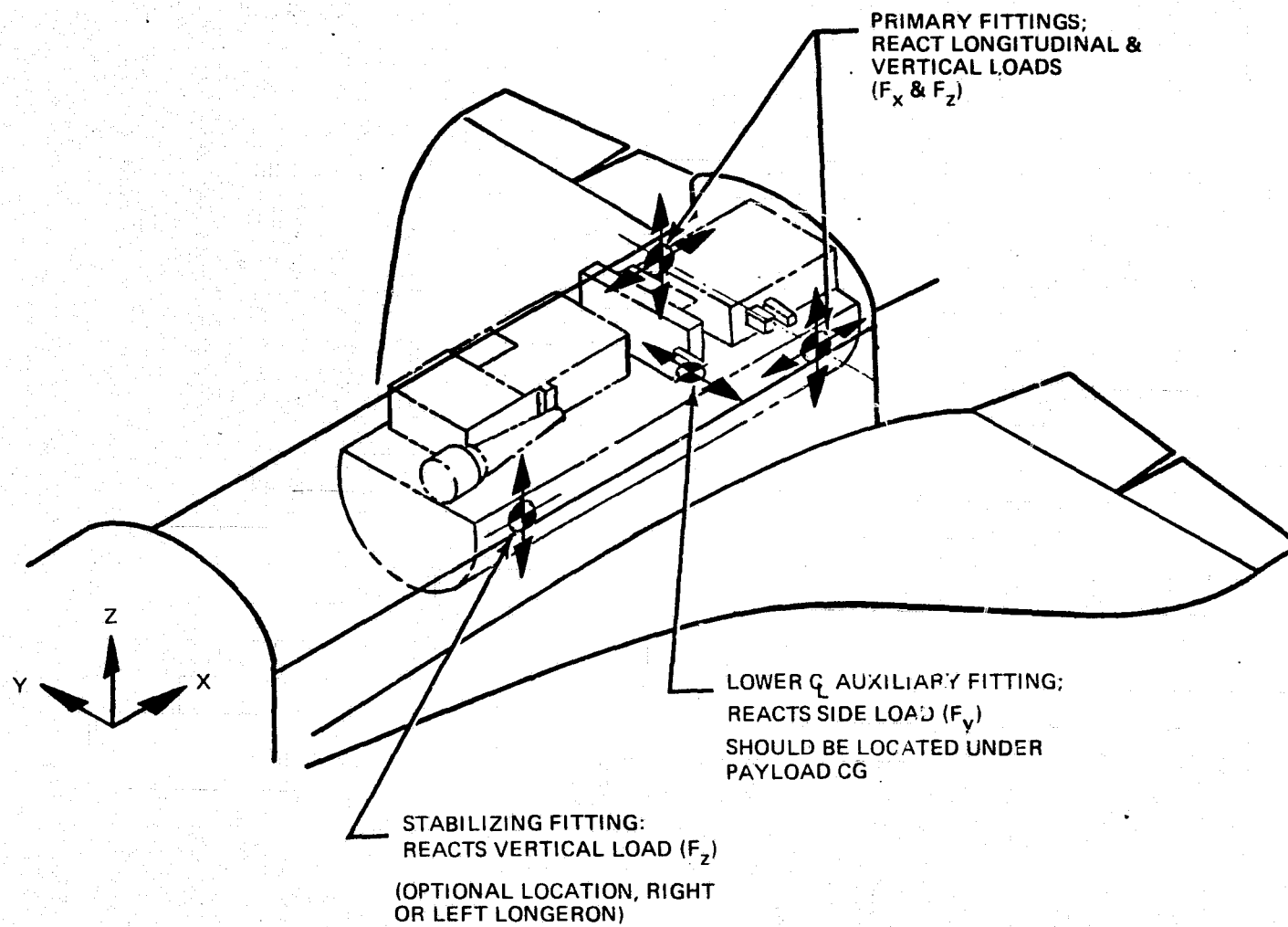
Figure 2-19.   Payload Retention System (Typical Payload)
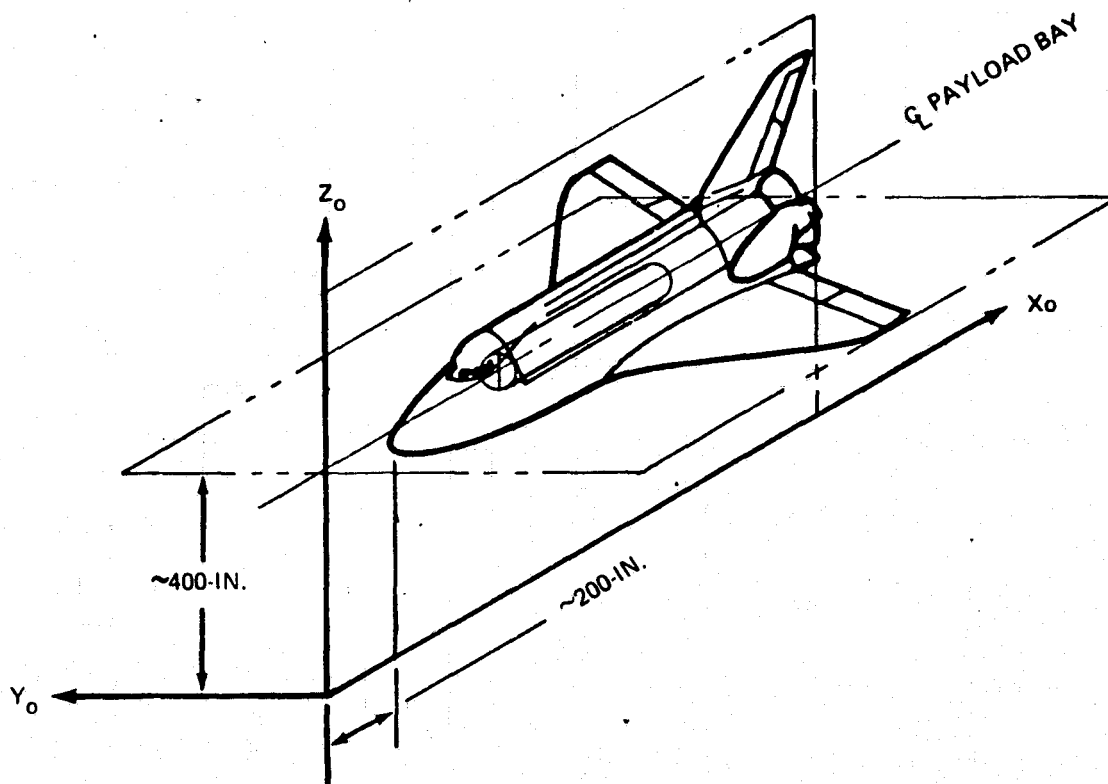
TYPE: ROTATING, ORBITER REFERENCED

ORIGIN: APPROXIMATELY 200-INCHES AHEAD OF THE NOSE AND APPROXIMATELY
          400-INCHES BELOW THE CENTERLINE OF THE PAYLOAD BAY

ORIENTATION AND LABELING:

          THE X AXIS IS PARALLEL TO THE CENTERLINE OF THE PAYLOAD BAY,
          NEGATIVE IN THE DIRECTION OF LAUNCH

          THE Z AXIS IS POSITIVE UPWARD IN LANDING ATTITUDE

          THE Y COMPLETES THE RIGHT-HANDED SYSTEM

          THE STANDARD SUBSCRIPT IS o

Figure 2-20.   Orbiter Coordinate System

RETENTION POINTS ⟶ X_o

(715) (774) (833) (892) (951) (1010) (1069) (1128)

$Y_o = 94$

$\cent\!\!\!\!\Large\L$ $Y_o = 0$

PAYLOAD ENVELOPE

$Y_o = -94$

7 EQUAL SPACES
(59-INCHES EACH)

8 (X & Z) LOAD RETENTION BEAM ATTACH
POINTS ON EACH LONGERON

PAYLOAD ENVELOPE

$Z_o = 414$

$\cent\!\!\!\!\Large\L$ $Z_o = 400$

8 LATERAL LOAD RETENTION BEAM
ATTACH POINTS AT LOWER CENTER-
LINE $Z_o = 305$
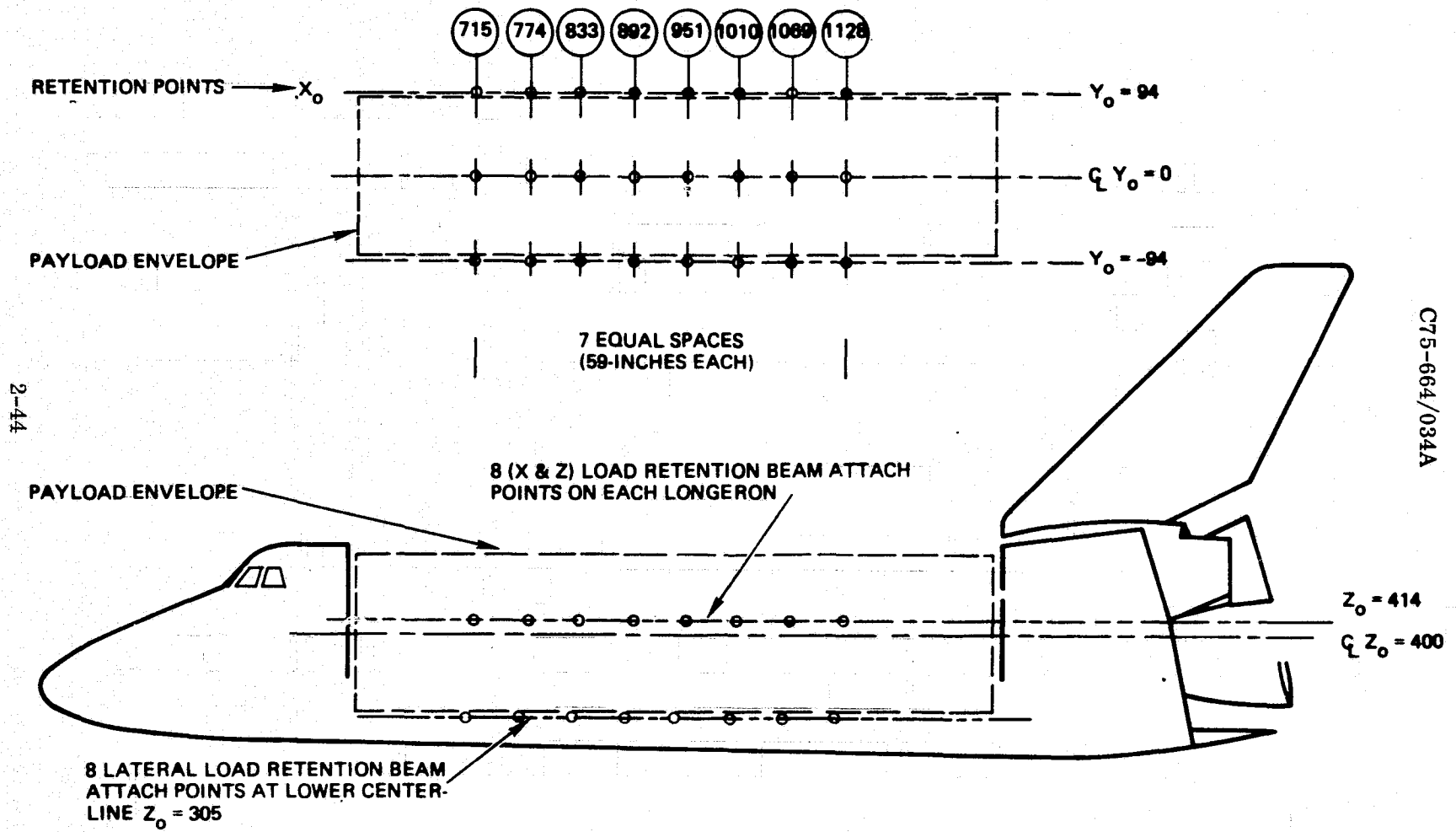
Figure 2-21.   Payload Primary Attachment Locations

2-44

C75-664/034A

defines a plane normal to the payload bay center line. The spacing of the fittings along the payload bay coincides with the 59 inch spacing between primary and stabilizing fittings on the antenna, providing a number of positions and orientations for mounting the antenna. The orbiter provides for the installation of vernier bridges which accommodate bolt-down payload fittings at 11.8 in. spacing as currently defined in JSC-07700. Figure 2-22 illustrates the concept and provides the currently configured candidate positions. Rockwell drawing VC70-004105 Rev "A" (see appendix) shows a modification to be incorporated in JSC-07700 which will reduce the vernier increments to 3.933 in. Table 2-5 is a listing of orbiter stations at which the coplaner fittings on SIMS-A may be located while having available a longeron fitting 59.0 in. away to pick up the stabilizing fitting on the antenna. The table also identifies the location as primary (P) or vernier (V) and describes the possible orientations of the antenna. There are 63 positions of which 40 may have the feed wheel forward or aft. The maximum forward limit for any part of the antenna is $X_O = 666$. The maximum aft limit depends on whether there is an OMS (Orbital Maneuvering System) kit aboard. With no kit and the feed wheel forward the maximum aft limit is $X_O = 1209$. With an OMS kit and the feed wheel aft the maximum aft limit is $X_O = 1168$. With an OMS kit aboard the aftmost position will probably be prohibited since only 16 to 26 in. would remain between the aft edge of the antenna and the forward edge of the kit (JSC-07700 locates the forward end of kit at $X_O = 1184$ and VC70-004105 Revision A locates it at $X_O = 1194$, See Figure 2-23).

Standard Payload Attachment Interface

The antenna shall provide for attach fittings which will mate to the orbiter payload attachment fittings and shall be capable of transferring to the orbiter fittings the loads generated when the mass of the antenna is accelerated to the limits described in Para 2.3.2.3. Design details and manufacturing tolerances for payload attachment fittings (both orbiter and payload mounted) shown on drawing no. VC70-004105 are to be determined. The configuration shown on the antenna in Figures 2-7 and 2-8 and on the reflector/main frame in Figures 2-10 and 2-11 are scaled to tentative dimensions called out on drawing no. VC70-004105 and provide sufficient volume to satisfy load requirements.

Electrical Power Requirements

The antenna drive system power requirements are given in Table 2-6. The orbiter power system has 115 VAC 400 Hz available but only with Level II NASA approval. With the approval approximately 2 KW of 400 Hz power will be available on-orbit but never during launch or re-entry. However, there are no standard provisions through which a payload can tap the 400 Hz power source. Therefore a junction box must be installed in one of the two wiring trays (See View F-F, Figure 2-24) along the side of the payload bay in order to provide a connection to the antenna. If Level II approval is not obtained, a DC to 400 Hz inverter must be supplied with the antenna. The power for the inverter can be obtained through one of the two mid-payload bay electrical interfaces located on the right side of the bay approximately at Station $X_O = 695$ (Y_O and Z_O to be determined) or from one of two interfaces located on the aft bulkhead ($X_O = 1307$; Y_O and Z_O are to be determined) Candidate electrical interface locations are shown in Figure 2-24.

Any of the locations described has adequate capacity for the antenna drive system. Table 2-7 describes the power available at each location.
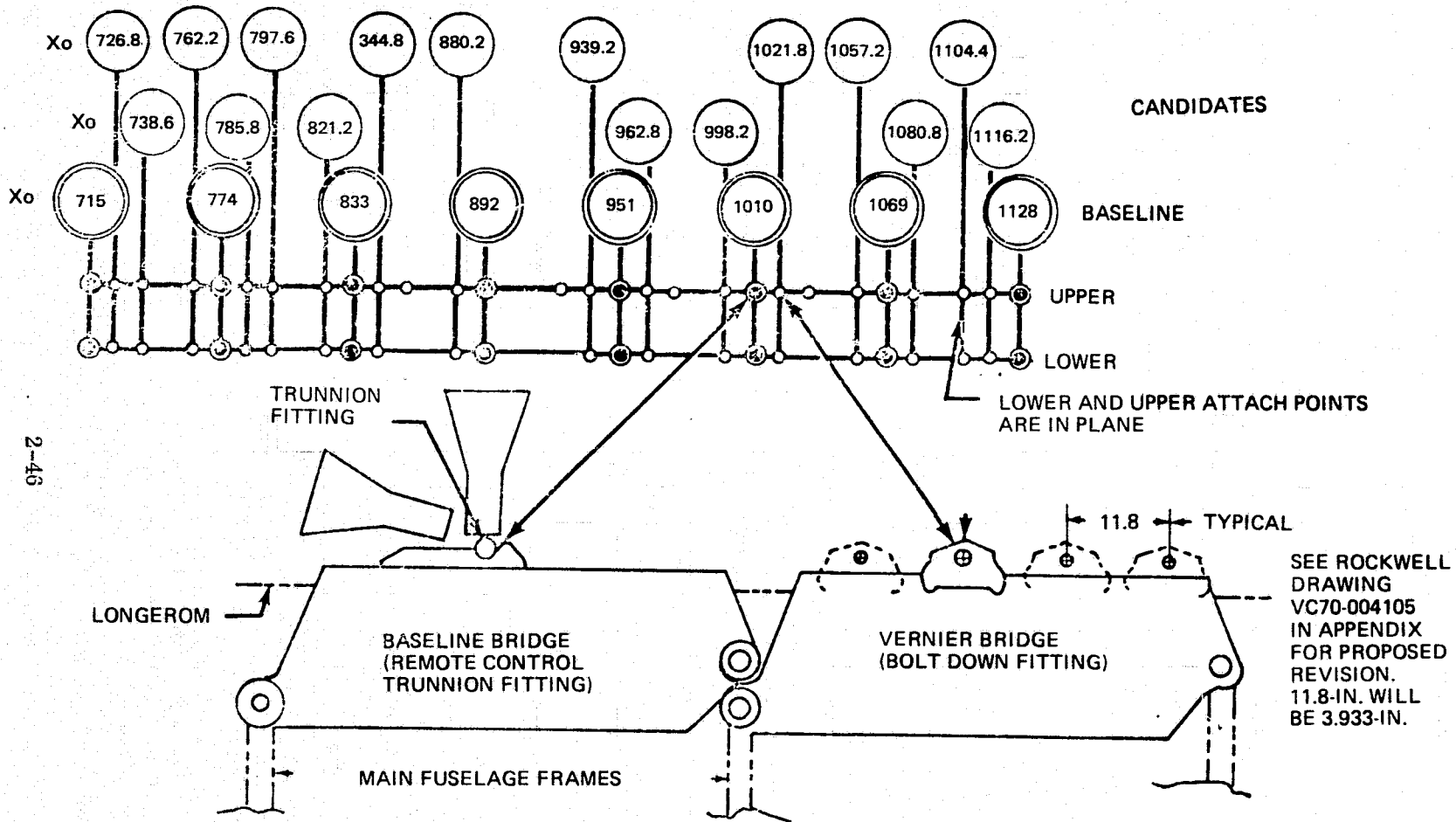
Figure 2-22. Potential Locations for Non-deployable Payload Primary Attachment Fittings

Table 2-5. Shuttle Orbiter Stations for Locating Vernier (V) and Primary (P)
Fittings for SIMS-A

No.	X_0	Type	Comments
1	703.201	V	Feed Wheel Forward Only
2	707.134	V	
3	711.067	V	
4	715.000	P	
5	718.933	V	
6	722.866	V	
7	726.799	V	
8	730.732	V	
9	734.665	V	
10	742.531	V	Feed Wheel Forward Only
11	766.134	V	Feed Wheel Forward or Aft
12	770.067	V	
13	774.000	P	
14	777.933	V	
15	781.866	V	
16	785.799	V	
17	789.732	V	
18	793.665	V	Feed Wheel Forward or Aft
19	797.598	V	Feed Wheel Forward Only
20	825.134	V	Feed Wheel Forward or Aft
21	829.067	V	
22	833.000	P	
23	836.933	V	
24	840.866	V	
25	844.799	V	
26	848.732	V	Feed Wheel Forward or Aft
27	852.665	V	Feed Wheel Aft Only
28	880.201	V	Feed Wheel Forward or Aft
29	884.134	V	
30	888.067	V	
31	892.000	P	
32	895.933	V	Feed Wheel Forward or Aft

Table 2-5. Shuttle Orbiter Stations for Locating Vernier (V) and Primary (P)
Fittings for SIMS-A (Cont)

No.	X_0	Type	Comments
33	899.866	V	Feed Wheel Forward or Aft
34	935.268	V	
35	939.201	V	
36	943.134	V	
37	947.067	V	
38	951.000	P	
39	954.933	V	
40	958.866	V	Feed Wheel Forward or Aft
41	962.799	V	Feed Wheel Forward Only
42	970.655	V	Feed Wheel Forward Only
43	998.201	V	Feed Wheel Forward or Aft
44	1002.134	V	
45	1006.067	V	
46	1010.000	P	
47	1013.933	V	
48	1017.866	V	
49	1021.799	V	Feed Wheel Forward or Aft
50	1025.732	V	Feed Wheel Forward Only
51	1029.665	V	Feed Wheel Aft Only
52	1057.201	V	Feed Wheel Forward or Aft
53	1061.134	V	
54	1065.067	V	
55	1069.000	P	
56	1072.933	V	Feed Wheel Forward or Aft
57	1108.335	V	Feed Wheel at aft end only if OMS kit is installed otherwise either end
58	1112.268	V	
59	1116.201	V	
60	1120.134	V	
61	1124.067	V	Feed Wheel at aft end only if OMS kit is installed otherwise either end
62	1128.000	P	
63	1131.933	V	Feed Wheel Aft Only
	63 total locations		
	40 locations wheel can be forward or aft		

50.2 FT MAXIMUM ALLOWABLE PAYLOAD LENGTH WITH OMS KIT
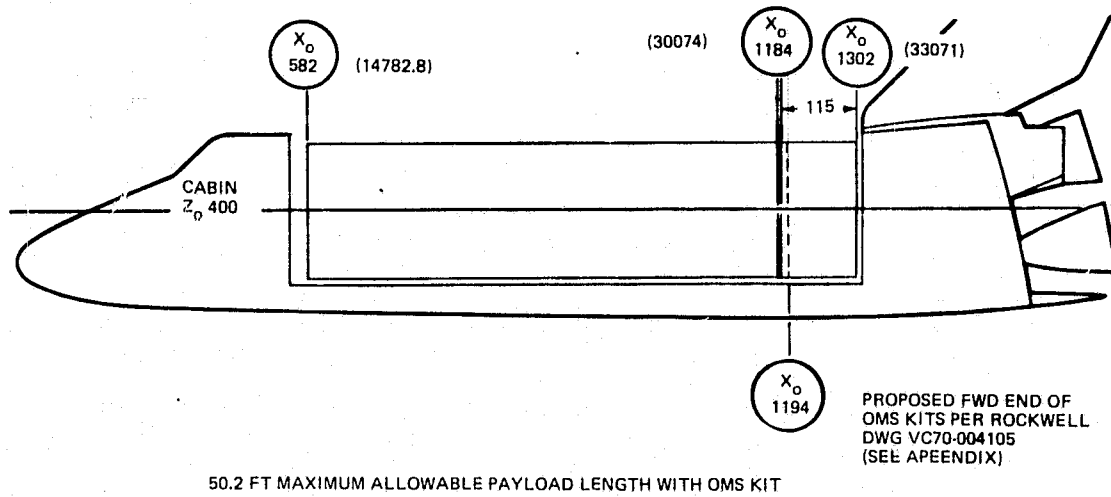
Figure 2-23. OMS Payload Bay Kits

Table 2-6. Drive Power Requirements

400 Hz Power (with Power Factor Correction)

Three phase, four wire
400 ± 0.5 Hz

115 volts RMS Line to Neutral and
199.2 volts RMS Line to Line ± 2 percent

Starting Power: (10 minutes duration)
365 watts (3 ph)
3.19 Amps per line
≈ 0.33 PF
1.1 KVA (3 ph) (incl brake)

Running Power (Estimate at synch speed)
101 watts (3 ph)
0.32 Amps per line
1.0 PF
0.11 KVA (3 ph) (incl brake)

Encoder Power

$+6.0$ VDC $\pm 1\%$, 0.5 AMP
-6.0 VDC $\pm 1\%$, 0.07 AMP

PAYLOAD ELECTRICAL SERVICE PANEL

PAYLOAD BAY ENVELOPE

PREFLIGHT SERVICE PANEL

X_o 1307

X_o 695

F 36

B

B

F

Z_o 400
(10160)

VIEW B-B
LOOKING AFT
BLKHD 1307
(33197.8)

P/L ELECTRIC PANEL 524-02

P/L ELECTRIC PANEL 524-01

Y_o 0

PAYLOAD ELECTRICAL SERVICE
PANEL X_o = 695 (APPROX)

SECONDARY POWER CABLE
(ORBITER BUSS SYSTEM)

PRIMARY POWER CABLE
(DEDICATED FUEL CELL)

ELECTRICAL WIRE TRAY

PAYLOAD ENVELOPE

VIEW F-F LOOKING FWD RH SIDE

Figure 2-24. Electrical Interface Locations

Table 2-7. Payload Power Interfaces

● **Mid Payload Bay (Dedicated Fuel Cell Interface)**

1. Ascent and Descent (Power Source Shared with Orbiter) 27.0 to 32.0 volts dc with peak-to-peak ripple of 0.9 volts or less at any single frequency and 1.6 volts or less over a broad band of frequencies, provided the payload meets the requirements of JSC Specification SL-E-0002, dated June 4, 1973, "Electromagnetic Characteristics, Requirements for Space Shuttle Program," at the interface.

2. On Orbit (Power Source Dedicated to Payload) 27.0 to 32.0 volts dc (2 to 12 kw) with TBD ripple except that generated by the payload.

3. Mid Payload Bay (Power Source Shared with Orbiter) 27.0 to 32.0 volts dc with peak-to-peak ripple of 0.9 volts or less at any single frequency and 1.6 volts or less over a broad band of frequencies, provided the payload meets the requirements of JSC Specification SL-E-0002, dated June 4, 1973, "Electromagnetic Characteristics, Requirements for Space Shuttle Program," at the interface.

● Aft Payload Bay — 24.0 to 32.0 volts dc with peak-to-peak ripple of 0.9 volts or less at any single frequency and 1.6 volts or less over a broad band of frequencies, provided the payload meets the requirements of JSC Specification SL-E-0002, dated June 4, 1973, "Electromagnetic Characteristics, Requirements for the Space Shuttle Program," at the interface.

Use of the orbiter 400 Hz power source is more desirable than use of an inverter due to the accurate 1 part in (10^8) frequency control by the orbiter master timer.

● Grounding — The Orbiter electrical power is a 2-wire structure ground system. Payloads should carry all ground return through the Orbiter electrical interface to the Orbiter structure ground.

Characteristics

The antenna configuration shown in Figure 2-6 weighs approximately 1400 lb. See Table 2-8 for the distribution of weight. The weight indicated for the feed wheel includes JPL supplied radiometers, power supplies and other electronic hardware.

The antenna system can be contained in a cylinder 15 ft in diameter and 9.84 ft long. The actual volume occupied by the system is shown in Figures 2-7 and 2-8.

Table 2-8. Weight Distribution

Item	Weight (lb)
Feed Wheel	290
Drive Mechanism	150
Calibration Targets	60
Reflector/Main Frame	820
Misc hardware, cables, inverter, etc.	80
Total	**1400**

Payload Electrical Energy

The Orbiter EPS[*] will provide 50 kwh of electrical energy to the payload. To support payloads requiring more than 50 kwh, provisions will be made to the Orbiter for installing one reactant storage kit outside the payload envelope. Volume for four additional kits can be provided outside the payload envelope. Each kit shall be capable of providing approximately 840 kwh of additional energy. The weight of the kits, including reactants, shall be charged to the payload.

The 50 kwh value is based on a nominal seven-day mission; excess Orbiter electrical energy as available, may be utilized by the payload.

The power consumed by the drive system at steady state operation is approximately 101 watts (Table 2-6) assuming a motor efficiency of 93 percent with the 0.25 HP (rated) drive motor producing 0.130 HP. Assuming a conversion efficiency in the rotating transformer of 95 percent, 253 watts of orbiter power are required to produce the 240 watts needed by the JPL equipment mounted on the feed wheel. Total steady-state requirements are 351 watts and spin-up requires less than 0.1 kw-hr. 49.9 kw-hr consumed at 0.351 kw will last 142 hrs or 5.92 days. For missions longer than five days, consideration must be given to the installation of reactant tanks described above. Since the JPL furnished components will not require power until spin-up is complete, the maximum power drain will be 0.365 kw required to start the drive wheel.

Although the antenna design presented does not require caging of the feed wheel for structural reasons, a brake is required to stop the wheel prior to de-orbit. A lock preventing rotation during launch and re-entry is considered desirable but not mandatory. The simplest brake concept is to reverse the motor. If desired a toggle actuated holding device will then prevent rotation. The actuating device would require power only to change state.

2.3.2.2 Functional

Rotating Feed Wheel and Subreflector

The antenna feed wheel rotates at a constant rate, f = 324 RPM (ω = 33.93 rad/sec). The rate is dictated by RF performance parameters and limitations on the number of radiometers available. The wheel structure, the mounted components, and the fastenings joining them are subjected to radial accelerations,

$$a \text{ (g's)} = \frac{r \text{(ft)} \left[\omega \left(\frac{\text{rad}}{\text{sec}} \right) \right]^2}{32.2 \text{ (ft/sec}^2)}$$

$$a \text{ (g's)} = 35.75 \text{ r} \qquad \text{(r in feet)}$$

---

[*]Electrical Power System

The radial force, F_r, exerted on the wheel by an elemental mass, W, of the wheel or a mounted component, W, located at a radius, r, is,

$$F_r = W \text{ (lbs) } r \text{ (ft) } 35.75$$

When these forces act out of the center plane (or neutral axis) of the wheel they produce bending moments equal to the product of the force times the distance between its line-of-action and the neutral axis. These bending moments will produce deflections unless balanced by reversed moments due to a balancing mass located on the opposite side of the neutral axis. If one side of the wheel is exposed to the sun or other source of radiant heat flux while the opposite side is not, the resulting difference in temperature will produce a deformation of the wheel if the thermal coefficient of expansion and the temperature difference are of sufficient magnitude. Testing of the antenna in the terrestrial environment will expose the feed wheel to a 1 g load acting parallel to the axis of rotation which also will cause a deflection. Since testing is to be done by a static procedure (wheel not rotating), the deflection caused by radial forces will not appear during testing and similarly the deflection caused by gravity will not be present during the orbital use of the antenna. Gravity deflection of the feed wheel concept presented here is 0.0017 in. The orientation for testing must be such that the gravity deflection is in the same direction a deflection caused by unbalanced radial forces. The magnitude of unbalanced radial forces must not produce deflections greater than the deflection produced by gravity.

Dynamic balancing of the feed wheel reduces the deflection to less than 0.0017 in. Static balancing of the wheel assures that the center-of-mass of the entire assembly is sufficiently close to the axis of rotation that deflection of the shaft due to static imbalance is less than 0.0001 in.

The sub-reflectors deflect less than 0.0005 in. at any point on their surface when their mass is subjected to the acceleration of constant rotational speed.

The rotational inertia of the feed wheel without consideration for inertia due to balance weights is 9027 slug-in^2. The analysis for the speed control system used 10,000 slug-in.^{2} which allows 973 slug-in.^{2} for drive shaft, gear train, and balance weight inertias.

After adjustment of sub-reflectors and feeds for optimum RF performance and after the feed wheel has been balanced, both statically and dynamically, all attached components are dowel pinned to the wheel.

The deflection allowables discussed above are summarized in Table 2-9.

Drive System

The drive system gear train provides reduction (36.962429:1) of drive motor shaft speed of 12,000 RPM to a feed wheel drive shaft speed of 324.324 RPM while multiplying the maximum motor shaft torque output from 80 in.-oz to 15.385 lb-ft at the feed wheel drive shaft. Helix angles on the gearing are chosen which accommodate the pitch line velocities and produce minimum thrusts on the shafts.

Table 2-9. Feed Wheel Data

Deflection of sub-reflector @ 33.93 rad/sec (radial)	= 0.00050 max
Deflection of wheel perimeter @ 33.93 rad/sec (radial)	= 0.00010 max
Deflection of wheel perimeter @ 33.93 rad/sec (axial)	= 0.00170 max
Deflection of wheel perimeter @ 1g (axial)	= 0.00170 max
Deflection of wheel perimeter @ $\Delta T = 10^{o}F$ (axial)	= 0.00034

Machining for fit of bearings and for the location of gears and shafts uses jig-bore tolerances. Bearings are ABEC Class 7 and gears are Precision 2.

The drive shaft is made from graphite-epoxy with the fibers wound to provide a thermal coefficient of expansion of 7.0×10^{-6} in./in./^{o}F in the radial direction which corresponds to the coefficient of the bearing race and drive system housing material. The winding will also result in a minimal (less than 1×10^{-6} in./in./^{o}F) coefficient in the axial direction. The axial direction coefficient is minimized in order to prevent defocusing of the system due to change in length of the shaft.

The critical frequency of the free end of the drive shaft is over 2100 RPM sufficiently greater than 324 RPM to exclude any possibility of supporting resonances.

All bearings, gears and other friction surfaces are lubricated with vacuum deposited film lubricants bearing the generic name Vac-Kote developed by Ball Brothers Research Corporation, Boulder, Colorado.

Speed Control

A synchronous motor will accelerate any inertia load to synchronous speed that it can start rotating, and which has a running (friction) torque requirement that is less than the motor pull-in torque rating. It is convenient to relate all values to the load shaft for discussion. The motor-speed to load-shaft-speed gear ratio (N) is 36.962429 to one. The developed motor torques are tabulated below at the motor and at the load shaft.

$$T_L = N\,(Tm)\,(5.203 \times 10^{-3})$$

T_L = Load torque (lb - ft.)

T_m = Motor torque (oz. - in.)

N = Gear ratio

Developed Torque	T_M (oz in.)	T_L (lb ft)
Starting Torque	80.0	15.38524
Pull-in torque	27.2	5.23098
Pull-out Torque	25.0	4.80789
Rated Torque	21.0	4.03862

Starting torque of a motor is the torque which the motor will develop at rest at any angular position of the rotor.

Pull-in torque is the maximum torque under which the motor will pull into synchronous speed as the rotor approaches synchronous speed.

Pull-out torque is the maximum torque which the motor will develop at synchronous speed.

Rated torque is the recommended maximum requirement at synchronous speed for continuous duty.

The synchronous speed of the selected motor is 12000 RPM which yields 324.65398 at the load shaft.

Breakaway friction torque (at load shaft) is:

Two Main Bearings at 80 oz in.	160 oz in.
Motor and geartrain (estimate)	40 oz in.
Encoder	0.5 oz in.
	200.5 oz in.

or $\boxed{1.04 \text{ lb ft}}$

Total Inertia (at load shaft) including wheel, shaft, motor, geartrain, encoder, and an estimate for wheel balancing weights is 10,000 slug-in^2 which converts to $\boxed{69.5 \text{ lb ft sec}^2.}$

The motor starting torque reflected to the load shaft is 15.385 lb ft. During the acceleration period the running friction torque requirement will be similar to the breakaway friction torque requirement which leaves about 14 lb ft of developed torque to accelerate the load inertia. Starting acceleration will be:

$$\alpha = \frac{T_L}{J_L} = \frac{14}{69.5} = \boxed{0.2014 \text{ Rad/sec}^2}$$

At about one half of synchronous speed the running friction torque requirement will begin to increase reducing the torque available to accelerate the load. Time required to achieve synchronous speed will be less than ten minutes.

At synchronous speed, the inertia torque requirement is zero, and motor torque developed will be required only to overcome system losses due to friction. It is estimated that the main shaft bearing friction torque requirement may be 200 percent greater than the starting value at the synchronous speed of 324.65 RPM. Allowing a similar increase for the other friction contributors, the running friction torque required at synchronous speed may be $\boxed{2.1 \text{ lb ft.}}$

The rated torque is 4.04 lb ft as previously stated, then the required torque is about half of the rated value, which provides a good margin.

Shaft Angle Data

The optical shaft angle position encoder selected provides the shaft angle data in unambiguous natural binary format. The output is available on 13 parallel lines and is TTL/DTL compatible, i.e., logic ONE is 3.5 VDC minimum to 6.0 VDC maximum, and logic ZERO is 0.0 ± 0.5 VDC. Output for 360 deg. is 8192 counts with each count, or least significant bit (LSB), equal to 0.0439453 degrees of arc, or 2.636718 minutes of arc. The binary format is:

Angle (deg)	Count	Binary LSB
0 (Ref)	0	0000000000000
0.0439	1	0000000000001
0.0879	2	0000000000010
90	2048	0100000000000
180	4096	1000000000000
359.956	8191	1111111111111

To provide an unambiguous output, a V-scan technique is used, with a decode circuit, to detect the four least significant data bits. This decoding is accomplished within the encoder. The encoder will generate a Data Ready gate, about 4 microsecond long, to indicate the data is stabilized.

At synchronous speed, a single bit value of 0.0439 degrees is traversed in about 22.5 μs.

Tolerances

The drive mechanism will lock-in at synchronous speed and hold that speed subject to the frequency of the input power. The 400 Hz frequency tolerance is ±0.5 Hz which is ±0.12 percent. Thus the synchronous speed will have a tolerance of ±0.12 percent resulting in a minimum value of 324.26 RPM and a maximum value of 325.04 RPM.

The shaft angle encoder binary word has a digital incremental accuracy of ±0.5 LSB and an alignment accuracy of ±0.9 LSB for an RSS tolerance of about ±1.03 LSB equals ±0.045 deg.

Reflector/Main Frame

The reflector/main frame works as an integral unit to provide a parabolic torus reflecting surface which is maintained at its fabricated contour with virtually no distortations when subjected to the environment (functional, not launch) of the SIMS-A mission. The reflector shell is laminated from graphite-epoxy in order to minimize thermal distortions which would otherwise degrade the RF performance. The material used has a thermal coefficient of expansion less than 0.1 μ in./ in./$^{\circ}$F.

The surface will be coated with a conductive coating. Initial plans are to electrodeposit nickel over the surface.

The shell is attached to a rigid space truss which provides the paths by which all vibratory, acoustic, linear acceleration or other loadings reach the orbiter trunnion fittings. The elements of the space truss are designed to have thermal strains which are compatible with the thermal strains of the reflector shell. The main frame includes truss structured walls which span the assembly at each end. The wall spanning the vertex end of the parabolic torus provides support for the drive mechanism (with feed wheel attached) which represents a concentrated load of 440 lbs on the wall. The same wall also provides support for the calibration target housings which can be represented as 2 concentrated loads of 30 lbs each. The reflector/main frame design shown in Figure 2-10 (2 sheets) weighs approximately 820 lbs and a computer analysis of the structure under a 20 g static load provides confidence in the integrity of the structure. (See Para 3.2.2) The truss width in the vicinity of the trunnion fittings and keel tongue fitting provides adequate length for rigidly installing these fittings. These fittings transfer all SIMS-A loading to the orbiter trunnion fittings. The design of the fittings is dictated by JSC-07700.

2.3.2.3 Environmental

The conceptual design antenna described must satisfy the environmental parameters associated with a circular orbit of 340 kilometers altitude and a nominal duration of seven days but with a duration of up to 30 days maximum possible. The natural and induced environments to which the antenna may be subjected due to operation with the Space Shuttle System are applicable design requirements and are summarized below. The applicable paragraph numbers of JSC 07700 are given in parentheses. When an asterisk (*) appears before a referenced JSC 07700 paragraph number it indicates that JSC-07700 should be referred to for the requirements or for additional information.

Natural Environments

1. Atmospheric (4.1.1)

   Pressure   ●   12.36 to 15.23 psia (surface), 3.28 psia (35,000 ft) (4.1.1.1)

Temperature ● -23°F to +115°F (surface), -65°F nominal
(25,000 ft)   (4.1.1.2)

Fungus ● Antenna shall use non-fungi nutrient
materials   (4.1.1.3)

Humidity ● Zero to 100 percent relative humidity at temperature
extremes defined above.* (4.1.1.4)

Lightning ● TBD   (4.1.1.5)

Ozone ● 3 to 6 parts per hundred million (phm) - (surface)
100 phm (35,000 ft) * (4.1.1.6)

Salt Spray ● One percent (wt) salt (NaCl) solution for 30 days
*(4.1.1.7)

Sand/Dust ● Equivalent of 140 mesh silica flour with velocity up to
500 ft/min and particle density 0.25 gr./ft^3 (4.1.1.8)

2. Space (above 90 kilometers)   (4.1.2)

Pressure ● 1.4×10^{-5} to 8×10^{-6} Torr   (129 kilometer)

2.2×10^{-6} to 4.7×10^{-7} Torr   (185 kilometer)

2.2×10^{-9} to 4.7×10^{-11} Torr   (926 kilometer)

approx 1×10^{-11} Torr   (2222 kilometer)
(4.1.2.1)

Solar   (4.1.2.2)
(Thermal) ● Solar radiation   443.7 Btu/ft^2/hr

Earth albedo   30%

Earth radiation   77 Btu/ft^2/hr

Space sink temperature   0° Rankine

Solar   (4.1.2.3)
(Nuclear) ● Galactic cosmic radiation   * (4.1.2.3.1)

Trapped radiation   * (4.1.2.3.2)

Solar Particle events   * (4.1.2.3.3)

Meteroids ● * (4.1.2.4)

Induced Environments   (4.2)

Ground Handling and Transportation   (4.2.1)

Temperature ● * (4.2.1.1)

Purge Gas ● * (4.2.1.2)

Shock ● Bench - 20 g terminal sawtooth shock pulse of 20 millisecond duration in each of six axes

Transportation - as simulated by sinusoidal impulses in the frequency range from 3 to 5 Hz controlled to 1-inch double amplitude displacement (4.2.1.3)

Acceleration ● Hoisting 2 g vertical within a ±20 deg. cone angle
(4.2.1.4)

Vibration ● 4 sweeps at 1/2 octave/min. (Sinusoidal motion)

2 - 5 Hz at 1.0 inch double ampl.

5 - 26 Hz 1.3 g peak

26 - 500 Hz 0.36 inch double ampl.

500 - 1000 Hz 5 g peak (4.2.1.5)

Flight Environment (4.2.2)

Pressure ● Figures 2-24a and 2-25 (4.2.2.1)

Vibration ● Launch - about 29 second at levels shown in Figure 2-26 (4.2.2.2)

Acoustics ● Spectra in Figure 2-27 (4.2.2.3)
Time history per Figure 2-28

Acceleration ● Table 2-10 for 65,000 lb up 32,000 lb down
Table 2-11 for 65,000 lb down *(7.5)

Shock ● Pyrotecnic - TBD (4.2.2.5a)

Landing *(4.2.2.5b)

Crash Safety Shock *(4.2.2.5c)

Transient Vibration *(4.2.2.5d)

Contamination ● Outgassing — Selection criteria shall be one percent
Control total mass loss and 0.1 percent volatile condensable material (VCM) as defined in JSC spec SP-R-0022
*(4.3)
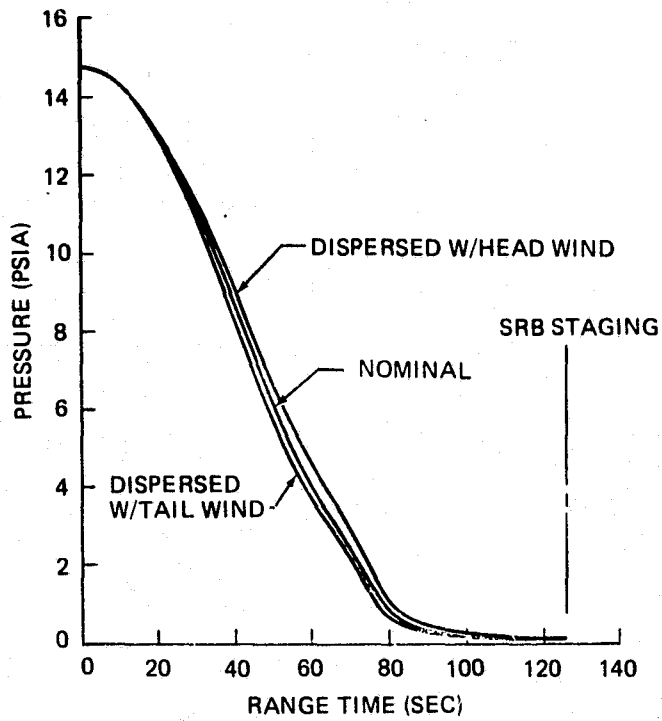
Figure 2-24a. Orbiter Payload Bay Internal Pressure Histories during Ascent
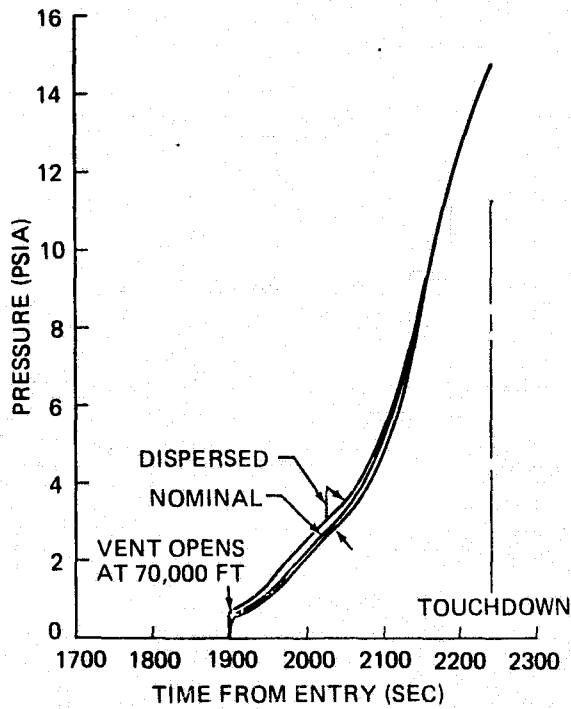
Figure 2-25. Orbiter Payload Bay Internal Pressure Histories during Entry

**ACTUAL VIBRATION INPUT TO PAYLOADS WILL DEPEND ON
TRANSMISSION CHARACTERISTICS OF MIDFUSELAGE –
PAYLOAD SUPPORT STRUCTURE AND INTERACTIONS WITH
EACH PAYLOAD: WEIGHT, STIFFNESS, AND CG**
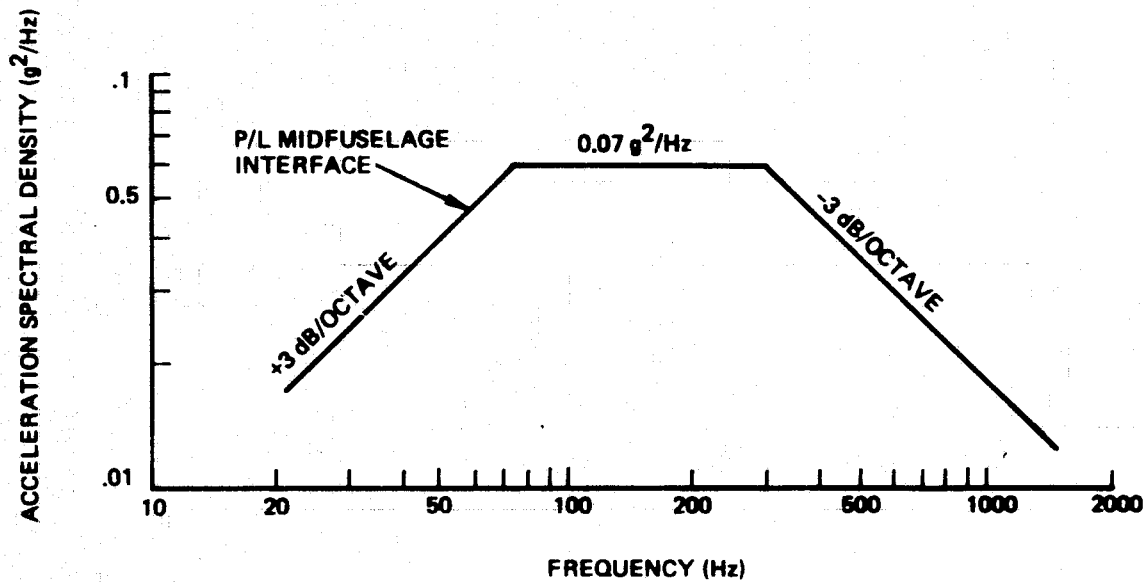
**THESE LEVELS ARE TYPICAL OF LIFT OFF, TRANSONIC
AND MAX q FLIGHT**

Figure 2-26.   Random Vibration at Payload Midfuselage Interface and In Cabin
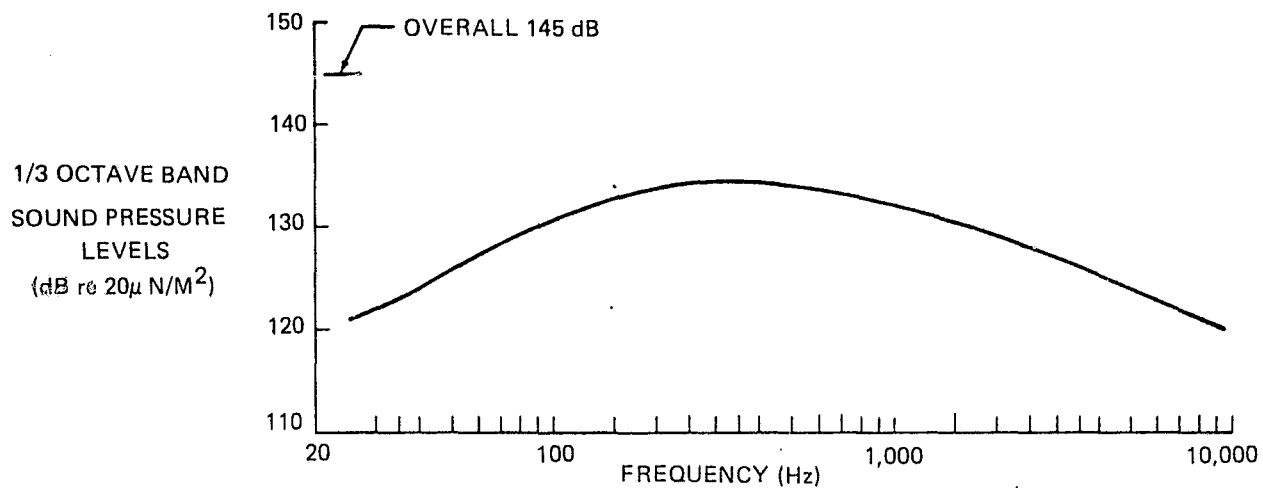
Figure 2-27. Analytical Predictions Maximum Orbiter Payload Bay
Internal Acoustic Spectra
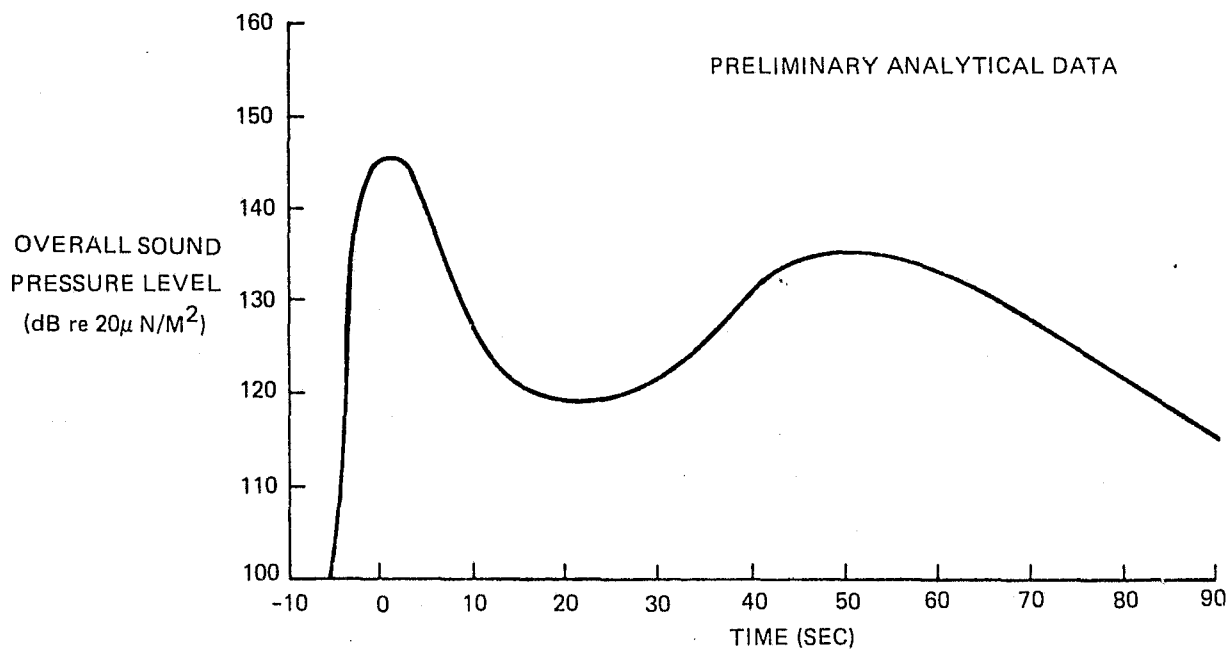
Figure 2-28. Orbiter Payload Bay Internal Acoustic Time History

Table 2-10. Cargo Limit Design Accelerations
for 65 KLB Up and 32 KLB Down

CONDITION	LINEAR - g			ANGULAR - RAD/SEC²		
	X	Y	Z	X-X	Y-Y	Z-Z
Lift-off	-0.1	+1.0	+1.5	+0.10	+0.15	+0.15
	-2.9	-1.0	-1.5	-0.10	-0.15	-0.15
High-Q Boost	-1.6	+0.5	+0.5	+0.10	+0.15	+0.15
	-2.0	-0.5	-0.6	-0.10	-0.15	-0.15
Boost-Max. LF (Stack)	-2.7	+0.2	-0.3	+0.20	+0.25	+0.25
	-3.3	-0.2	-0.3	-0.20	-0.25	-0.25
Boost-Max. LF (Orb Alone)	-2.7	+0.2	-0.75	+0.20	+0.25	+0.25
	-3.3	-0.2	-0.75	-0.20	-0.25	-0.25
Entry and Desc Pitch Up	+1.06	0	+2.5	+0.25	+0.75	+0.30
	-0.02	0	-1.0	-0.25	-0.75	-0.30
Entry and Desc Yaw	+0.75	+1.25	+1.0	+0.25	+0.30	+0.75
	+0.75	-1.25	+1.0	-0.25	-0.30	-0.75
Landing	+1.0	+0.5	+2.9	+0.25	+1.25	+0.30
	-0.8	-0.5	+2.2	-0.25	-0.75	-0.30
Crash	+9.00	+1.50	+4.5			
	-1.5	-1.50	-2.0			
Crash (Crew Compartment Interior)	+20.0	+3.3	+10.0			
	-3.3	-3.3	-4.4			

NOTES

Sign convention follows that of the Orbiter coordinate system. Angular accelerations follow the right hand rule.

Crash accelerations are ultimate. The longitudinal accelerations are directed in all aftward azimuths within a cone of 20 deg half-angle. The specified accelerations shall operate separately.

Crash landing loads shall be carried through the payload support fittings and their attachment fasteners only. Support structure shall be designed to withstand the fastener loads locally.

Ascent and landing conditions include dynamic transients effects but do not include the dynamic response of the payload.

For payload weights between 32 KLB and 65 KLB, use a linear interpolation between the accelerations given in Tables 2-10 and 2-11 for the entry, landing and crash condition.

Table 2-11. Cargo Limit Design Accelerations for 65 KLB Down

CONDITION	LINEAR - g			ANGULAR - RAD/SEC²		
	X	Y	Z	X-X	Y-Y	Z-Z
Entry and Desc Pitch	+0.92 / -0.02	0 / 0	+2.18 / -0.87	+0.22 / -0.22	+0.65 / -0.65	+0.26 / -0.26
Entry and Desc Yaw	+0.65 / +0.65	+1.09 / -1.09	+1.0 / +1.0	+0.22 / -0.22	+0.26 / -0.26	+0.65 / -0.65
Landing	+0.87 / -0.70	+0.44 / -0.44	+2.35 / +1.7	+0.22 / -0.22	+1.09 / -0.65	+0.26 / -0.26
Crash	+4.43 / -0.738	+0.738 / -0.738	+2.215 / -0.985			
Crash (Crew Compartment Interior)	+9.85 / -1.62	+1.62 / -1.62	+4.92 / -2.17			

Sign convention follows that of the Orbiter coordinate system. Angular accelerations follow the right hand rule.

Crash accelerations are ultimate. The longitudinal accelerations are directed in all forward azimuth within a cone of 20 degrees half-angle. The specified accelerations shall operate separately.

Crash landing loads shall be carried through the payload support fittings and their attachment fasteners only. Support structure shall be designed to withstand the fastener loads locally.

Ascent and landing conditions include dynamic transients effects but do not include the dynamic response of the payload.

For payload weights between 32 KLB and 65 KLB, use a linear interpolation between the accelerations given in Tables 2-10 and 2-11 for the entry, landing and crash conditions.

*Thermal   ●   Payload Bay Wall Thermal Environment per Table 2-12   (4.2.2.7.1)

Payload Bay Data Point Locations per Figure 2-29   (4.2.2.7.1)

Payload Bay Entry Thermal Environment per Figures 2-30a, b, c   (4.2.2.7.1)

Payload Bay Surfaces per Figure 2-31   (4.2.2.7.1)

On-Orbit Thermal Environment of Empty Payload Bay per Figure 2-32   (4.2.2.7.1) (one possible SIM-A orbit configuration is the "port side to sun" column.)

Table 2-12. Payload Bay Wall Thermal Environment

CONDITION	DESIGN MINIMUM	DESIGN MAXIMUM
Prelaunch	+ 40°F (4.5°C)	+ 120°F (49°C)
Launch	+ 40°F (4.5°C)	+ 150°F (65.5°C)
On-Orbit (doors closed)	See C&D	See A&B
Entry and postlanding	-100°F (-73°C)	+ 200°F (93.5°C)

Heat leak criteria into or out of a 100°F (37.5°C) constant payload are as follows:

A. Total bay heat gain, average $\leq$ 0 Btu/Ft²-hr (0 Watt/Meter²)

B. Heat gain, local area $\leq$ 3 Btu/Ft²-hr (9.5 Watt/Meter²)

C. Total bay heat loss, average $\leq$ 3 Btu/ft²-hr (9.5 Watt/Meter²)

D. Heat loss, local area $\leq$ 4 Btu/ft²-hr (12.6 Watt/Meter²)

*Thermal   ● Orbiter Attitude Hold Capabilities per Figure 2-33
(Cont)   (4.2.2.7.2)

Payload Bay Entry Air Temperature per
Figure 2-34   (4.2.2.7.3)

*Payload Bay Nodes and Mission Attitude per
Figure 2-35

*Temperature vs time — Nodes 671 and 673 per
Figure 2-36

*Temperature vs Time — Nodes 4877 and 5371 per
Figure 2-37

---

*Advance data for a mission profile similar to SIMS-A
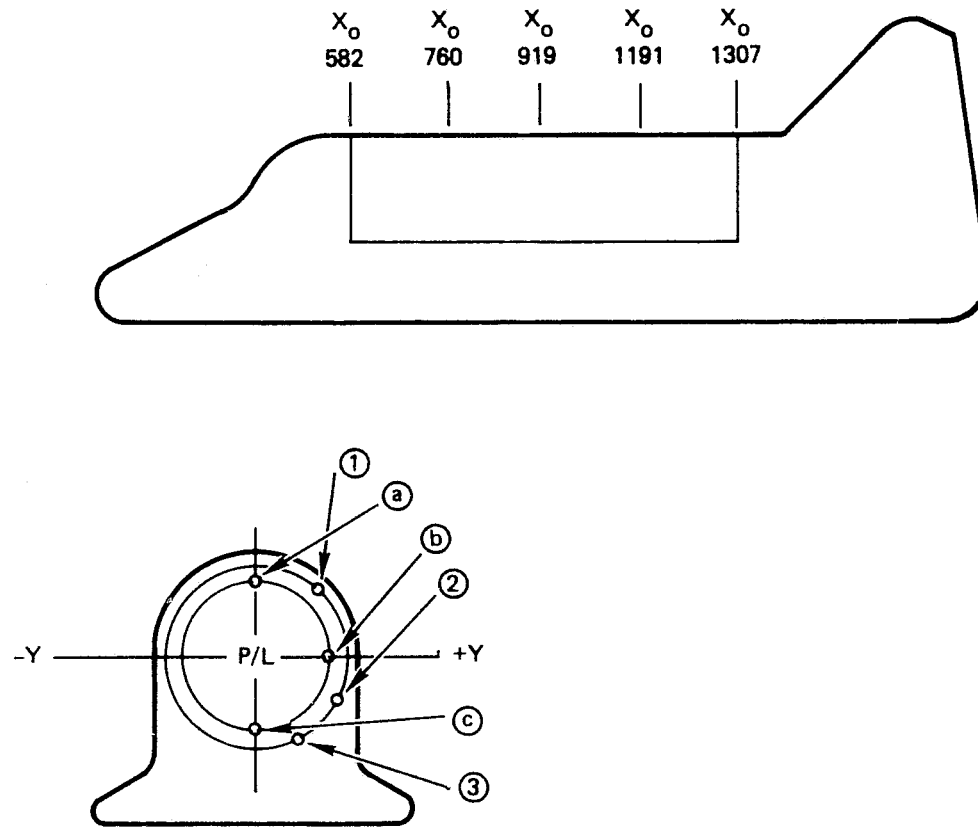
Figure 2-29. Payload Bay Wall and Payload Data Point Location
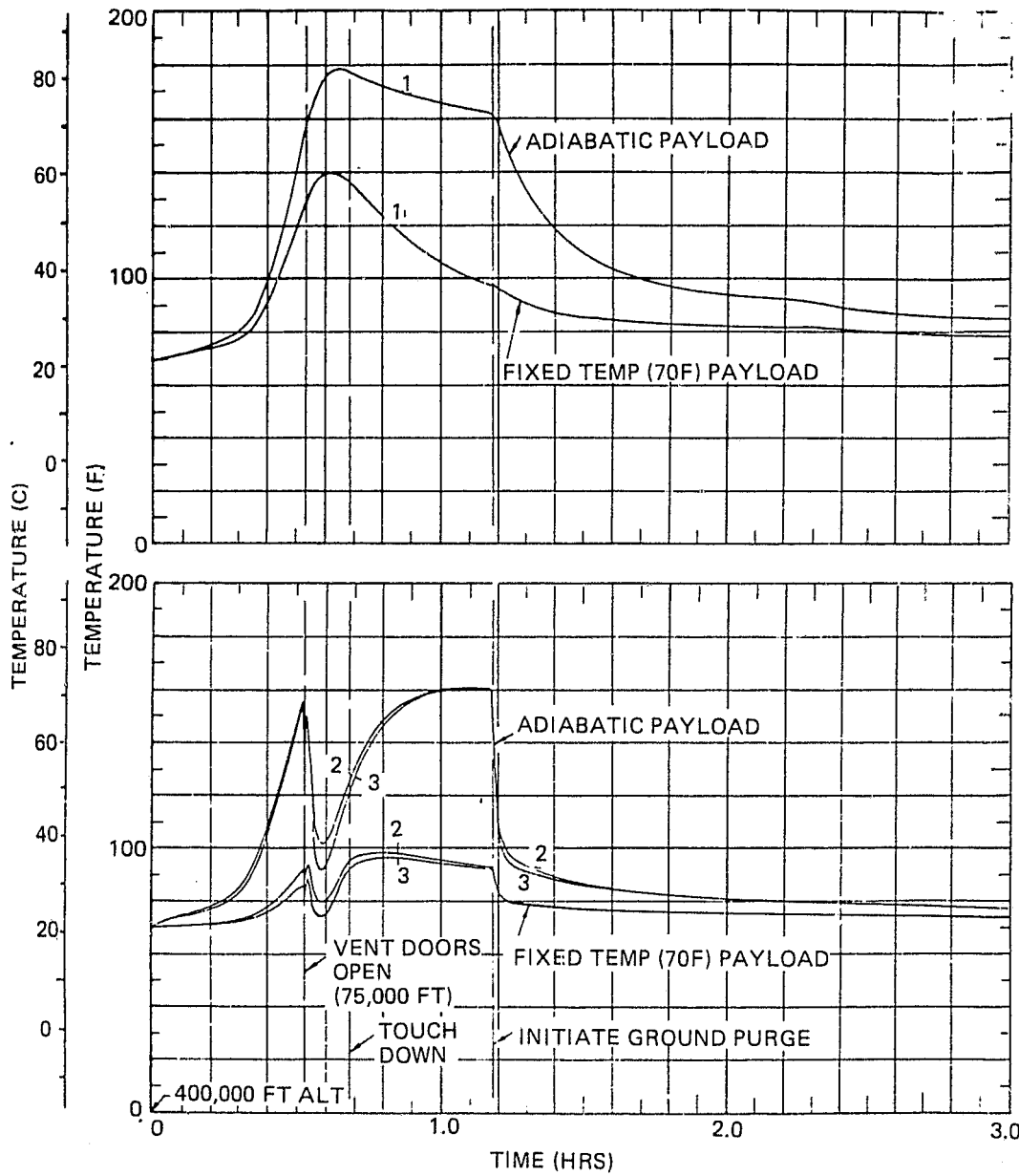
(a) X_o = 582 TO 760
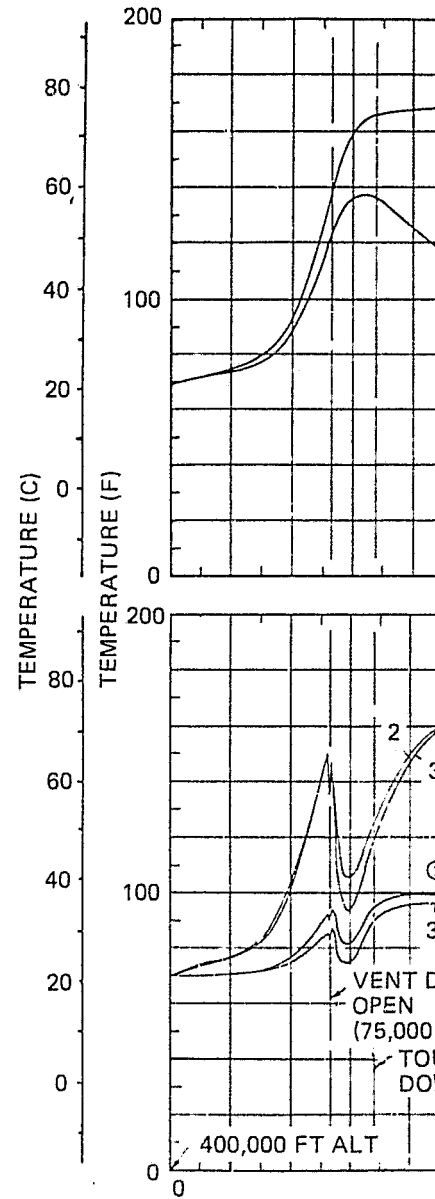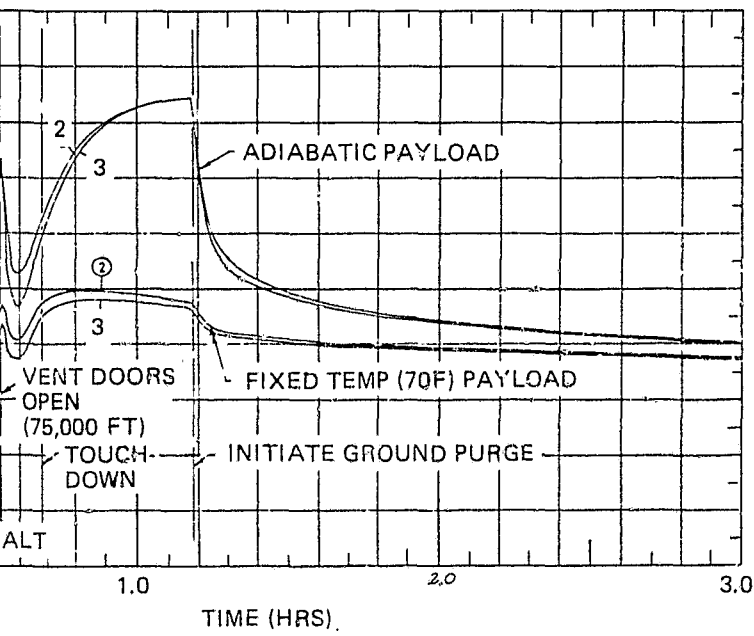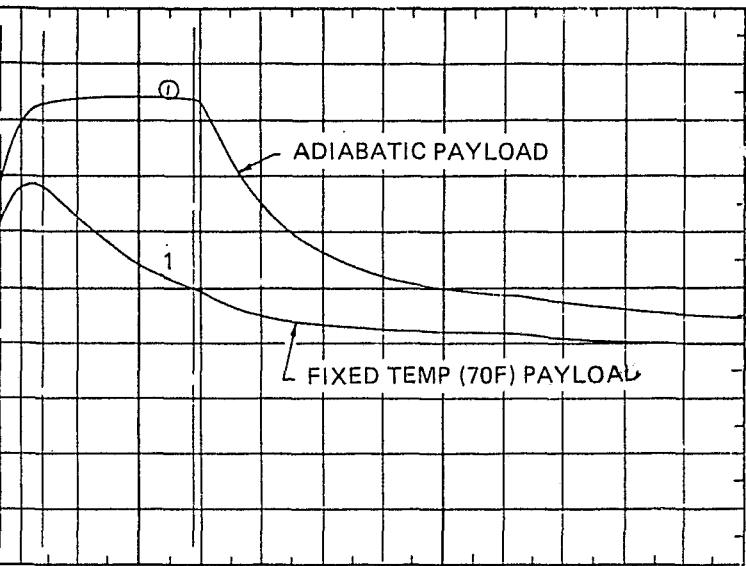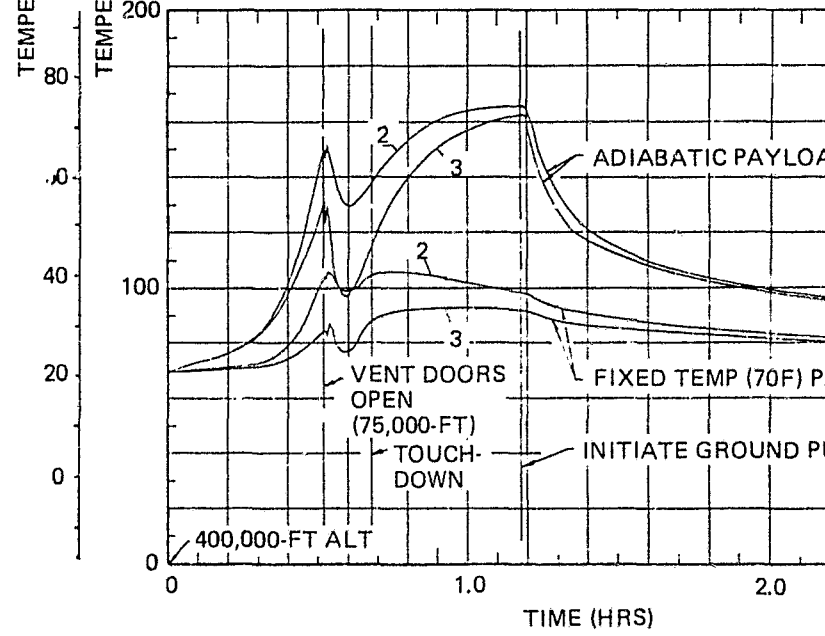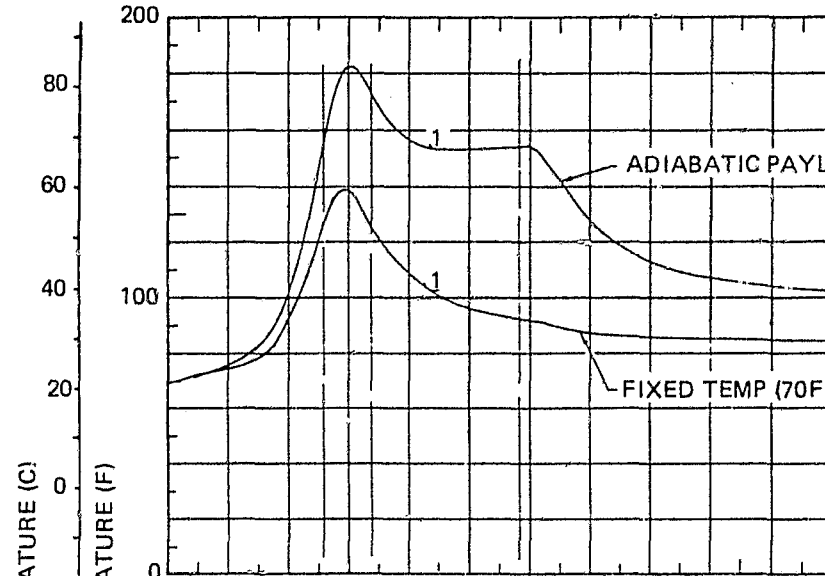
(b) X_o = 760 TO 919

(c) X_o = 919 TO 1191

Figure 2-30. Entry Thermal Environment X_o = 582

2-67/2-68

(c) X_O = 919 TO 1191

Figure 2-30. Entry Thermal Environment X_O = 582 to 1191.

2-67/2-68

(DOOR CLOSED)
RSI
BULK INSULATION
RADIATOR

(DOOR CLOSED)
RSI
BULK INSULATION
RADIATOR

$\alpha/\epsilon \leq .4$

PAYLOAD LINER
(TBD)

PAYLOAD LINER
(TBD)

2.5"

SECTION A-A   SECTION B-B
(X_o = 578-919) (X_o = 919-1191)

A   B

A   B
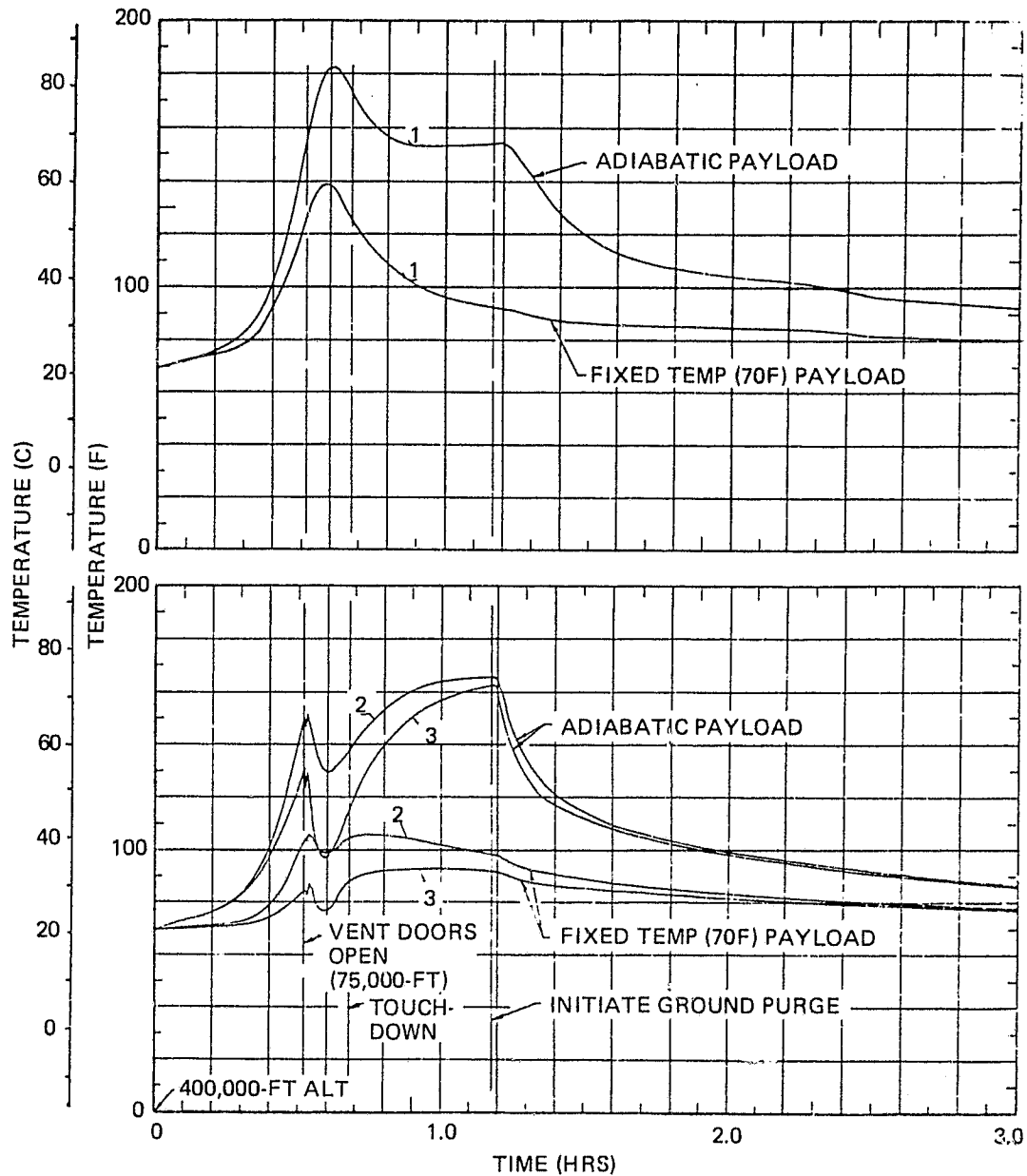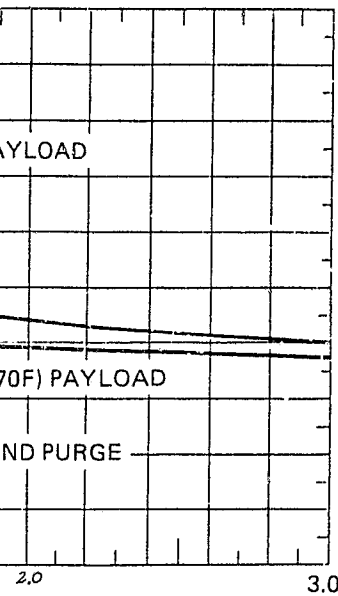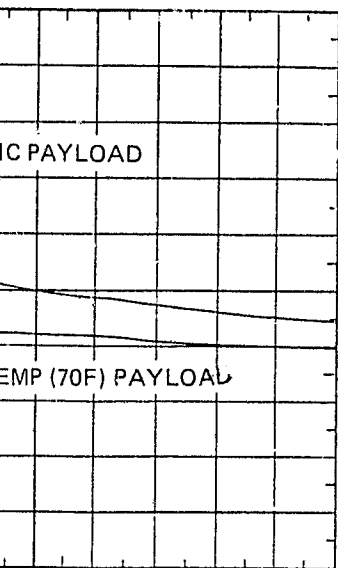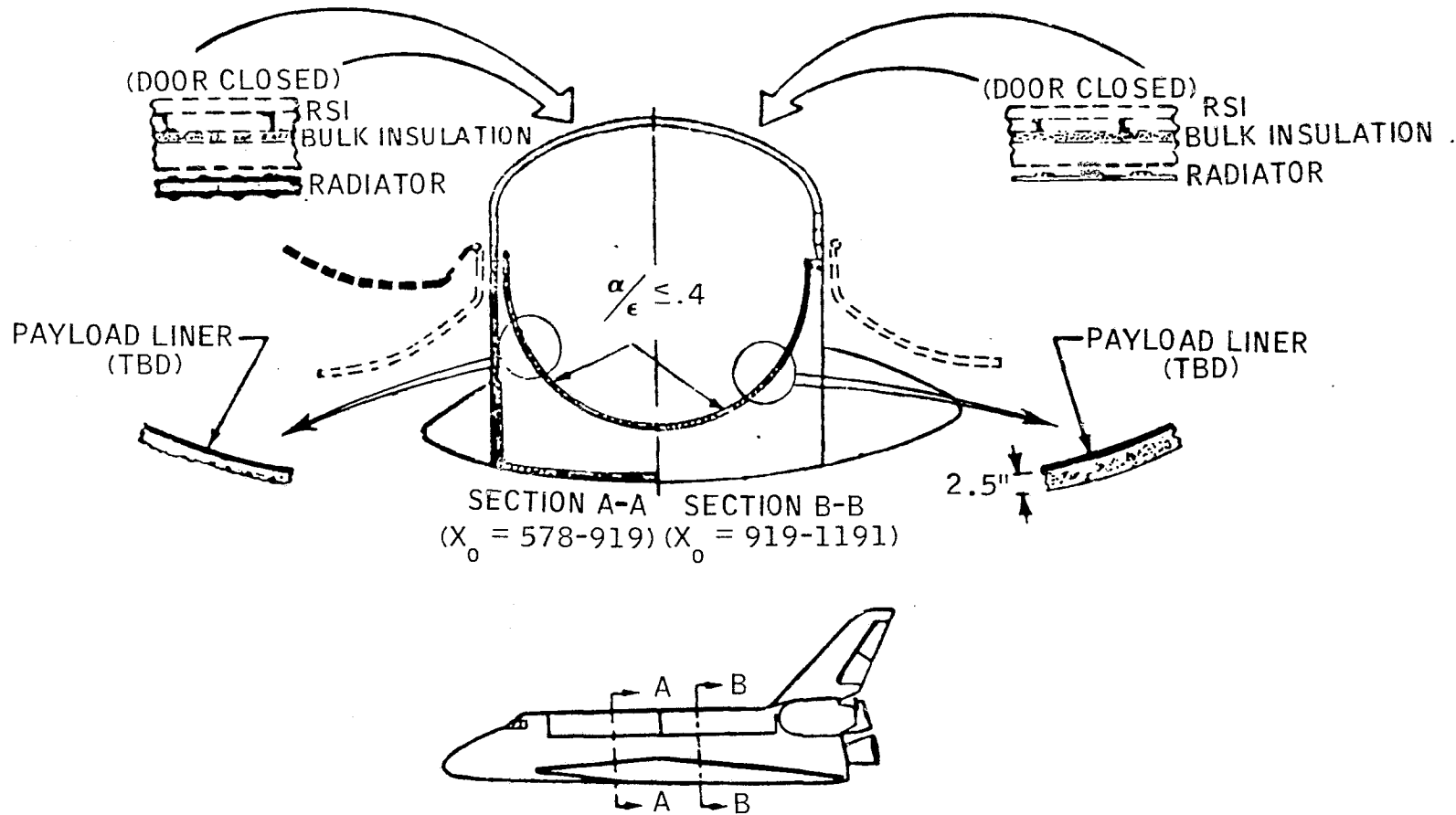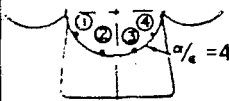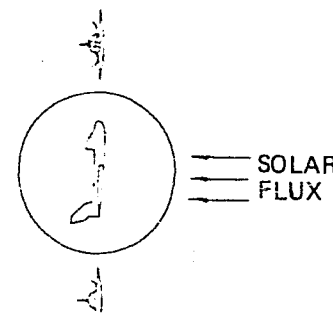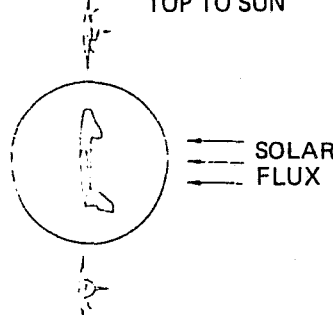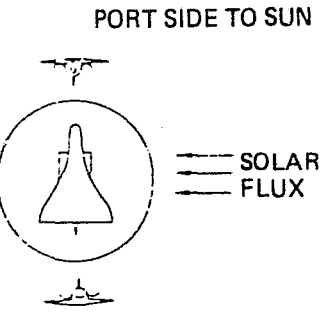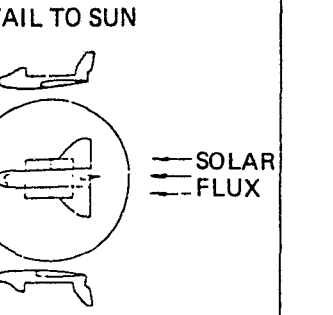
Figure 2-31. Payload Bay Surfaces

DATA POINT LOCATION (See Figure)	BOTTOM TO SUN		TOP TO SUN		PORT SIDE TO SUN		TAIL TO SUN	
	T	Q	T	Q	T	Q	T	Q
X = 582 TO 760								
1	-117(-82.78)	2.015(0.6357)	171(77.22)	48.851(15.4111)	-6(-21.11)	19.384(6.1151)	-210(-134.44)	0.0
2	-111(-79.44)	3.608(1.1382)	209(98.33)	72.664(22.9865)	+3(-16.11)	23.546(7.4281)	-215(-137.22)	0.0
3	-105(-76.11)	8.871(2.7985)	198(92.22)	66.688(21.0381)	+4(-15.56)	23.643(7.4587)	-212(-135.56)	0.0
4	-47(-43.89)	16.101(5.0794)	150(65.56)	37.568(11.8576)	-3(-19.44)	19.722(6.2217)	-210(-134.44)	0.0
X = 760 TO 919								
1	-130(-90.00)	2.445(0.7713)	156(68.89)	51.360(16.2026)	-10(-23.33)	23.354(7.3675)	-214(-136.67)	0.0
2	-125(-87.22)	4.354(1.3736)	188(86.67)	73.155(23.0783)	0(-17.78)	28.718(9.0597)	-244(-153.33)	0.0
3	-87(-66.11)	10.690(3.3724)	175(79.44)	64.989(20.502)	-7(-21.67)	26.805(8.4562)	-244(-153.33)	0.0
4	-58(-50.00)	16.026(5.0557)	130(54.44)	57.564(11.8503)	-8(-22.22)	23.728(7.4855)	-235(-148.33)	0.0
X = 919 TO 1191								
1	-150(-101.11)	2.421(0.7638)	163(72.78)	52.279(16.4925)	-10(-23.33)	23.058(7.2741)	-283(-175.00)	0.0
2	-143(-97.22)	4.340(1.3691)	194(90.00)	73.440(23.1682)	-1(-18.33)	28.264(8.9165)	-296(-182.22)	0.0
3	-100(-73.33)	10.632(3.3541)	180(82.22)	65.552(20.6797)	0(-17.78)	28.378(8.9524)	-294(-181.11)	0.0
4	-70(-56.67)	15.855(5.0018)	137(58.33)	38.629(12.1863)	-7(-21.67)	23.438(7.3940)	-280(-173.33)	0.0
X = 1191 TO 1307								
1	-150(-101.11)	1.834(0.5766)	166(74.44)	46.532(14.6797)	0(-17.78)	23.120(7.2937)	-281(-173.89)	0.0
2	-132(-91.11)	3.203(1.0105)	200(93.33)	70.737(22.3155)	-9(-22.78)	21.555(6.8000)	-250(-156.67)	0.0
3	-87(-66.11)	10.520(3.3188)	181(82.78)	65.186(20.5643)	-10(-23.33)	21.674(6.8375)	-248(-155.56)	0.0
4	-80(-62.22)	11.695(3.6894)	170(76.67)	48.046(15.1571)	-16(-26.67)	17.773(5.6069)	-273(-169.44)	0.0

PORT   STBD $\alpha/_{\epsilon}$ =40

T - TEMPERATURE - °F (°C)
Q - ORBITAL AVE. ABS. SOLAR + EARTH HEAT FLUX, - Btu/hr - sq ft - (Watts/sq cm x10⁻³)

Figure 2-32.   On-orbit Thermal Environment Empty Payload Bay

β — SOLAR INCIDENCE ANGLE, DEG
i — ORBITER ORBIT INCLINATION (DEG)
i_s — ECLIPTIC PLANE INCLINATION (DEG)

90°

EQUATORIAL PLANE

β

i

ECLIPTIC
PLANE

$i_s = 23.5°$

0° ◄— SOLAR VECTOR

ORBIT PLANE

$\beta_{MAX} = \pm (i + 23.5)$, DEG
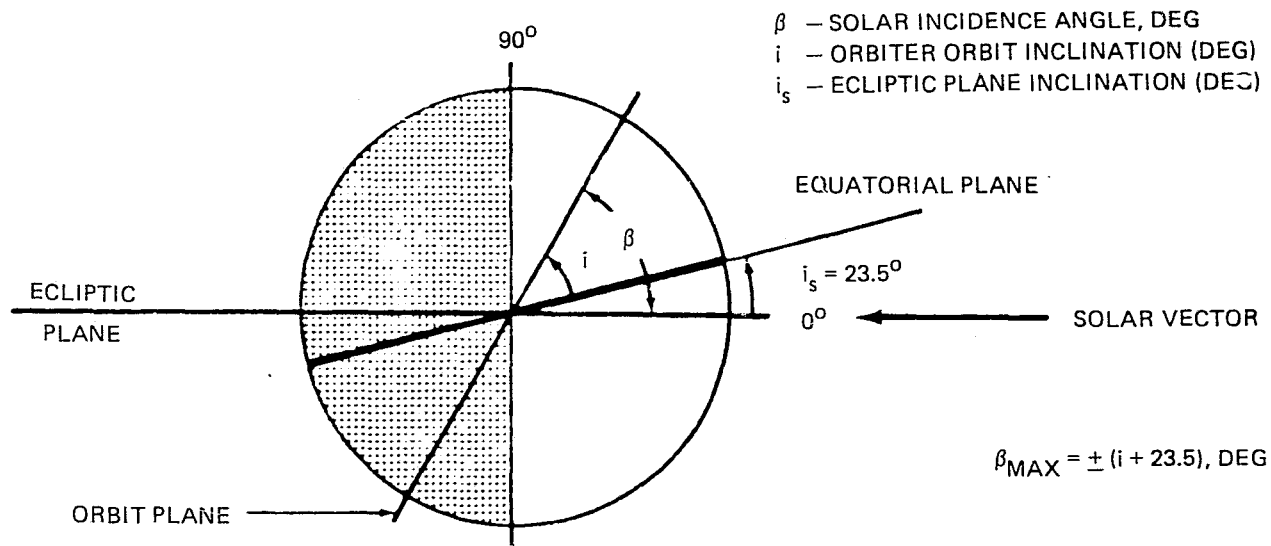
β RANGE DEGREES	ORBITER ORIENTATION	HOLD CAPABILITY HOURS	PREENTRY THERMAL CONDITIONING REQUIREMENTS HOURS
0 TO 60	ANY	≥ 160	≤ 12
60 TO 90	A. OTHER THAN 3-AXIS INERTIAL HOLDS	CYCLES OF 6-HOUR HOLDS FOLLOWED BY 3 HOURS OF THERMAL CONDITIONING FOR WORST THERMAL ATTITUDES	≤ 7
	B. 3-AXIS INERTIAL HOLDS	≥ 160	≤ 12

Figure 2-33.   Orbiter Attitude Hold Capabilities
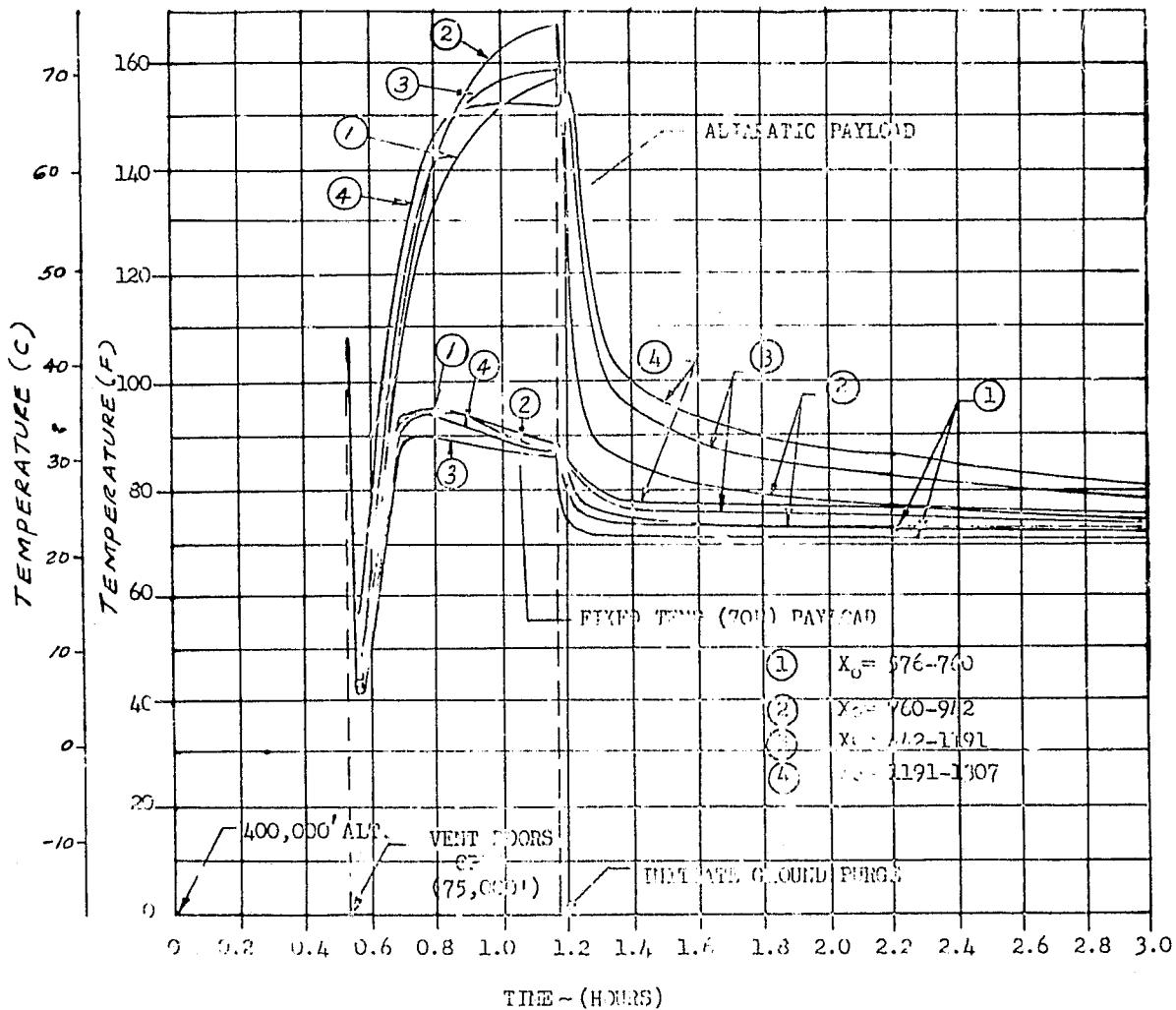
Figure 2-34. Entry Thermal Environment Payload Bay Air Temperature
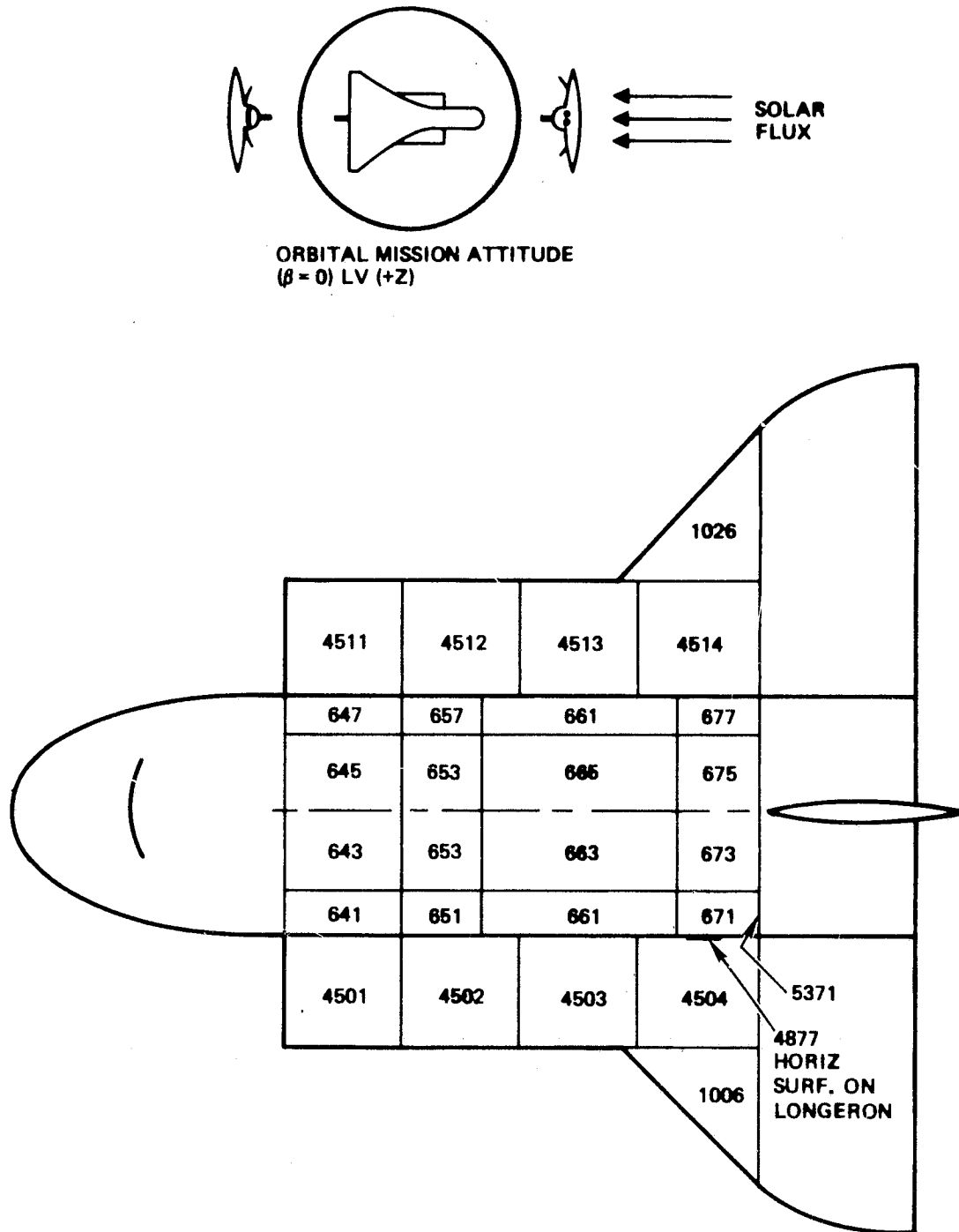
Figure 2-35. Shuttle Orbiter Payload Bay Thermal Model Nodes
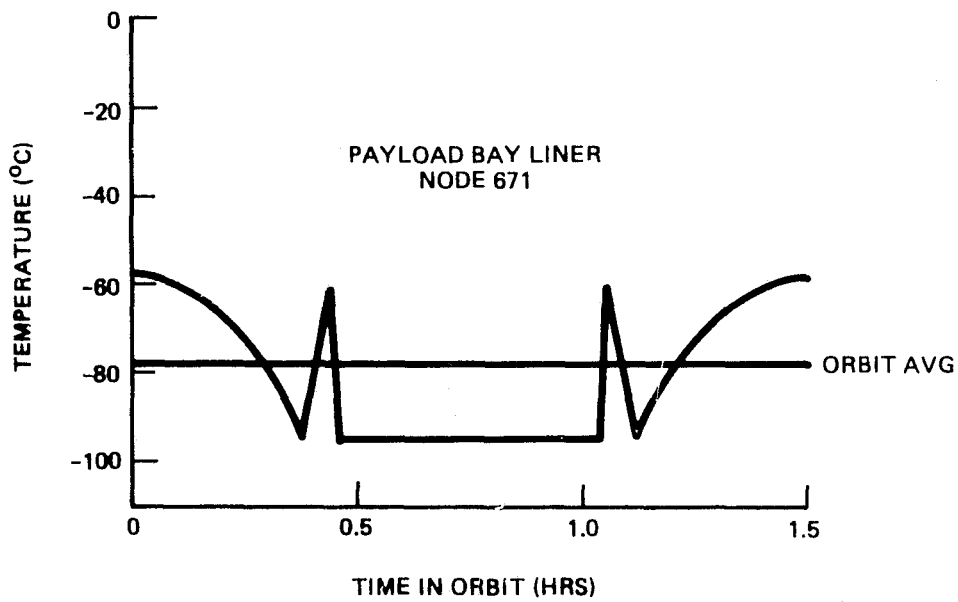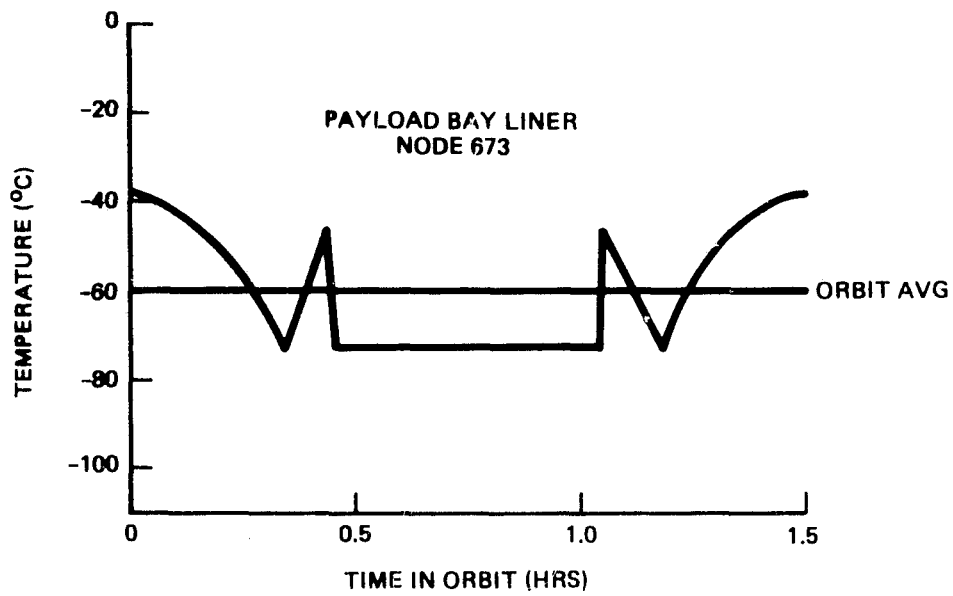
Figure 2-36. Temperature vs Time – Nodes 671 and 673.
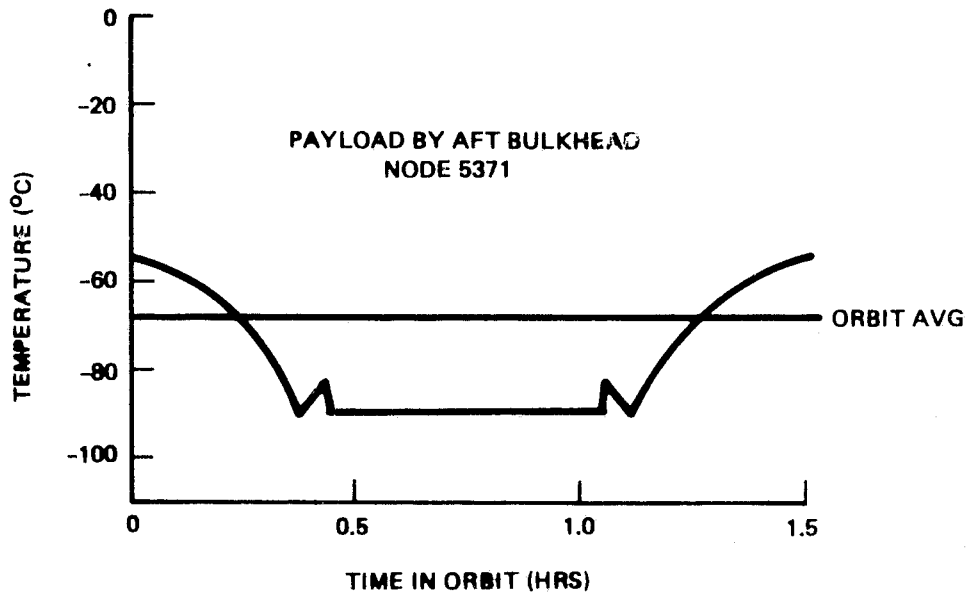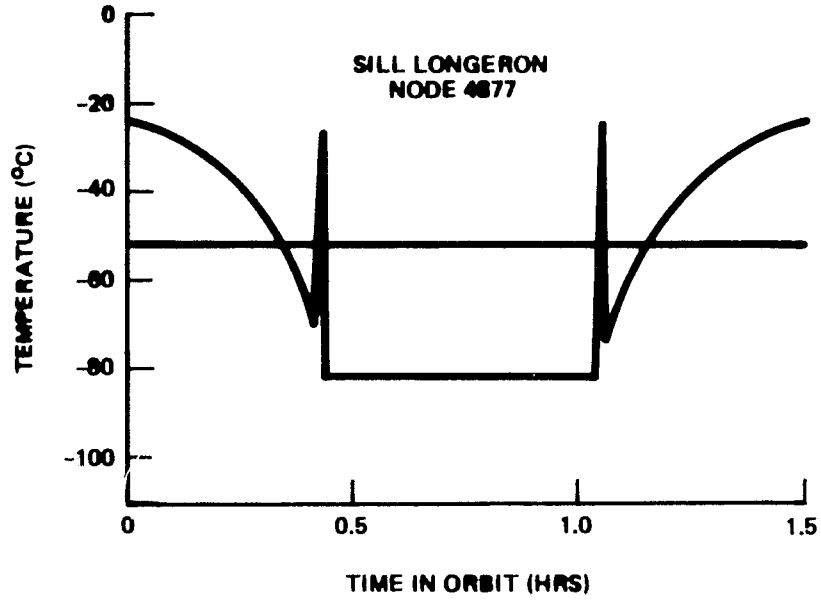
Figure 2-37. Temperature vs Time – Nodes 4877 and 5371.

3. DESIGN APPROACH AND ANALYSIS

3.1 ELECTRICAL ANALYSES

3.1.1 Gregorian Feeds

3.1.1.1 Design Approach

Initially the offset parabolic torus main reflector and the surface contour and trimline of the Gregorian subreflector were designed using geometric optics exclusively. Subsequently the total system was analyzed in detail using physical optics. Such parameters as the position of the subreflector relative to the paraxial focus, the position of the feed relative to the subreflector, and the inclination angle of the feed were optimized by Gustincic. For each set of parameters, maps of the power density transformation ratio "T" were generated. This ratio compares the solid angle subtended by a bundle of optical rays at the feed to the incremental area of the bundle in the aperture plane. A high transformation ratio means the energy in the feed is being concentrated in a relatively small area of the aperture. This will reduce the aperture taper in that area. Designing the antenna for high main beam efficiency requires a smooth aperture illumination with more than 10 dB of aperture taper at the edges to reduce the sidelobe levels, so high values of T cannot be tolerated.

The various designs were also compared relative to cross polarization loss and the subreflector size and shape. A relatively large size is preferred to allow good operation at the lower frequencies by minimizing diffraction losses. A small size is preferred, however, to allow placing a number of subreflectors around the feed wheel. The subtended angles of the feed in azimuth and elevation were also considered to assure that the design would utilize a feed that would be practical to achieve. All of these considerations led to the choice of the design parameters listed in Table 3-1. The various parameters are defined in Figure 3-1, which also shows the coordinate systems used in the analysis. This design optimization, which was performed by Gustincic, appeared to be entirely satisfactory and was not investigated.

Table 3-1. Subreflector Design Parameters

$H = 0.0813\,R_0$
$F = 0.5625\,R_0$
$S = 0.4000\,R_0$
$TF = 90^\circ$
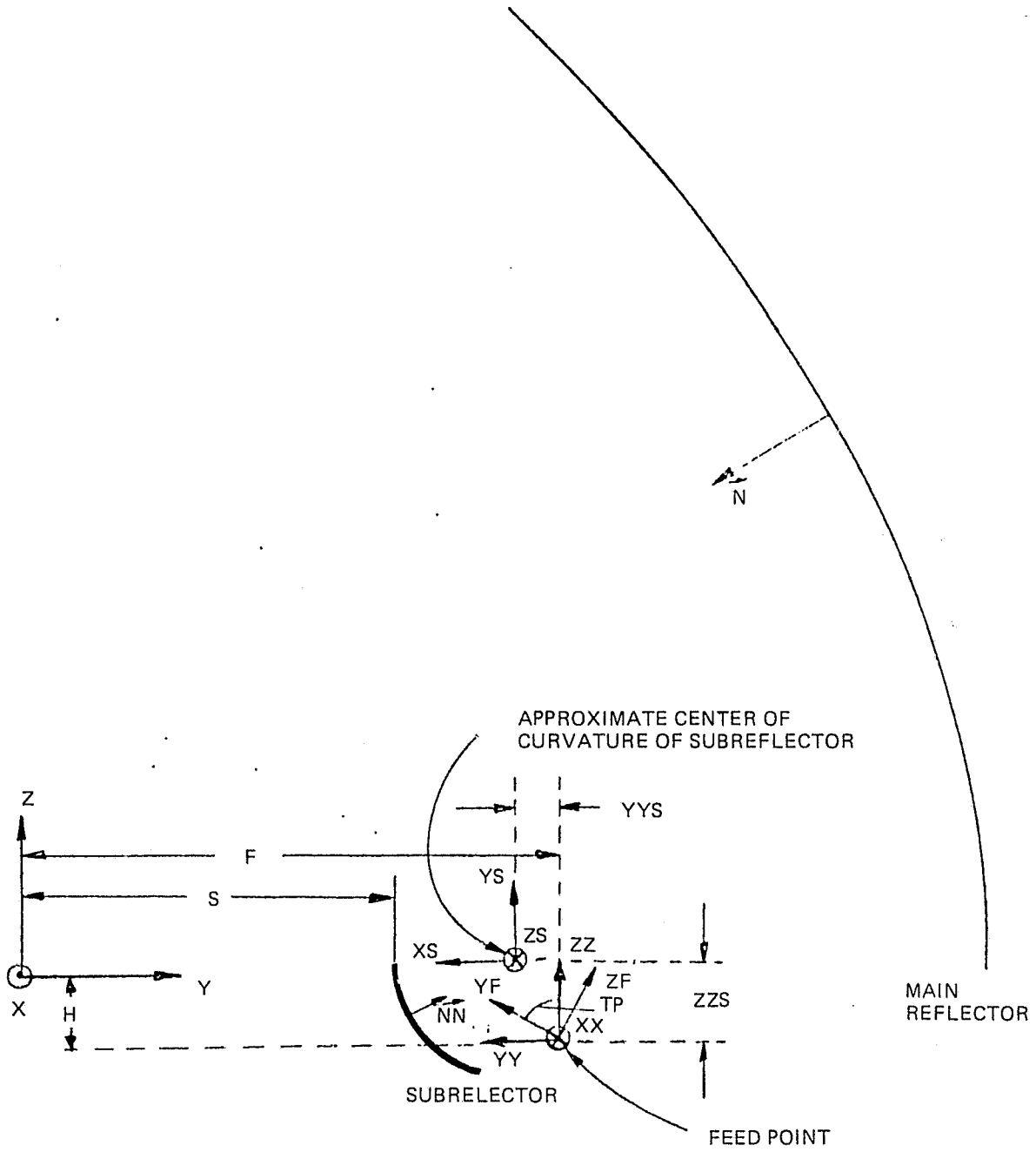
Figure 3-1. Coordinate Relationships

In Gustincic's design, the subreflector periphery was defined relative to a twelve sided aperture shape. Each point in the aperture periphery, traced back to the subreflector along the corresponding optical ray, defines the subreflector contour. Flat sides in an aperture are undesirable, however, because they cause a pedestal in the effective linear aperture distribution and therefore raise the sidelobe level in the pattern cuts that pass through the aperture flats. A rounded aperture shape, however, has a zero at the ends of the effective linear aperture distribution. The sidelobe level and main beam efficiency would thus be better. Furthermore, the aperture shape was too complex to handle conveniently in the analysis. Consequently, a dual ellipse aperture shape which closely approximates Gustincic's aperture shape was chosen. It is illustrated in Figure 3-2. The corresponding subreflector shape is quite irregular and has no straight surfaces at all. It was illustrated in Figure 2-16.

One minor change should be made to this overall design during the hardware phase. Presently, the top of all subreflectors and the bottom of the main reflector are in the same plane, and the lowest ray from the main reflector grazes the subreflector. This leaves no room for a calibration tunnel to pass over the subreflector without blocking the aperture. Consequently, the entire dual-ellipse aperture contour should be moved up about 0.03R. (6 cm), which will also lower the trim line on the subreflector, to leave about 0.036 R. (7.2 cm) clearance. This allows for the calibration cavity, clearance between the cavity and subreflector, and clearance between the aperture and top of the cavity to avoid blocking the near field of the main reflector. The effect of this slight change on the antenna performance should be minimal.

3.1.1.2 Analysis of the Gregorian Reflector System

Geometric Optics Design

The first phase of the analysis was to repeat the geometric optics design procedure used by Gustincic. This was done to check those results and, more importantly, to obtain the subreflector surface coordinates with high accuracy and in the form of a subroutine for use in the analysis program.

The result of this analysis is a subroutine GEODES, which has the input/output parameters of Table 3-2. The variable names* are the same as those used by Gustincic, and like his analysis all length parameters are normalized to the radius of the main reflector. All vectors relate to the unit vectors of the basic (X, Y, Z) coordinate system. FORTRAN program listings are given in Appendix A.

Physical Optics Analysis Approach

The subreflector was first broken up into approximately equal area segments. The currents on each segment were calculated using the physical optics approximation. The main reflector was then broken up into approximately equal segments, and the scattered field from the subreflector at each main reflector point was calculated by summing the contribution (using the exact near field expressions) of each subreflector segment. The main reflector current was then approximated using

---

*FORTRAN type variable names are used, giving an unusual appearance to the equations but good correspondance to the FORTRAN code.
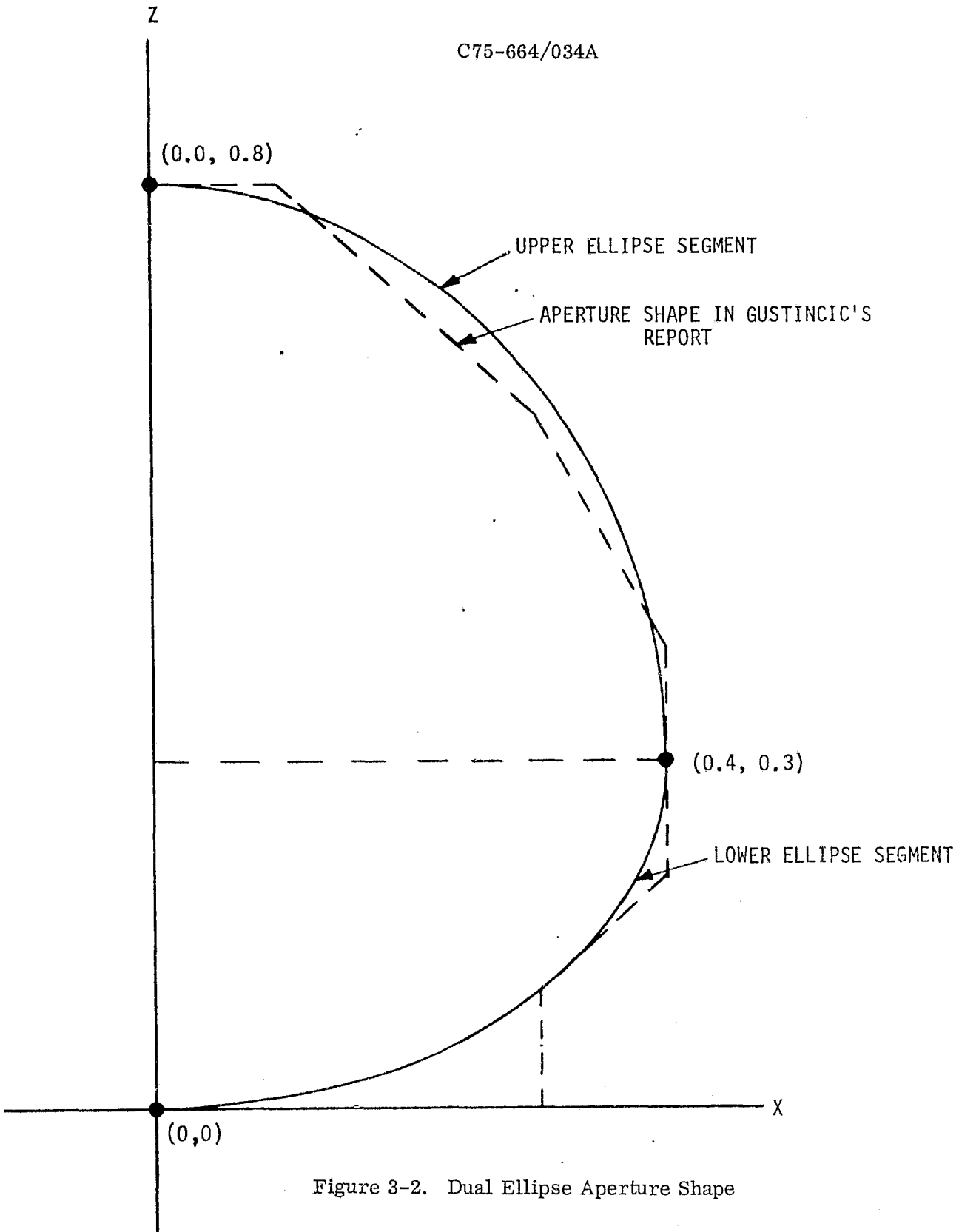
Figure 3-2. Dual Ellipse Aperture Shape

Table 3-2. Input/Output Parameters of Geodes

Inputs

X : X coordinate on the main reflector (also aperture)
Z : Z coordinate on the main reflector (also aperture)

Outputs

Y   The Y coordinate on the main reflector.

$\vec{RR}$ The vector from the feed point to the subreflector point. This vector is expressed as follows, using the local (XX, YY, ZZ) coordinate system

$\hat{X}(-XX) + \hat{Y}(-YY) + \hat{Z}(+ZZ)$

$\vec{NN}$ The unit normal vector of the subreflector.

The subroutine also uses the following design parameters which are communicated in common block REFPRM

$\left. \begin{matrix} F \\ H \end{matrix} \right\}$ Parameters defined by Gustincic

K $2 - S + \sqrt{H^2 + (F - S)^2}$, which is the total path length from the feed to the aperture plane $y = 0$.

physical optics, and the contribution of each segment was added for each far field point.

The field of the primary feed was normalized so that it contained unit power. This normalization was maintained throughout, so that integrating the far field pattern out to the 1.25 beamwidth radius gave the fraction of the total feed power contained in the 2.5 beamwidth circle. This was then related to main beam efficiency by properly accounting for the power spilled over past the subreflector and past the main reflector.

Choice of Subreflector Segments

In order to compute the main reflector currents induced by the field scattered off the subreflector, $N_m \cdot N_s$ individual field contributions must be calculated, where N_m is the number of main reflector segments and N_s is the number of subreflector segments. This product can be 10^6 or more, so the computer execution time can become impractically large. Consequently, the choice of a grid of points on the subreflector was made with care in order to minimize the number of subreflector segments. The use of a regular grid with equal area segments gives the fewest elements, but the irregular shape and considerable curvature of the subreflector makes this difficult.

The subreflector is, however, approximately spherical in shape. Assuming it was a sphere, a grid of exactly equal area segments could be chosen as in Figure 3-3 by placing the points on latitude lines (constant θ in spherical coordinates) and spacing them circumferentially by the angular increment $d\phi = \frac{d\theta}{\sin\theta}$. This only works well on a portion of a sphere, which is no problem in this case. These equal area segments were then projected onto the subreflector.

The description of the analysis is complicated by the use of three local coordinate systems (XX, YY, ZZ), (XF, YF, ZF), and (XS, YS, ZS) along with the basic (X, Y, Z) system, as shown in Figure 3-1. All vectors, however, are expressed in terms of the basic unit vectors X, Y, and Z. The use of a local system is noted where it occurs.

The (XS, YS, ZS) system is centered at the approximate center of curvature of the subreflector, and rotated as shown to place the plane of symmetry in the X-Y plane. Conventional spherical coordinate angles (TH, PH) are also defined in the local system. The relationship to the basic system is:

$$XS \; = \; F - Y - YYS \tag{1}$$

$$YS \; = \; Z + H - ZZS \tag{2}$$

$$ZS \; = \; -X \tag{3}$$

The spherical coordinate angles are defined by the equations:

$$COS(TH) \; = \; \frac{ZS}{\sqrt{XS^2 + YS^2 + ZS^2}} \tag{4}$$

$$TAN(PH) \; = \; \frac{YS}{XS} \tag{5}$$

For the half of the subreflector with XX>0, coordinate points are then chosen equally spaced in TH from THMIN to $\pi/2$, where THMIN is the minimum value reached on the periphery of the subreflector (about 29 deg in the present design). For each value of TH used, the value of PH at the bottom of the subreflector, or minimum value of PH, must be calculated. This is done in the computer program by systematically perturbing the (X, Z) aperture coordinate on the periphery of the aperture (using the subroutine GEODES) until the desired value of TH is obtained. The value of PH is then stored as PH1 at that point. If the spacing in TH is DTH, then the spacing in PH is

$$DPH \; = \; \frac{DTH}{SIN(TH)} \tag{6}$$

The spherical angles of each subreflector point are thus defined. They are summarized below.

$$TH \; = \; PI/2 - DTH \cdot (I - 1/2) \tag{7}$$

$$PH \; = \; PH1 + DPH \cdot (J - 1/2) \tag{8}$$

where PH1 is the value of PH at the bottom of the subreflector for this value of TH.
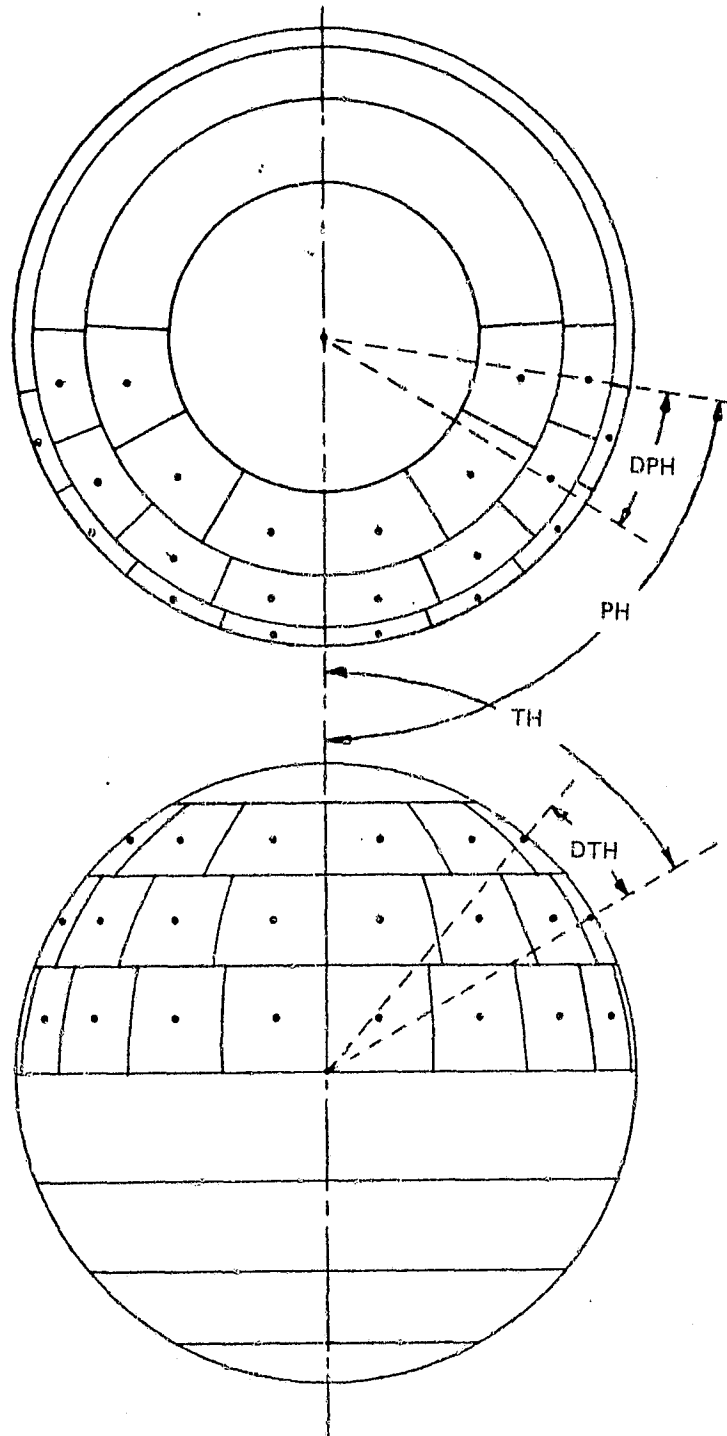
Figure 3-3. Division of a Sphere into Equal Area Segments

The actual point on the subreflector that has the spherical angles (TH, PH) is found by two-dimensional iteration of the aperture coordinates X and Z, using the subroutine GEODES, until the angles of the subreflector point are sufficiently close to the desired values. A two dimensional form of Newton's method is used and convergence takes two to four iterations. The coordinates of the center of each sub-reflector segment are thus defined by this procedure. The next step is to calculate the actual area of each segment.

For each subreflector point, let $\vec{VS}$ be the vector from the subreflector point to the approximate center of curvature. It is defined as

$$\vec{VS} = \vec{OS} - R\vec{R} \tag{9}$$

where
$$\vec{OS} = \hat{Y}(F - YYS) + \hat{Z}(-H + ZZS) \tag{10}$$

The magnitude of $\vec{VS}$ is the distance from the approximate center of curvature to the subreflector point. The surface normal vector is $\vec{NN}$*. The actual incremental surface area DS can then be calculated using the area of the adjacent spherical segment and the angle between the surface normal and the sphere radius vector VS.

$$DS = \frac{|\vec{VS}|^2 \cdot \text{SIN(TH)} \cdot \text{DTH} \cdot \text{DPH}}{(\vec{VS} \cdot \vec{NN})/|\vec{VS}|} \tag{11}$$

The fact that the subreflector is not exactly a sphere causes $|\vec{VS}|$ to vary from 0.150 to 0.163 over the subreflector surface, while the denominator varies from 1.00 to 0.986 due to the fact that $\vec{NN}$ and $\vec{VS}$ do not remain parallel. A variation in DS of 20 percent over the subreflector is the result, but this is quite good considering the subreflector shape. A total of 550 subreflector points (both sides of the symmetry plane) spaced 0.4λ apart are required at 6.6 GHz, and 1332 points would be required at 10.69 GHz.

Primary Pattern

The primary pattern was chosen to be that of a rectangular aperture with a cosine aperture distribution in both planes, as shown in Figure 3-4. This would represent the patterns of a rectangular corrugated horn fairly accurately. The vector representation of the pattern was defined assuming that the aperture power was equally transmitted by electric and magnetic currents. Again, this represents the horn aperture fairly accurately, because the aperture is far from cutoff. To normalize all of the further computations, the primary patterns were integrated over the forward half sphere to determine the directivity, and the on-axis directivity PKGN was used to normalize the primary patterns so that unit power is transmitted. In the local feed coordinates (XF, YF, ZF) the primary pattern magnetic field is $\text{HPP} \cdot \hat{\phi} + \text{HTP} \cdot \hat{\theta}$. These vector components are given by the following equations, assuming a distance of one meter. The equations are derived from the closed form expressions of the far field patterns of a cosine amplitude distribution given in Silver[6].

---

*NN is obtained from the geometric optics design program GEODES as an intermediate step in determining the subreflector coordinates.
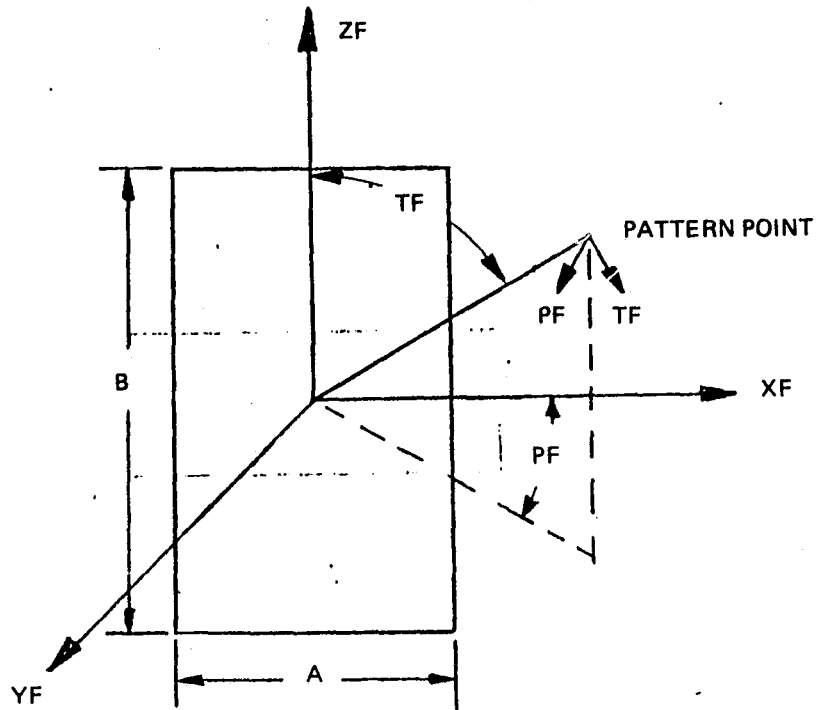
Figure 3-4. Coordinate System for the Primary Horn Aperture

$$HPP = \frac{AF}{2}\left[1 + \frac{SIN(PF)}{\sqrt{1 - \left[SIN(TF) \cdot COS(PF)\right]^2}}\right] \tag{12}$$

$$HTP = -\frac{AF}{2}\left[\frac{COS(TF) \cdot COS(PF)}{\sqrt{1 - \left[SIN(TF) \cdot COS(PF)\right]^2}}\right] \tag{13}$$

$$AF = \frac{COS(U1) \cdot COS(U2) \cdot \sqrt{\frac{SIN(TF) \cdot SIN(PF) \cdot PKGN}{4 \cdot PI \cdot ETA}}}{\left[1 - \left(\frac{2 \cdot U1}{PI}\right)^2\right] \cdot \left[1 - \left(\frac{2 \cdot U2}{PI}\right)^2\right]} \tag{14}$$

$$UI = \frac{EK \cdot A \cdot SIN(TH) \cdot COS(PH)}{2} \tag{15}$$

$$U2 = \frac{EK \cdot B \cdot COS(TH)}{2} \tag{16}$$

$$\text{ETA} = \sqrt{\mu/\epsilon} \tag{17}$$

$$\text{EK} = 2\pi/\lambda \tag{18}$$

$$\text{A} = \text{Width of aperture}$$

$$\text{B} = \text{Height of aperture}$$

TF, PF are the conventional spherical coordinate angles.

The factor SIN(TF) · SIN(PF) term in the equation (14) is equal to the cosine of the angle off the horn axis. This additional term gives a pattern which is closer to the measured patterns plotted in Silver[6], pages 344-345.

These formulas were computed by a subroutine PRIPAT, with inputs and outputs as outlined in Table 3-3.

Subreflector Currents

The final step in this portion of the analysis is to compute the subreflector currents. Looking ahead to the later physical optics (P.O.) analysis, the quantity actually calculated is $\vec{J}_s$ds, which according to the P.C. approximation is equal to:

$$\text{JSDS} = 2 \cdot \text{DS} \cdot (\vec{NN} \times \vec{HP}) \tag{19}$$

Where $\vec{HP}$ is the incident magnetic field. In the following analysis, $\vec{HP}$ is referenced to unit radius and does not include the phase term e^{-jkr}. The magnitude of the current-area product and the path length "PATH" is calculated and stored for each subreflector segment. In the calculation of the subreflector currents, the feed is

Table 3-3. Input/Output Parameters of PRIPAT

Input Parameters	
STP (1)	SIN(TF)
STP (2)	COS(TF)
STP (3)	SIN(PF)
STP (4)	COS(PF)
A	Width of aperture (parallel to X axis)
B	Height of aperture
EK	$2\pi/\lambda$
Output Parameters	
HTP	$\hat{\text{TF}}$ component of the magnetic field at a distance of one meter
HPP	$\hat{\text{PF}}$ component of the magnetic field at a distance of one meter

allowed to be offset from its nominal design position. This allows evaluation of cases where two feeds of different bands are placed side-by-side and feed the same subreflector, or cases where the feed is offset due to manufacturing tolerances or mechanical deflections. The vector from the nominal feed position to the offset position is

$$\vec{OS} = \hat{Z} \cdot FZ - \hat{Y} \cdot FY \tag{20}$$

The offset is limited to the Z and Y axes in order to preserve the symmetry of the antenna and thus greatly reduce computation time. The negative sign occurs because of the relationship between the $\hat{XX}$, $\hat{YY}$, and $\hat{ZZ}$ feed coordinate system and the basic system.

The subreflector point must be expressed in spherical coordinates relative to the offset and inclined feed coordinates to obtain the feed pattern using the PRIPAT routine. The feed rectangular coordinate unit vectors are

$$\hat{XF} = -\hat{X} \tag{21}$$

$$\hat{YF} = -\hat{Y} \cdot SP + \hat{Z} \cdot CP \tag{22}$$

$$\hat{ZF} = \hat{Y} \cdot CP + \hat{Z} \cdot SP \tag{23}$$

Where SP = SIN(TP), CP = COS(TP), and TP is the pointing angle of the feed relative to vertical.

The spherical coordinate unit vectors $\hat{TF}$ and $\hat{PF}$ are related to the corresponding rectangular coordinate vectors $\hat{XF}$, $\hat{YF}$, and $\hat{ZF}$ as follows:

$$\hat{TF} = \hat{XF} \cdot COS(TF) \cdot COS (PF)$$
$$+ \hat{YF} \cdot COS(TF) \cdot SIN(PF) - \hat{ZF} SIN(TF) \tag{24}$$

$$\hat{PF} = \hat{YF} \cdot COS(PF) - \hat{XF} \cdot SIN(PF) \tag{25}$$

Substituting (21) – (23) into (24) and (25),

$$\hat{TF} = \hat{X} \cdot \left[-COS(TF) \cdot COS(PF) \right]$$
$$+ \hat{Y} \cdot \left[-SP \cdot COS(TF) \cdot SIN(PF) - CP \cdot SIN(TF) \right] \tag{26}$$
$$+ \hat{Z} \cdot \left[CP \cdot COS(TF) \cdot SIN(PF) - SP \cdot SIN(TF) \right]$$

$$\hat{PF} = \hat{X} \cdot SIN(PF) - \hat{Y} \cdot SP \cdot COS(PF) + \hat{Z} \cdot CP \cdot COS(PF) \tag{27}$$

Finally, the incident magnetic field is calculated in the subroutine PRIPAT in the form

$$\vec{HP} = \hat{TF} \cdot HTP + \hat{PF} \cdot HPP \tag{28}$$

Substituting (26) and (27) into (28) gives

$$\vec{HP} = \hat{X}[-HTP \cdot COS(TF) \cdot COS(PF) + HPP \cdot SIN(PF)]$$
$$+Y\{HTP \cdot [-SP \cdot COS(TF) \cdot SIN(PF) - CP \cdot SIN(TF)]$$
$$-HPP \cdot SP \cdot COS(PF)\} \qquad (29)$$
$$+Z\{HTP \cdot [CP \cdot COS(TF) \cdot SIN(PF) - SP \cdot SIN(TF)] + HPP \cdot CP \cdot COS(PF)\}$$

This expression for HP is referenced to unit radius. Taking into account the range dependance of the primary pattern, the current induced in the subreflector is then

$$\vec{JSDS} = (2 \cdot DS/R\emptyset) \cdot (\vec{NN} \times \vec{HP}). \qquad (30)$$

Where $R\emptyset = RO \cdot |\vec{RR}|$, RO being the radius of the main reflector and $\vec{RR}$ is the vector from the feed point to the subreflector point. All of the main- and subreflector coordinates are normalized to the main reflector radius as in Gustincic's analysis, so the factor RO appears frequently to obtain absolute lengths where needed.

At this point, the vector $\vec{RR}$, the vector $\vec{JSDS}$, and the path length $RO \cdot |\vec{RR}|$ from the feed to the subreflector point are all placed in permanent computer storage. The Z and X components of the main reflector current are then calculated along the reflector cut lines shown in Figure 3-5 to evaluate the results at this stage and to define the limits of the main reflector to be integrated to obtain the far field pattern.
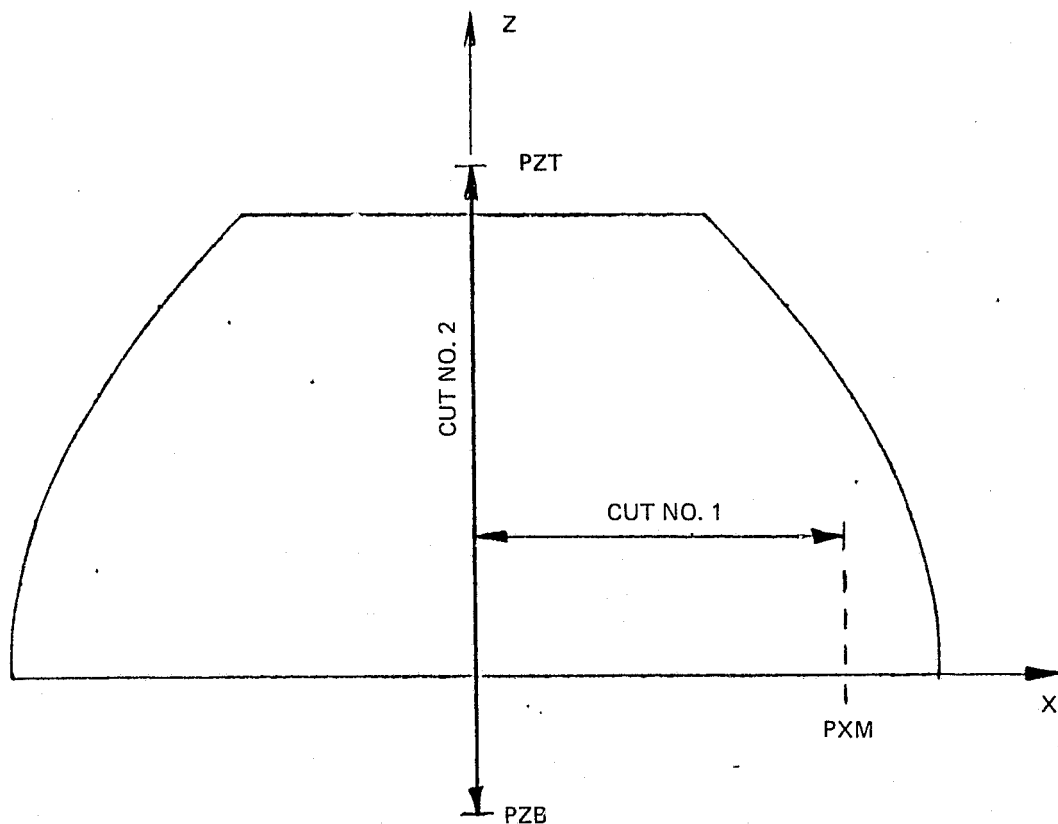
Figure 3-5. Lines on Main Reflector Used for Interim Evaluation

Main Reflector Currents

The second computer program reads the value of $\vec{RR}$, $\vec{JSDS}$, and PATH for each subreflector point and computes first the main reflector currents and then the far field patterns.

To compute the main reflector current, the near field form of the diffracted magnetic field in Rusch and Potter[7] is used.

$$\vec{HP} = \frac{1}{4\pi} \int_s (\vec{J}_s \times \vec{a}_r)(jk + \frac{1}{r})(e^{-jkr}/r)ds \tag{31}$$

This equation was obtained by substituting (2.6-5) into (2.6-4) of Rusch and Potter and setting the magnetic current to zero.

The main reflector point is defined by the vector $\vec{P} = X\hat{X} + (Y - F)\hat{Y} + (Z + H)\hat{Z}$ extending from the feed point to the main reflector point. The subreflector point is defined by the vector $\vec{RR}$ extending from the feed point to the subreflector point. Then, a vector $\vec{SM}$ which extends from the subreflector point to the main reflector point and absolute distance RSM are defined:

$$\vec{SM} = \vec{P} - \vec{RR} \tag{32}$$

$$RSM = RO \cdot |\vec{SM}| \tag{33}$$

rather than the normal vector $\vec{a}_r$, the length vector $\vec{SM}$ is used to save a computation step. They are related by the formula

$$\vec{a}_r = \vec{SM} \cdot RO/RSM \tag{34}$$

Finally, the magnetic field is obtained by a summation of the contributions

$$d\vec{H} = [RO/(4 \cdot PI \cdot RSM^2)](\vec{JSDS} \times \vec{SM})(j \cdot EK + 1/RSM) \\ [e^{-j \cdot EK \cdot (RSM + PATH)}] \tag{35}$$

Here the term PATH is included in the exponential term to take care of the phase of the subreflector current.

The integration over the main reflector uses a rectangular grid in the aperture plane projected back on the main reflector. The incremental area is

$$DS = \frac{DX \cdot DZ \cdot RO^2}{|\vec{N} \cdot \hat{Y}|} \tag{36}$$

Where DX and DZ are the aperture coordinate increments and $\vec{N}$ is the surface normal unit vector of the main reflector, which is given in Gustincic as follows:

$$\vec{N} = -\hat{X} \cdot X / \sqrt{(1 + Z^2) \cdot (X^2 + Y^2)}$$
$$-\hat{Y} \cdot Y / \sqrt{(1 + Z^2) \cdot (X^2 + Y^2)} \tag{37}$$
$$-\hat{Z} \cdot Z / \sqrt{(1 + Z^2)}$$

The vector $\vec{JM}$ is then computed, representing $\vec{J}_S dS$ on the main reflector. It is equal to

$$\vec{JM} = 2 \cdot DS \cdot (\vec{N} \times \vec{HP}) \tag{38}$$

Far Field Pattern

The Fraunhofer approximation to the vector diffraction equation for the magnetic field, when it is referenced to a one meter distance, is

$$\vec{HF} = \frac{1}{4\pi} \int_S (\vec{J}_s \times \vec{a}_r)(jk)(e^{+j\vec{k} \cdot \vec{r}})ds \tag{39}$$

The far field is obtained by a summation of the individual contributions

$$d\vec{H} = [j \cdot EK/(4 \cdot PI)] \cdot (\vec{JM} \times \vec{AR}) \cdot (e^{+j \cdot EK \cdot (\vec{AR} \cdot \vec{R})}) \tag{40}$$

Where $\vec{R}$ is the vector from the origin to the main reflector segment and $\vec{AR}$ is the unit vector in the direction of the far field pattern point. To allow taking pattern cuts in a coordinate system centered on the main beam, the pattern coordinate system is oriented at an angle TB from the vertical as shown in Figure 3-6. The vector $\vec{AR}$ is then

$$\vec{AR} = \hat{X}' \cdot STP \cdot CPP + \hat{Y}' \cdot STP \cdot SPP + \hat{Z}' \cdot CTP \tag{41}$$

Where STP = SIN(TP)
CTP = COS(TP)
SPP = SIN(PP)
CPP = COS(PP)
TP and PP are the spherical coordinate angles

The relationship between the rotated and basic unit vectors is given by the expressions

$$\hat{X}' = \hat{X} \tag{42}$$

$$\hat{Y}' = \hat{Y} \cdot CTB + \hat{Z} \cdot STB \tag{43}$$

$$\hat{Z}' = -\hat{Y} \cdot STB + \hat{Z} \cdot CTB \tag{44}$$

Where STB = SIN(TB) and CTB = COS(TB). Substituting Eq. (42) – (44) into (41) gives the following expression for $\vec{AR}$
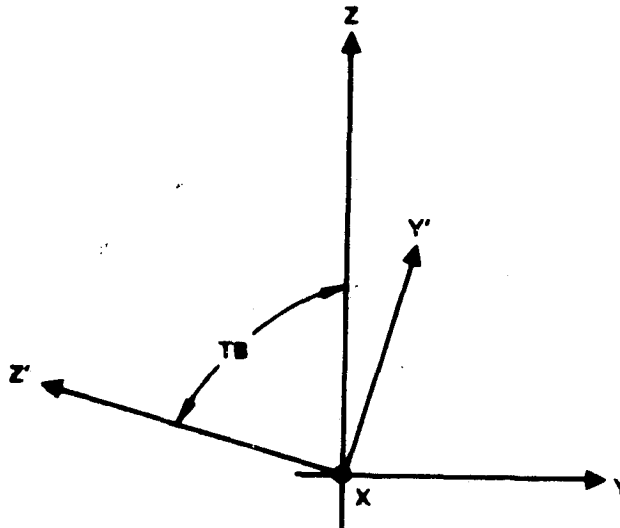
Figure 3-6. Coordinate System for Far Field Patterns

$$AR = \hat{X} \cdot STP \cdot CPP$$
$$+\hat{Y} \cdot (CTB \cdot STP \cdot SPP - STB \cdot CTP) \tag{45}$$
$$+\hat{Z} \cdot (STB \cdot STP \cdot SPP + CTB \cdot CTP)$$

To separate the Fraunhofer magnetic field into vertically and horizontally polarized components, the following unit polarization reference vectors were defined:

$$\vec{HV} = \hat{X}[-CT \cdot CP^2 - SP^2] + \hat{Y}[-ST \cdot CP] + \hat{Z}[SP \cdot CP \cdot (1 - CT)] \tag{46}$$

$$\vec{HH} = \hat{X}[SP \cdot CP \cdot (CT - 1)] + \hat{Y}[ST \cdot SP] + \hat{Z}[CP^2 + CT \cdot SP^2] \tag{47}$$

Where ST = SIN(TH)
CT = COS(TH)
SP = SIN(PH)
CP = COS(PH)

TH is the angle between the $(-\hat{Y})$ axis and $\vec{AR}$, and PH is the rotational angle of the pattern point. The vector $\vec{AR}$ expressed in terms of these angles is

$$\vec{AR} = \hat{X} \cdot ST \cdot CP - \hat{Y} \cdot CT + \hat{Z} \cdot ST \cdot SP \tag{48}$$

Therefore,

$$ST = \sqrt{ARX^2 + ARZ^2} \qquad (49)$$

$$CT = -ARY \qquad (50)$$

$$SP = ARZ/ST \qquad (51)$$

$$CP = ARX/ST \qquad (52)$$

Where ARX, ARY, and ARZ are the corresponding components of $\vec{AR}$.

These reference vectors are the same ones that occur when various pattern cuts are taken on a pattern range using the lower azimuth table, with the elevation table tilted forward to point the beam at the transmitter. The upper azimuth table gives the angle of the pattern cut, and the transmitted polarization is rotated along with the upper azimuth table when changing the cut angle. It is surprising that the form of these reference vectors is so complicated.

The magnitudes are then

$$HP = \left| \vec{HF} \cdot \vec{HV} \right| \qquad (53)$$

$$HC = \left| \vec{HF} \cdot \vec{HH} \right| \qquad (54)$$

and the gain at any point is

$$G = 4 \cdot PI \cdot ETA \cdot HP^2$$

Finally, the radiated power is integrated according to the formula

$$PP = \int_{O}^{TL} \int_{O}^{2 \cdot PI} ETA \cdot HP^2 \cdot SIN(TS) \cdot DTH \cdot DPH \qquad (55)$$

$$PT = \int_{O}^{TL} \int_{O}^{2 \cdot PI} ETA \cdot (HP^2 + HC^2) \cdot SIN(TS) \qquad (56)$$

$$\cdot DPH \cdot DTH$$

Here PP is the principly polarized power contained in the pattern from the center of the beam to the angle TL and PT is the corresponding total power. The value of PP at TL $= 1.25\,\Theta$ gives the total power in the main beam, while the ultimate value of PT should equal

$$PT(PI) = \eta_{s1} \cdot \eta_{s2} \qquad (57)$$

where η_{s1} is the subreflector spillover efficiency

η_{s2} is the main reflector spillover efficiency

3.1.1.3 Results of Gregorian Reflector Analysis

Performance vs. Frequency

The first objective of the physical optics analysis was to determine the performance of the Gregorian design at various frequencies. This would evaluate the effect of diffraction on the overall main beam efficiency and consequently define the lowest frequency for which this design approach is viable.

The subreflector currents were calculated at 2.695 GHz, 6.6 GHz, and 10.69 GHz. Following that; the main reflector current along the lines X = 0 and Z = 0.3 was calculated for each frequency. This data is illustrated in Figure 3-7 through 3-18. A considerable improvement in phase error and spillover past the main reflector (indicated by the magnitude of the current for values of Z<0.0 and Z>1.0) can be seen for 6.6 GHz relative to 2.695 GHz. The main reflector current at 10.69 GHz is very similar to 6.6 GHz, however, indicating that the geometric optics limit may have already been reached.

The far field patterns were calculated at 2.695 GHz and 6.6 GHz. They are conveniently summarized in the contour plots shown in Figures 3-19 and 3-20, respectively. The calculated performance at these two frequencies is summarized in Table 3-4.

The main beam efficiency was estimated assuming a portion of the subreflector and main reflector spillover components are absorbed rather than scattered into sidelobe regions of the pattern.

In the physical optics analysis, they were simply lost and the pattern integration up to the 2.5Θ point accounted for those losses due to the fact that the patterns were normalized for unit total power transmitted by the feed. The total power contained in the pattern is thus equal to the product of the main reflector spillover efficiency and subreflector spillover efficiency. If 80 percent of the spillover components is absorbed, the total power contained in the pattern would be

$$Pp + 0.2 (1 - Pp) \tag{57}$$

Table 3-4. Performance Calculated According to Physical Optics

Characteristic	Value @ 2.695 GHz	Value @ 6.6 GHz
Average 3 dB Beamwidth	4.76 deg	2.06 deg
Angle at 2.5 Beamwidth Circle	5.95 deg	2.58 deg
Fraction of feed power contained within 2.5 Θ circle	87.70%	91.26%
Power Contained in Pattern	93.49%	96.11%
Main Beam Efficiency	92.52%	94.19%

PRINCIPLE POLARIZATION AMPLITUDE
AZIMUTH CUT ALONG Z= 0.3055

PHASE RELATIVE TO G. O. PHASE
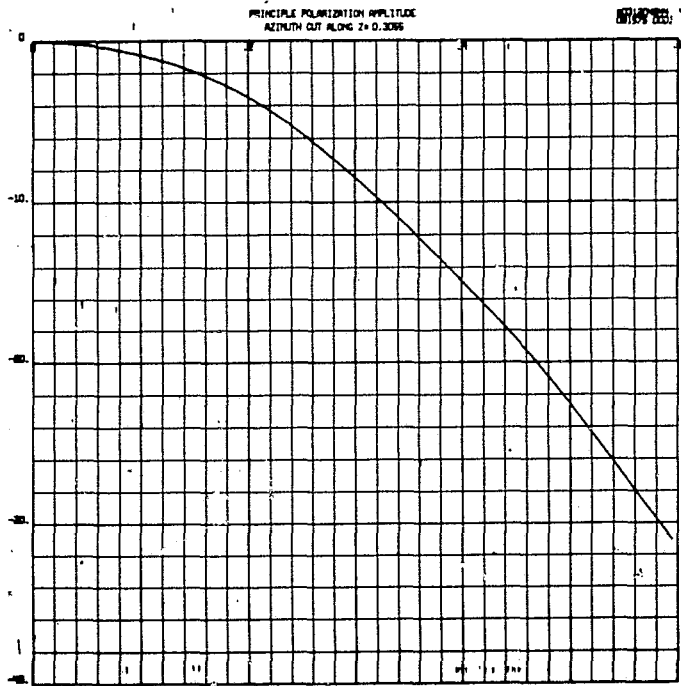
Figure 3-7. Azimuth Cut of Reflector
Current, 2.695 GHz
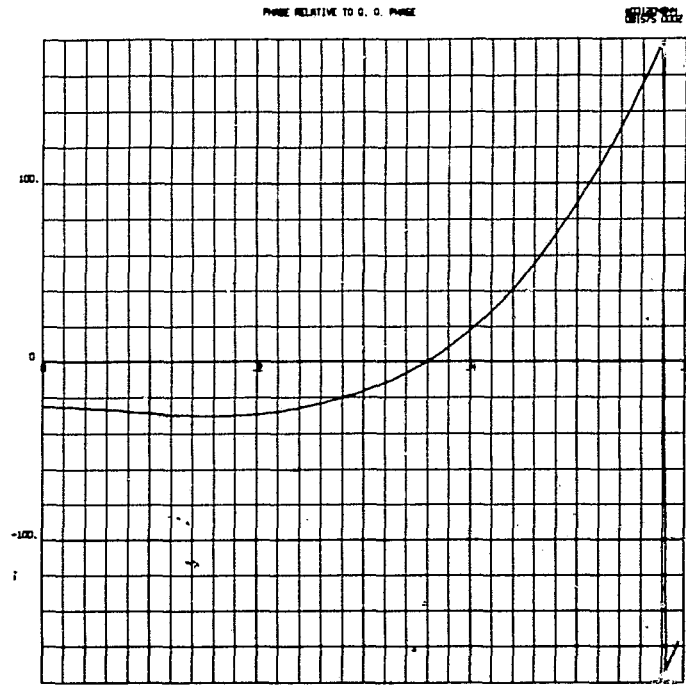
Figure 3-8. Azimuth Cut of Phase,
2.695 GHz

C75-664/034A

PRINCIPLE POLARIZATION AMPLITUDE
ELEVATION CUT ALONG X=0.0000

PHASE RELATIVE TO C 0 PHASE
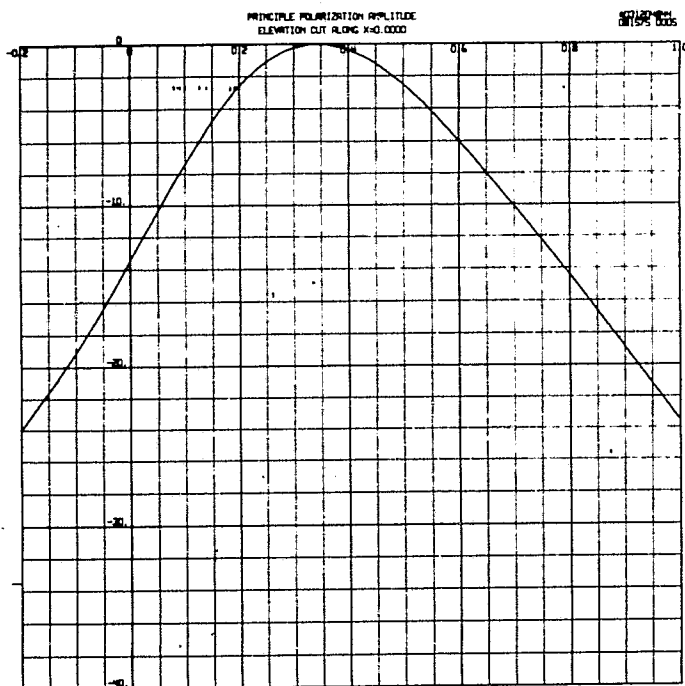
Figure 3-9.   Elevation Cut of Reflector
Current, 2.695 GHz
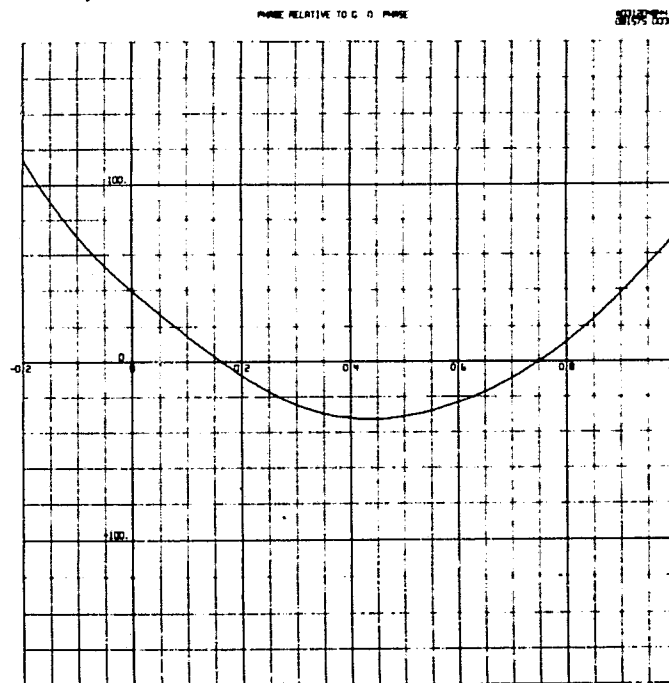
Figure 3-10.   Elevation Cut of
Phase, 2.695 GHz
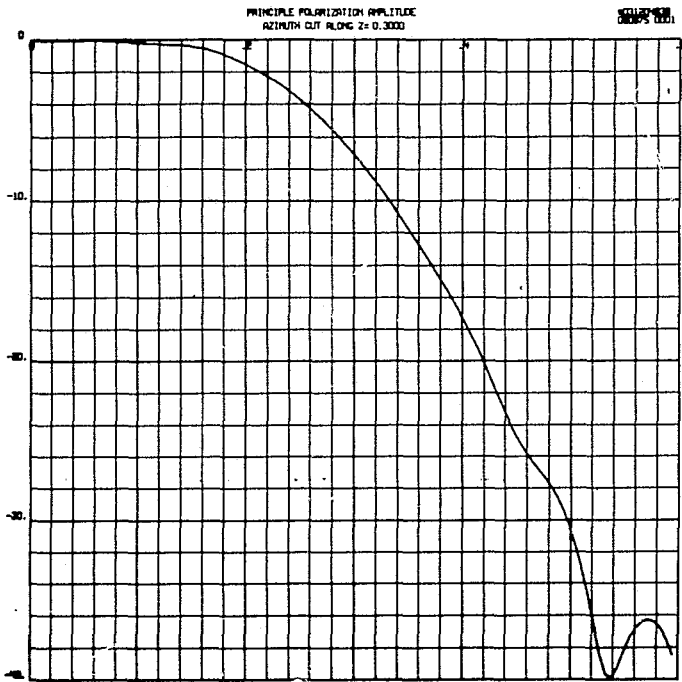
Figure 3-11. Azimuth Cut of Reflector
Current, 6.6 GHz
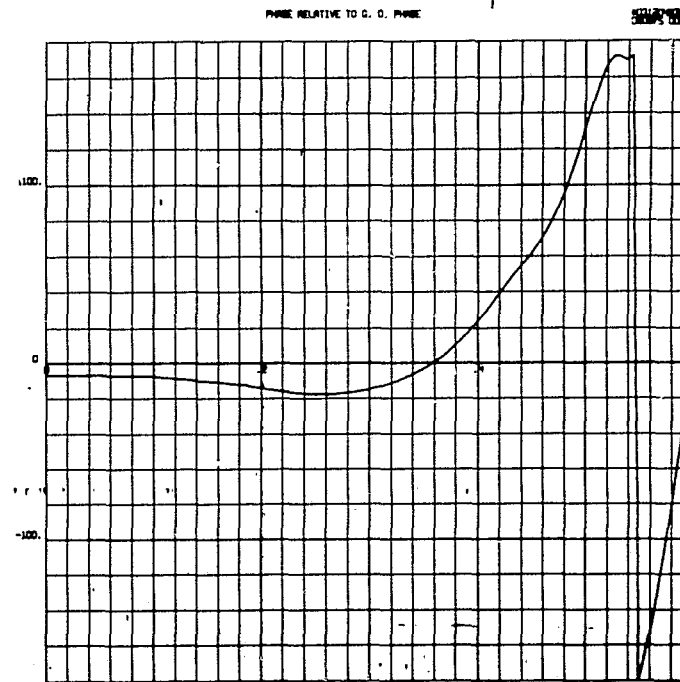
Figure 3-12. Azimuth Cut of Phase,
6.6 GHz
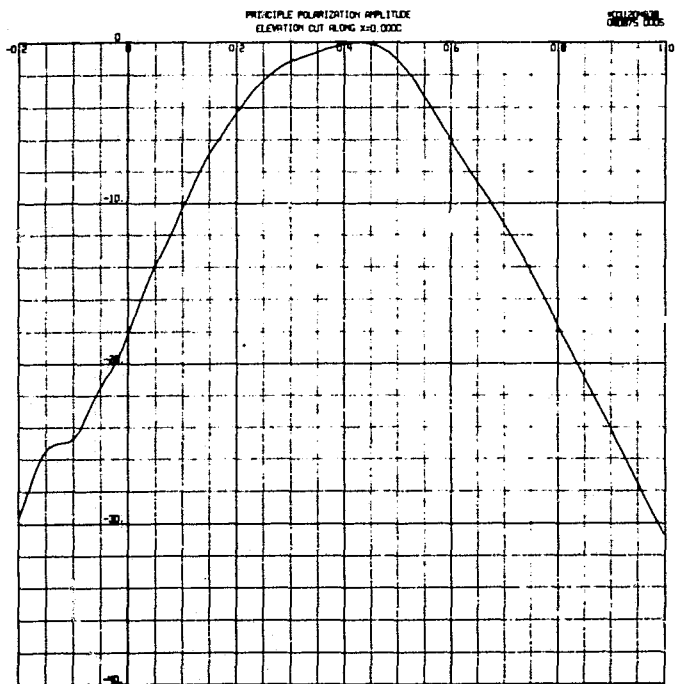
Figure 3-13. Elevation Cut of Reflector
Current, 6. 6 GHz
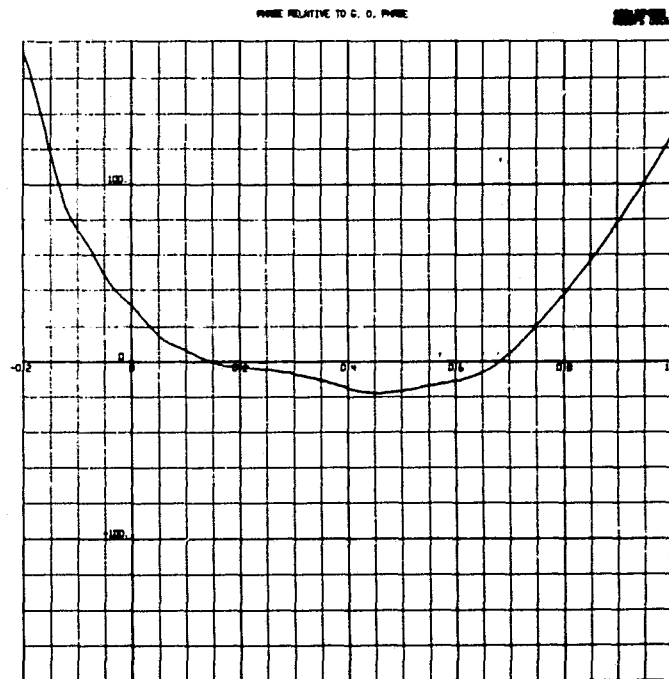
Figure 3-14. Elevation Cut of
Phase, 6. 6 GHz

C75-664/034A

PRINCIPLE POLARIZATION AMPLITUDE
AZIMUTH CUT ALONG Z= 0.3000

PHASE RELATIVE TO G. O. PHASE
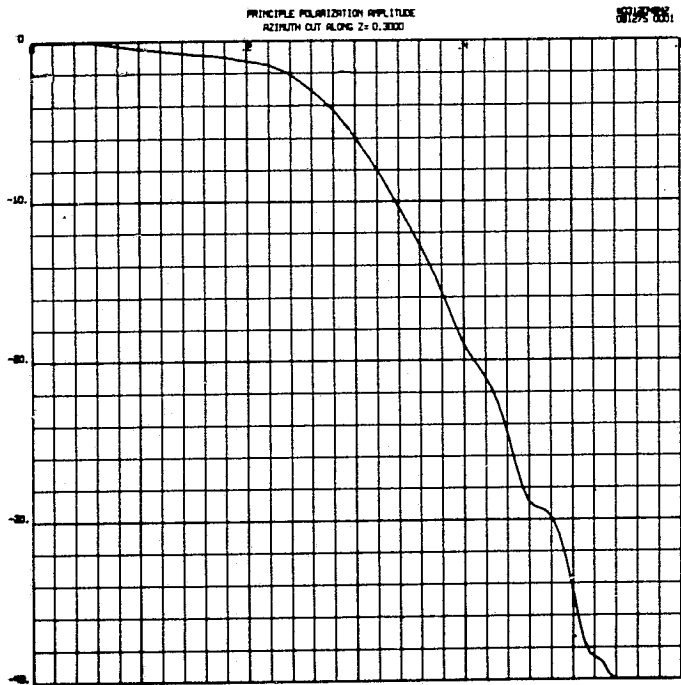
Figure 3-15.   Azimuth Cut of Reflector
Current, 10.69 GHz
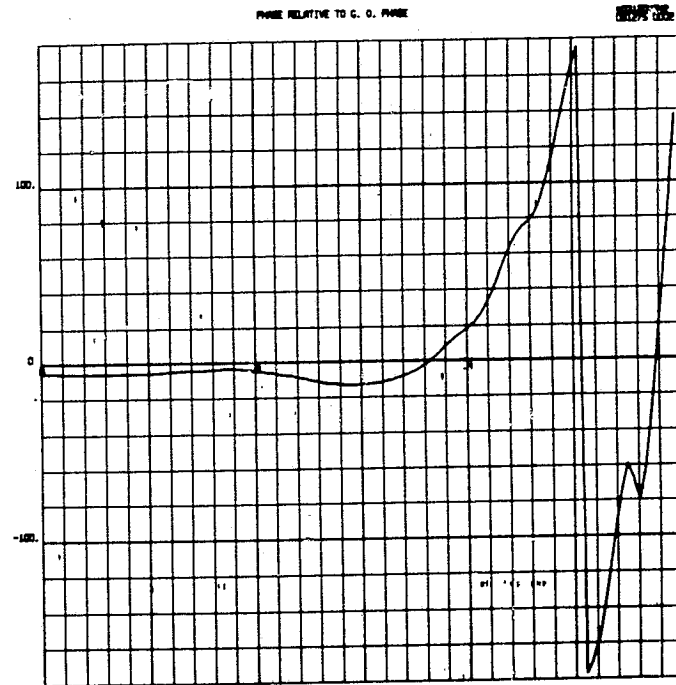
Figure 3-16.   Azimuth Cut of
Phase, 10.69 GHz

PRINCIPLE POLARIZATION AMPLITUDE
ELEVATION CUT ALONG X=0.0000

PHASE RELATIVE TO G. O. PHASE
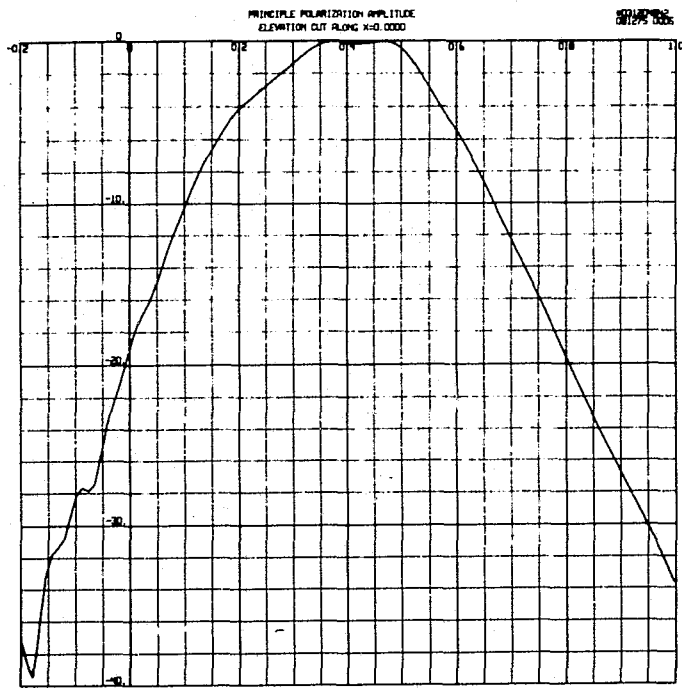
Figure 3-17. Elevation Cut of Reflector
Current, 10.69 GHz
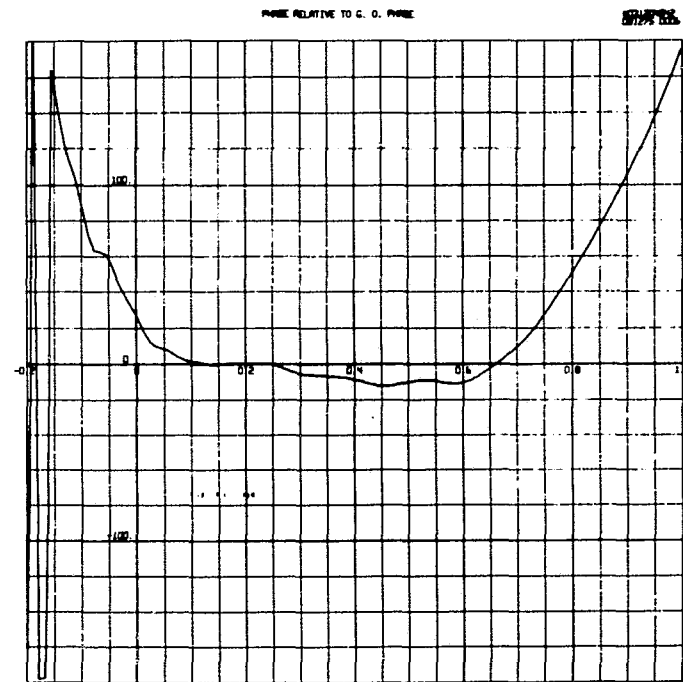
Figure 3-18. Elevation Cut of
Phase, 10.69 GHz
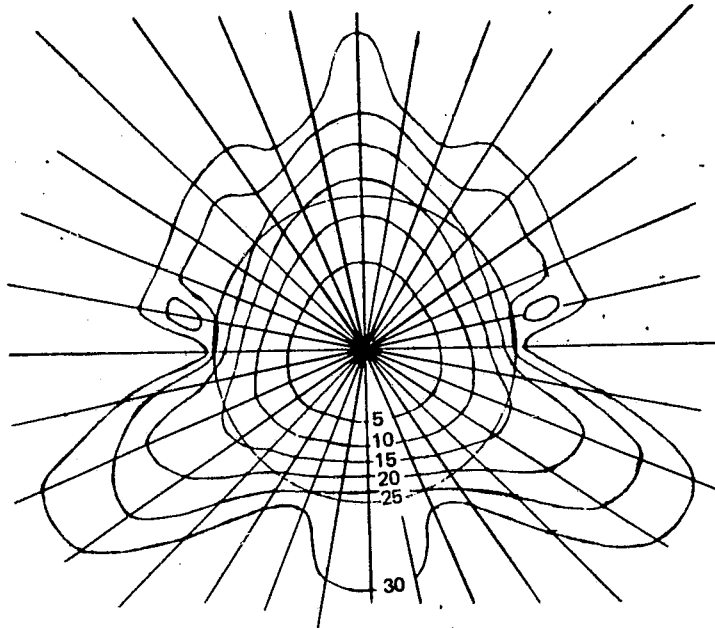
Figure 3-19. Contour Plot of Far Field Pattern, 2. 695 GHz
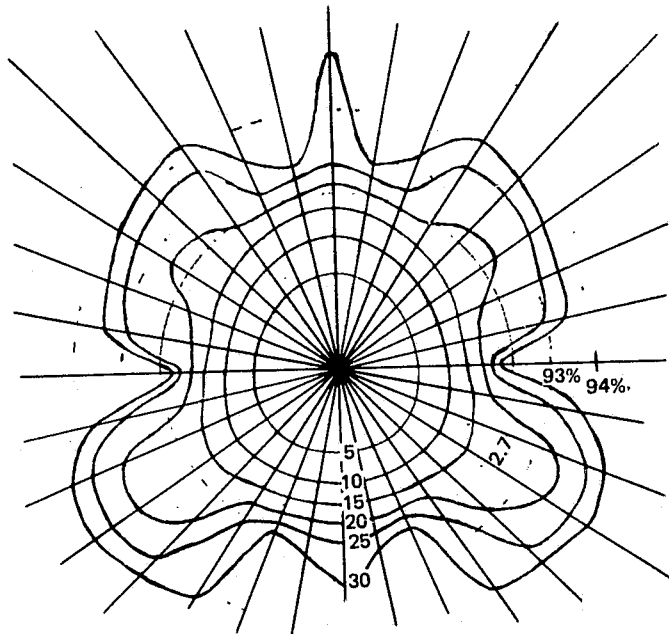
Figure 3-20. Contour Plot of Far Field Pattern, 6. 6 GHz

Where Pp is the fractional power contained in the entire physical optics pattern. The main beam efficiency with this assumption is

$$\eta_{mb} = \frac{2\pi \int_o^{1.25\Theta} \int_o^{2\pi} P(\theta,\phi)\sin\theta d\phi d\theta}{Pp + 0.2\ (1 - Pp)} \tag{58}$$

Bandwidth

To determine whether some adjacent channels could use the same feed aperture a bandwidth study was conducted. Keeping the same feed aperture size (1.5λ by 2.6λ at fo) the operating frequency was varied to determine the performance over a given bandwidth. Potential pairs of candidate channels which could be combined are; the 20 and 22 GHz pair, and the 94 and 118.7 GHz pair. Table 3-5 shows the results of this bandwidth study. The range 0.95 fo to 1.05 fo covers 20 to 22 GHz, and the performance is excellent over this bandwidth, and combining 20 and 22 GHz into one feed aperture is feasible if desired.

The range 0.95 fo to 1.20 fo covers the 94 and 118.7 GHz frequencies, which is the only other pair that could be combined. The higher frequency would suffer about 12 percent loss in resolution compared to the baseline single frequency design. However, because 118.7 GHz is used for atmospheric mapping, resolution is not as critical at this frequency. The combination is thus feasible if some way of separating the two frequencies without excessive loss is devised.

Table 3-5. Results of Bandwidth Study

| f (GHz) | f/fo | Gain (dB) | Beamwidth | | Average Beamwidth Factor | Main Beam Efficiency* (%) |
			Az (deg)	El (deg)		
6.27	0.95	38.85	2.03	2.19	70.5	93.25
6.60	1.00	39.13	1.98	2.15	72.6	94.19
6.93	1.05	39.35	1.94	2.11	74.8	94.38
7.26	1.10	39.51	1.89	2.10	77.1	94.78
7.59	1.15	39.64	1.85	2.08	79.7	95.12
7.92	1.20	39.73	1.83	2.07	82.6	95.41

*80 percent of spillover absorbed.

Offset Feed Evaluation

The performance of the Gregorian reflector system was then analyzed for the case of a feed offset by half the feed dimension in ZZ direction. This would represent a general offset dual frequency feed like that of Figure 3-21. In an optical system, displacement by half the feed height should have the same effect on the pattern at all frequencies. Consequently, the performance was calculated at 6.6 GHz to be representative of all frequencies above that.

The amplitude of the main reflector current along the line Z = +0.3 is shown in Figure 3-22 and its phase in Figure 3-23. Correspondingly, the amplitude and phase along the reflector symmetry line X = O are shown in Figures 3-24 and 3-25. The elevation amplitude (Figure 3-24) shows slight asymmetry due to the fact that the feed was not rotated as it was displaced. The spillover loss, however, was less with the displaced feed (0.04 dB vs 0.12 dB) so this should not degrade performance appreciably. The phase, however, shows considerable phase distortion caused by the offset.

This phase distortion caused considerable beam broadening. The peak gain dropped from 39.1 dB down to 34.8 dB, a loss of 4.3 dB. The average half-power beamwidth increased from 2.06 to 3.24 deg, indicating considerable loss in resolution. The contour plot of Figure 3-26 shows the beam shapes become nearly triangular and the skirts are broadened considerably compared to the on-axis contour plot of Figure 3-20. The beam efficiency was not as seriously degraded, however. 88.7 percent of the feed power was contained within the 2.5 (H) circle as compared to 91.3 percent on-axis.
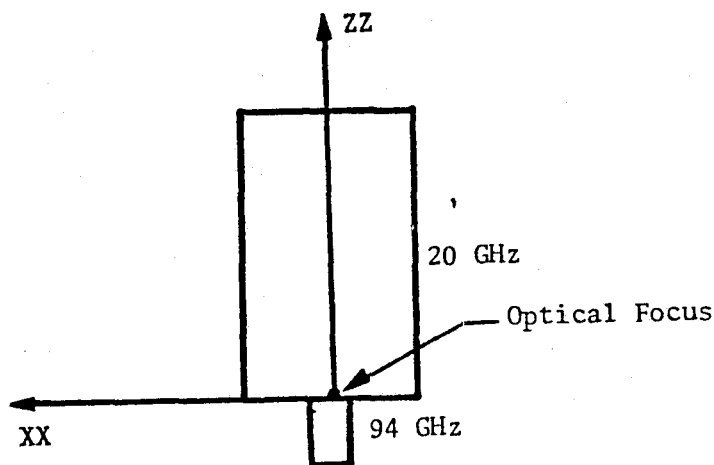
Figure 3-21. Typical Dual Frequency Offset Feed
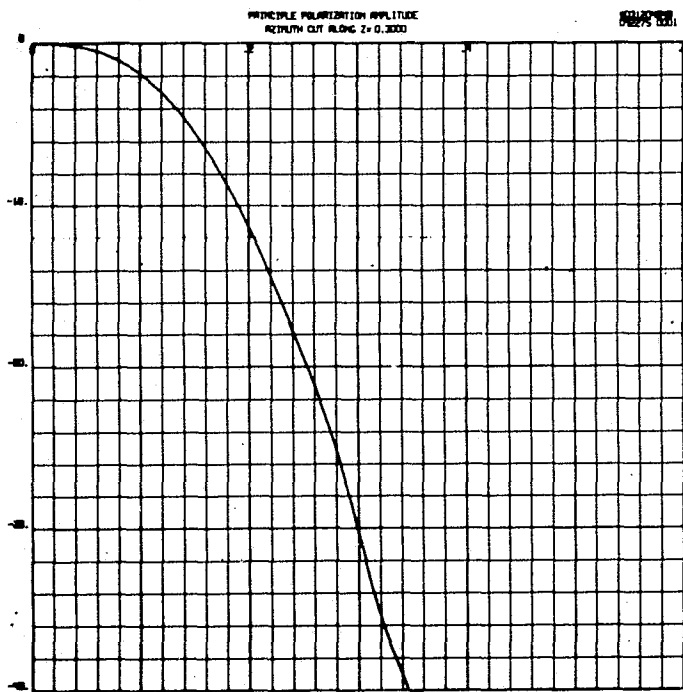
Figure 3-22.   Azimuth Cut of Reflector
Current for Offset Feed
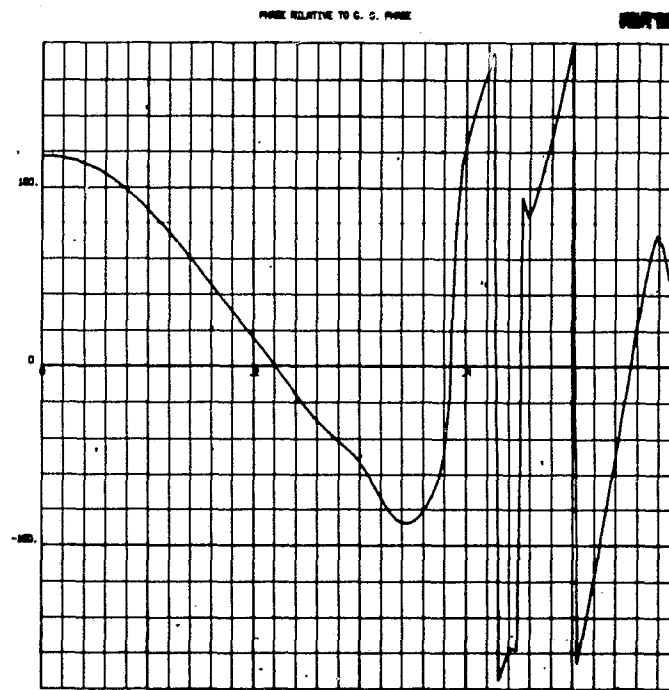
Figure 3-23.   Azimuth Cut of Phase for
Offset Feed

PRINCIPLE POLARIZATION AMPLITUDE
ELEVATION CUT ALONG X=0.0000

PHASE RELATIVE TO C. O. PHASE
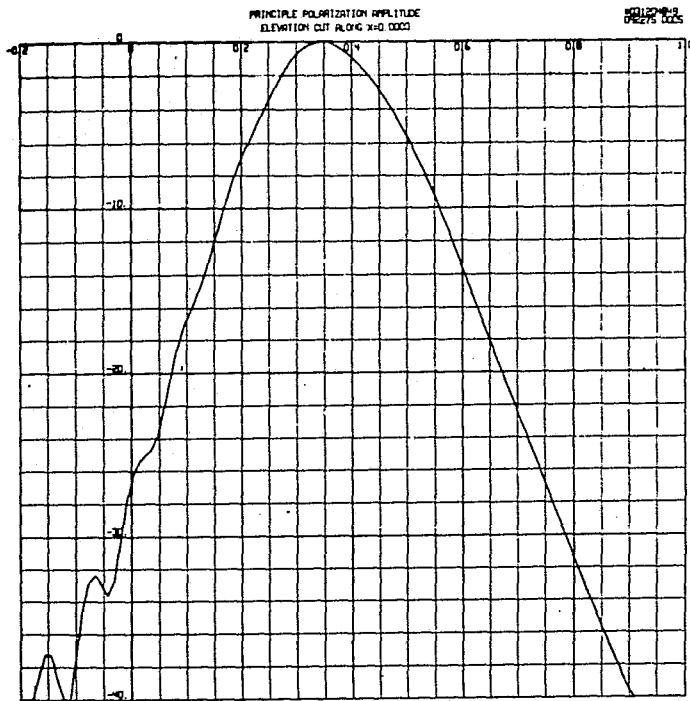
Figure 3-24. Elevation Cut of Reflector
Current for Offset Feed
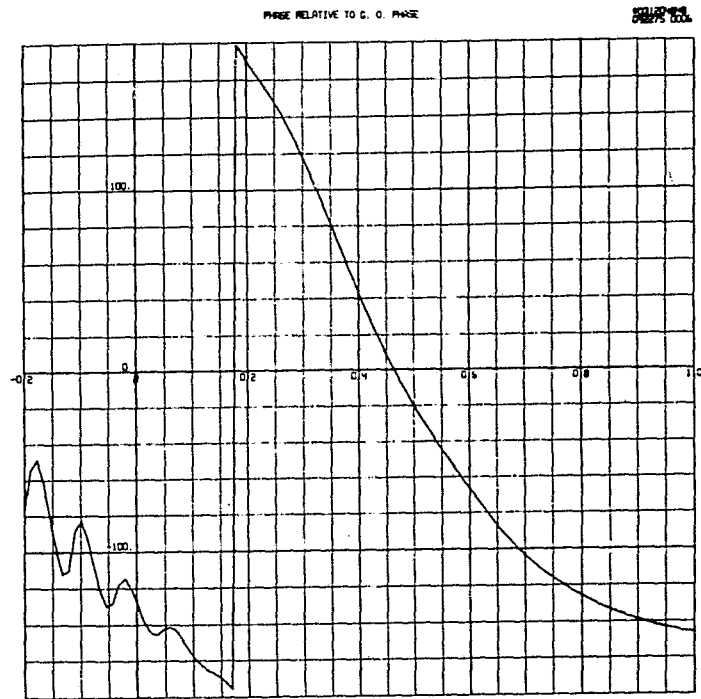
Figure 3-25. Elevation Cut of Phase
for Offset Feed

2.5XΘ

5
10 15 20
25 30

SCAN PLANE

AVERAGE 3 dB BEAMWIDTH = 3.24°

BEAM EFFICIENCY = 88.7%
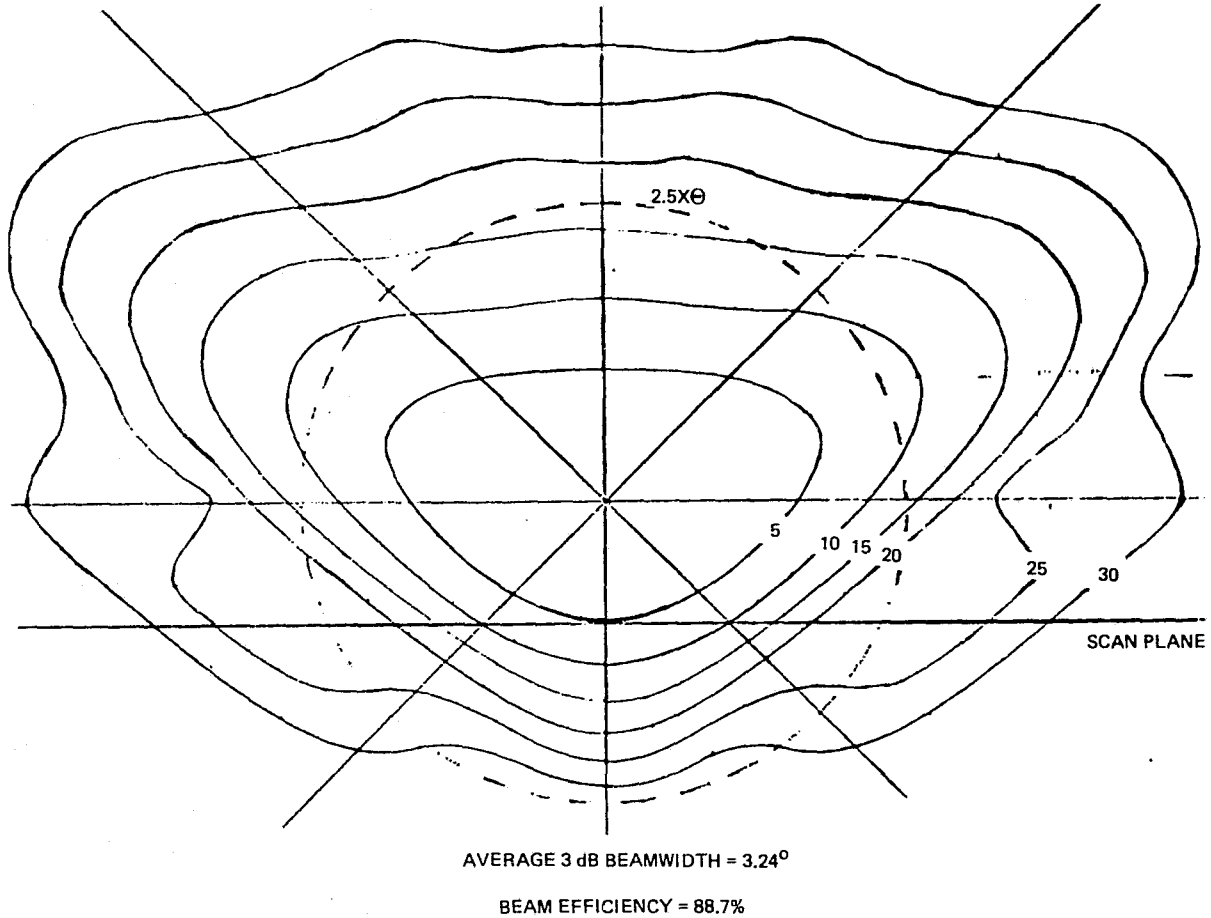
Figure 3-26.   Contour Plot-Offset Feed

Conclusions

The conclusions drawn from this data are as follows:

1. The Gregorian concept should be used at 6.6 GHz and above. Although 2.695 GHz main beam efficiency appears marginally acceptable, the patterns are severely distorted and furthermore the subreflector would not be in the far field of the feed. At the lower three frequencies a prime focus type of feed should be used because diffraction effects would be severe.

2. Covering 20/22 GHz or 94/118.7 GHz with one feed aperture is feasible provided a suitable way of separating the channels can be devised.

3. Dual frequency operation using offset feeds is not a good concept due to excessive pattern distortion and beam broadening. Multifrequency concentric feeds should give much better performance.

3.1.2 Prime Focus Feeds

3.1.2.1 Overall Approach

The physical optics analysis indicated that prime focus feeds are needed for 0.61, 1.413, and 2.695 GHz. Measurements in Gustincic indicate that a four dipole feed was adequate for 0.61 GHz. At 2.695 and possibly 1.413 GHz, some type of aberration correction is needed to correct the severe aberration of the parabolic torus.

Several feed concepts were considered, such as end fire elements, line source feeds, and arrays. Because three frequencies are required at one prime focus feed location, the driving function in the choice among them turned out to be how well the concept was adaptable to multiple frequency operation. An array approach was chosen on that basis since multiple banding arrays using interlaced elements and look-through elements is well understood and practical. Furthermore, control of the amplitude and phase of the pattern of an array is relatively precise compared to other approaches, so aberration correction should be easily achieved.

Feed pattern synthesis was performed by visualizing the feed as a multiple beam array. Each beam illuminates a portion of the torus and thus gives control of the amplitude and phase of that segment. The various beam excitations blend together into a smooth aberration correcting feed pattern due to the natural interpolation process inherent with rounded beam shapes. The amplitudes and phases of the aperture distributions required for each beam are then added in the aperture plane to give the composite aperture distribution required, so the multiple beams exist in concept only — a simple corporate feed producing the desired amplitudes and phases is all that is required.

One constraint imposed on the multiple frequency prime focus feed was that they not project above the focus vertex plane so that they would pass through the calibration enclosures. This necessitated a feed center depressed considerably below the paraxial focus, giving beam positions that were elevated up to 7.8 deg. above the horizon.

An analysis program using physical optics to approximate the torus currents was developed. Far field patterns were calculated in the same way as for the Gregorian analysis. The feed radius was optimized for best operation at 1.413 GHz using a simple feed approach. The performance at 0.61 GHz using the same feed location was then calculated, and a seven beam feed for 2.695 GHz was synthesized.

3.1.2.2. Analysis

The objective of the prime focus feed analysis is the calculation of the Vector $\vec{HP}$, which is the magnetic field of the feed at the main reflector point. The calculation of the main reflector current using the physical optics approximation and calculation and evaluation of the far field patterns proceeds identically to that of the Gregorian analysis, using equation (38) through (57). The geometry of the torus and feed are given in Figure 3-27. The feed radius is FD and its depression is HD.
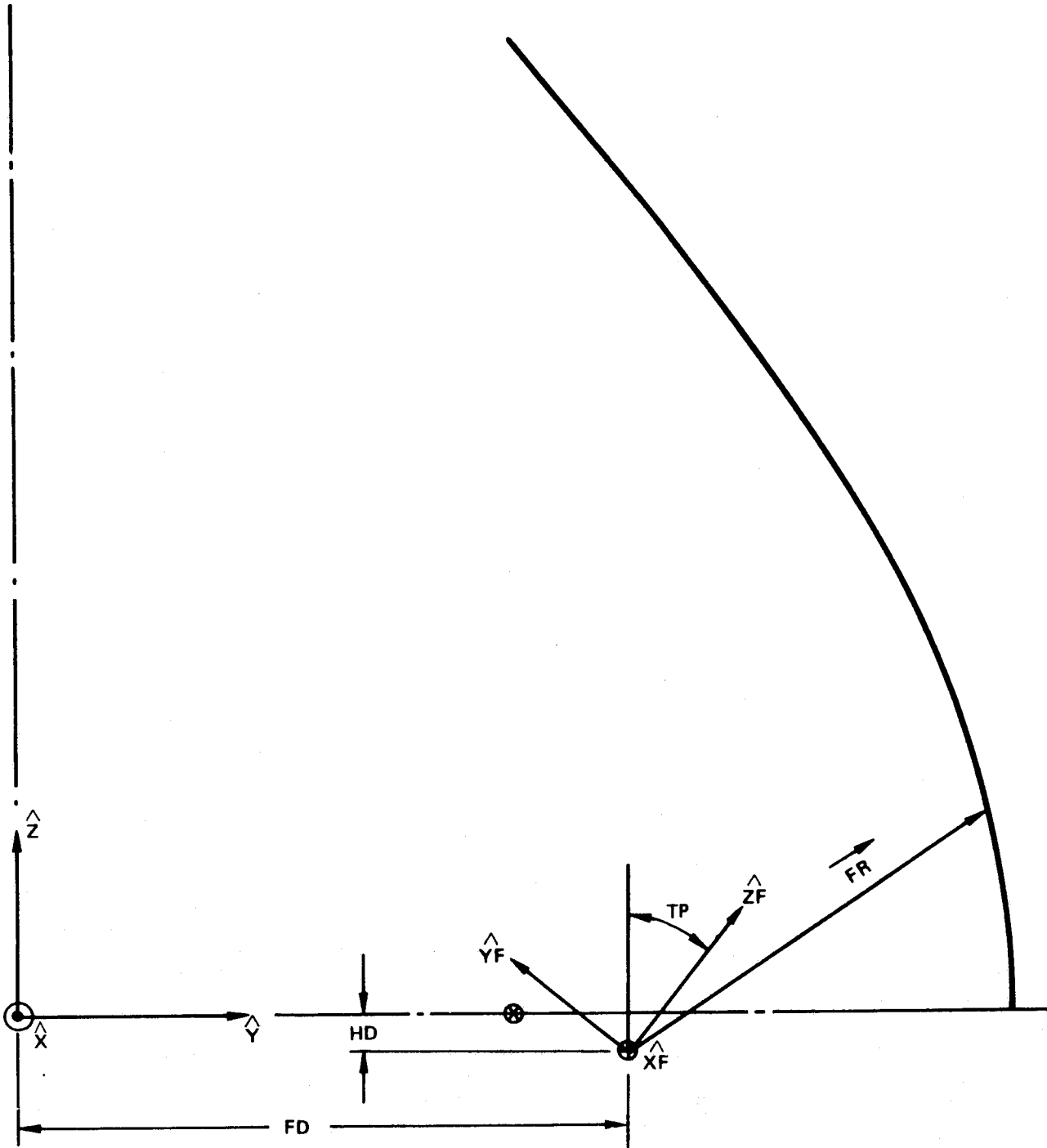
Figure 3-27 Coordinate Systems for Prime Focus Feed Evaluation

Like the previous analysis, a subroutine PRIPAT is used to calculate the feed pattern in the local feed coordinate system (XF, YF, ZF) and normalized for unit radius. Inputs and outputs for the prime focus feed version of PRIPAT are summarized in Table 3-6.

Table 3-6. Input/Output Parameters for
PRIPAT (Prime Focus Feed Version)

Input Parameters

SCA(1)	=	SIN(TF)
SCA(2)	=	COS(TF)
SCA(3)	=	SIN(PF)
SCA(4)	=	COS(PF)

Where TF and PF are the conventional spherical coordinate angles of the primary pattern point.

IE	=	1 for vertically polarized slot element
		2 for horizontally polarized slot element
		3 for vertically polarized dipole element
		4 for horizontally polarized dipole element
NE	=	Number of elements in array
X } Y }	=	Arrays giving positions of elements
A	=	Complex array giving complex amplitude of each element
EK	=	Wave number
PD	=	Peak directivity

Output Parameters

HXF } HYF } HZF }	=	Rectangular components of magnetic field referenced to one meter radius.

For the purposes of calculating the feed pattern, the sine and cosine of the spherical coordinate feed angles TF and PF are required. They are calculated according to the formulas

$$COS\ (TF) = \hat{ZF} \cdot \vec{FR} / |\vec{FR}|$$

$$SIN\ (TF) \cdot COS\ (PF) = \hat{XF} \cdot \vec{FR} / |\vec{FR}|$$

$$SIN\ (TF) \cdot SIN\ (PF) = \hat{YF} \cdot \vec{FR} / |\vec{FR}|$$

Where $\vec{FR}$ is the vector from the feed to the reflector point, given by the formula

$$\vec{FR} = \hat{X} \cdot X + \hat{Y} \cdot (Y - FP) + \hat{Z} \cdot (Z + HP)$$

The feed pattern, whether from a simple or an aberration correcting feed, is calculated in PRIPAT by a summation of the contributions of each individual dipole or slot. They are normalized to carry unit power by a calculation of the feed directivity in a separate program.

The feed coordinate unit vectors are related to the basic unit vectors according to the equations

$$\hat{XF} = - \hat{X}$$

$$\hat{YF} = \hat{Z} \cdot STP - \hat{Y} \cdot CTP$$

$$\hat{ZF} = \hat{Z} \cdot CTP + \hat{Y} \cdot STP$$

Where STP = SIN (TP), CTP = COS (TP), and TP is the angle of the feed relative to vertical.

The magnetic field of the feed at the surface of the main reflector is then

$$\vec{HP} = -\frac{e^{-j \cdot EK \cdot |\vec{FR}| \cdot RO}}{|\vec{FR}| \cdot RO} \Big[\hat{X}\ (-HXF) + \hat{Y}\ (HZF \cdot STP - HYF \cdot CTP) + \hat{Z}\ (HZF \cdot CTP + HYF \cdot STP) \Big]$$

3.1.2.3 Optimization and Evaluation of Prime Focus Feeds

Integration of Three Frequency Bands

A four dipole feed spaced 0.5λ on a side was first evaluated at several frequencies. With a depressed feed position, however, the spillover loss was 10 percent and the main beam efficiency was too low due to insufficient edge taper. Consequently, 0.63λ dipole spacing was evaluated. The spillover dropped to only 3.1 percent and the main beam efficiency was very nearly 90 percent at 0.61 GHz. However, the aberrations were too severe at 1.413 GHz so a still narrower feed beamwidth was chosen for that frequency. A seven dipole feed (a center dipole surrounded by a ring of six dipoles with -6 dB relative amplitude) gave adequate performance, with 1.4 percent

spillover and 94.1 percent main beam efficiency. With a 19 slot array for 2.695 GHz, a configuration as shown in Figure 2-18 was chosen. This places the 1.413 GHz feed somewhat closer to the paraxial focus than the other two, but the 1.413 GHz elements exactly interlace the 2.695 GHz slots which will minimize interaction effects.

1.413 GHz Feed

The position of the feed relative to the paraxial focus was optimized for 1.413 GHz with the rationale that this was the most critical of the three. At 2.695 GHz aberration correction would be available using the array feed while at 0.61 GHz the aberration should be less. From the layout of the feed, it was determined that the center of the 1.413 GHz feed would have to be depressed 0.065 RO (13 cm) to maintain the 52 cm x 52 cm feed system clear of the vertex plane. The feed radius was varied from 0.50 to 0.56, keeping the feed centered in the included angle of the reflector by varying the pointing angle. The results are summarized in Table 3-7.

As can be seen, the three performance parameters do not optimize at the same feed radius. A value of 0.52 was chosen as a good compromise position.

0.61 GHz

The location of the 0.61 GHz feed was now defined as

FD = 0.5438

HD = 0.0854

TP = 40.61°

At this location, the average beam width is 17.4 deg. and the feed power contained within the 2.5 Θ circle is 89.86 percent with 3.14 percent spilled over the main reflector. The effective beam efficiency can be easily raised above the required 90 percent by the use of absorber below the vertex of the torus, where most of the spillover occurs, or by phasing the feed to scan the beam up slightly.

Table 3-7. Feed Position Trade-off

Feed Radius	Feed Pointing Angle (deg)	Average Beamwidth (deg)	Gain (dB)	Main Beam Efficiency (%)
0.50	41.30	9.19	26.27	94.38
0.52	40.61	8.96	26.35	94.16
0.54	39.90	8.94	26.32	93.73
0.56	39.19	8.94	26.18	92.69

2.695 GHz

A simple feed at 2.695 GHz produced a disappointing efficiency of 85 percent but gave a starting point for aberration correction. The 19 slot array was visualized as producing seven beams which illuminate different portions of the parabolic torus reflector to give a systematic optimization technique. The amplitude of each outer beam was made equal to -8dB relative to the center beam to give an aperture illumination of the desired shape. The scan angle of each outer beam was 21 deg. from broadside, and an amplitude distribution which gave -25dB sidelobe level for the individual beams was used. The relationship of the seven beams to the parabolic torus is shown in Figure 3-28. If the phase of the center beam is arbitrarily set to 0 deg., the phase of the remaining six beams give six degrees of freedom which can be optimized. Even with symmetry, there are four degrees of freedom. Some analysis is needed to reduce this because optimization in four dimensions is almost impossible.

If the six degrees of freedom are identified with the phase modes $\cos n\phi$ and $\sin n\phi$ of the outer six beams, the effect of each can be identified as in Table 3-8.

The odd modes can be eliminated because they correct for aberration errors which cannot exist due to reflector symmetry. The mode with order 1 primarily corrects for the scan angle of the beam, so it can be eliminated because the beam does not have to be at any particular angle above the horizon. Furthermore, very little
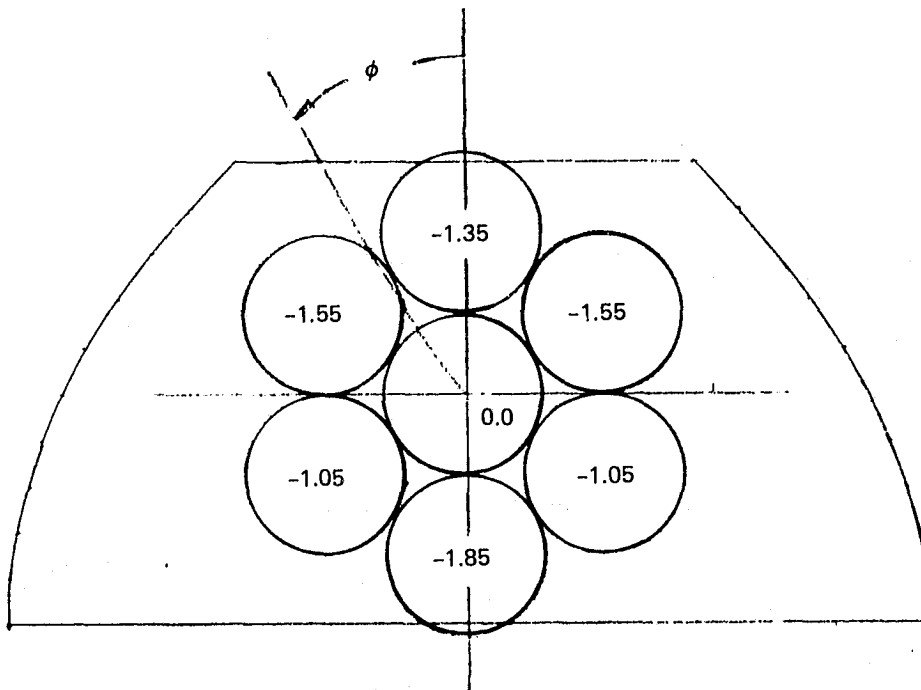
Figure 3-28. Feed Beam Locations Showing the Optimum Phases

Table 3-8. Effect of Phase Modes

Order	Type	Expression	Dominant Effect
0	Even	$\Phi = \Phi_0$	Focus correction
1	Even	$\Phi = \Phi_1 \cos \phi$	Elevation scan
1	Odd	$\Phi = \Phi_2 \sin \phi$	Azimuth scan
2	Even	$\Phi = \Phi_3 \cos 2\phi$	Principle plane astigmatism
2	Odd	$\Phi = \Phi_4 \sin 2\phi$	Diagonal plane astigmatism
3	Even	$\Phi = \Phi_5 \cos 3\phi$	Third order phase

astigmatism was noted in the phase plots that were made for the simple feed, so only focus and third order phase errors were included at first for two degrees of freedom. These were iteratively optimized for best performance. The optimum third order correction was only 0.25 radians, while the major phase error turned out to be in focus. A plot of main beam efficiency, gain, and beam width as a function of focus correction is given in Figure 3-29. The performance trade-off is aperture utilization vs main beam efficiency as evidenced by the decreasing efficiency and decreasing
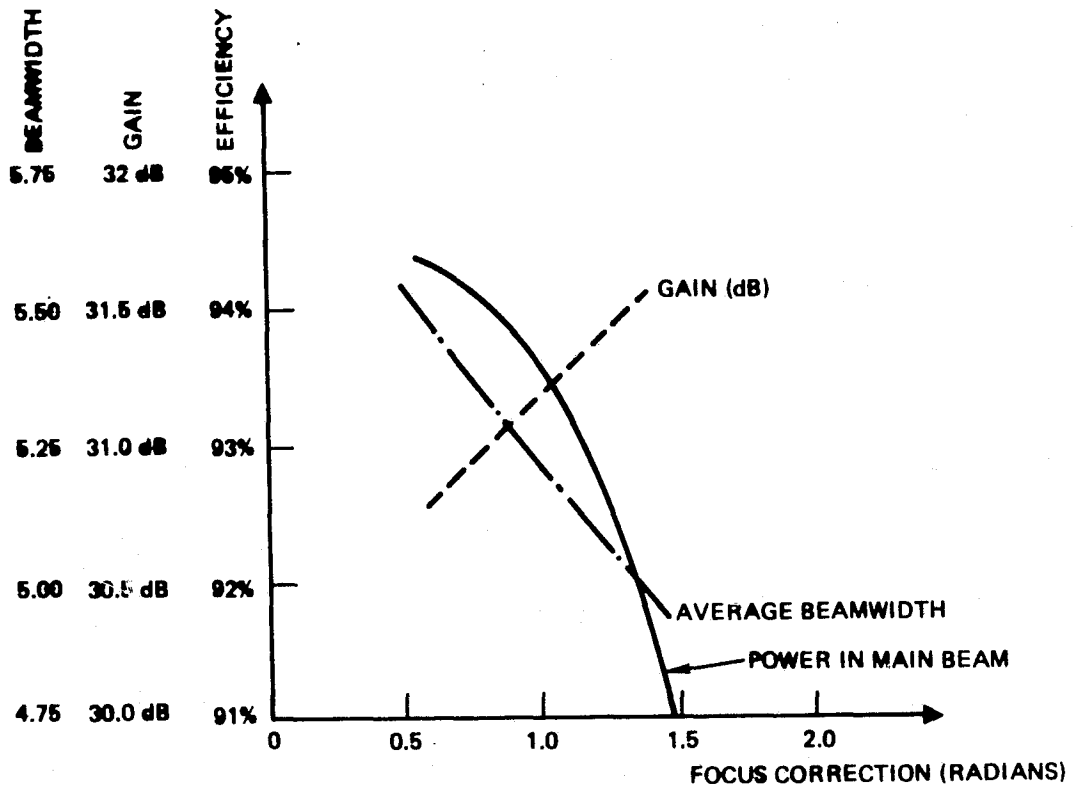
Figure 3-29. Performance vs Focus Correction

beamwidth with increases in the focus correction. With 1.4 radians of focus correction, the effective aperture size is slightly over 1.6 meters while the power in the main beam is 91.64 percent. A final correction for astigmatism was made, indicating that 0.2 radians of astigmatism correction gave a slight decrease in beamwidth at the expense of 0.11 percent in efficiency. The beam phases are shown in Figure 3-28, and the primary patterns of the feed are shown in Figures 3-30 and 3-31. The composite amplitude and phase distribution is given in Table 3-9. The performance of the antenna at 2.695 with this feed is summarized in Table 3-10. The increase in performance from a simple feed to the 19 slot array feed is evident, particularly in terms of main beam efficiency and gain. The main beam efficiency in Table 3-10 again assumes that 80 percent of the spillover is absorbed.
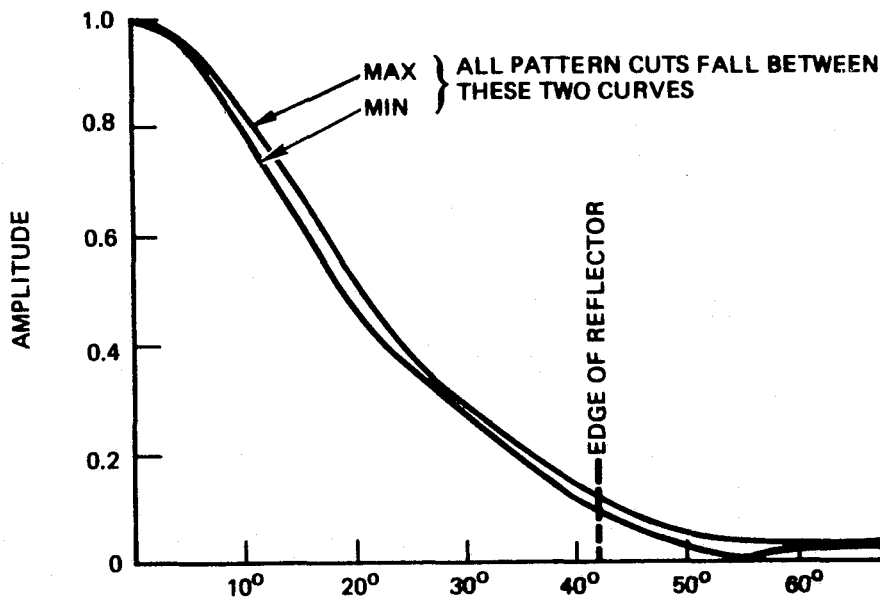
Figure 3-30. Amplitude Envelope of Feed Pattern
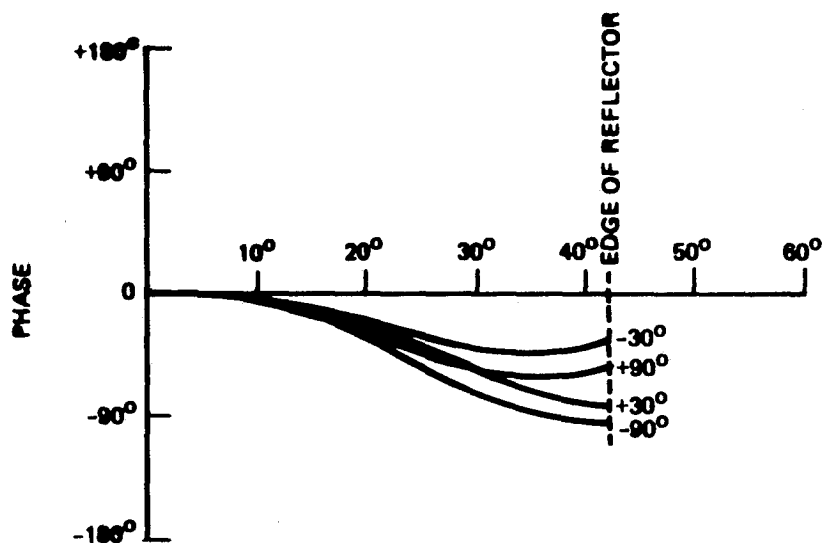
Figure 3-31. Phase of Feed Pattern for Various ϕ Angles

Table 3-9.   Slot Array Excitation for 2.695 GHz

Element	XF	ZF (cm)	Amplitude	Phase (deg)
1	−7.231	−12.524	0.03199	+52.0
2	0.000	−12.524	0.05155	+24.2
3	+7.231	−12.524	0.03199	+52.0
4	−10.846	−6.262	0.03999	+53.0
5	−3.615	−6.262	0.09724	−15.3
6	+3.615	−6.262	0.09724	−15.3
7	+10.846	−6.262	0.03999	+53.0
8	−14.461	0.000	0.02081	+62.5
9	−7.231	0.000	0.08983	−21.0
10	0.000	0.000	0.20803	−31.6
11	+7.231	0.000	0.08983	−21.0
12	+14.461	0.000	0.02081	+62.5
13	−10.846	+6.262	0.03738	+20.5
14	−3.615	+6.262	0.09331	−18.1
15	+3.615	+6.262	0.09331	−18.1
16	+10.846	+6.262	0.03738	+20.5
17	−7.231	+12.524	0.03029	+53.0
18	0.000	+12.524	0.04666	+50.1
19	+7.231	+12.524	0.03029	+53.0

Table 3-10. Performance at 2.695 GHz

Characteristic	4-Dipole Feed	19 Slot Feed
Beamwidth, Az x El	4.55^0 x 5.17^0	4.86^0 x 5.02^0
Aperture, Az x El	1.77m x 1.56m	1.66m x 1.61m
Gain	30.84 dB	31.61 dB
Main Beam Efficiency	84.81%	93.18%

3.1.3 Radiometric Calibration Techniques

3.1.3.1 Calibration Techniques and Errors

The output of a microwave radiometer is usually a voltage that is proportional to the radiometric brightness temperature at the input to the radiometer receiver. Since the dynamic measurement range of a SIMS channel is not likely to exceed 6 dB (75^0K to 300^0K) it is reasonable to assume a linear response,

$$V = \frac{T(V_2 - V_1) + V_1 T_2 - V_2 T_1}{T_2 - T_1} \qquad (59)$$

where V_1 and V_2 are the output voltages that occur when two known radiometric calibration temperatures T_1 and T_2 are established at the input.

One source of measurement error arises because of the difficulty in establishing precise values for the temperatures T_1 and T_2. We now assess these errors for two different calibration techniques.

3.1.3.2 Switched Load Calibration

In this case the radiometer's antenna is first replaced by a matched termination that is maintained at a known physical temperature T_1 and then by a second load at a different temperature T_2. The terminations act as black body radiators with emissivity of unity, so that T_1 and T_2 are equal to the radiometric brightness temperatures at the input. When the antenna is reconnected and pointed to a source whose brightness temperature is T_b the presence of loss in the antenna and its feed transmission line modifies the brightness temperature as seen by the radiometer. The actual brightness temperature is given by

$$T = (1 - L) T_b + LT_o \qquad (60)$$

where L is the fractional loss, assumed here to be at a constant physical temperature equal to T_o. The loss L would include the asymmetrical part of any switch loss, if one is used.

Under these circumstances the radiometer's output voltage is given by (59) after substitution of (60); we find,

$$V = \frac{[T_b + L(T_o - T_b)] (V_2 - V_1) + V_1 T_2 - V_2 T_1}{T_2 - T_1}$$

Letting the output voltage be V_o in the absence of loss, we have for the error

$$\Delta V = V - V_o = L(T_o - T_b) \frac{V_2 - V_1}{T_2 - T_1} \tag{61}$$

From (1) and (2) we have

$$dV = (1 - L) \frac{V_2 - V_1}{T_2 - T_1} dT_b$$

hence (3) becomes

$$\left. \begin{array}{l} \Delta T_b = \frac{L}{1 - L} (T_o - T_b) \\[2em] \simeq (T_o - T_b) \text{ for small } L \end{array} \right\} \tag{62}$$

The resulting measurement error is directly proportional to the fractional loss and to the difference between antenna physical temperature T_o and target brightness temperature T_b. For example, assume 1 dB loss in an S-band radiometer antenna, at temperature $T_o = 290^\circ K$, viewing the ocean, whose brightness temperature will be about $100^\circ K$. The error in observed brightness temperature will be about $49^\circ K$. If the loss is reduced to 0.1dB the error becomes about $4.5^\circ K$ which is still large enough to require correction. If the correction is to be estimated to an accuracy of 0.45 deg. (i.e., 10 percent) then L and $T_o - T_b$ must be known to 5 percent i.e., to 0.005 dB and 14.5 deg., respectively. Such an accuracy is not easy to achieve and the difficulty is compounded by the fact that the loss L is invariably distributed and the temperature T_o is rarely uniform.

A technique that avoids the difficulty has been described by Hardy[8], and will now be discussed.

3.1.3.3 Antenna Aperture Calibration

We assume that black body emitters are coupled in turn to the antenna aperture, thereby establishing calibration temperatures T_{b1} and T_{b2} at the aperture. For ideal black bodies these temperatures will simply be the thermometric temperatures of the emitters. Due to loss in the antenna, however, the temperatures T_1 and T_2 at the radiometer receiver input must be obtained from equation (60) and the same applies during target observation. When the appropriate substitutions are made in equation (59) the loss factors L and 1 - L cancel and we have

$$V = \frac{T_b(V_2 - V_1) + V_1 T_{b2} - V_2 T_{b1}}{T_{b2} - T_{b1}} \tag{63}$$

But this is of exactly the same form as (59), and since L does not appear there is no measurement error due to antenna loss. The effect of loss has been "calibrated out". This is true only if T_0 remains constant during target observation and throughout both calibration cycles.

For the system described by Hardy (see previous reference) it was possible to ensure essentially 100 percent coupling between black body and antenna. For the SIMS radiometers it is not possible to guarantee unity coupling factor and, as we shall discuss below, this is a source of measurement error. Coupling factor, as used here, is synonomous with the emissivity of the black body/antenna system.

3.1.3.4 Error Due to Imperfect Coupling

We assume that the black body sources are constructed in identical fashion, so that each couples to the antenna with a coupling coefficient β. The complement of β, that is $1 - \beta$, represents the coupling between the antenna and all the surrounding space external to the black body. This surrounding space will be characterized by some brightness temperature T_s which we assume to be very nearly the same for the two calibrating conditions. The radiometric calibration temperatures at the antenna aperture are now given by

$$\left. \begin{array}{l} T_{b1} = \beta T_1 + (1 - \beta) T_s \\[2em] T_{b2} = \beta T_2 + (1 - \beta) T_s \end{array} \right\} \tag{64}$$

where T_1 and T_2 are the temperatures of the two black body sources.

After performing these calibrations the radiometer output for a target whose brightness temperature is T_b may be found by substituting (64) into (63), giving

$$V = \frac{V_o}{\beta} + \frac{1 - \beta}{\beta} \left[\frac{V_2 T_1 - V_1 T_2 - T_s (V_2 - V_1)}{T_2 - T_1} \right]$$

where V_0 is the output that would occur under ideal coupling conditions, i.e., $\beta = 1$. Thus the error is $\Delta V = V - V_0$ where

$$\Delta V = \frac{1 - \beta}{\beta} (T_b - T_s) \frac{V_2 - V_1}{T_2 - T_1}$$

From (5) and (6) we also have

$$dV = \frac{V_2 - V_1}{\beta (T_2 - T_1)} \, d T_b$$

hence the temperature error becomes

$$\Delta T_b = (1 - \beta) (T_b - T_s) \tag{65}$$

This has the same form as (4) with coupling loss replacing ohmic loss and external brightness temperature T_s replacing the physical temperature T_o. The aperture calibration technique is thus no better than the switched load calibration unless the coupling factor β can be made to approach unity very closely. In fact, for equal coupling loss in the one case and ohmic loss in the other, the switched load method is probably preferable on grounds that a more accurate correction can be derived. This is because the physical temperature T_o of the antenna loss can be measured more accurately than can the rather nebulous brightness temperature T_s of the external space. The same remark probably also applies to measurement of ohmic loss, L, and coupling factor β .

3.1.3.5 Application to SIMS-A

The present concept for the SIMS-A antenna utilizes an offset parabolic torus reflector with multiple frequency radiometers and feed systems mounted on a rotating wheel. Each feed provides a 60 deg. cone of illumination that sweeps over the torus through an angle of 180 deg., then experiences a dead period as the wheel turns through the remaining 180 deg. This dead time between scans is available for radiometric calibration; either one of the techniques discussed previously can be adapted for this use. In the case of the aperture technique, it will not be possible to couple to the main reflector aperture but it is possible to couple to the individual feed systems if the wheel is arranged to pass through an absorbing tunnel during the dead time. * This is indicated in the accompanying fold-out drawing, Figure 3-38, in which two sector-shaped absorbing tunnels are shown. These "cavities" must be maintained at constant and uniform temperatures T_1 and T_2 in order to constitute black body calibration sources.

The absorbing material used to line the cavities should be thin and capable of broadband operation over a wide range of angles of incidence. Of the standard materials listed by Emerson & Cuming, type AN best meets all these requirements. Thus, AN75 material is 1-1/8 in. thick and has less than -20 dB reflectivity at normal incidence (-17 dB at 70 deg. incidence angle) over the range from 2.5 to >50 GHz. This does not represent an exceptionally low reflectivity (many micro-wave absorbers achieve -40 dB at normal incidence) but a very low reflection coefficient is not necessarily needed. Multiple reflections within the cavity will create a very small effective, or overall, value of reflectivity; this is the principal behind optical black body sources. The absorptivity of the material must be high, and the AN type material appears to be satisfactory in this respect. Making the cavity of conducting metal walls, lined on the inside with AN75 absorber, will ensure that rays from the feed horn that strike the Gregorian sub-reflector will be essentially absorbed after two or more internal reflections at the cavity walls. In the worst case, i.e., -17 dB reflectivity at 70 deg. incidence, two reflections produce a net reflectivity of -34 dB, corresponding to an emissivity of 0.996.

---

* Note that this requires that the ohmic losses outside of the subreflector be minimized. In particular, the spillover past the main reflector should be as low as possible.

TRUSS STRUCTURE ENVELOPE

BLACK BODY AT T_1

DRIVE MECHANISM HOUSING

BLACK BODY AT T_2

3M

SECTOR-SHAPED TUNNEL OR
"CAVITY" OF CONDUCTING
METALLIC WALLS LINED
WITH AN75 ABSORBER

SUBREFLECTOR
(6 IDENTICAL)

TO NADIR

FEED ASSY
(TYPICAL 6 PLACES)

RADIOMETER CLUSTER
(30 RADIOMETERS TOTAL)

PAYLOAD BAY CLEARANCE ENVELOPE

DRIVE MECHANISM HOUSING

ROTATING FEED DISC

PARAB

2M R

TRUSS ENVELOPE

MAXIMUM ENVELOPE

4M

2M

Figu

TRUSS STRUCTURE ENVELOPE

BLACK BODY AT T_1

DRIVE MECHANISM HOUSING

R

TER
OTAL)

AYLOAD BAY CLEARANCE ENVELOPE

BLACK BODY AT T_2

TRUSS STRUCTURE ENVELOPE

SCALE: 1-INCH = 1 METER

3M

PARABOLIC TORUS REFLECTOR SURFACE

ROTATING FEED DISC

DRIVE MECHANISM HOUSING

PARABOLA CONTOUR

NOTE:
TO REDUCE WALL THICKNESS AND HENCE MINIMIZE APERTURE BLOCKING THIS WALL COULD BE A METALLIC MIRROR (I.E., NO ABSORBER ON INNER SURFACE)

2M R

TRUSS ENVELOPE

MAXIMUM ENVELOPE

PAYLOAD BAY FLOOR

2M

Figure 3-38.   Calibration Loads Location

There remains to be considered those rays from the feed horn that do not strike the sub-reflector and that might therefore "escape" through the open sides of the tunnel. Calculations have shown that this feed spillover past the sub-reflector amounts to 2.6 percent. It is a relatively simple matter to place additional reflecting surfaces on the wheel in such a way as to block these spillover rays and ensure that they, too, are reflected toward the absorbing cavity walls. Figure 3-39 shows sectional views of a sector-shaped absorbing cavity in which the supplementary reflectors are indicated by dotted lines. By this means, the already small spillover can be reduced to a negligible value. It appears feasible to achieve an overall coupling coefficient (or emissivity) of 0.995 in a carefully designed cavity of this type. The supplementary mirrors should be designed to reflect spillover energy to the back and bottom walls of the cavity, and to avoid illuminating the main dish.

A possible alternative to the standard AN material is Emerson and Cumings CR117, a castable absorber. This is a ferrite loaded resin having a dielectric constant of about 20, with moderate dielectric loss (t an $\delta_e \simeq 0.05$) but high magnetic loss (tan $\delta_m \simeq 1$). Loads and reference terminations using this material have been developed by Dr. Richard Iwasaki at JPL, making clever use of the Brewster angle to achieve low reflectivity.

The material is cast in the form of triangular ridges, bonded to an aluminum plate to form a tile, as shown in Figure 3-40. The Brewster angle for this material (arc tan $\sqrt{\epsilon}$) is about 77.5 deg. Hence, if the included angle of each triangular ridge is 25 deg. there will be almost no reflection for a wave incident normally on the tile. This applies only for parallel polarization, however, and assumes the tile is thick enough for complete absorption. The reflectivity for perpendicular polarization will be high. Techniques for dealing with this problem are being developed by Dr. Iwasaki. An obvious solution here would be to use two cavities, one for each polarization.

Since reflectivity is small only near the Brewster angle, special curving and shaping of the tiles would be needed to ensure this condition. This could lead to such a large increase in cavity dimensions as to create significant aperture blocking of the main reflector.

At the two lowest frequencies 0.6 and 1.4 GHz, the AN75 material is not thick enough (1-1/8 in.) to absorb incident radiation effectively and the coupling of cavity to antenna will be decreased. Hence the switched load technique appears better suited to calibration of these channels.

A method for implementing this technique is shown in Figure 3-41. The components within the dotted lines must be housed in a temperature regulated enclosure accurately stabilized at a temperature T_0 which will be assumed to be about 240°K as discussed in the next section. A SPDT switch is required to switch the radiometer receiver from the antenna to the calibrating circuit at the end of each scan. This is preferably a latching circulator device in which switching energy is small so that little power will be dissipated that could cause local heating and temperature gradients. The scan rate at 324 rpm is 5.4 lines per second, hence the circulator must latch 10.8 times per second. Latching energy can be held to 5 millijoules or less so that switching power will be less than 50 milliwatts and should cause negligible local heating.

METAL WALL
AN75 LINING

WHEEL
RIM

SUPPLEMENTARY
REFLECTORS

~60°

A

A

METAL WALLS
LINED WITH
AN75

WHEEL

AXIS
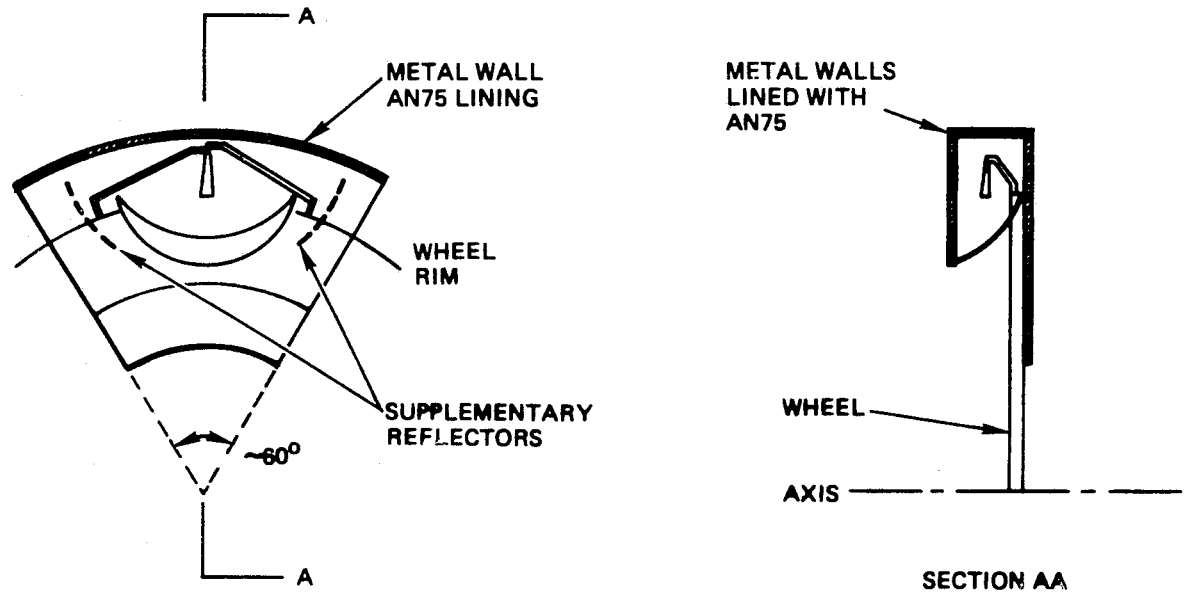
SECTION AA

Figure 3-39. Sector Shaped Black Body Cavity
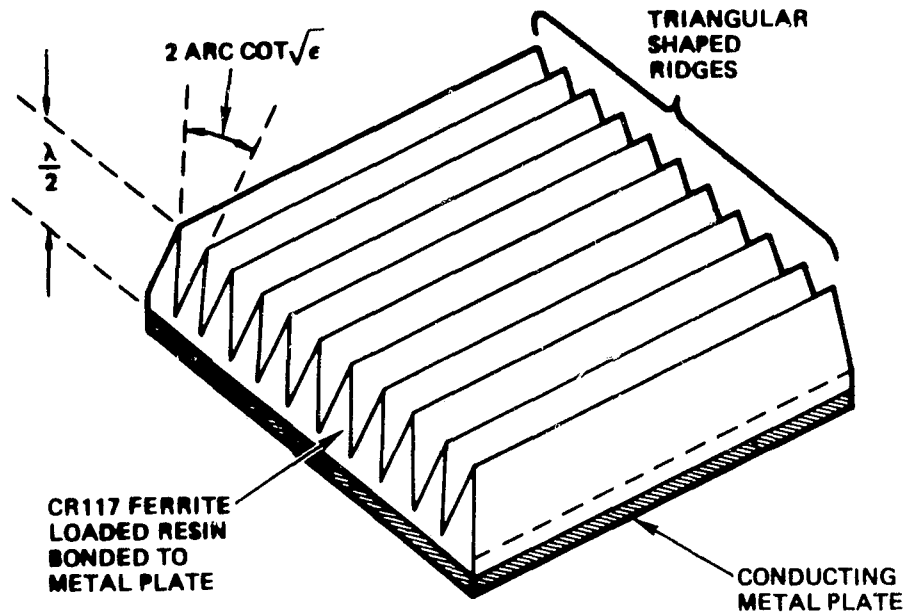
Figure 3-40. Absorbing Tile
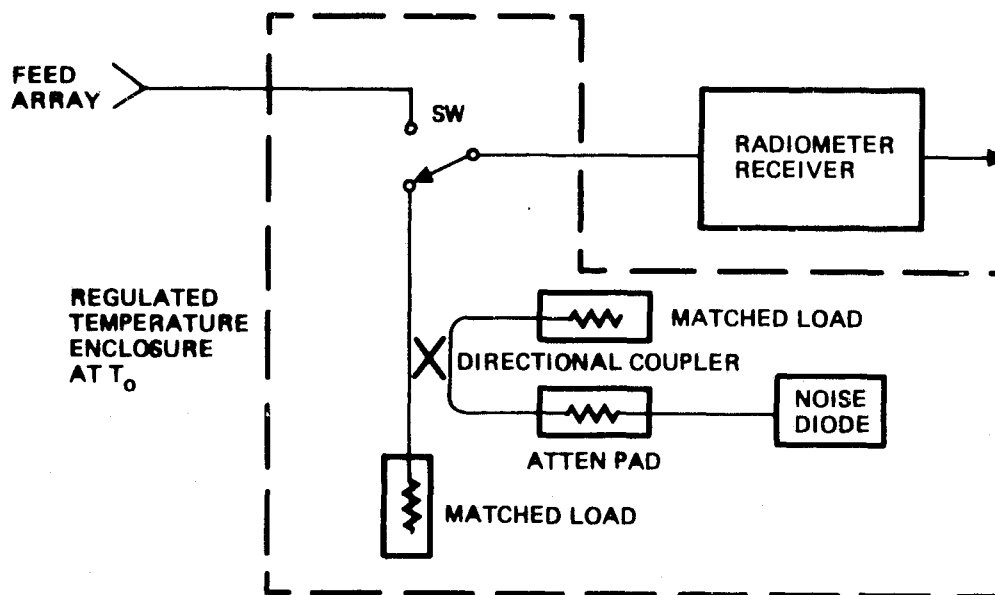
Figure 3-41. Switched Load Calibration

With the avalanche noise diode turned off, the calibration circuit will establish a temperature T_{c1} equal to T_0 at the receiver input. Halfway through the dead cycle between scans the avalanche diode bias is turned on and a second calibration temperature T_{c2} is established at the input, where

$$T_{c2} = \gamma T_0 + (1 - \gamma) T_N \qquad (66)$$

γ is the coupling coefficient for the directional coupler and T_N is the temperature of the attenuated avalanche diode noise. If the attenuator pad shown in Figure 3-41 has a transmission coefficient of α then we have

$$T_N = \alpha T_{diode} + (1 - \alpha) T_0 \qquad (67)$$

where T_{diode} is the noise temperature of the avalanche diode. Such diodes are usually described by their so-called excess temperature ratio, t, expressed in decibels above the standard temperature $290^\circ K$,

$$t = \frac{T_{diode}}{290} - 1$$

and units are commercially available with values of t around 15.25 dB for general use and considerably higher (e. g., 36 dB) for special applications. The effective temperature for the general purpose units is thus about $10,000^\circ K$.

If a 10 dB directional coupler is used ($\gamma = 0.9$) and it is desired to place the calibrating temperature T_{c2} at $300^\circ K$ while $T_{c1} = T_0 = 240^\circ K$ then (66) indicates that T_N should be $840^\circ K$. Equation (67) then shows that, for $T_{diode} = 10,000^\circ K$, a 12.1 dB attenuator pad ($\alpha = 0.061$) will be needed in order to make $T_N = 840^\circ K$.

The insertion loss of the circulator switch will increase the receiver noise figure and hence degrade the temperature resolution by a small amount. It will not affect accuracy of the calibration, however, except to the extent that this loss is different for the two positions of the switch. Any such asymmetrical loss is equal to the (small) difference in insertion loss between the antenna switch position and the calibration switch position. Its effect can be correlated for quite accurately (assuming that the loss has been accurately measured) for the loss will always occur at constant temperature T_0.

The error due to antenna losses ahead of the calibration circuit is not so accurately calculable, for the antenna and its transmission line will probably not be at a uniform temperature, and an accurate ohmic loss measurement on an antenna is not easy. It will be advisable to place a thermal insulating section of RF transmission line at the antenna port of the circulator switch in order to prevent heat transfer from the regulated enclosure to the antenna. Otherwise, temperature gradients will be set up in the enclosure and T_0 will not be uniform and constant. The discussion on temperature control in the next session has direct applicability to the design of this enclosure, even though it is specifically addressed to the black body cavities.

Avalanche diodes have proven to be highly reliable and stable noise sources when operated at constant temperature and constant reverse bias current. Stability tests conducted on type MC 7026 (Microwave Semiconductor Corp.) avalanche diodes demonstrated stabilities of 0.001 dB per day and 0.0015 dB per week in the excess noise temperature ratio [9]. The absolute value of this ratio was found to vary from 35 to 36. dB for different units so it is clear that they are not absolute standards. Reference [10] also has useful information on noise diode stability.

A suitable diode for the SIMS-A channels at 0.6 and 1.4 GHz is the type MC 1100, a coaxial unit rated at 15.5 + 0.5 dB ENR from 10 MHz to 1.5 GHz. It operates with reverse bias of 28 volts at 6 ma. The whole calibration circuit will require calibration itself, since the avalanche diode is not an absolute source. This is best done by comparing it against a carefully built oven load, using a radiometer as the comparison sensor. For example, the calibration circuit and the oven load can be connected to the two arms of a Dicke switch. If the oven temperature is varied until a null balance is obtained then the calibration circuit temperature will be equal to that of the oven. In this way the diode, attenuator pad and directional coupler are all calibrated at once.

3.1.3.6 Temperature Control of the Calibration Sources

During operational use of the SIMS-A system the open shuttle payload bay will face the earth while the antenna scans in the cross-track direction. (This geometry makes it impractical to use the black body radiation of space itself, at $2.7^{\circ}K$, for calibration purposes.) The orbiter will, to a large extent, screen the SIMS antenna and the black body sources from space itself and they will be radiatively coupled to the earth below. It is possible to analytically determine the temperature anywhere within the payload as a function of time for a given orbit. This was done for an orbit nearly identical to the proposed one. The results from that study show that, in the region of the calibration sources, the maximum skin temperature of the payload bay to be expected is $-38^{\circ}C$ ($235^{\circ}K$)*, and the minimum $-95^{\circ}C$ ($178^{\circ}K$) (Figures 2-36 and 2-37). It is therefore possible to achieve an equilibrium temperature somewhat below $-38^{\circ}C$. This is accomplished by appropriate surface treatment that creates a small value of α/ϵ where α is the absorption coefficient for solar radiation and ϵ is the emissivity for infrared radiation from the earth. If the black body sources are to be treated this way they must also be thermally well insulated from other structures such as the wheel. Fortunately, convection will play no role, otherwise the open sides of the black body cavities would make temperature regulation impossible.

The two black body sources can be counted on to reach an "ambient" temperature that does not exceed $235^{\circ}K$, but which will fluctuate by a few degrees below this level during orbit. Heaters and suitable sensing and regulating circuitry can then be added in order to raise and stabilize one of the sources to the temperature T_1 equal to, say, $240^{\circ}K$. The other will be raised to and stabilized at a higher temperature, T_2, which we take to be $300^{\circ}K$. It is desirable to make the difference $T_2 - T_1$ large, in order to reduce extrapolation errors. Such errors will occur because most targets will have radiant temperatures that lie below $240^{\circ}K$ (as low, even, as $100^{\circ}K$ at the low frequencies) making extrapolation necessary beyond the range T_2-T_1.

---

* These thermal calculations were for an empty bay. Other experiments may modify this condition.

However, if T_2 is made very much larger than T_1 then problems due to radiative coupling between the two black bodies will be encountered. It is not recommended to lower T_1 below the suggested value because cryogenic cooling would be required.

Successful control of the temperatures of the calibrating sources will require extremely careful design due to the critical nature of the thermal problems involved. One problem that we have heretofore ignored will be caused because the wheel must rotate into and out of the two black body cavities. Hence it will radiatively couple directly to the absorbing materials unless the wheel, and all components on it, have a very low emissivity in the infrared. We assume that this can be achieved.

An additional problem is posed by the presence on the wheel of the two low frequency switched calibration circuits. These must be thermally insulated from the wheel, and we have already assumed that each will be stabilized and controlled to a temperature of 240°K. No problem occurs if these enclosures couple radiatively to the black body cavity that is also maintained at 240°K. A difficulty will arise, however, if they couple to the second cavity, for it is maintained at a higher temperature, 300°K, and a mutual perturbation of the temperatures will occur. It therefore appears desirable to mount the two low frequency calibration circuits near the hub of the wheel so that they need not pass through either black body during rotation. This, however, lengthens the feed lines for the 0.6 and 1.4 GHz channels, and causes only a negligible increase in antenna feed line loss.

In the thermal design of all the calibration circuitry the emphasis must be on attaining uniformity of temperature by elimination of gradients. Thermal time constants should be long compared to the period of rotation of the wheel, so that when thermal equilibrium is reached any temperature modulation caused by the wheel will be negligibly small. Long term variations in the temperatures of the calibration sources, such as will occur during the course of full orbit, will be minimized by the temperature regulating circuitry. The effect of any small long term variations can be rendered negligible by continuously monitoring the temperatures using thermistors as diode sensors.

It appears feasible to attain an overall accuracy of $\pm 0.25^{\circ}$K in the knowledge of the physical temperatures T_1, $T_{c1} = T_0$ (about 240°K) and T_2 (equal to about 300°K). The accuracy to be expected for T_{c2} is more difficult to estimate. Since the ENR of the noise diode depends on the diode's physical temperature (which is $T_0 = 240^{\circ}$K), the accuracy of T_{c2} can be no better than that of T_0 and may be considerably worse. It is therefore desirable to stabilize and monitor T_0 as accurately as possible.

3.1.4 Miscellaneous Analysis

3.1.4.1 Field of View

. A field of view of ± 60 deg. is required. There is no optical blockage in the Gregorian channels from 6.6 GHz up, as shown in Figure 3-42 where the reflector is seen at 60 deg. scan. There may be some effect at 6.6 GHz between the near rim of the reflector and the diffracted aperture field, but the clearance of 0.06R (12 cm) between the optically illuminated region and the reflector rim should make this a very minor effect. In the lower channels that are prime focus fed, the effective aperture is larger and some effect will definitely be seen. The undegraded field of view and the extent of degradation to 60 deg. scan should be determined for the lower three
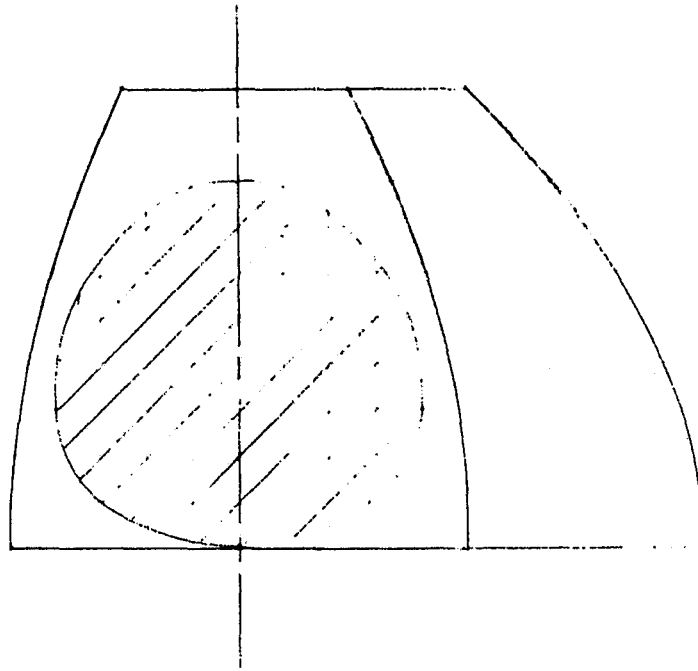
Figure 3-42. View of the Dual Ellipse Aperture Compared to the
Reflector at 60 Deg. Scan

channels. This should be done experimentally because a theoretical evaluation would
be very difficult and probably inaccurate due to the geometry of the problem.

3.1.4.2 Tolerance Requirements

The most critical item in terms of relative tolerance is the main reflector,
because the accuracies on the order of one mm over a diameter of 4 meters are
required. Because surface contour errors have a much more severe effect on beam
efficiency than the more normal antenna parameters such as gain or sidelobe level,
this tolerance will need to be more stringent than would normally be assigned.

Ruze's tolerance analysis[11] is appropriate for this problem. Because the torus is an
offset reflector it is difficult to define an equivalent F/D ratio. The curvature in the
elevation plane is like that of a reflector with F/D = 0.31, while in the azimuth plane
it is about 0.62. The aperture diameter is 1.6 meters at the high frequencies where
the tolerance effects occur, while the focal length is one meter. An average F/D
of 0.4 was assigned for the purposes of performance analysis.

Measuring the contour along the direction of propagation (y axis), the effective
tolerance according to Ruze is

$$\epsilon = \frac{\Delta y}{1 + (D/4F)^2},$$
(68)

where Δy is the rms reflector tolerance measured parallel to the y axis and ϵ is the effective rms tolerance. For $F/D = 0.4$, this makes $\epsilon = 0.72 \Delta y$. The correlation length of the reflector contour errors is relatively small compared to the antenna diameter, as required by Ruze's analysis. This was determined by investigating the error contours of typical large reflector antennas. Consequently, the tolerance efficiency according to Ruze is

$$\eta_T = e^{-(4\pi \epsilon / \lambda)^2} \tag{69}$$

Because the random errors will reduce the gain without appreciably affecting the antenna beamwidth, the main beam efficiency is also reduced by this same factor. Figure 3-43 is a plot of (69), expressed as gain loss in percent vs. the rms tolerance parallel to the y-axis. Tolerance is expressed in inches so as to be related to normal industrial practice. Strictly interpreting the requirements for beam efficiency, a tolerance of 0.002 in. rms is indicated. However, because the 118.7 GHz channel is in an atmospheric resonance region and thus is used for atmospheric temperature mapping rather than terrain mapping, the main beam efficiency can be defined relative to the 5 Θ circle rather than the 2.5 Θ circle. This gives more margin before the effect of reflector tolerance is included so 0.003 in. rms is allowable. A subreflector tolerance of 0.001 in. rms was used because it is practically achievable in the smaller size, and the overall performance will not be appreciably affected by errors of that magnitude.

Should operation at 300 GHz (reflector only) be desired, an appropriate tolerance relative to the 300 GHz loss curve of Figure 3-43 should be chosen. This tolerance would be a trade-off of cost vs. performance. A reflector in the tolerance range required has never been built in this size, so development risk would also be a factor.

3.1.4.3 Temperature Resolution

The number and distribution of feeds and radiometers were defined in Para 2.2.1.2. The expected temperature resolution can be calculated from

$$\Delta T = \frac{L T_s}{\sqrt{Bt}}$$

where t $= \dfrac{Nh\Theta^2}{v_s \theta_s} =$ integration time (sec)

$\Delta T =$ Nadir temperature resolution ($^{\circ}$K)

$L =$ Loss expressed as $10^{|\alpha|/10}$, $\alpha =$ attenuation in dB

$T_s =$ System noise temperature ($^{\circ}$K)

$B =$ Predetection bandwidth (Hz)
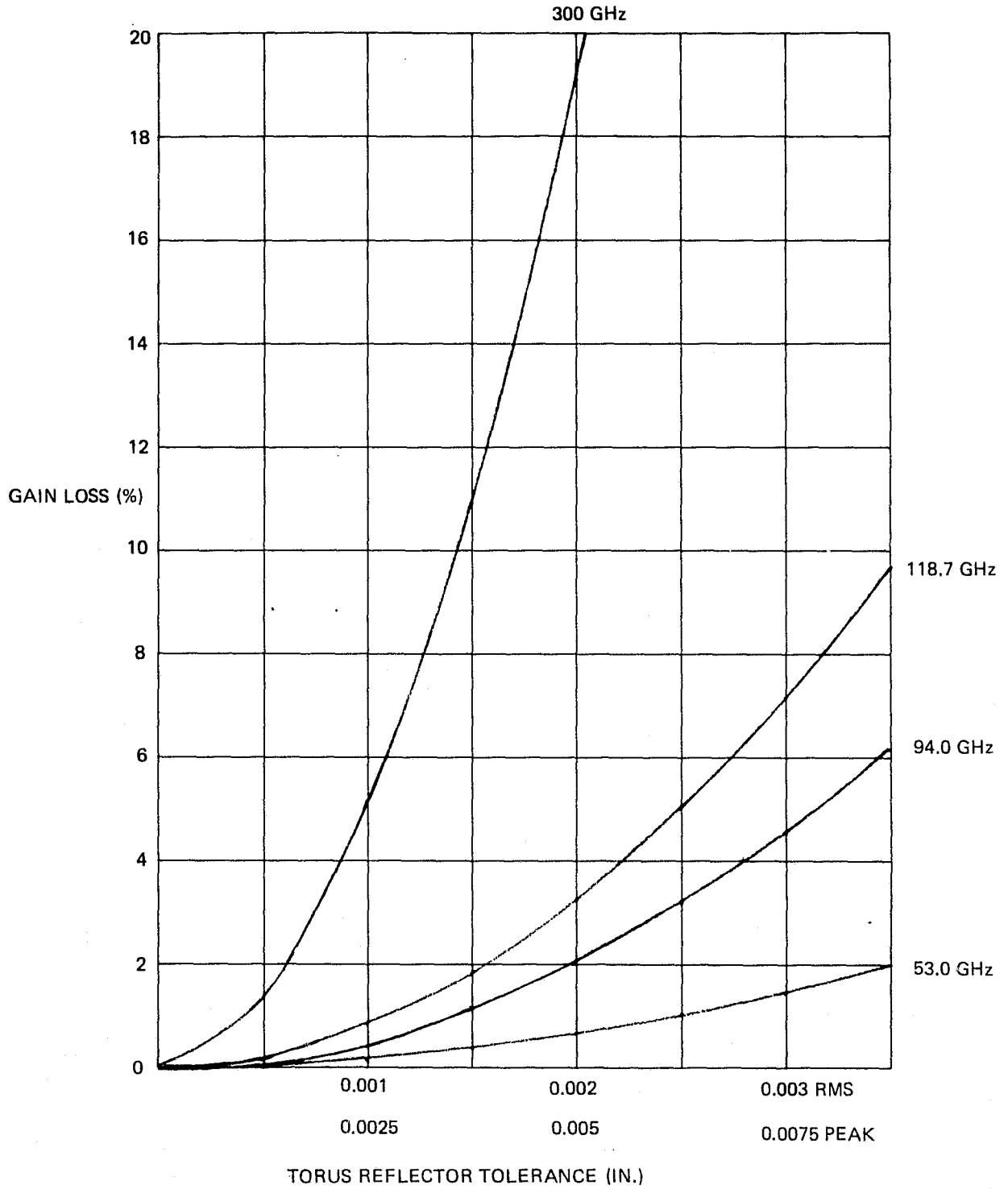
Figure 3-43. Torus Reflector Tolerance (in)

N = Number of beams integrated

h = Altitude = 340 Km

Θ = 3 dB beamwidth (radians)

v_s = Track velocity = 7.3 Km/sec

θ_s = Total feed rotation = .2 π radians

The results are given in Table 3-11. The temperature resolution for the lossless case is given in the column headed $\Delta T/L$. Losses will be minimized by locating mixer pre-amps directly behind the feeds. Estimated attenuation (α) is given and the net temperature resolution (ΔT) is seen in the last column. The loss in channels 1 and 2 is principally attributed to coax connectors and spillover. Channel 3 has the highest loss which includes that of the stripline array. Losses for channels 4 through 11 consist of waveguide junctions, orthomode transducer, a very short length of waveguide and 80 percent of the spillover loss. These feeds are concentric and the high frequency feed, while being electrically longer than the outer feed (low frequency), introduces a discontinuity which results in a small amount of loss. For this reason it is expected that all gregorian feed losses will be approximately equal to 0.34 dB including 0.14 dB of absorbed spillover. These results agree favorably with those of Table 3-11.

Table 3-11. Preliminary Temperature Resolution

f (GHz)	T_s ($^\circ$K)	N	B (MHz)	(deg)	$\Delta T/L$ ($^\circ$K)	α (−dB)	ΔT ($^\circ$K)
0.610	400	2	8	17.8300	0.120	0.31	0.13
1.413	400	2	25	7.7000	0.150	0.25	0.16
2.695	400	2	10	4.0400	0.470	0.68	0.55
6.600	400	4	300	2.0600	0.120	0.34	0.13
10.690	500	2	300	1.2700	0.340	0.34	0.37
20.000	800	2	1000	0.6800	0.550	0.34	0.59
22.200	800	2	1000	0.6120	0.615	0.34	0.67
37.000	800	2	2000	0.3670	0.720	0.34	0.78
53.000	1000	4	500	0.2560	1.840	0.34	1.99
94.000	1500	4	2000	0.1450	2.430	0.34	2.63
118.700	1500	4	700	0.1145	5.210	0.34	5.63

v_s = 7.3 Km/sec

h = 340 Km

θ_s = 360

$\dot{\theta}_s$ = 5.4 rps

3.1.5 Antenna Patterns

The calculated antenna patterns are enclosed for reference purposes.

The first pattern set, Figures 3-44 through 3-50 gives the various cuts through the beam at 30 deg. angular increments at 0.61 GHz using the four dipole feed. Figure 3-51 is the integrated power vs. angle. All patterns are given as relative power (dB) vs. angle from beam center. The rotation angle $\phi = 180$ deg. is the azimuth cut, and $\phi = 270$ deg. is the elevation pattern downward from beam center. In all cases, the two curves in the pattern represent principle and cross polarization while the two curves in the integrated power plot represent principly polarized power and total power.

Figures 3-52 through 3-58 give the various pattern cuts at 1.413 GHz using the seven dipole feed, and Figure 3-59 gives the integrated power vs angle at that frequency.

Figures 3-60 through 3-66 give the various pattern cuts at 2.695 GHz using the optimized 19 slot array feed, and Figure 3-67 gives the corresponding integrated power.

Figures 3-68 through 3-72 give the calculated pattern cuts for 6.6 GHz in 45 deg. rotational increments using the Gregorian subreflector, and Figure 3-73 gives the corresponding integrated power.
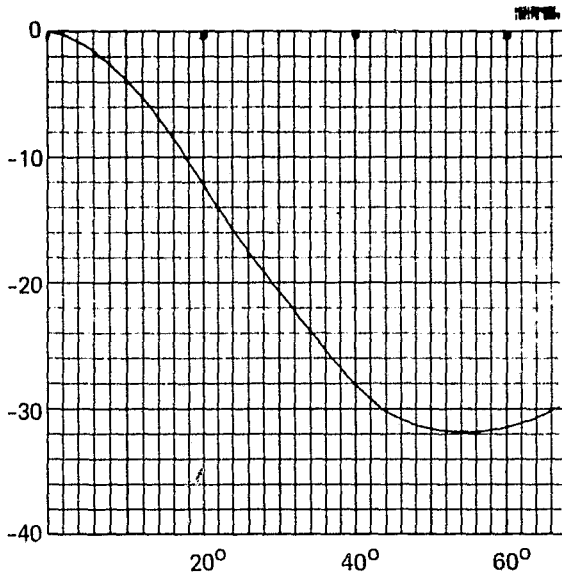
Figure 3-44. Pattern Cut, 0.61 GHz, $\phi = 90^\circ$
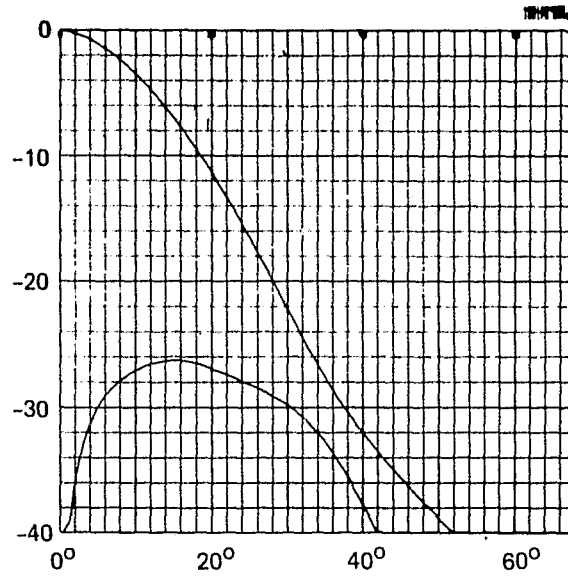
Figure 3-45. Pattern Cut, 0.61 GHz, $\phi = 120^\circ$
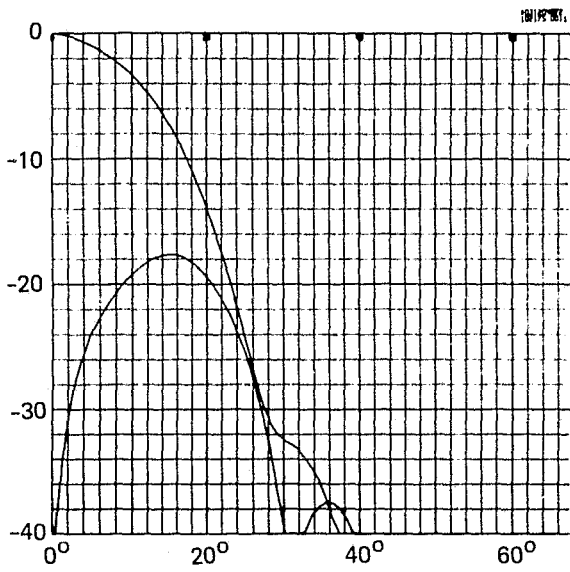
Figure 3-46. Pattern Cut, 0.61 GHz, $\phi = 150^\circ$
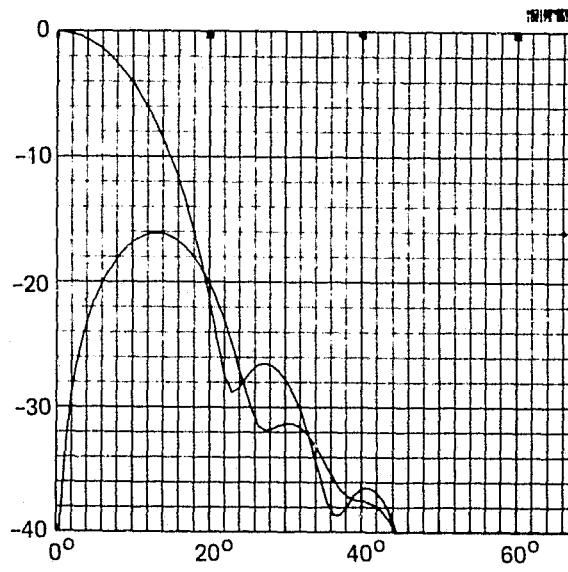
Figure 3-47. Pattern Cut, 0.61 GHz, $\phi = 180^\circ$
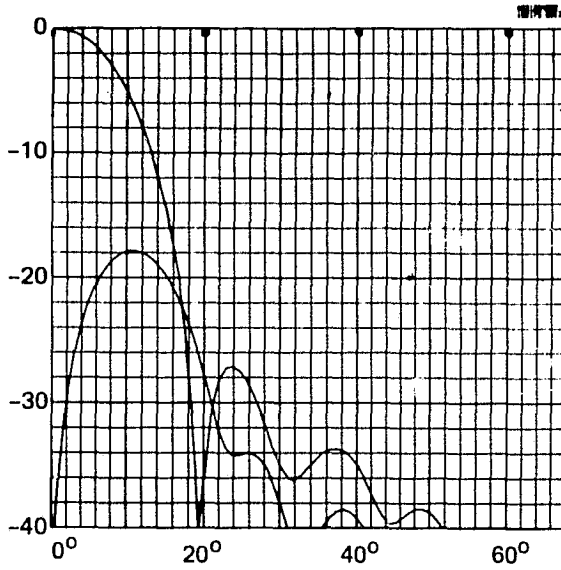
Figure 3-48. Pattern Cut, 0.61 GHz, $\phi = 210^O$
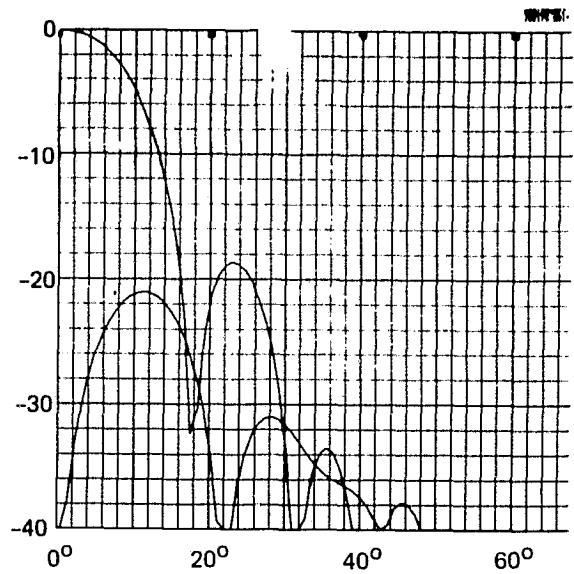
Figure 3-49. Pattern Cut, 0.61 GHz, $\phi = 240^O$
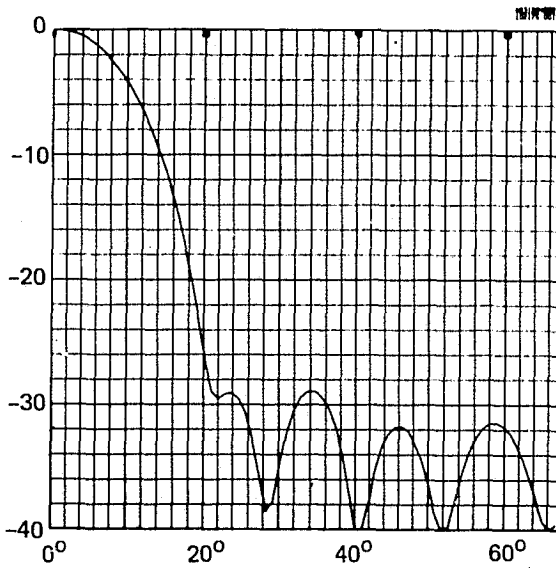
Figure 3-50. Pattern Cut, 0.61 GHz, $\phi = 270^O$
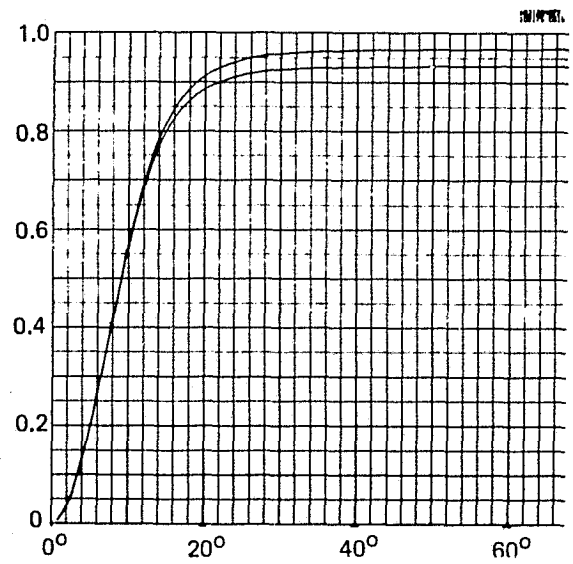
Figure 3-51. Integrated Power for 0.61 GHz
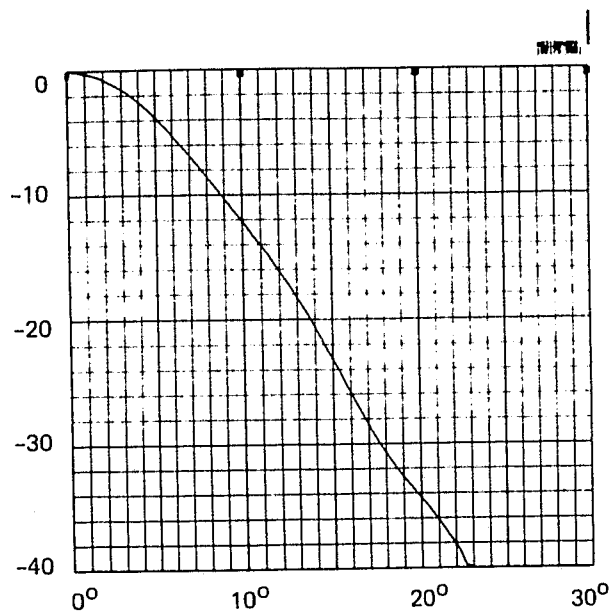
Figure 3-52. Pattern Cut, 1.4 GHz, $\phi = 90^\circ$
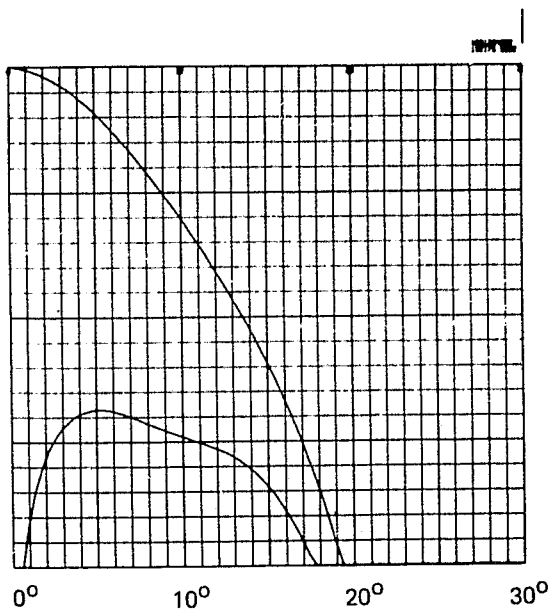
Figure 3-53. Pattern Cut, 1.4 GHz, $\phi = 120^\circ$
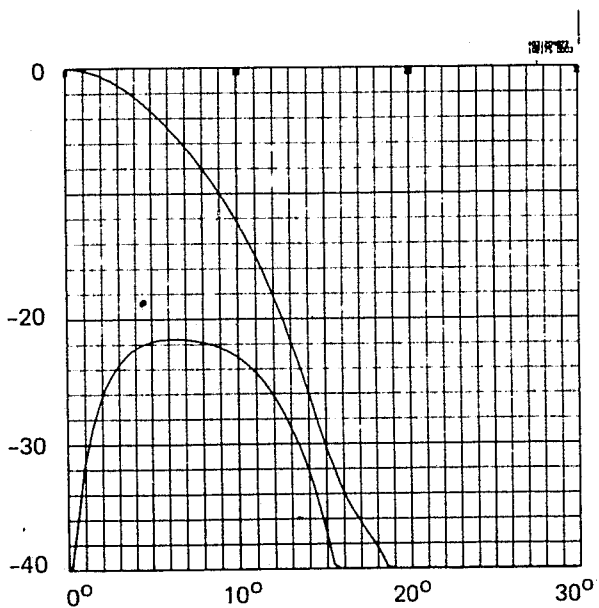
Figure 3-54. Pattern Cut, 1.4 GHz, $\phi = 150^\circ$
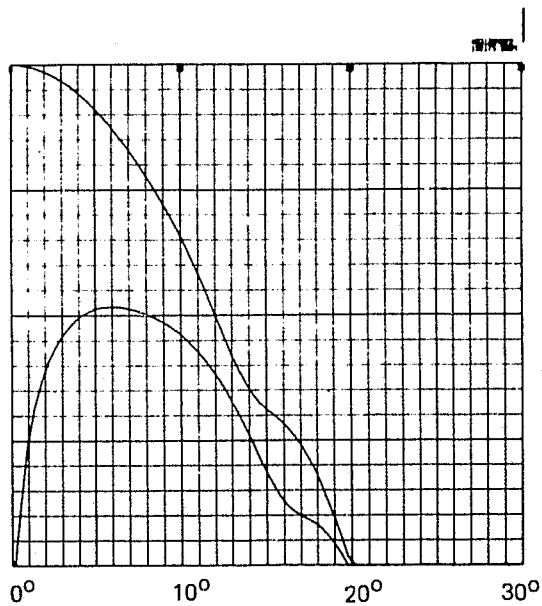
Figure 3-55. Pattern Cut, 1.4 GHz, $\phi = 180^\circ$
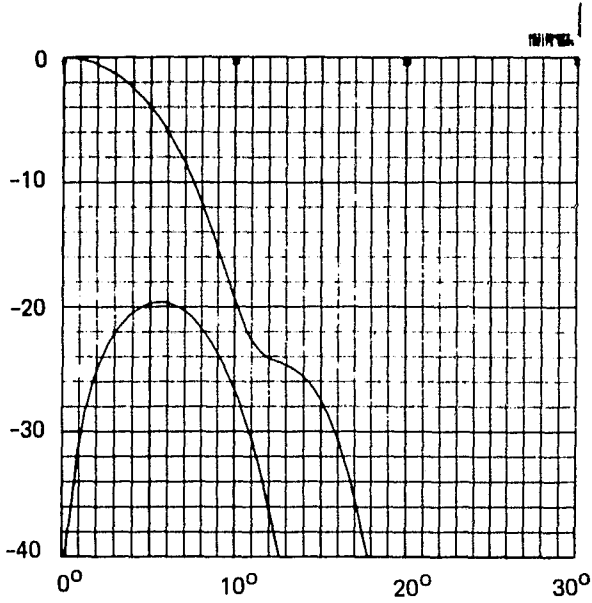
Figure 3-56. Pattern Cut, 1.4 GHz, φ = 210°
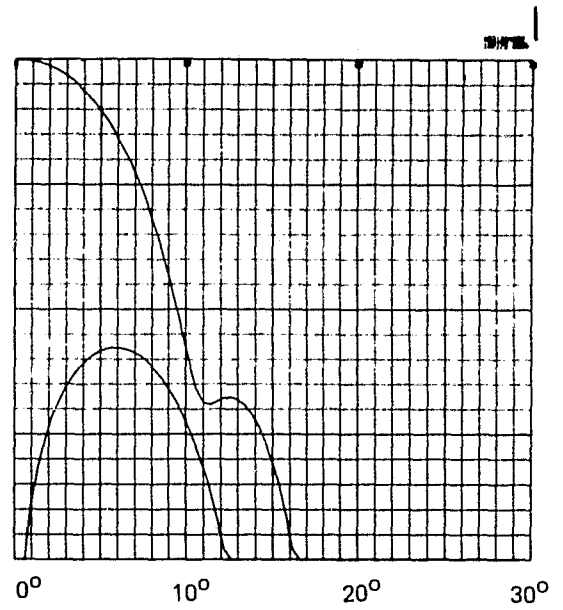
Figure 3-57. Pattern Cut, 1.4 GHz, φ = 240°
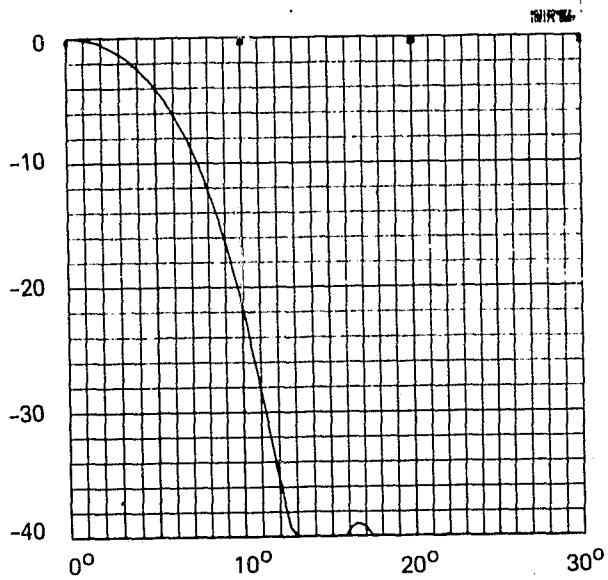
Figure 3-58. Pattern Cut, 1.4 GHz, φ = 270°
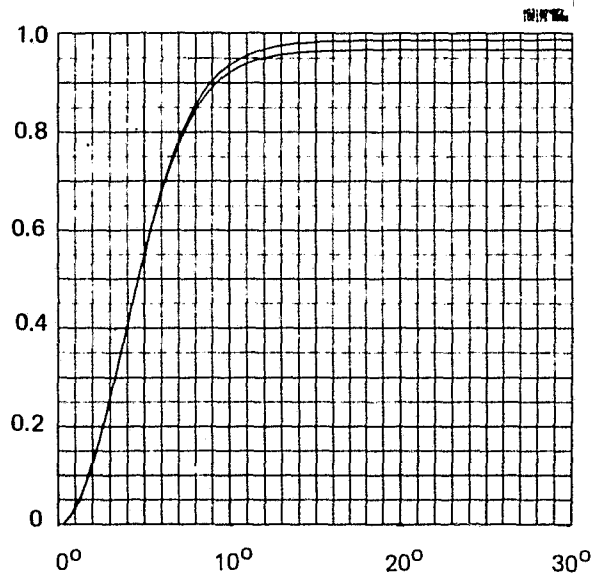
Figure 3-59. Integrated Power for 1.4 GHz
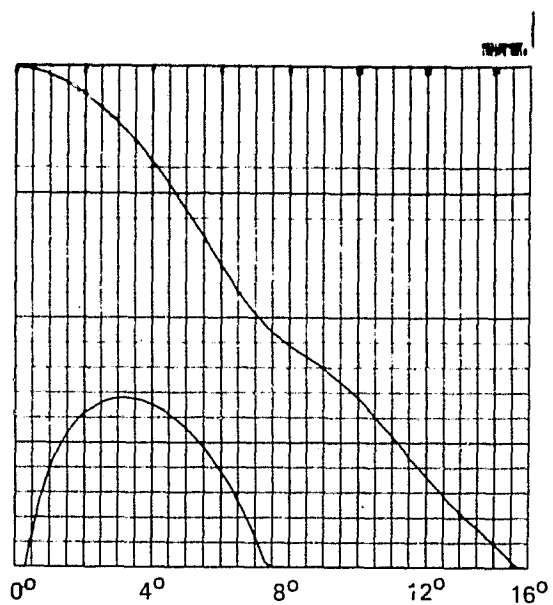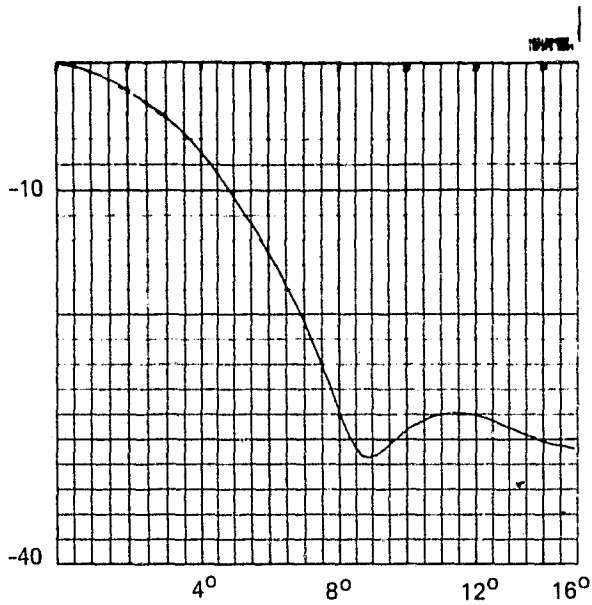
Figure 3-60. Pattern Cut, 2.7 GHz, $\phi = 90°$

Figure 3-61. Pattern Cut, 2.7 GHz, $\phi = 120°$
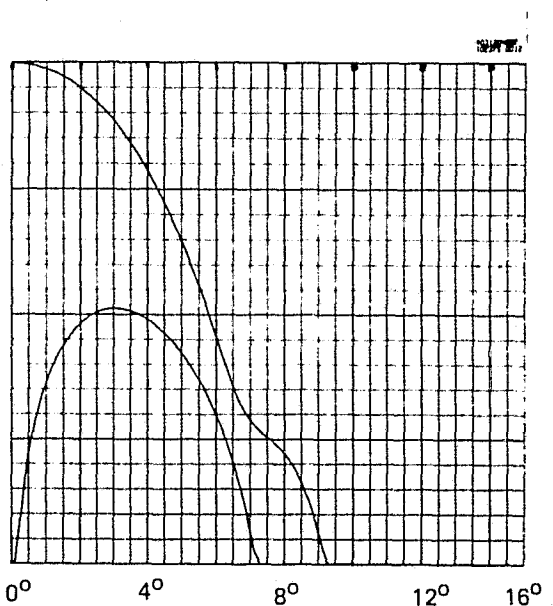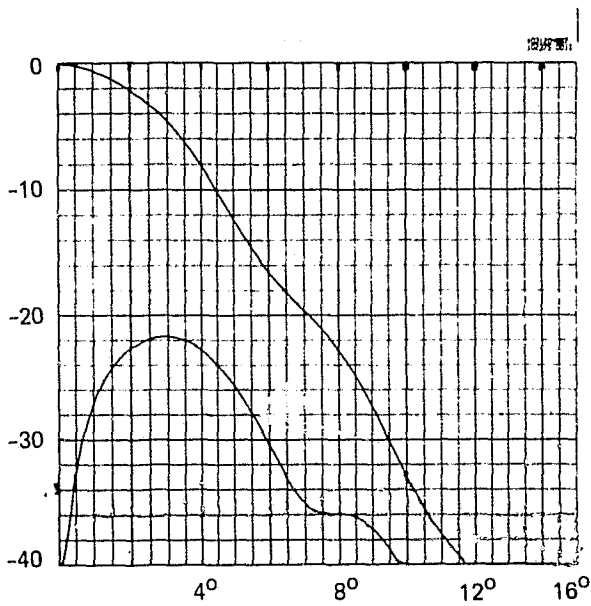
Figure 3-62. Pattern Cut, 2.7 GHz, $\phi = 150°$

Figure 3-63. Pattern Cut, 2.7 GHz, $\phi = 180°$
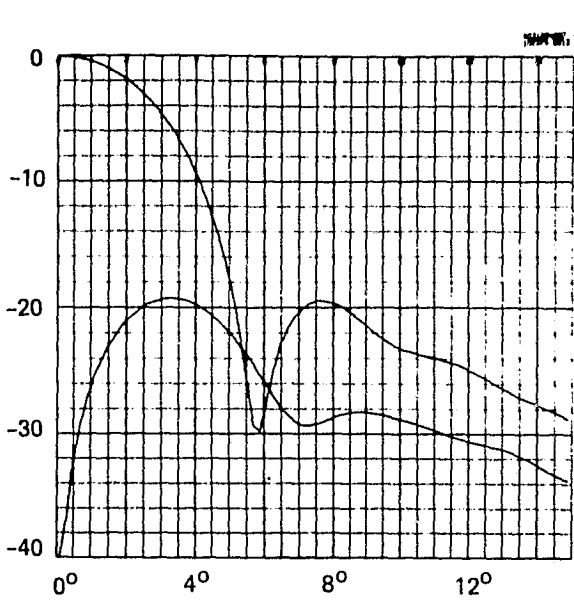
Figure 3-64. Pattern Cut, 2.7 GHz, ϕ = 210°
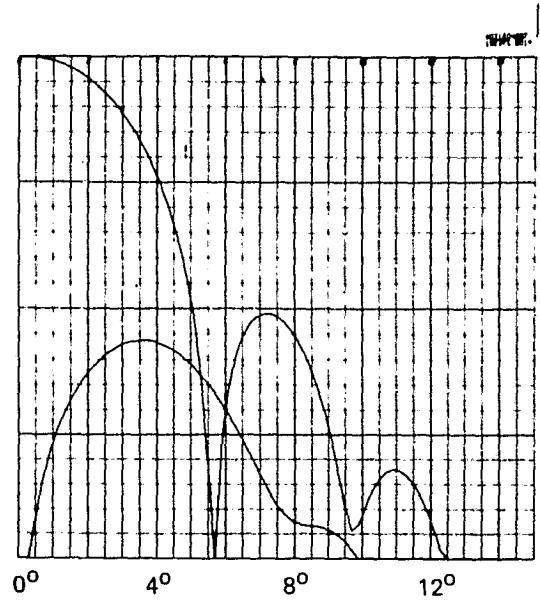
Figure 3-65. Pattern Cut, 2.7 GHz, ϕ = 240°
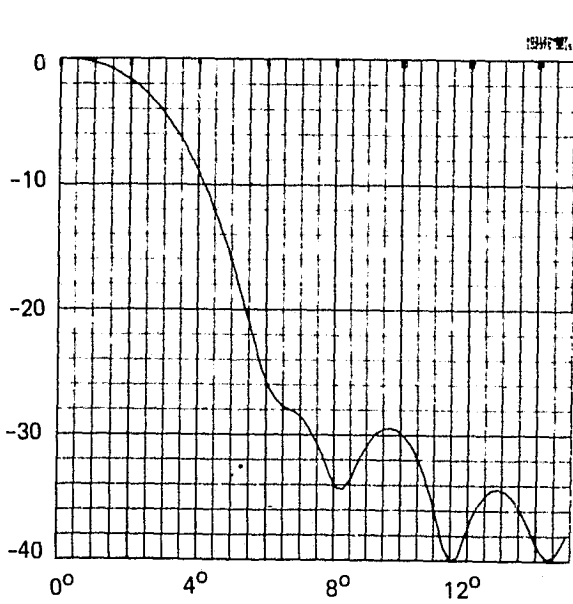
Figure 3-66. Pattern Cut, 2.7 GHz, ϕ = 270°
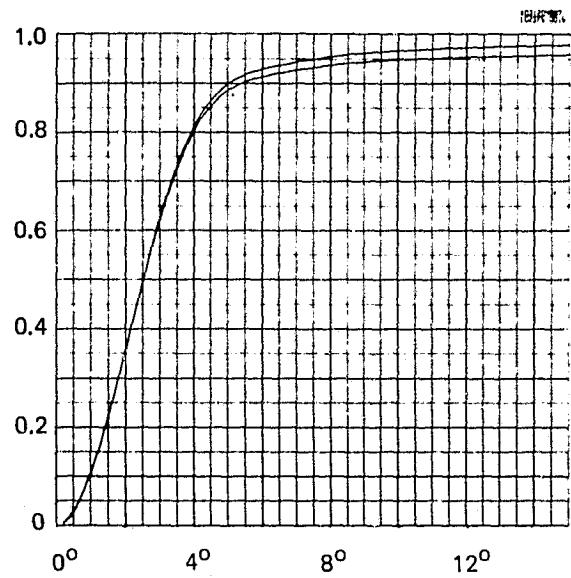
Figure 3-67. Integrated Power for 2.7 GHz
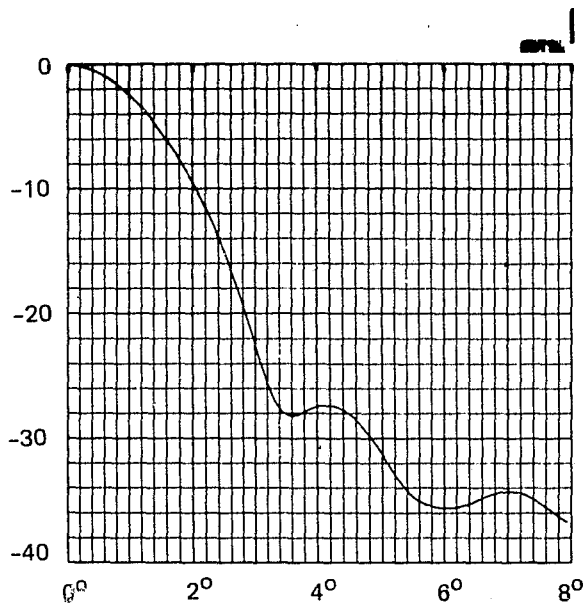
Figure 3-68. Pattern Cut, 6.6 GHz, $\phi = 90^{\circ}$
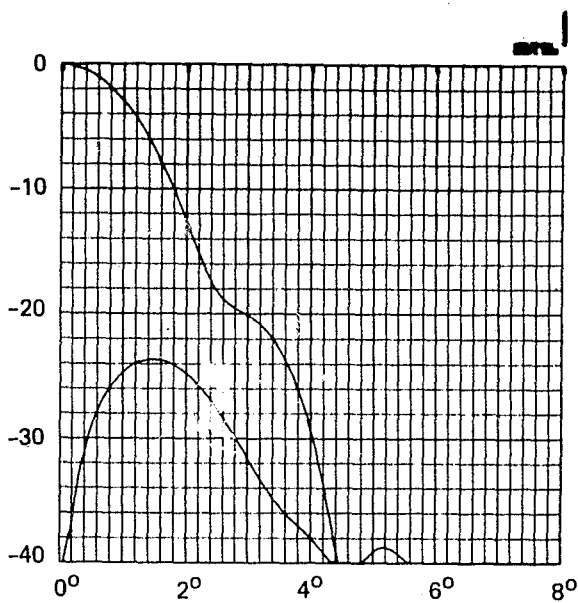
Figure 3-69. Pattern Cut, 6.6 GHz, $\phi = 135^{\circ}$
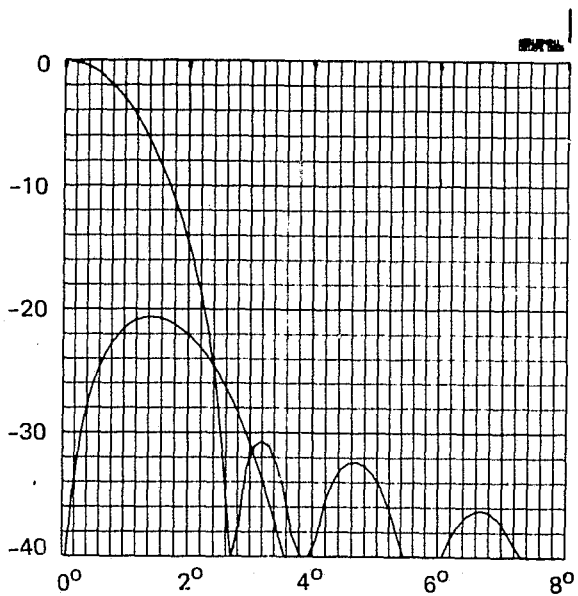
Figure 3-70. Pattern Cut, 6.6 GHz, $\phi = 180^{\circ}$
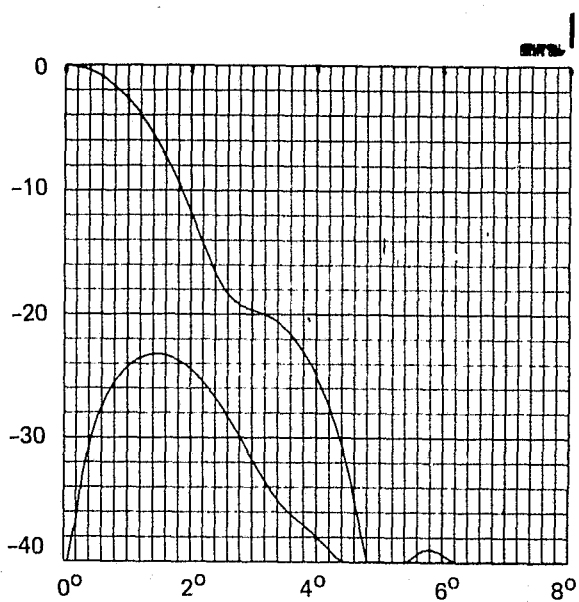
Figure 3-71. Pattern Cut, 6.6 GHz, $\phi = 225^{\circ}$
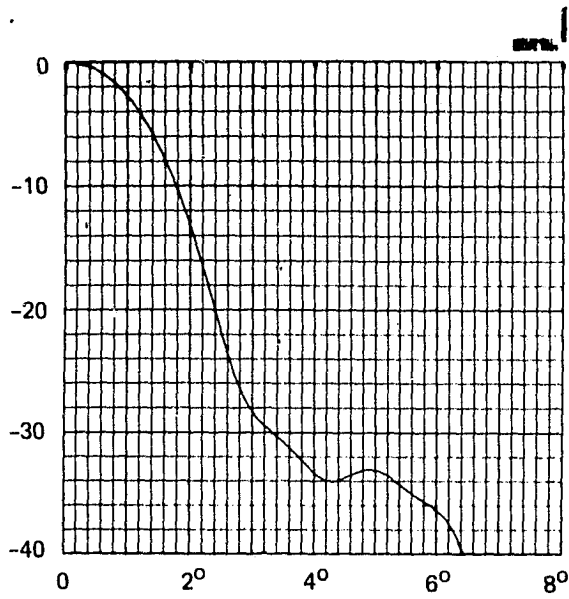
Figure 3-72. Pattern Cut, 6.6 GHz, $\phi = 270^{\circ}$
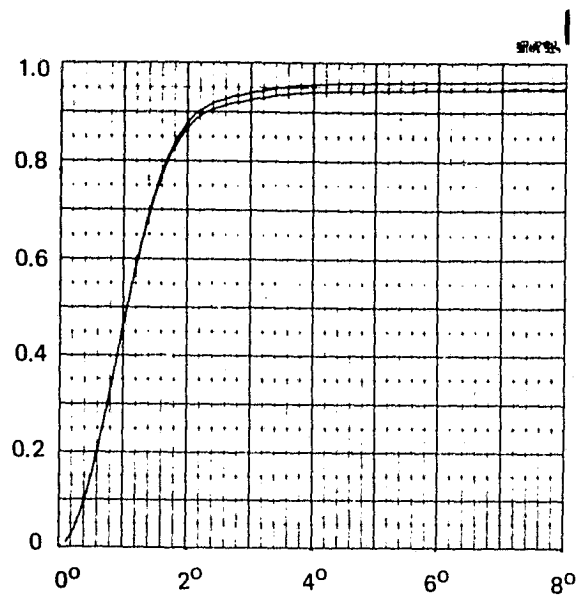
Figure 3-73. Integrated Power for 6.6 GHz

3.2 MECHANICAL ANALYSES

3.2.1 Overall System

Layout

A preliminary layout was prepared to establish the relationship of the various subassemblies of the system to one another and to establish an overall envelope which could be located in the orbiter payload bay. The layout used the initial computer generated contours for both the primary and sub-reflectors and these contours have been maintained throughout the study. The layout indicated a system using a 4 meter (13.123 ft) diameter parabolic torus reflector and 2.82 meter (9.25 ft) diameter feed wheel could be located in the 15 ft diameter orbiter payload bay with adequate room for supporting structure and mounting provisions.

Interface Fitting Locations

Figure 1(c), "sketch of possible configuration of SIMS-A antenna system on shuttle orbiter," of Exhibit II accompanying the contract, indicated SIMS-A may be located in the aftmost section of the payload bay. Examination of JSC-07700 indicated that the amount of OMS (Orbital Maneuvering System) propellant carried aboard the orbiter depends on the payload weight, height of orbit, launch site, orbit inclination, and other factors. When the mission requires more propellant than is carried in the integral tank, additional OMS propellant is supplied in kits located in the aft end of the payload bay. When used, these kits extend from the aft bulkhead forward to $X_O = 1194$. If SIMS-A were configured to fit in the aftmost part of the payload bay, it could not be moved forward to accommodate an OMS kit because the relationship between keel and longeron fittings at the aft candidate primary fitting locations ($X_O = 1187$ and $X_O = 1246$) does not correspond to the relationship at primary fitting locations between $X_O = 715$ and $X_O = 1128$. At these latter locations all longeron and keel fittings fall on the same orbiter station. If SIMS-A is configured to have the longeron (primary) fittings and the keel (auxiliary) fitting form a plane and to have the other longeron (stabilizing) fitting located 59.0 in. (the distance between primary fittings in the orbiter) from this plane, then 8 primary and a large number of vernier locations are available for retention of SIMS-A. Because this arrangement will provide more opportunities for the SIMS-A experiment to be included in a shuttle sortie, it was selected for the design presented.

Examination of Thermal Criteria

JSC-07700 contains thermal information for various theoretical payload and orbit configurations. Examination of the available information provided minimal information on any orbit configuration approximating that of SIMS-A. The column of Figure 2-32 labeled "port side to sun" represents a possible orbital configuration for SIMS-A (open payload bay toward earth for entire orbit). The temperatures developed in the payload bay are constant with time and relatively constant with respect to location in the bay (from -15.56°C (+4°F) to -23.33°C (-10°F) in the X_O range of interest). The entry thermal environment curves shown in Figures 2-30 a, b, and c for three payload bay sections indicate a maximum temperature of 82.22°C (180°F) may be expected between $X_O = 582$ and $X_O = 760$. Temperature versus time plots of general nodes in the payload bay for the orbital configuration shown at the top of Figure 2-35 were

obtained from JSC through Rockwell's Space Division. The curves are shown in Figures 2-36 and 2-37. The curves show a maximum on-orbit temperature of -38°C (-36.4°F) at node No. 673 and a minimum on-orbit temperature of -95°C (-139°F) at node No. 671. The curves also indicate rates of change during the eclipses of approximately 0.5°C/sec (0.9°F/sec). The temperature range determined thus far is from a maximum of 88.22°C (180°F) during re-entry to a minimum of -95°C (-139°F) on-orbit. Table 2-12 has design minimums and maximums of -73°C (-100°F) and $+93.5^\circ$C (200°F) respectively for the payload bay wall. From the data examined a preliminary design temperature range of -100°C (-148°F) to $+95^\circ$C ($+203^\circ$F) with an operating range of -95°C (-139°F) to -15°C ($+5^\circ$F) appears reasonable for SIMS-A. Consideration should be given to JSC-07700 paragraph 4.2.2.7: "Thermal Environment. The determination of the temperature environments which the payload will actually experience in the payload bay requires knowledge of the specific mission environment from boost through entry, the type of thermal control provided by the Orbiter and the payload, and the payload bay and payload thermal characteristics. To obtain this information requires detailed knowledge of the actual Orbiter and payload design, as well as the specific inflight orientations which probably will vary for each different mission objective."

3.2.2 <u>Reflector/Main Frame</u>

<u>Material</u>

The examination of thermal information obtained from Johnson Space Center via Rockwell International's Space Division indicates that on-orbit temperatures in the orbiter payload bay vary from about -37°C (-35°F) to -95°C (139°F) and fluctuations of 35°C (63°F) can occur in 30 to 40 seconds. It is likely that such rapid changes will take place over portions of the reflector due to shading (by the feed wheel for example). Thermal expansion or contraction of such areas will be restrained by other areas not subjected to the same thermal change, thus setting up internal stresses which manifest themselves as distortions in the reflector surface. Therefore a material with very low CTE (Coefficient of Thermal Expansion) must be used to satisfy the RF performance requirements of SIMS-A. The material should be of low density to minimize loading on the supporting structure and to reduce the costs of placement in orbit. The modulus of elasticity should be sufficiently high that a thin reflector shell (30 to 60 mils thick) supported by nodes moderately spaced (approx. 15 inches) would not deflect under its own weight in the 1g terrestrial testing environment.

Graphite-epoxy, an advanced composite material, satisfies the design requirements of SIMS-A. Design and fabrication practices are well established and are adaptable to development of SIMS-A. The development of graphite-polymide, a higher temperature, more moisture resistant material, is progressing rapidly, but its benefits are not required by SIMS-A. If the development should result in a graphite-polymide material with cost lower than graphite-epoxy then it would become a good candidate material. For the present, graphite-epoxy is the material selected for the reflector shell and the supporting structure.

The reflector conductive surface must be capable of withstanding the stresses of differential thermal expansion or contraction. The temperature extremes encountered during orbit and re-entry can produce a negative ΔT of 121°C (218°F) and

a positive ΔT of 74°C (133°F) from a fabrication temperature of 21°C (70°F). From the stress-strain relationship it follows that

$$\sigma = \epsilon E$$

where

σ = stress

ϵ = strain

E = modulus of Elasticity

and for a thermal strain,

$$\epsilon = (\alpha_{RC} - \alpha_{G-E}) \Delta T$$

where

α_{RC} = CTE of reflective coating

α_{GE} = CTE of graphite-epoxy

$\approx 0.1 \ \mu in/in/°F$

ΔT = temperature change

Therefore,

$$\sigma_{RC} = (\alpha_{RC} - \alpha_{G-E}) \Delta T \ E_{RC} \tag{70}$$

Equation (70) was solved for several materials with adequate reflective qualities for the ΔT's of interest and the resulting σ_{RC} was compared to the yield stress of the material. Electro-deposited nickel, the only material examined which did not reach its yield stress, has been tentatively selected as the conductive coating for the reflector. However, additional study should be conducted and simulation tests should be made before the selection is finalized.

Configuration

The main frame must provide support for the reflector shell, the drive mechanism/feed wheel assembly, and the calibration targets. Acceleration of these masses (due to launch, landing, etc) produce forces which must be reacted by the orbiter structure. The main frame must provide load paths for these forces from their points of origin to the retention trunnions. In order to obtain first cut numerical data on structural member sizing, weight, and magnitudes of stresses and deflections to be encountered, it was decided to model a main frame structure and subject it to a static load computer analysis. It was required that the configuration to be modeled be feasible with respect to fabrication and performance requirements and yet be easily modeled. Several configurations for modeling are described in

Table 3-12. Configuration 1 in the table was selected for modeling because it lends itself to the design of an efficient structure while providing uniform shell support spacing and being fairly easy to model.

Analysis

The reflector/main frame modeled for computer analysis consists of a parabolic torus reflector surface made from 0.032-inch thick graphite epoxy supported by a truss structure having 10 truss frames which are perpendicular to the centerline of the parabolic torus. The truss frames are spaced to provide equal spacing (15.066 inches) along the curvature of the parabola. The support nodes on any frame are spaced at approximately 15 in. intervals along the length of the radius arc for the particular frame. The support nodes are connected to each other by plate elements which represent the reflector shell. The frames are constructed from round elements having an outside diameter of 1.0 inch with 0.125 inch walls. Similar longitudinal and diagonal elements join adjacent frames.

The structural analysis of the reflector and truss structure was performed on NASTRAN, a finite element computer program for structural analysis that is intended for general use. Structural elements are provided for the specific representation of the antenna construction, which can be rods, beams, shear panels, plates and shells of revolution. The range of analysis types in the program include: Static response to concentrated and distributed loads, to thermal expansion and to enforced deformation; dynamic response to transient loads, to steady state sinusoidal loads and to random excitation; determination of real and complex eigenvalues for use in vibration analysis, dynamic stability analysis, and elastic stability analysis. NASTRAN uses a finite element structural model, wherein the distributed physical properties of a structure are represented by a finite number of structural elements which are interconnected at a finite number of grid points, to which loads are applied and for which displacements, velocities and accelerations are calculated.

The model was analyzed for 20 g static loads applied along the longitudinal (orbiter, X) and vertical (orbiter, Z) axes of the structure. This arbitrarily chosen input is somewhat higher than the 3σ value of the rms (5.5 g) acceleration due to random vibration.

The program sub-routines were called which provide axial force, total axial stress, bending stress, deflection of nodes, system weight, system C.G. location, and plate principle stresses. The sub-routine which generates a CRT display of sectional or perspective views as requested was called to produce the views shown in Figure 3-74 through 3-87.

Due to the symmetrical configuration of the structure only one-half of the structure was modeled for the computer analysis. The drive mechanism and feed wheel assembly were not modeled, but were included in the analysis as lumped masses concentrated at appropriate points on the structure. The half structure consisted of about 1000 rod (truss) elements and 47 plate (reflector) elements. Tables 3-13 and 3-14 give the element numbers, nodal limits, and the stress values for the 9 highest, and 10 lowest stressed elements respectively. Stresses in the elements located radially around the trunnions and data on the highest stressed plate element are given in Table 3-15. The total output was too voluminous to include in the report.

Table 3-12. Main Frame Computer Model Candidate Configurations

No.	Type	Advantages	Disadvantages
1	Thin shell on truss with frames perpendicular to torus axis.	1. Efficient structure. Elements not concentrated at one end. 2. Spacing of nodal supports uniform in both directions 3. Truss provides ideal (axial) loading for graphite-epoxy. 4. Fairly easy to model for computer analysis. 5. Easy to develop contour adjustments.	1. Non-uniform truss frames. 2. Cost higher than with truss frames radial.
2	Thin shell on truss with frames located radially about the torus axis.	1. Simplest structure 2. Identical (or similar) frames 3. Lowest Cost 4. Truss provides ideal (axial) loading for graphite-epoxy. 5. Easy to model for computer analysis. 6. Easy to develop contour adjustments.	1. Concentration of elements at one end. 2. Spacing of nodal supports not uniform.
3	Stiffened shell on framed structure with stiffening panels on outside (Monocoque)	1. Very rigid.	1. Large spacing between nodal supports requires stiffened shell (e.g. honeycomb). 2. More difficult to model for computer analysis. 3. Contour tolerance met by grinding.

C75-664/034A
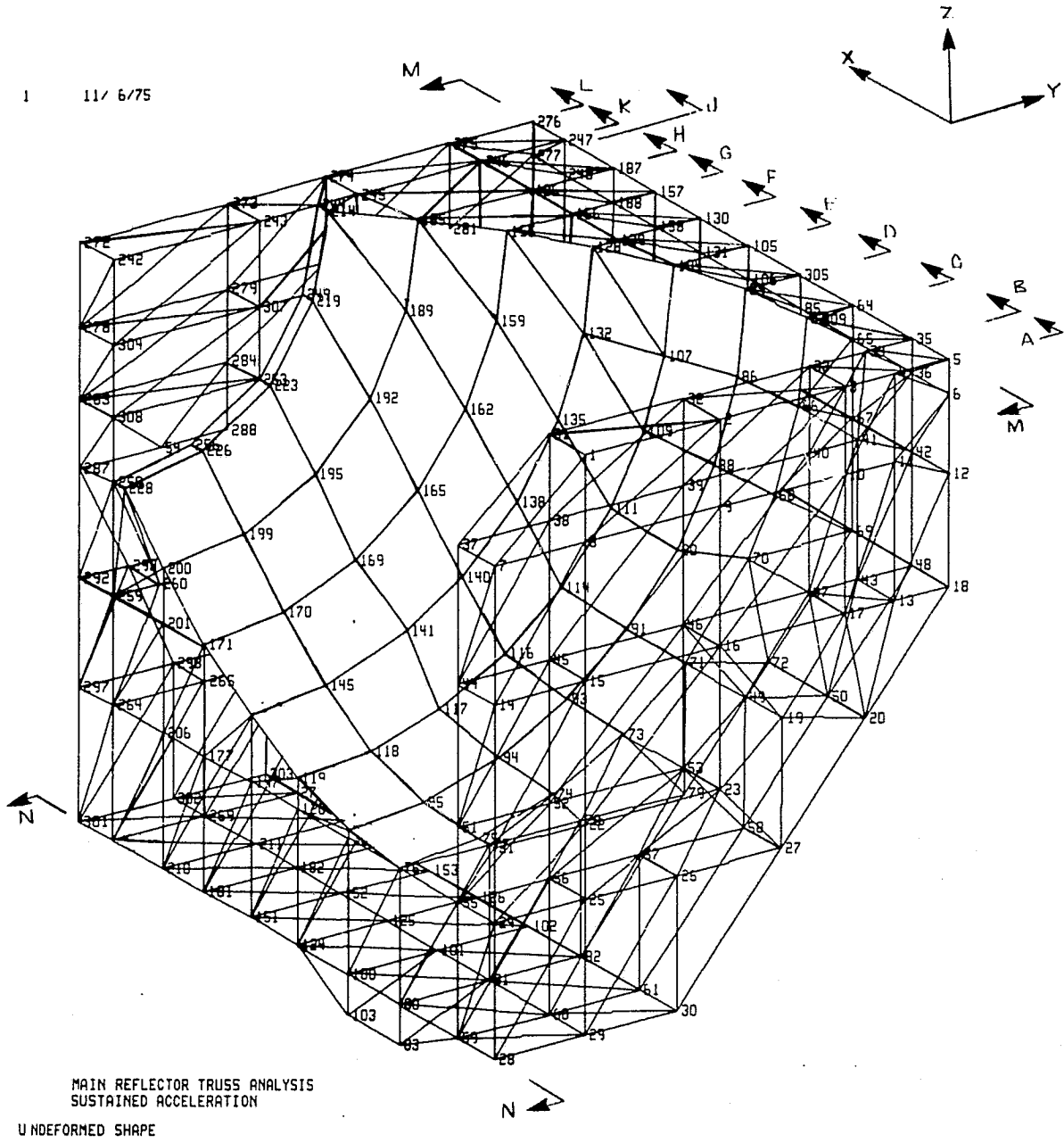
Figure 3-74. Computer Perspective of Antenna Main Frame and Reflector
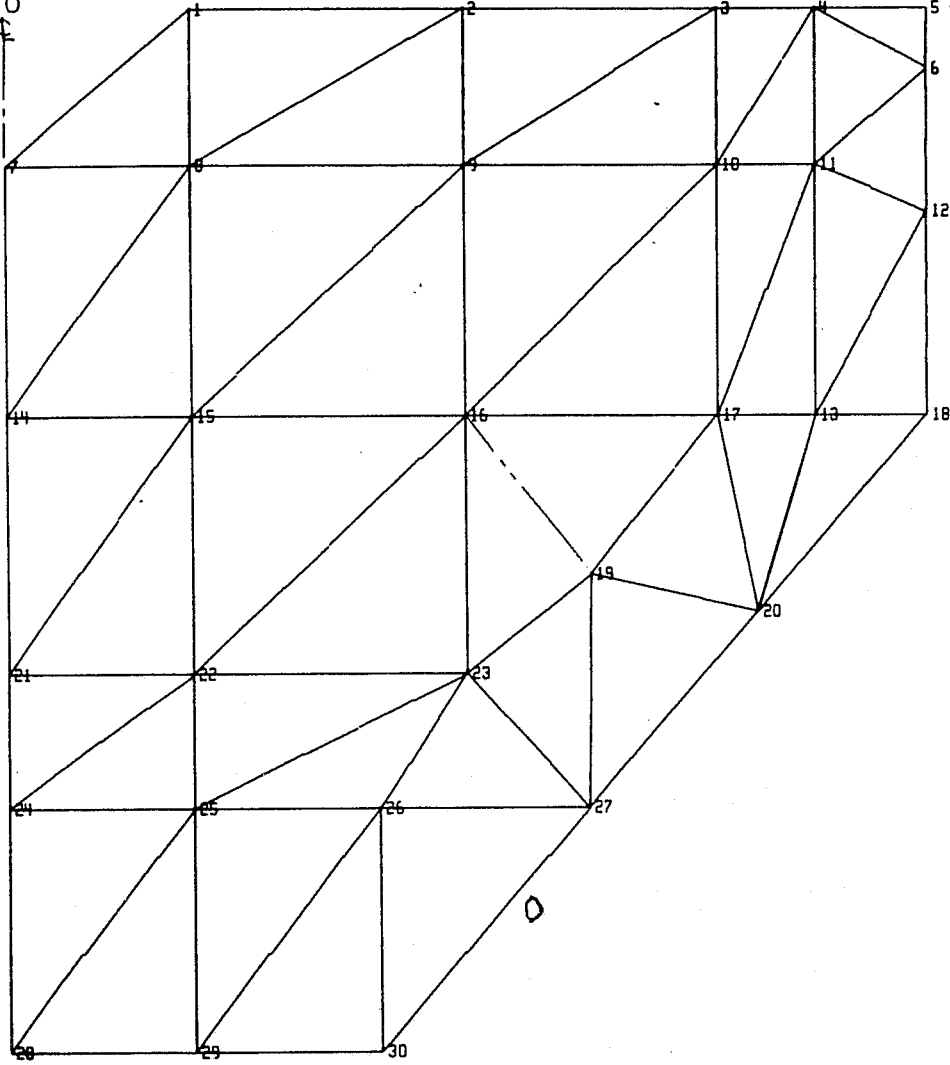
Figure 3-75. View A (x = 0)
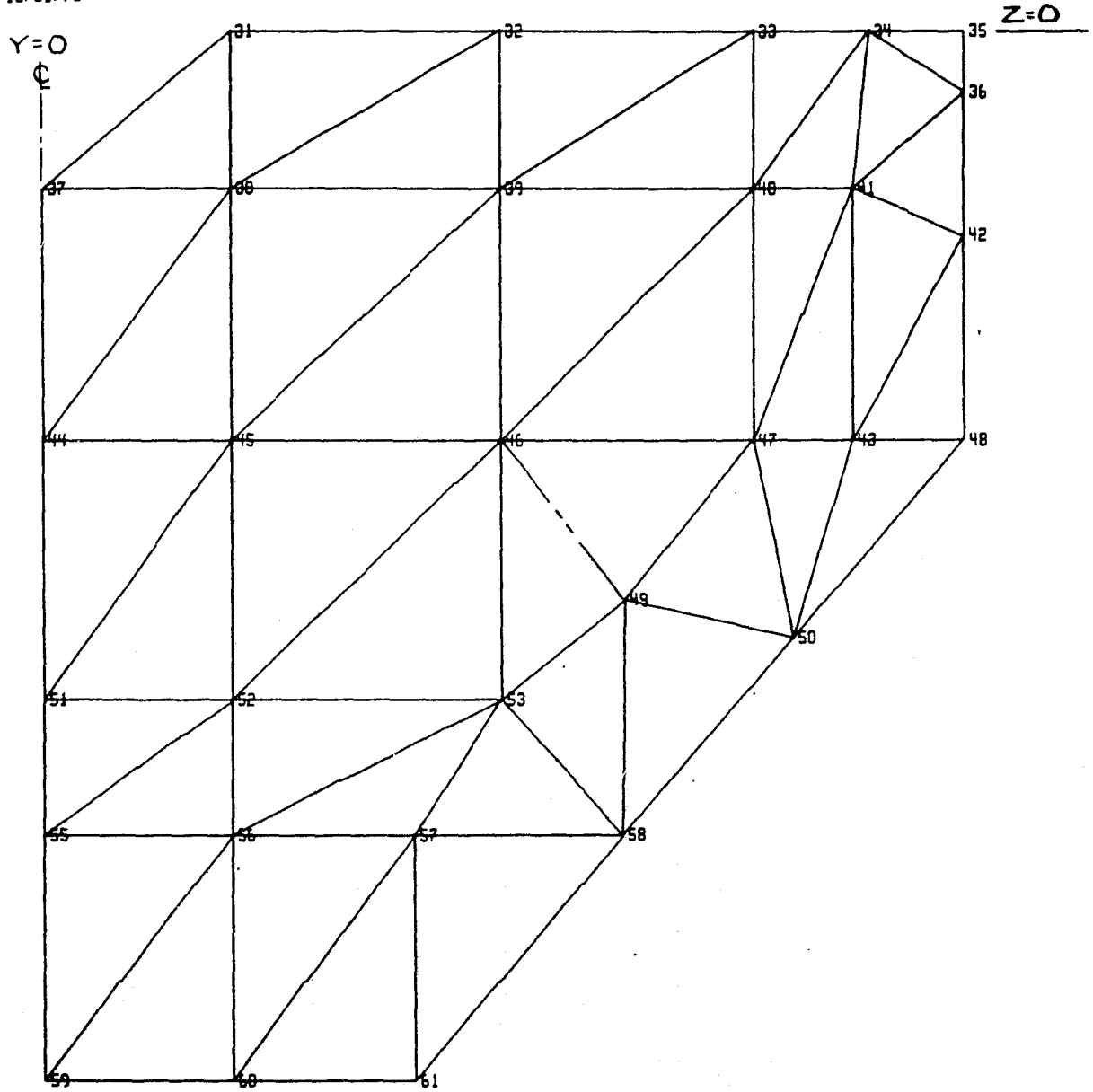
Figure 3-76. View B
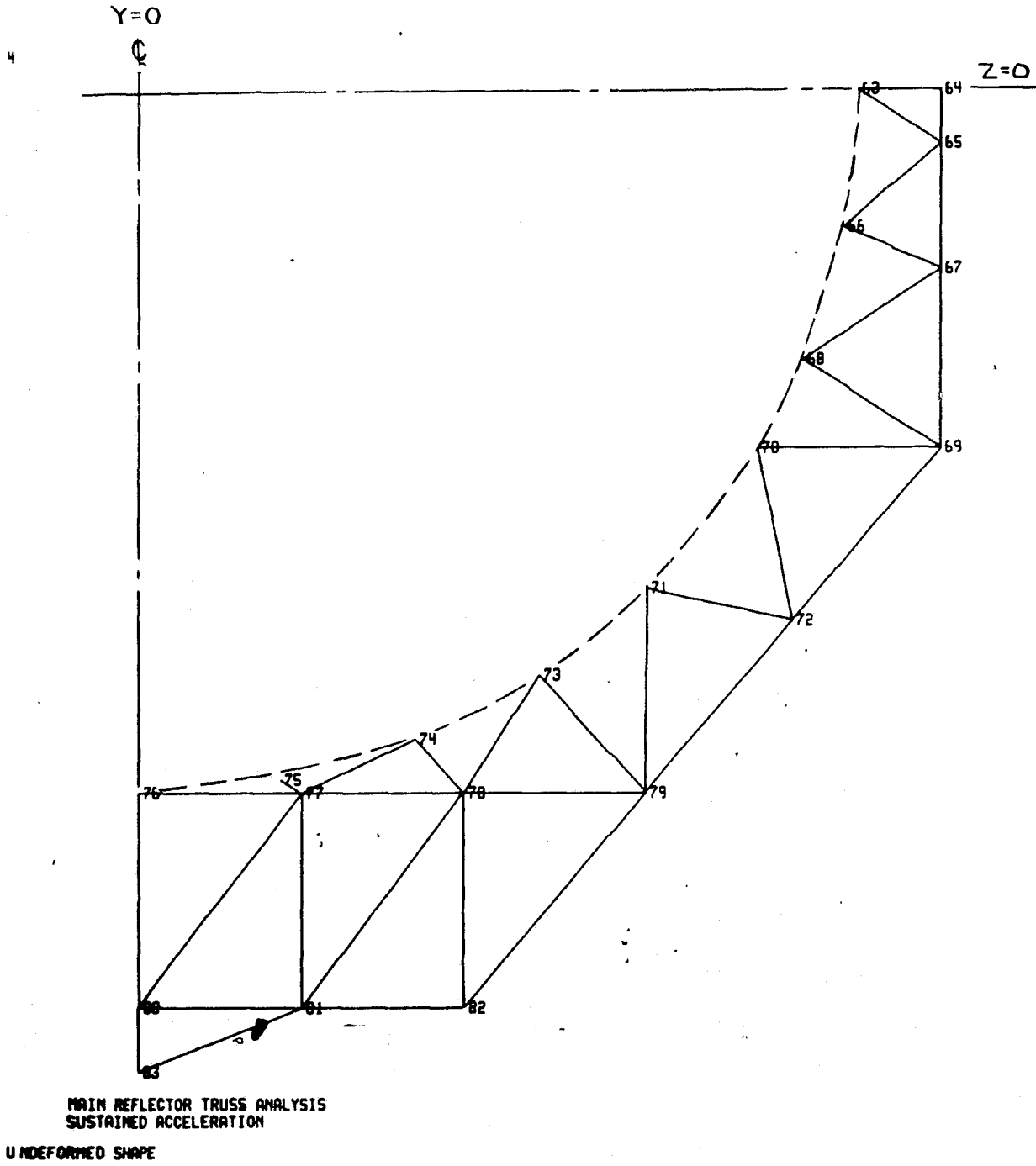
Figure 3-77. View C
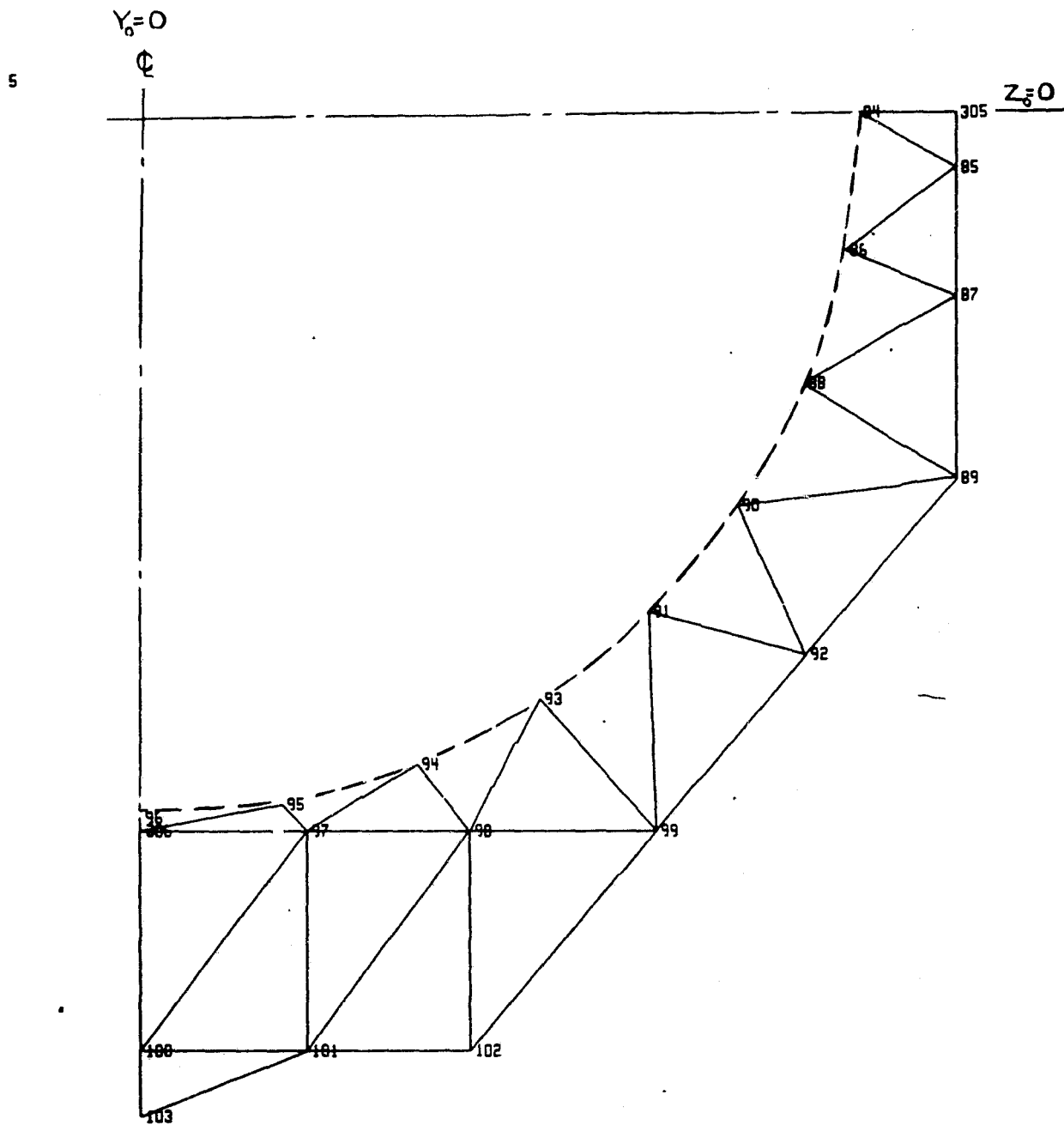
Figure 3-78. View D
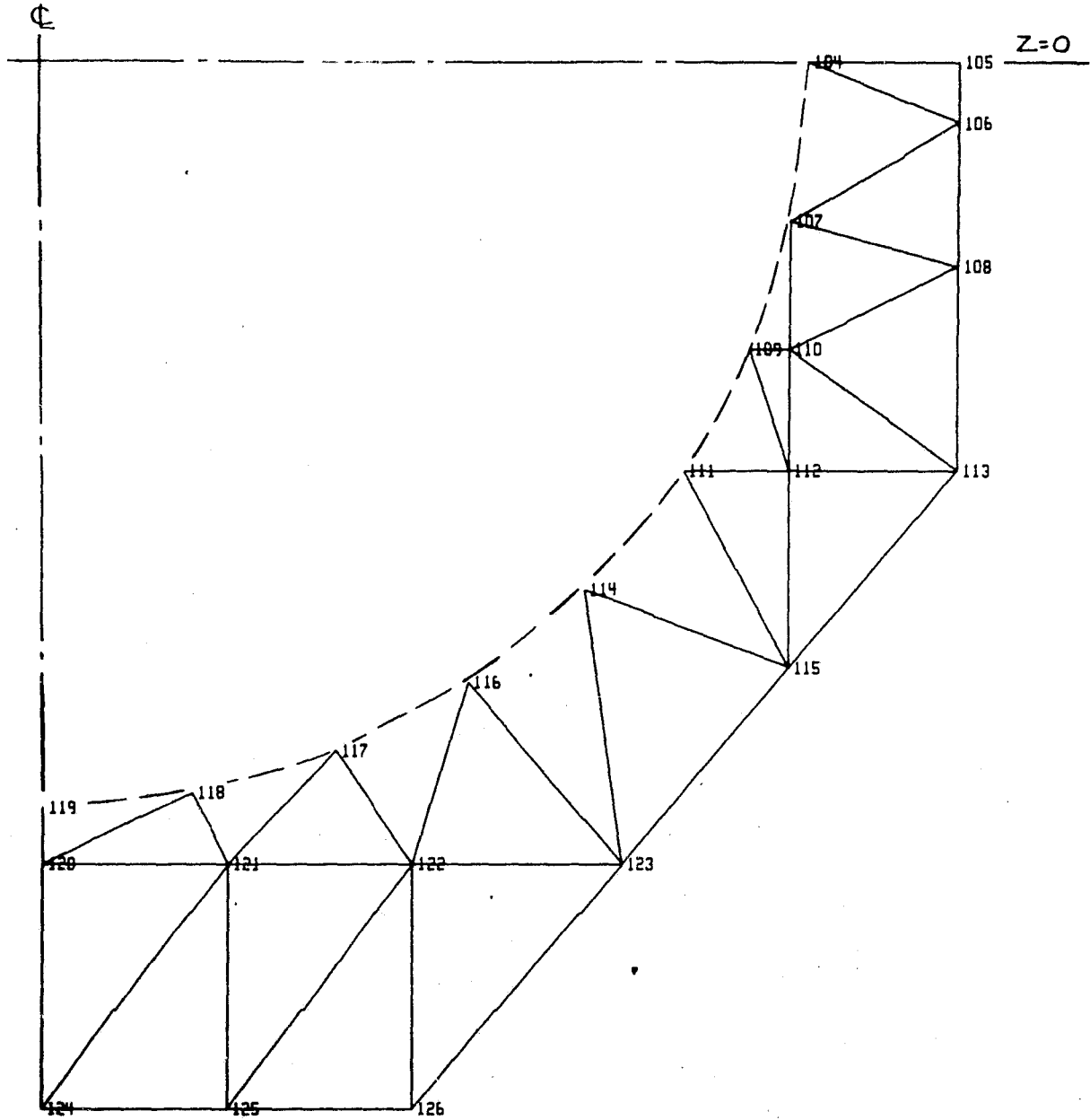
Figure 3-79. View E
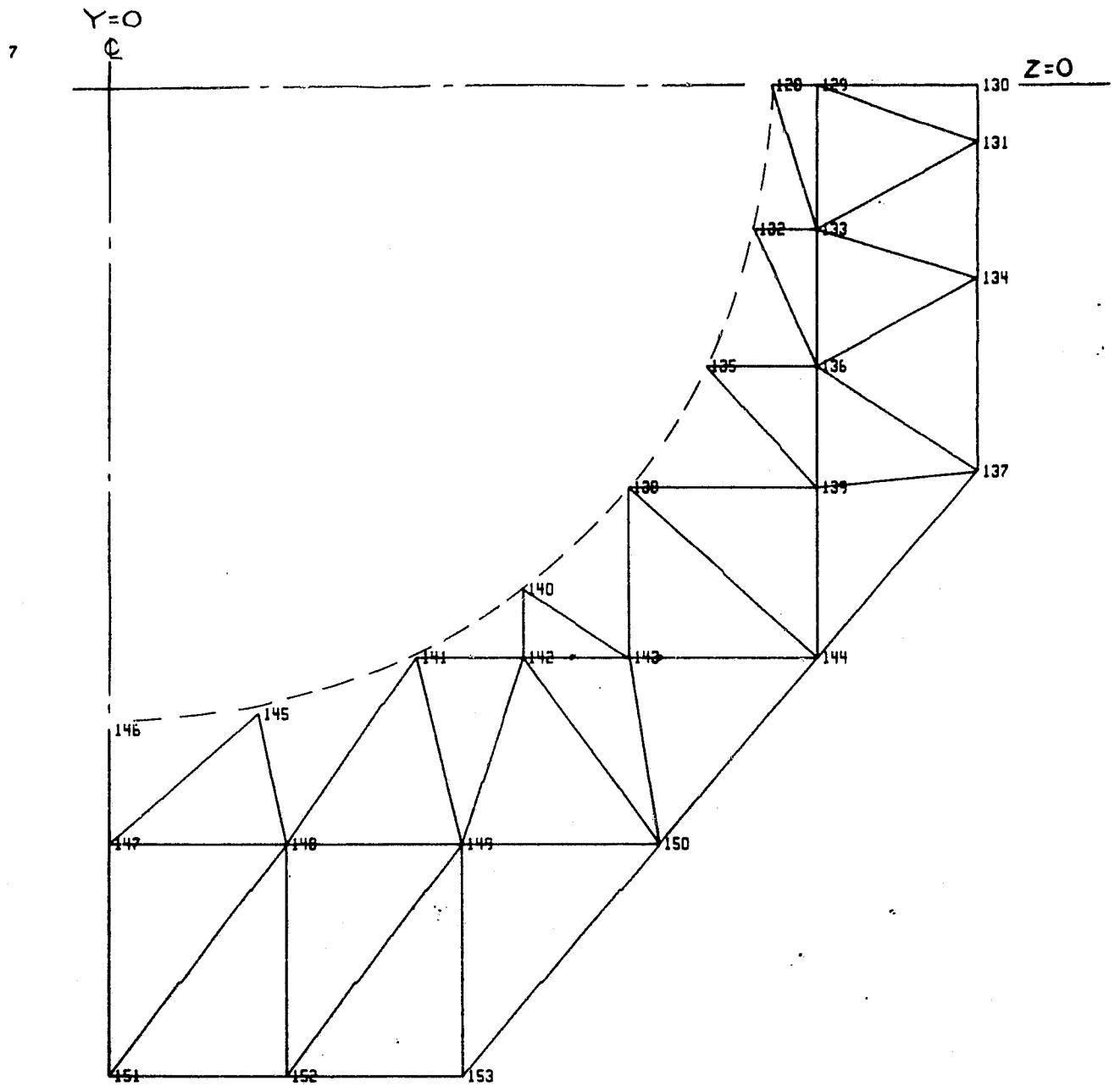
MAIN REFLECTOR TRUSS ANALYSIS
SUSTAINED ACCELERATION

UNDEFORMED SHAPE

Figure 3-80. View F

MAIN REFLECTOR TRUSS ANALYSIS
SUSTAINED ACCELERATION

U NDEFORMED SHAPE

Figure 3-81. View G

MAIN REFLECTOR TRUSS ANALYSIS
SUSTAINED ACCELERATION

UNDEFORMED SHAPE

Figure 3-82. View H

MAIN REFLECTOR TRUSS ANALYSIS
SUSTAINED ACCELERATION
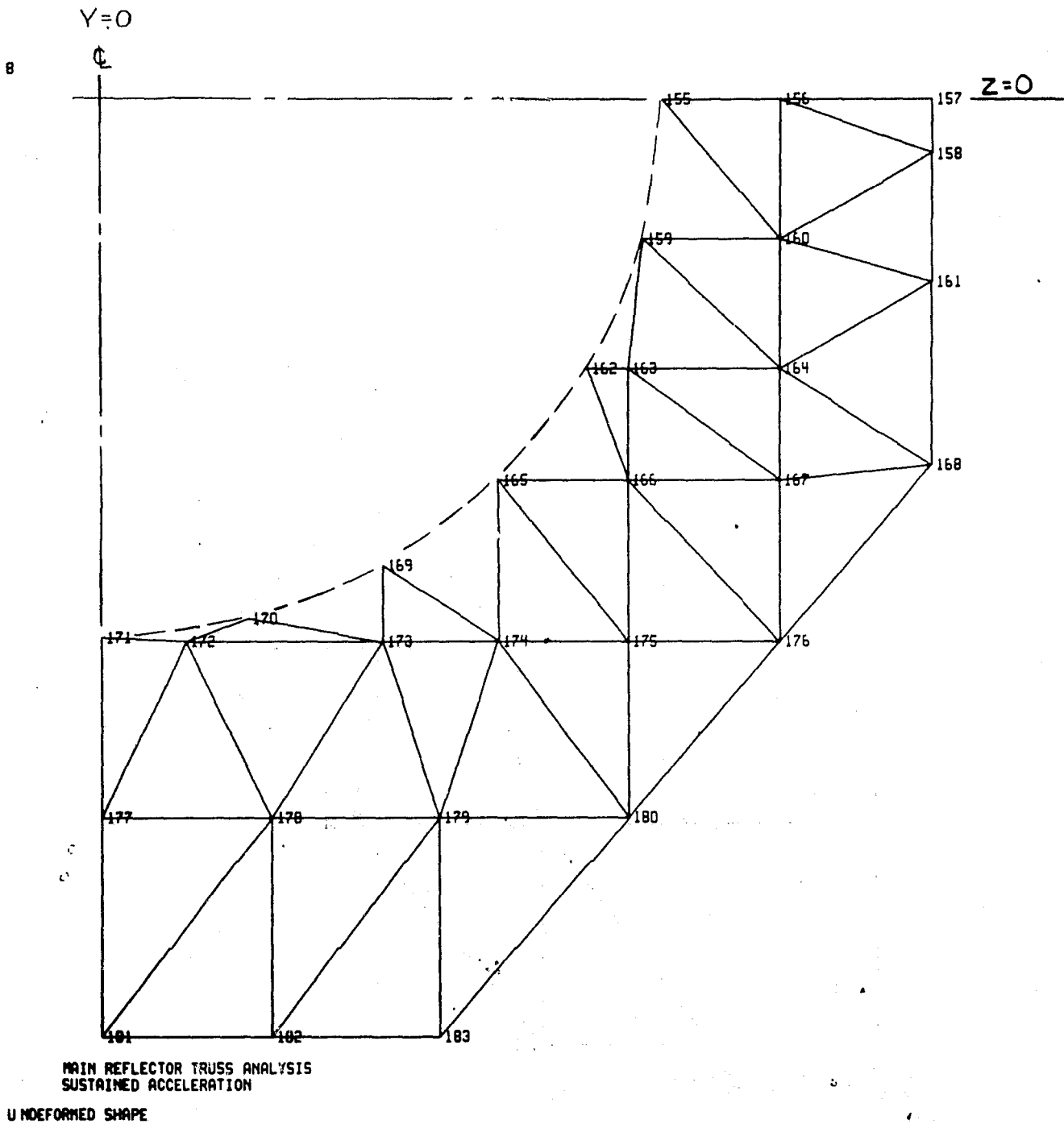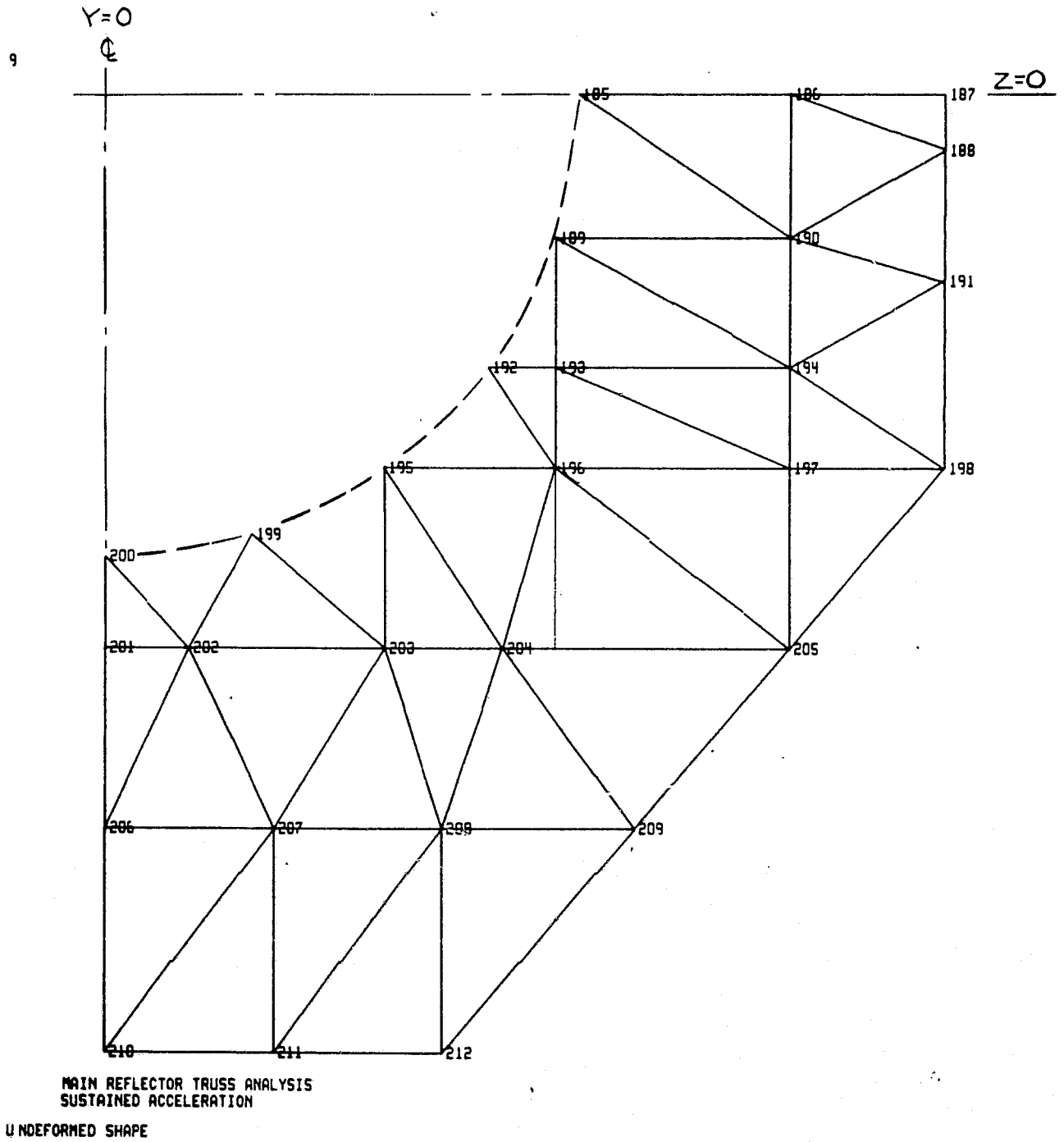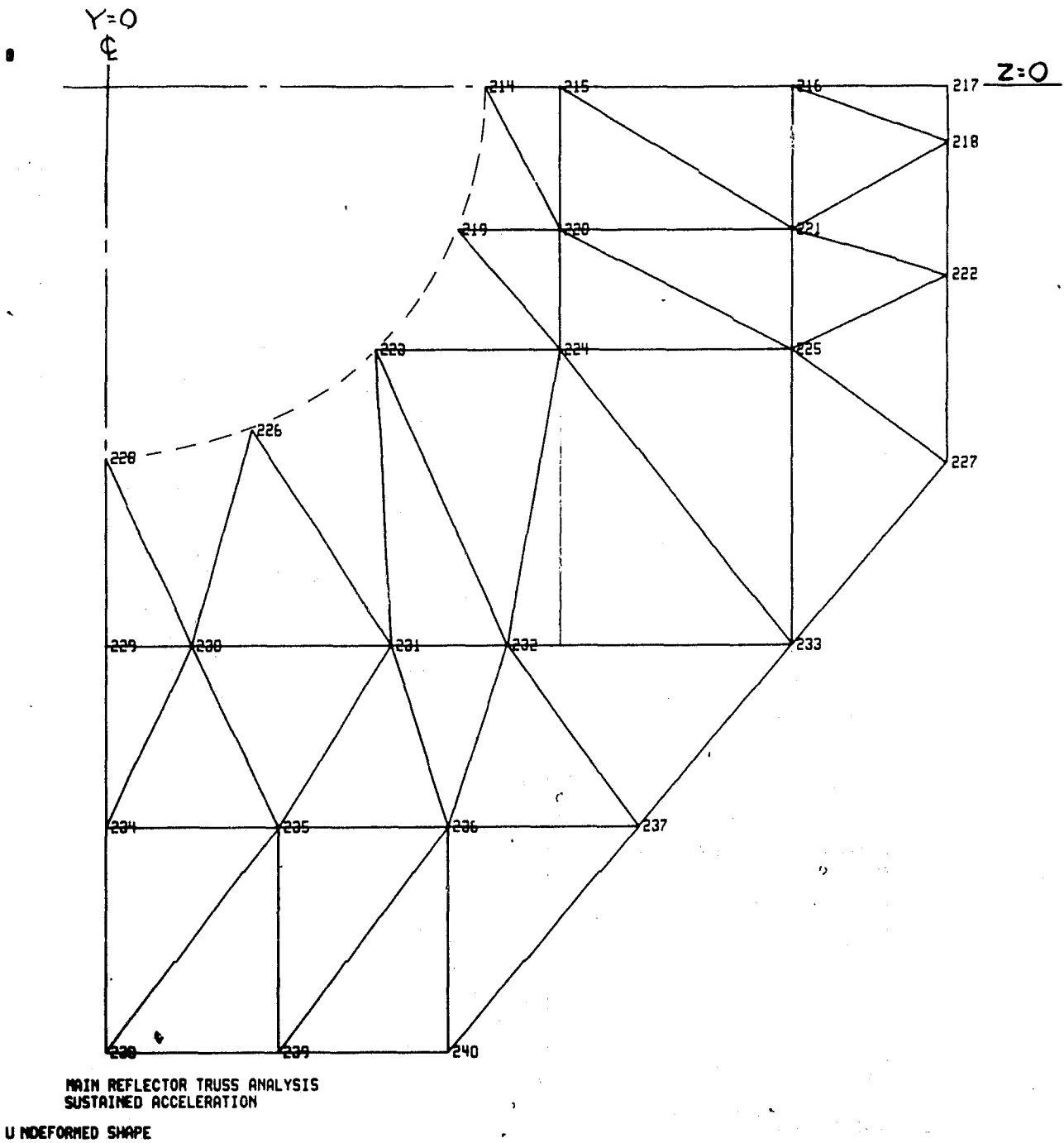
U NDEFORMED SHAPE

Figure 3-83. View J
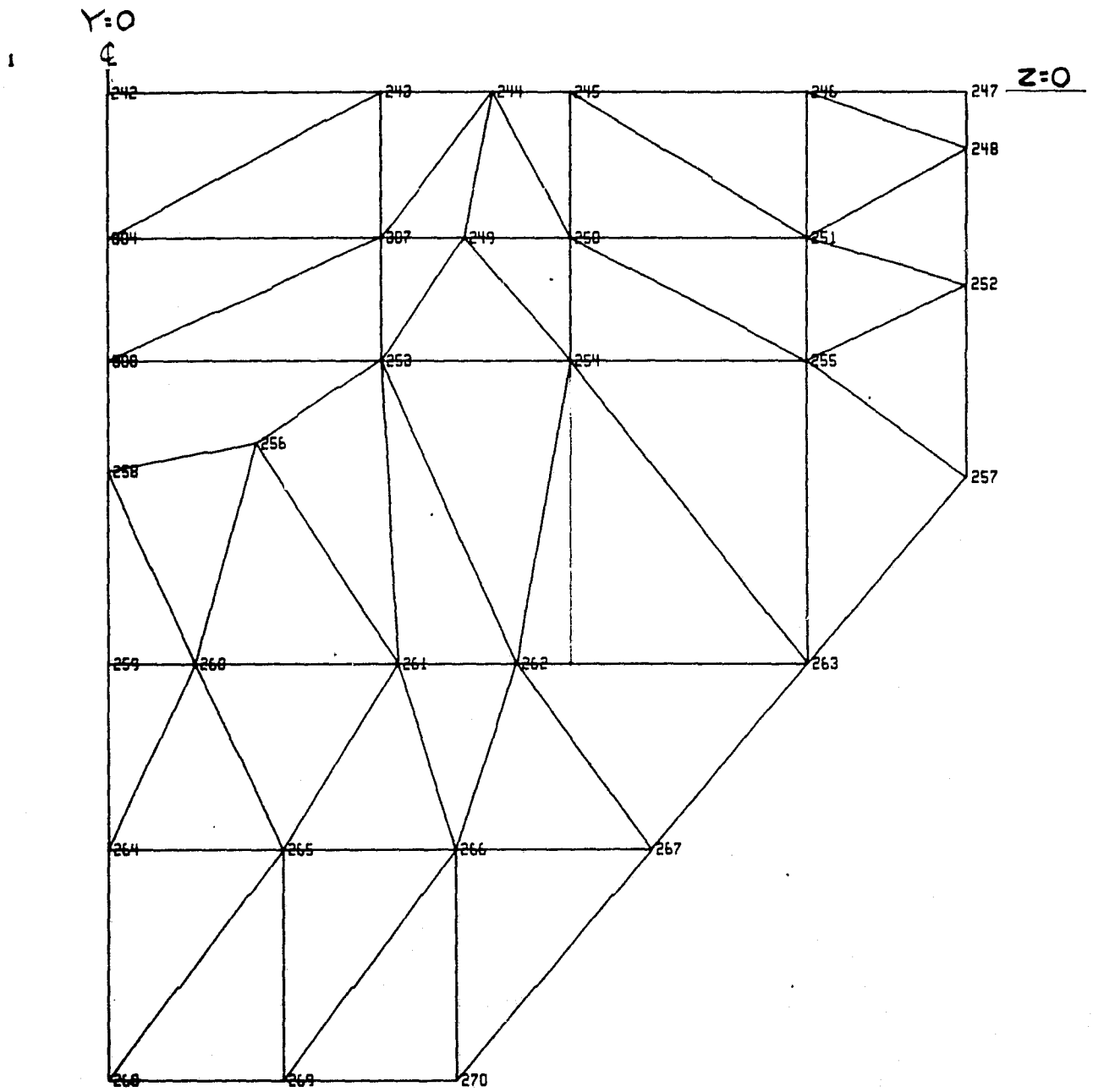
MAIN REFLECTOR TRUSS ANALYSIS
SUSTAINED ACCELERATION

UNDEFORMED SHAPE

Figure 3-84. View K
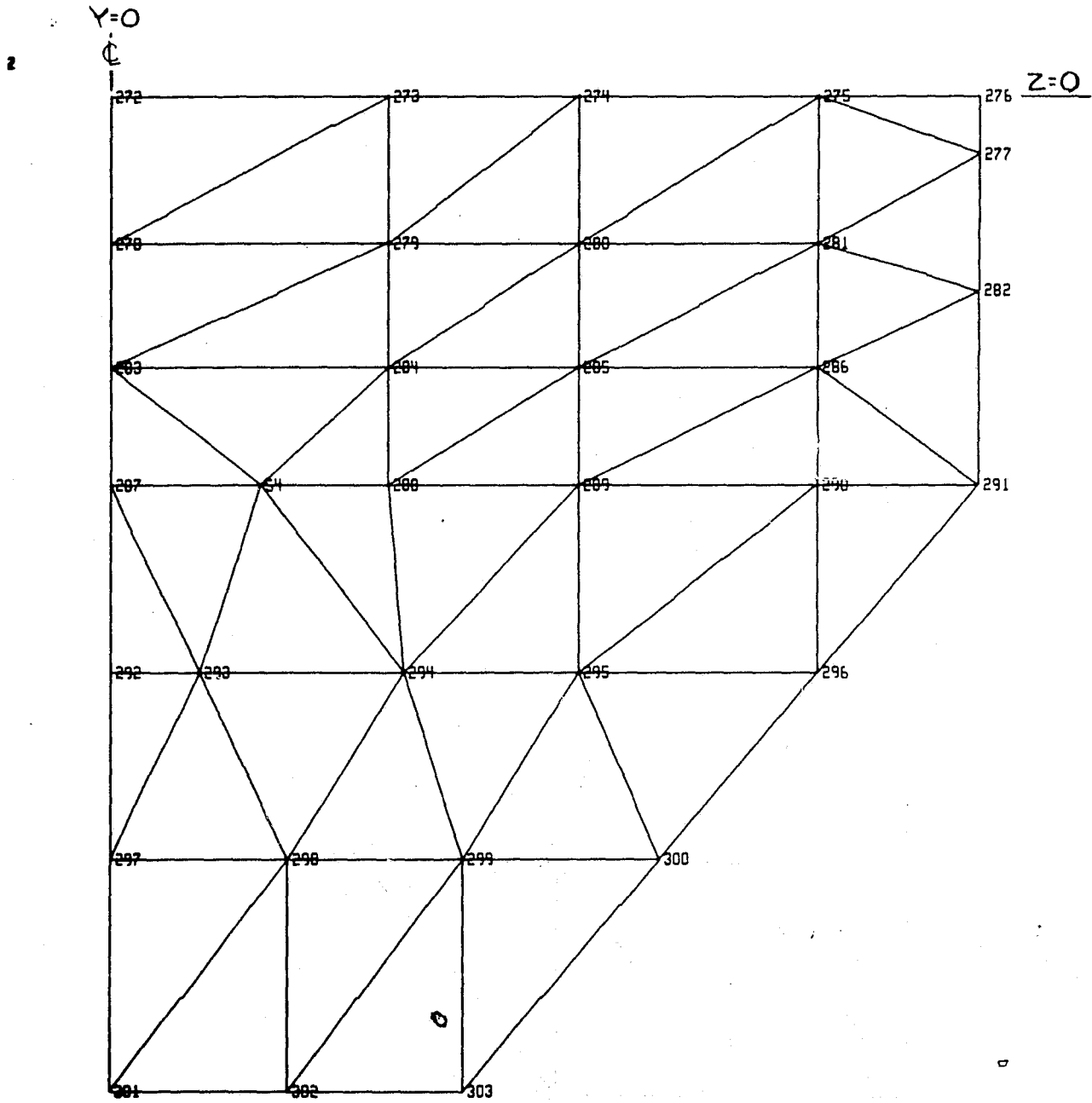
MAIN REFLECTOR TRUSS ANALYSIS
SUSTAINED ACCELERATION

U NDEFORMED SHAPE

Figure 3-85. View L
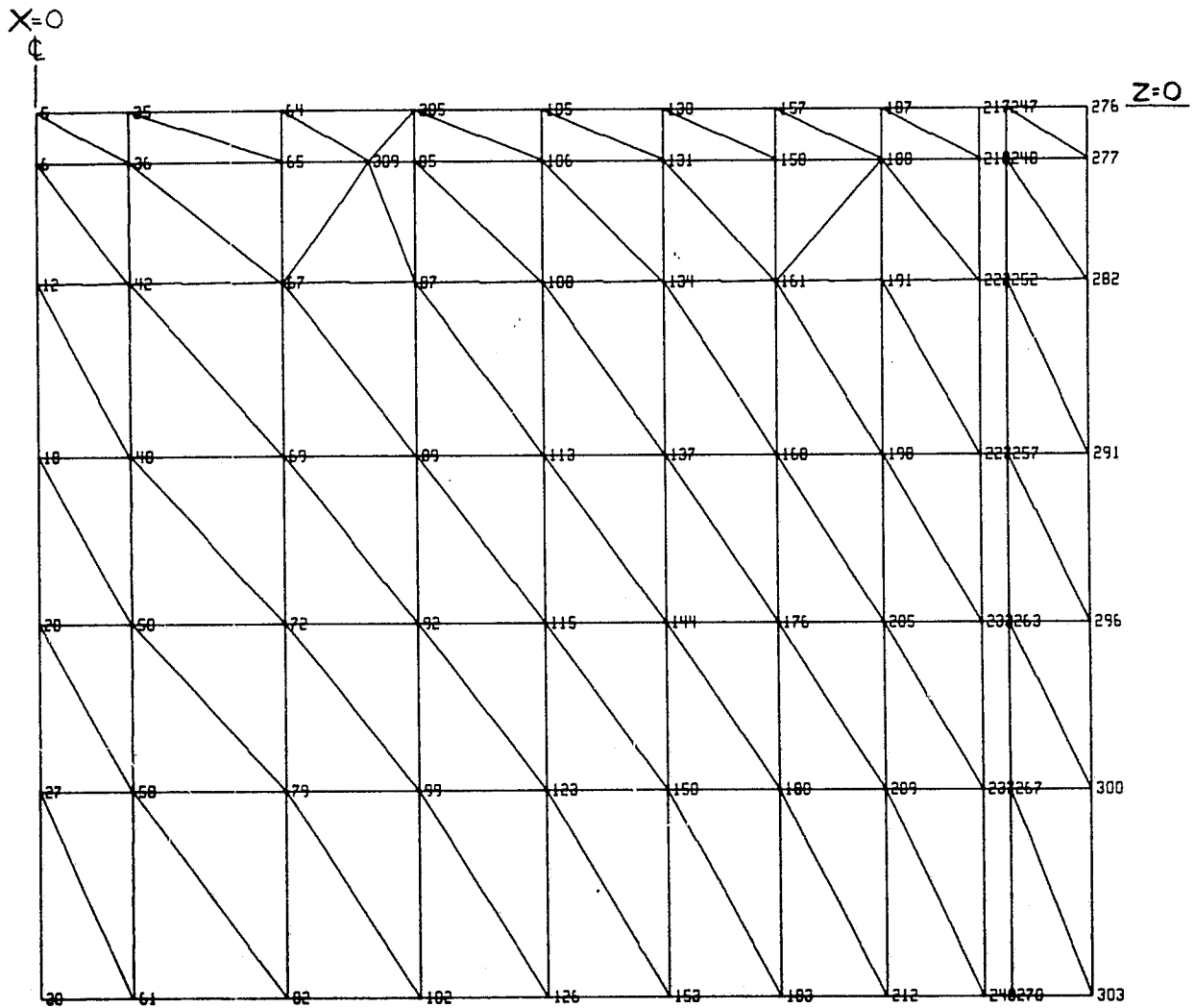
MAIN REFLECTOR TRUSS ANALYSIS
SUSTAINED ACCELERATION

U NDEFORMED SHAPE

Figure 3-86. View M
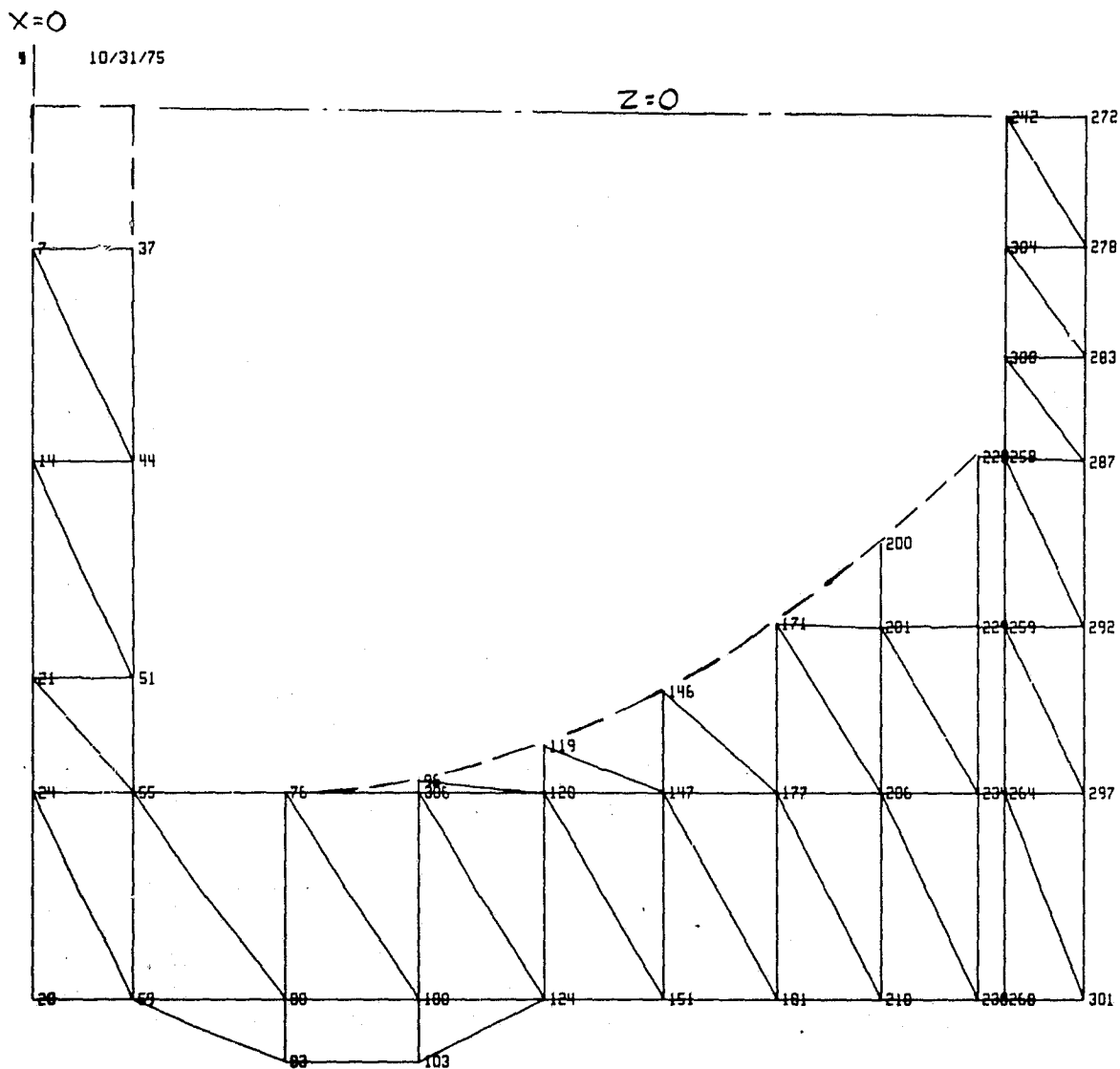
Figure 3-87. View N

Table 3-13. Stress Levels in High Stressed Elements

Element No. ①	Node Limits ①	Total Axial Stress psi ②	Bending Contributions psi ②
115	11-6	33,000	19,000
118	8-9	32,500	6,500
189	41-42	35,900	29,000
769	42-67	32,400	30,000
869	21-51	33,500	19,700
996	2-32	29,000	18,000
997	3-32	33,300	4,300
1002	35-63	32,300	24,000
1028	1-31	28,700	23,000

① Most elements can be located in Figures 3-74 through 3-87.

② Stress with double load for drive mechanism applied.

Table 3-14. Stress Levels in Low Stressed Elements

Element No. ①	Node Limits ①	Total Axial Stress psi ②
713	297-293	159
858	304-278	133
866	258-287	172
885	264-297	150
892	177-210	70
895	264-301	75
933	265-298	157
979	260-294	120
986	261-295	113
1068	289-262	132

① Most elements can be located in Figures 3-74 through 3-87

② Stress with double Load for drive mechanism applied.

Table 3-15. Stress Levels in Elements Around Trunnion

	Element No. ①	Mode Limits ①	Total Axial Stress psi ②	Bending Contribution psi ②
Primary Support	743	64-309	18,400	2,000
	752	65-309	24,900	7,000
	761	87-309	6,500	1,500
	838	85-309	10,400	6,000
	1056	305-309	3,500	300
	1058	67-309	4,200	2,200
Stabil- izing Support	464	187-188	3,600	1,900
	756	158-188	4,600	1,800
	757	218-188	6,800	2,600
	765	161-188	7,900	400
	766	222-188	3,000	1,000

① ② Plate element (relfector) No. 2016 bounded by nodes 86, 84, 107 & 104 had a maximum principle stress of 5100 psi.

① Most elements can be located in Figures 3-74 through 3-87

② Stress with double load for drive housing applied.

The results of the analysis indicated that a few truss members had negative margins of safety. These members were in the area of the structure that supports the drive mechanism and feed wheel assembly. Upon re-examination of the computer model, it was discovered that twice the mass of the drive mechanism and feed wheel assembly had been added to the structure. With the reduction of this mass to its actual value, the negative margins of safety would be eliminated. Additional examination showed that bending stress contributions in many elements were abnormally high (loads applied at nodes of ideal trusses produce only axial loads in the elements) and other elements were stressed so low they might well be eliminated if stability is maintained. The entire weight modeled was 818 lbs, of which 440 lbs was the concentrated load of the drive mechanism and feed wheel assembly (only 220 lbs should have been used). The remaining weight of 378 lbs is distributed between 1/2 of the reflector shell and truss structure, thus the total weight of the analytical main frame and reflector is 756 pounds.

This weight can be considered a maximum since the stress levels discussed indicate that lightening is certainly a possibility. It was previously mentioned that this configuration lends itself to the design of an efficient structure and it can be seen from the analytical results which elements are candidates for weight removal or addition in order to distribute the stresses uniformly. It is concluded from the results of the analysis conducted that the conceptual design of the main reflector and truss structure is structurally reliable to perform its intended purpose, although weight reduction and optimization of stress distribution could be achieved with additional analysis.

Tolerance and Fabrication Techniques

The tolerance of the reflector surface is an RF performance parameter, determined in section 3.1 to be 0.003 inch rms. The tolerance on dimensions between retention fittings is not currently defined, but since the 4-point retention system prevents shuttle motions from inducing distortion of the payloads, it is expected they will not be severe.

The methods of fabrication using advanced composites such as graphite-epoxy are well developed and several companies have broad experience in the design and fabrication of both space and terrestrially oriented hardware incorporating this material.

An informal specification for the SIMS-A reflector/main frame was prepared and submitted to several of these companies for the following reasons:

1. This structure represents the single predominating item in all cost considerations, therefore it was desired that as many conceptual design configurations as possible be considered.

2. A good response would better define the problem areas to be encountered in fabrication.

3. Advance knowledge of a program such as SIMS-A by potential fabricators can prove beneficial to the program as interest is generated.

4. To secure, as a benefit to SIMS-A, the experience in advanced composites of those companies responding.

Two responses to the informal specification were obtained:

1. Shuttle Imaging Microwave System (SIMS)

   Main Reflector

   A report to Rockwell-International
   29 October, 1975
   from: General Dynamics
         Convair Aerospace Division
         San Diego, CA 92112
   (Appendix C)

2. Technical Description of SIMS-A Antenna

   October, 1975
   from: Rockwell-International, Inc.
         Tulsa Division
         Mingo Facility
         Tulsa, OK 74151
   (Appendix D)

The two responses appear in the noted appendices. It was not intended that the multiple configurations represent any kind of design competition. The companies solicited were informed that a response would be considered indicative of their interest in SIMS-A.

Potential Problem Areas

Some areas which will require additional investigation or analyses are given below:

1. Selection of reflective coating

2. Method of deposition of coating

3. Contour adjustment devices

4. Establish surface finish requirements

5. Facilities for performing environmental tests

6. Venting of honeycomb or closed structures if used

7. Moisture control

3.2.3 Feed Wheel and Sub-Reflectors

Initial Feed Wheel Configuration and Sub-Reflector Material Tradeoff

Dimensions based on initial calculations of the subreflector contours were used to establish the feed arrangements considered. Calculations of scan time were made from the following equation

$$t_s = \frac{hN \Delta\theta}{\nu_s} = 46.448 \ N\Delta\theta \tag{71}$$

where

t_s = scan time required for the feed assembly to complete one revolution

h = height of orbit = 340 KM

N = effective number of feeds

= $\dfrac{360°}{\text{largest angle of rotation between successive feeds of the same frequency (}^0\text{)}}$

$\Delta\theta$ = 0.10259° = 0.00179 radian (initial Beamwidth used)

ν_s = shuttle speed = 7.32 KM/sec.

The calculated value of t_s for 118.7 GHz (the critical frequency for determining rotation speed), with $N = 1$, was 0.0831669 second and

$$f = \frac{1}{t_s} \text{ (revolutions per second)}$$

or

$$f = 12.024 \text{ rps} = 721.44 \text{ rpm}$$

and

$$\omega = 2\pi f = 75.55 \text{ rad/sec}$$

for a frequency of 118.7 GHz. Several configurations of feed arrangement were considered, the largest angle between multiple feeds was determined for each of them and N was determined for 118.7 GHz. Actual speeds were calculated from

$$f_{ACTUAL} = \frac{f_{(N=1)}}{N} \quad \text{or} \quad \omega_{ACTUAL} = \frac{\omega_{N=1}}{N} \tag{72}$$

Accelerations were calculated from

$$a = \frac{r \, (\omega_{ACTUAL})^2}{9.8} \tag{73}$$

where

a = acceleration in g's

r = radial distance to sub-reflector C.G. ≈ 1.01 M.

All of the initial feed configurations had values of N (at 118.7 GHz) ranging from three to four and produced accelerations at the sub-reflector from 65 g down to 37 g. All of the initial configurations were rejected and replaced with a configuration having $N = 2$. The change was made in the interest of reducing the number of radiometers thus reducing the overall system cost. Material tradeoff studies for the sub-reflector had already been conducted prior to the change using the 38.15 g acceleration ($N = 3.926$, $\omega = 19.16$ rad/sec) of one of those initial configurations. The results of the studies were shown to be useful even after the change in configuration was made. The approach taken in the initial tradeoff studies follows:

The sub-reflector must withstand both thermal and inertial loads with minimum distortion. Inertial loading will predominate in producing distortion of the sub-reflector surface. The material selected should have a high flexural modulus-to-density ratio and also a coefficient of thermal expansion which closely matches that of the wheel structure. One of the materials considered was a honeycomb sandwich using glass-reinforced polyimide resin facings and core material. Since the deflection equation for sandwich construction has two terms and the equation for deflection of homogeneous materials has only one term, it was difficult to compare the two types with a single

parametric relationship. In order to present comparative information, a flat sandwich cantilever sample beam representing a one inch slice through the sub-reflector center was designed to produce a deflection of less than 0.005 inch (the same section within a doubly curved surface would not deflect as far). See Figure 3-88 for the relationship of the sample beam to the spinning disc.

From Hexcel, <u>Honeycomb Sandwich Design</u>, Brochure "E," pp. 7 and 9 (symbols partially changed)

$$\delta = \frac{q\ell^4}{8D} + \frac{q\ell^2}{2t_c G_c} \tag{74}$$

$$D_{approx} = \frac{E_f t_f t_c t}{2\lambda_f} \text{ per inch of beam width} \tag{75}$$

where

δ = deflection, inch

$q = wN_g$ = load, psi

w = beam weight per inch

ℓ = beam length, inches

G_c = shear modulus of core, psi

E_f = modulus of elasticity, psi

t_f = facing thickness, inch

t_c = core thickness, inch

t = total thickness, inch

$\lambda_f = (1 - \mu)^2$ where μ is Poisson's ratio

N_g = Number of g's acceleration

Polyimide facing weight was 6.59×10^{-5} lb/mil/in^2; 6 lb/ft^3 polyimide core weight was 3.47×10^{-3} lb/in/in^2

$E_f = 3.5 \times 10^6$ psi $\qquad\qquad \ell = 6.4$ inch

$\lambda_f = 0.98$ $\qquad\qquad\qquad N_g = 38.15$ $\qquad\qquad$ (76)

$G_c = 15 \times 10^3$ psi

ROTATION
AXIS

FLAT CANTILEVER SAMPLE BEAM

APPROX 6.4-IN.

DISC WEB ($\mathbb{c}_L$ PASSES THROUGH REFLECTOR CG)

ACTUAL SUBREFLECTOR

SUBREFLECTOR CG

APPROX 40-IN.

LOAD, q   = wN_g

    w   = BEAM WEIGHT PER INCH

    N_g = NUMBER OF g's ACCELERATION

δ = MAXIMUM DEFLECTION

ℓ = 6.4-IN.
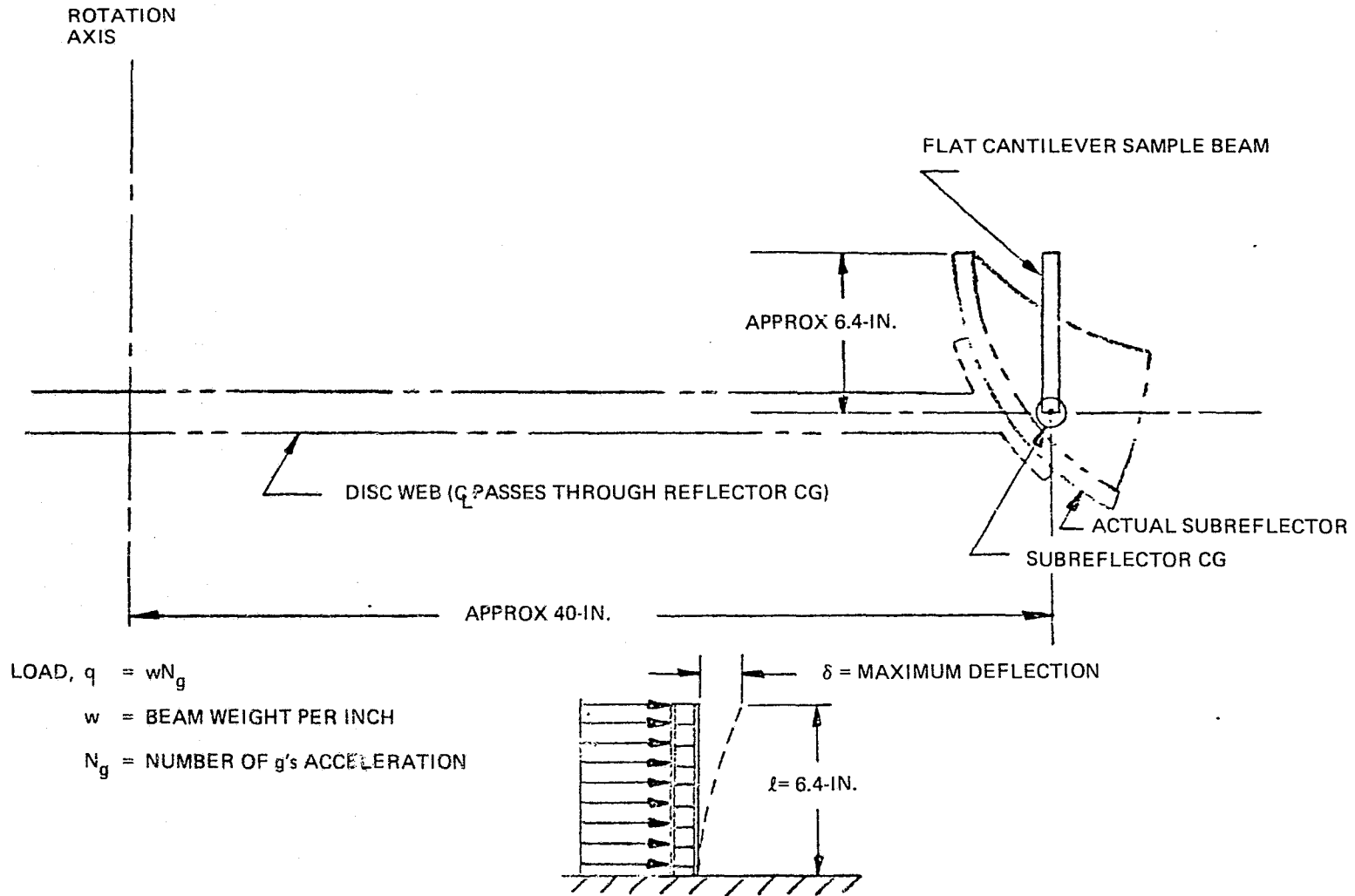
Figure 3-88.   Relationship of Beam Model to Disc Configuration for Initial Material Tradeoff

Reflective surface was 1 mil alum. = 9.72×10^{-5} lb/in^2. (alum. only in early analyses) A 0.50-in. thick sandwich consisting of 0.030-in. face sheets and 0.44-in. thick core produced a deflection of 0.0044 in. and weighed 0.0357 lb. Two comparisons were made between this sample beam material and that of homogeneous candidate materials. First, beams of homogeneous materials but with the same total weight were compared to the sandwich for deflection. For a one inch width beam to maintain the same weight, W, the thickness

$$t = \frac{W}{\zeta \ell} \tag{77}$$

where

t = thickness, inches

W = weight, lbs.

ζ = density, lbs/in^3

ℓ = length, inches

then

$$t = \frac{0.0357 \text{ lb.}}{\zeta \ (6.4 \text{ in.})} = \frac{0.00558}{\zeta} \text{in.}$$

The moment of inertia

$$I = \frac{bt^3}{12} = \frac{t^3}{12} \text{ (for 1-in. width)} \tag{78}$$

For a homogeneous cantilever beam

$$\delta = \frac{q\ell^4}{8EI} \tag{79}$$

where

δ = deflection, in.

$q = wN_g$ = load, psi

ℓ = length, in.

E = Modulus of Elasticity, psi

I = Moment of Inertia, in.^{4}

N_g = No. of g's acceleration

Equation (79) was used to determine the deflection of fixed weight (equal to sandwich beam weight) beams and the results were tabulated in Table 3-16 together with other pertinent data.

Table 3-16. Material Characteristics

Material	ζ (lb/in^3)	E (10^6 psi)	a (10^{-6} in/in/^{0}F)	Const. Wt. (0.0357 lb)			Const. δ (0.0044 in)			
				t (in)	I (10^{-5} in^4)	δ (in)	t (in)	I (10^{-5} in^4)	W Sample (lb)	W Reflector (lb)
Sandwich (Polyimide core and facings)	0.0112	3.5 (facing)	6.80	0.500	336.70	0.0044	0.500	336.7	0.0357	1.42
Beryllium	0.0670	44.0	6.40	0.083	4.80	0.0210	0.182	50.2	0.0780	3.11
Graphite-Epoxy (Solid)	0.0610	10.4 (isotropic)	<0.1	0.091	6.30	0.0660	0.358	382.4	0.1398	5.57
Aluminum	0.1070	10.6	13.70	0.052	1.17	0.3590	0.470	865.2	0.3219	12.83

Weights of beams which would produce the same deflection as the sandwich beam were also determined using:

$$t = \left(\frac{12q\ell^4}{8E\delta}\right)^{1/3} = \left(\frac{12\zeta\ell^4 \, N_g}{8E\delta}\right)^{1/2} \tag{80}$$

and

$$W = \zeta t\ell$$

with

$$\delta = 0.0044 \text{ in.} \tag{81}$$

The results of the weight comparison are also given in Table 3-16 with the equivalent total reflector weight based on an estimated 255 sq in. surface area.

The calculated data showed the sandwich construction merits the strongest consideration with respect to inertial loads. Cost analysis indicated the sandwich will be less costly than solid structures of beryllium or graphite-epoxy.

Beryllium has little if any thermal properties advantage over the sandwich and therefore was eliminated. Aluminum might prove the least costly but the high weight and high coefficient of thermal expansion were sufficient to eliminate it. The sandwich and solid graphite-epoxy remained as candidates. It is not necessary that the graphite-epoxy be as thick as shown since a truss structure of graphite-epoxy may be used to stiffen it (ultimately, a sandwich, using graphite-epoxy core and facings was selected). The assumption of a simple thick section was adequate for the tradeoff since it was retained as a candidate material.

Feed Wheel and Subreflector Final Configuration Selection

The feed wheel configuration shown in Figure 3-38 was selected as the final choice for SIMS-A, alternate 1. The wheel has $N = 2$ for 118.7 GHz which virtually doubled the speed of rotation over the initial candidates. Since inertial loading is proportional to the square of speed, the number of g s is increased by a factor of 4. Deflection in uniformly loaded beams is proportional to the fourth power of beam length, so the effect of shortening the sample beams previously discussed was studied. Deflection equations,

$$\delta = \frac{5\,wL^4}{384\,EI}$$
For a simple supported beam with span L. (83)

and

$$\delta = \frac{w\ell^4}{8\,EI}$$
For a cantilever beam of length ℓ. (84)

were set equal to each other and solved for ℓ in terms of L giving

$$\ell = 0.4705L \approx 0.5L \tag{85}$$

Figure 3-89 illustrates a double disc feed wheel configuration which has the effect of reducing the sample beam lengths to one-half their value when mounted on a single disc and which satisfies equation (85) for a reflector with overall height of 12.24 in.

When ℓ is replaced by $\ell/2$ in equation (85) the deflection is reduced by a factor of 16. Deflection was increased by a factor of four due to increasing the speed of rotation. The net effect of these two changes was to reduce the deflection of a sample beam to one-fourth its deflection when mounted on a single disc.
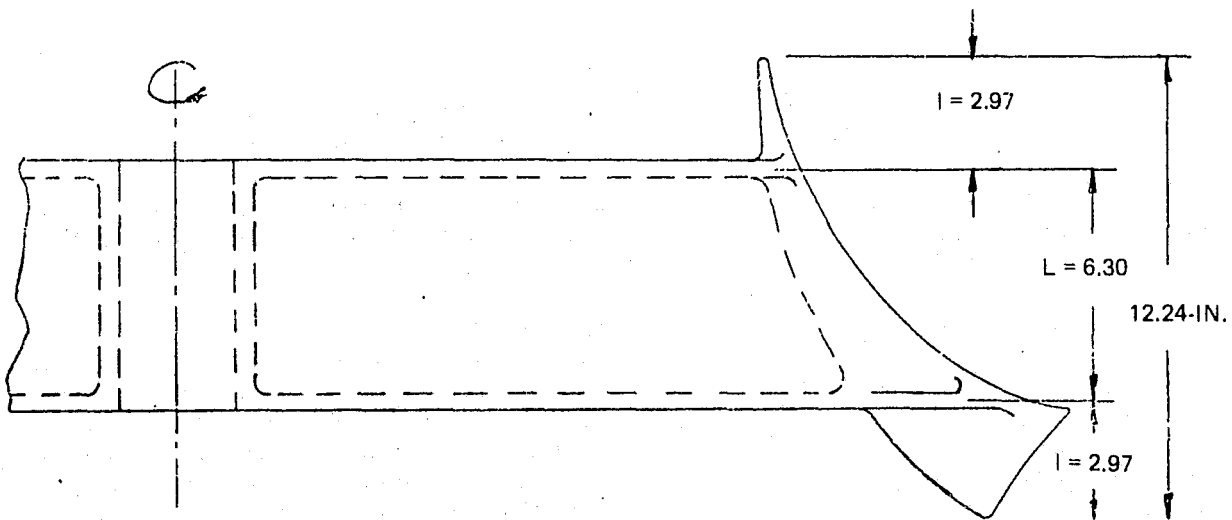
Figure 3-89. Dual Disc Reflector Support

Feed Wheel and Subreflector Final Material Selection

The wheel structure must expand or contract at the same rate as the main frame. If a material with a large difference in CTE is used and the system undergoes a large ΔT, the feed point on the periphery of the wheel will move by an unacceptable amount, thus defocusing the antenna. For example, a 1.0 meter radius feed wheel made from a material with a CTE of 6.0×10^{-6} μin./in./°F and the wheel axis supported by a main frame structure with a CTE of 0.1 μin./in./°F. Therefore, it was decided that mately 0.050 in. would occur. This is based on a fabrication temperature of 70°F and an orbital temperature of -148°F or a ΔT of -218°F. Therefore, it was decided that graphite-epoxy should also be used in the fabrication of the feed wheel structure. While researching various methods of fabricating the wheel from graphite-epoxy it was found that Hexcel Products, Inc., Dublin, Ca. has developed a 6.0 #/FT^3, 3/8 cell-size, honeycomb core made from graphite-epoxy. It is claimed that the material will be commercially available in the late 1970's at an anticipated ROM cost in that time frame of about $300/board ft.

The conceptual design drawing of the feed wheel and sub-reflector (CRB-751007), Figure 2-9 (2 sheets) was prepared, incorporating graphite-epoxy sandwich construction extensively.

The final value for the antenna beamwidth at 118.7 GHz was established at 0.1142 deg or 0.00199 radian. This resulted in a calculated t_s = 0.09259 second.

$$f_{(N=1)} = \frac{1}{t_s} = 10.8 \text{ rps} \tag{86}$$

$$f_{(ACTUAL)} = \frac{f_{(N=1)}}{N} = 5.4 \text{ rps} = 324 \text{ rpm} \tag{87}$$

$$\omega_{(ACTUAL)} = 2\pi f_{ACTUAL} = 33.93 \text{ rad/sec} \tag{88}$$

The acceleration at the subreflector was determined using a 0.91 meter (36 in.) radius for the C.G. location instead of the 1.01 meter used in previous analyses. A completed layout indicated the smaller figure was more accurate.

$$a = \frac{r(\omega)^2}{g} \approx 107 \text{ g} \tag{89}$$

A new sample sandwich beam with the shorter length (2.97 in.) derived from Figure 3-89 was analyzed for deflection. The design parameters were:

Facings: Graphite-epoxy 0.063 in.

$$E = 15.4 \times 10^6 \text{ psi (isotropic)}$$

$$\rho = 0.061 \text{ lb/in.}^3$$

$$\lambda = 1 - \mu^2 \approx 0.98$$

Core: Graphite-Epoxy 0.625 in. thick

                      3/8 in. cell size, 6 lb/ft^3 density

                      G_c = 50,000 psi
                              w direction

Total Sandwich: 0.751 in. thick

                      w = 0.0098 lb/in. + plating allowance

                      $\omega \approx$ 0.010 lb/in.

Total deflection of the graphite-epoxy sandwich beam is less than 0.0003 in. due to inertia load of constant angular rotation. The weight of the sandwich panel part of each reflector is about 2.33 lb and the attachment ribs, etc., weigh about 1.85 for a total of approximately 4.4 lb.

Analyses on the feed wheel were based on the dimensional data on the drawing (CRB-751007) and weights of:

1. 75 lb for wheel structure

2. 4.4 lb for each reflector

3. 1.8 lb for each power supply

4. 2.4 lb for each radiometer

5. 3.8 lb for each low frequency array

6. 16.0 lb for each feed support ancillary

7. 15.0 lb for all feeds

Total weight is approximately 290 lb. The wheel was analyzed for centrifugal loading due to the 33.93 rad/sec^2 rotation of the wheel and a 1 g load normal to the wheel.

For the centrifugal loading condition the outboard (away from drive shaft) disc was analyzed. For this analysis the disc was considered to be a solid isotropic material and an "effective" modulus of elasticity and thickness were determined in accordance with Paragraph 3.1.5 of ANC-23[12]. The maximum radial and tangential stresses in the disc were calculated according to Roark[13].

The maximum radial and tangential stresses in the disc were determined to be 48.3 psi and 123 psi, respectively. Due to these low stress levels it was concluded that the other components of the wheel would also be structurally adequate.

For the normal loading condition the radial ribs were analyzed to determine the maximum deflection of the wheel. The ribs were considered to be cantilevered beams supported at the hub with the weight of the wheel evenly distributed along their length. Each rib was assumed to support one-eighth of the total weight of the wheel. The ribs were also considered to be a solid isotropic material and "effective" modulus of elasticity and thickness were determined. Also an effective section of the outboard and inboard discs were also included in determining the moment of inertia of the ribs. The maximum deflection of the unsupported end of the beam was found to be 0.0017 in.

From this analysis it was concluded that the conceptual design of the feed wheel was structurally reliable for the specified environmental conditions. The analyses are shown below.

Outboard Disc

For this analysis the sandwich panel was considered to be a solid isotropic material. For this assumption, "effective" values of modulus of elasticity and thickness were used. (Ref Para 3.1.5 of ANC-23, "Sandwich Construction for Aircraft.")

$$E_e = \frac{H}{2\sqrt{3\lambda_f \, D/H}} \tag{90}$$

$$t_e = 2\sqrt{3\lambda_f \, D/H} \tag{91}$$

where:

$$\lambda_f = (1 - \mu_f^2) \cong 0.98 \tag{92}$$

$$D = \frac{E_f}{12\lambda_f}(t^3 - t_c^3) \tag{93}$$

$$H = E_f (t - t_c) \tag{94}$$

$$E_f = 15.4 \times 10^6 \text{ lb/in.}^2$$

$$t = 0.437 \text{ in.}$$

$$t_c = 0.375 \text{ in.}$$

$$D = \frac{15.4 \times 10^6 \text{ lb/in}^2}{12 \, (0.98)} \left[(0.437)^3 - (0.375)^3 \right]$$

$$= 40,227 \text{ lb-in.}$$

$$H = 15.4 \times 10^6 \text{ lb/in.}^2 (0.437 - 0.375)$$

$$= 954,800 \text{ lb/in.}$$

$$E_e = \frac{954800}{2\sqrt{3\ (0.98)\ 40227/954800}}$$

$$= 1.356 \times 10^6 \text{ lb/in.}^2$$

$$t_e = 2\sqrt{3\ (0.98)\ 40227/954800} = 0.704 \text{ in.}$$

Centrifugal Loading (Ref. Roark, Chap. 15, Case 8)

Radial tensile inertia stress, S_r

$$S_r = \frac{3+\mu}{8}\ \frac{w\ \omega^2}{386.4}\left(R^2 + R_o{}^2 - \frac{R^2\ R_o{}^2}{r^2} - r^2\right) \tag{95}$$

where:

μ = Poisson's ratio $\cong 0.14$

w = Density

ω = 33.93 rad/sec

R = 35.5 in.

R_o = 4.0 in.

r = Distance from center to point where stress is to be determined

Tangential tensile inertia stress, S_t

$$S_t = \frac{1}{8}\ \frac{w\ \omega^2}{386.4}\left[(3+\mu)\left(R^2 + R_o{}^2 + \frac{R^2\ R_o{}^2}{r^2}\right) - (1+3\mu)\ r^2\right] \tag{96}$$

For this analysis it is assumed that the weight of the disc, the weight of the power supplies, and the weight of one-half of the radiometers are evenly distributed throughout the disc

$$W_T = W_D + W_{PS} + \frac{1}{2}\ W_R \tag{97}$$

$$= 18.2 + 57.7 + 38.6 = 114.5 \text{ lb}$$

$$w = \frac{W}{At} = \frac{114.5}{\pi\ (\overline{35.5}^2 - \overline{4}^2)\ (0.704)} = 0.0416 \text{ lb/in.}^3$$

Max radial inertia stress occurs at $r = \sqrt{RR_o}$

$$S_{r_{MAX}} = \frac{3 + \mu}{8} \frac{w \, \omega^2}{386.4} (R - R_o)^2 \tag{98}$$

$$= \frac{3.14}{8} \frac{(0.0416) \, (33.93)^2}{386.4} (35.5 - 4.0)^2$$

$$= 48.3 \text{ lb/in.}^2$$

Max tangential inertia stress occurs at $r = R_o$

$$S_{t_{MAX}} = \frac{1}{4} \frac{w \, \omega^2}{386.4} \left[(3 + \mu) R^2 + (1 - \mu) R_o^2 \right] \tag{99}$$

$$= \frac{1}{4} \frac{(0.0416) \, (33.93)^2}{386.4} \left[3.14 \, (35.5)^2 + 0.86 \, (4.0)^2 \right]$$

$$= 123 \text{ lb/in.}^2$$

1g Load Normal to Plane of Wheel

Assume that this load is reacted by the 8 radial ribs which act as cantilevered beams anchored at the hub of the wheel
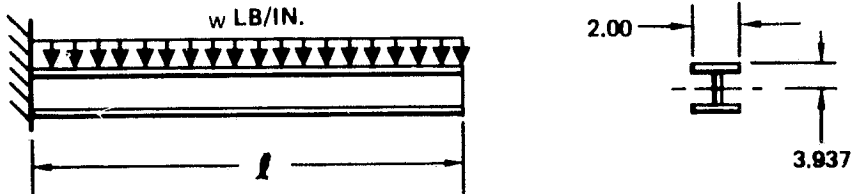
Assume solid material determine "effective" modulus of elasticity and thickness

$$E_e = \frac{H}{2 \sqrt{3\lambda_f D/H}} \tag{100}$$

$$t_e = 2 \sqrt{3\lambda_f D/H} \tag{101}$$

$$D = \frac{E_f}{12\lambda_f} (t^3 - t_c^3) \tag{102}$$

$$H = E_f (t - t_c) \tag{103}$$

$$E_f = 15.4 \times 10^6 \text{ lb/in.}^2$$

$$\lambda_f = 0.08$$

$$t = 0.81 \text{ in.}$$

$$t_c = 0.75 \text{ in.}$$

$$D = \frac{15.4 \times 10^6}{12 \, (0.98)} \, (0.81^3 - 0.75^3) = 143,479 \text{ lb-in.}$$

$$H = 15.4 \times 10^6 \, (0.81 - 0.75) = 924,000 \text{ lb/in.}$$

$$t_e = 2\sqrt{3 \, (0.98) \, 143479/924,000} = 1.35 \text{ in.}$$

$$E_e = \frac{H}{t_c} = \frac{924,000}{1.35} = 683,770 \text{ lb/in.}^2$$

$$\delta = \frac{w \ell^4}{8 E_e I_e}$$

$$w = \frac{286.5}{8 \, (25)} = 1.43 \text{ lb/in.}$$

$$I = \frac{1.35 \, (5.25)^3}{12} + 2 \left[2.0 \, (0.704) \, (3.937)^2 \right]$$

$$= 59.9 \text{ in.}^4$$

$$\delta = -\frac{1.43 \, (25)^4}{8 \, (683,770) \, (59.9)}$$

$$= -0.0017 \text{ in.}$$

An investigation into gyroscopic effects on the feed wheel was conducted from,

$$T_r = J \, \omega_r \, \omega_p \qquad \text{(reacted torque)} \qquad (104)$$

where

$$J = \text{wheel inertia} \approx 63 \text{ slug-ft}^2$$

$$\omega_r = \text{speed of wheel} = 34 \text{ rad/sec}$$

$$\omega_p = \text{pitch or yaw rate}$$

$$\approx 1°/\text{sec} \approx 0.01745 \text{ rad/sec}$$

$$T_r \approx 38 \text{ lb-ft}$$

The pitch rate due to orbit is

$$\omega_p = \frac{360 \text{ deg}}{1.55 \text{ hr x } 3600 \text{ sec/hr}} = 0.064°/\text{sec} = 0.00113 \text{ rad/sec}$$

which results in a constant yaw torque,

$$T_r = 2.4 \text{ lb-ft}$$

Both of the above values are very low with the high value being approximately equal to the bending moment induced into the wheel due to a 1 g gravity load normal to the plane of the wheel.

Deflection due to a temperature difference on opposite sides of the wheel can be determined from,

$$\delta = \frac{\Delta T \, \alpha \, L^2}{8t} \qquad , \qquad (105)$$

where:

· ΔT is the difference in temperature of faces separated by distance, t.

α = coefficient of thermal expansion

and

L is the undisturbed diameter of the wheel

$$\delta \approx \frac{\Delta T \, (0.1 \text{ x } 10^{-6}) \, (111)^2}{8 \, (6)}$$

$$\delta \approx 0.000026 \, \Delta T$$

A temperature difference of over 100°F would be required to deflect the wheel edge 0.003 in.

Fabrication Techniques and Potential Problem Areas

Fabrication with graphite-epoxy incorporates methods similar to those used in laminating with glass reinforced plastics. The primary difference is that in graphite-epoxy, the fabrication procedures are not standard or "shop practice" as in some other plastics, but instead, the procedures are specified in design. For example, contoured surfaces such as the subreflector are laminated from computer generated tiles of graphite reinforcement and the number of plies and their orientation would be specified on drawings. With other materials, choice of such parameters may be left to the shop.

Fabrication techniques are now well established for graphite-epoxy and the analytical tools used to define the parameters which result in a design meeting

specified structural requirements are fully developed. Therefore, the choice of materials and the physical arrangement of details forming the wheel results in a design which is structurally sound and physically attainable.

In preparing a final design consideration should be given to the following:

1. Provide adequate thickness in sandwich facings to prevent bearing failure at attachments.

2. Sub-reflector conductive surface (same as main reflector)

3. Early coordination with honeycomb core supplier to assure availability.

4. Shear pin requirements for all attached items to insure no movement from tested positions.

5. Methods for measuring deflections.

6. Techniques for preliminary alignment of sub-reflectors and feeds prior to RR tests.

7. Electrical cable feed-through from shaft to feed wheel.

8. Venting of honeycomb core or other closed structures.

3.2.4 Drive Mechanism

Several configurations of drive mechanization for SIMS-A were considered and a tradeoff of features is given in Table 3-17. The 2-pass helical gear train driven by a hysteresis synchronous motor was selected because the advantages stated are compatible with SIMS-A requirements.

The 8-in. diameter of the shaft was chosen arbitrarily in the early phases of the study because it would easily handle the largest loads that could be anticipated at that time and also because a large final drive gear could be installed on a large shaft without extending a great distance beyond the shaft diameter. The large diameter has been retained, which gives the shaft a high stiffness with 0.250 in. minimum thickness walls. The shaft is made from graphite-epoxy with fiber windings oriented to produce a coefficient of thermal expansion (CTE) equal to the CTE of the steel bearing races in the radial direction while having as low a CTE as possible in the axial direction in order to prevent defocusing due to temperature change. For the minimum properties section of the shaft,

$$I = \frac{\pi}{64} (d_o^4 - d_i^4) \tag{106}$$

$$I = \frac{\pi}{64} (7.00^4 - 6.5^4) = 30.24 \text{ in.}^4$$

$$E = 15 \times 10^6 \text{ psi} \quad \text{(estimated)}$$

Table 3-17. SIMS-A Drive Mechanism Tradeoff Study

Type of Drive	Advantages	Disadvantages
Motor/Belt/Pulley	Simplicity	Temperatures too low for belt materials Tension varies with temperature
Motor/Chain/Sprocket	Simplicity	Chain Links wear rapidly Inherent Backlash
Direct Drive Torque Motor	Simplicity (if available without development)	Should be D.C. Torque motor. Would require development to reach 324 rpm.
Low Speed Motor/Worm Gear Box	Low Cost (Standard Components)	Speed control not precise Worm gearing requires clutch for spin-down
Low Speed Motor/Helical Gear Box	Low Cost (Standard Components	Speed control not precise Helical gears produce thrust loads on shafts
High-Speed Hysteresis Synchronous Motor (motor pinion drives 28-inch dia spur gear)	Precise Speed Control *	Pitch line velocity too high >2400 ft/min) Lange gear has high inertia
High-Speed Hysteresis Synchronous Motor (motor pinion drives 2-pass spur gear train)	Precise Speed Control Less inertia *	Pitch line velocity still too high (with minimum dia pinion)
► High-Speed Hysteresis Synchronous Motor (motor pinion drives 2-pass helical gear train)	Precise Speed Control Smoother Operation Lower Pitch Line Velocity due to smaller pinion allowable, but helical gears can tolerate higher velocities. *	Helical gears produce thrust loads on shafts

► Selected Configuration

* Hysteresis Synchronous Motor Advantages
    Low noise and vibration
    Constant speed regardless of load and voltage variation
    Capable of synch on high inertia loads & uniform starting torque
    Will lock in at any position with respect to line voltage
    Available in 1/4 H.P. 3ϕ 2080 400 Hz with 80 in-oz start torque

The deflection of the free end of the shaft is determined from,

$$y = \frac{P a^2}{3 EI} (\ell + a) \tag{107}$$

where:

P = applied load

a = free end overhang $\approx$ 12 in.

ℓ = distance between bearings $\approx$ 8 in.

and spring rate,

$$K = \frac{P}{y} = \frac{(P) 3 EI}{(P) a^2 (\ell + a)} \tag{108}$$

$$K = \frac{(3) (15) (10^6) (30.24)}{(12)^2 (8 + 12)}$$

$$K = 472,500 \text{ lb/in.}$$

from which the deflection due to 1 g acting on the 290 lb (9 slug mass) wheel normal to the shaft axis is,

$$\delta = \frac{290 \text{ lb}}{472,500 \text{ lb/in.}} = 0.0006 \text{ in.}$$

and the critical speed

$$\omega_{CR} = \sqrt{\frac{K}{M}} \tag{109}$$

$$\omega_{CR} = \sqrt{\frac{472,500}{9}} = 299 \text{ rad/sec}$$

$$f_{CR} = \frac{\omega_{CR}}{2\pi} = \frac{229}{2\pi} = 36.4 \text{ rev/S}_e \tag{110}$$

$$f_{CR} = 2188 \text{ RPM}$$

The critical frequency is much higher than the 324 RPM speed of the feed wheel, and the 1 g deflection would permit testing the antenna with the wheel axis horizontal if it were expedient to do so. Therefore, the shaft design is structurally and functionally sound.

The drive shaft bearings are Kaydon (or equivalent) 8.00 I.D., 0.75-in. cross-section, angular contact type. The large cross section was selected because bearing

life is extended when the larger sizes are used. The maximum operating period of 30 days can be used to determine total revolutions for a single sortie, 14×10^6, but the number of sorties expected from one antenna is not known and the 0.75-in. bearing should provide a wide margin for expected service life. Angular contact was chosen because this type bearing is very tolerant of preload (which is anticipated) and is also capable of reacting against thrust loads caused by the helical gears. The reduction from motor shaft speed of 12,000 RPM to drive shaft speed of 324 RPM is accomplished in two passes through helical gears. See Table 3-18 for calculated data.

Helix angle on the gears will be selected in the final design to satisfy pitch line velocity requirements and produce minimal thrust. Helix angles will be oriented to prevent additive thrusts from the two meshes.

Gearing, bearings, shaft, and drive motor will be housed in a steel housing having the same CTE as bearings and gears.

Lubrication is to be a space qualified treatment developed by Ball Brothers Research Corp., Boulder, Colorado under the trade name Vac-Kote.

Some items to be considered in final design are:

1. Effect of different CTE between housing and main frame.

2. Thrust effects on motor torque requirements.

3. Optimum preload on bearings.

4. Helix angle and orientation.

3.2.5 Scan Drive Control

The three-phase, 400 Hz, synchronous motor was selected following consideration given to the several alternatives available. Other servo systems that may be considered include two-phase, 400 Hz, closed-loop servo, closed-loop dc servo, and a closed-loop about a dc torquer motor. Factors considered are available power,

Table 3-18. Gear Train Data

Gear	Type	Pitch Dia (inch)	No. Teeth	Size (Pitch)	Speed (RPM)	Pitch Line Velocity (ft/min)
1	Motor Shaft Pinion	0.6250	15	24	12,000	1963.50
2	Driven	3.0000	72	24	2,500	1963.50
3	Drive	1.5000	24	16	2,500	981.75
4	Driven (Output Shaft)	11.5625	185	16	324,324	951.75

system volume and weight requirements, and achievable accuracy. The advantages of a closed loop servo system are minimized when the drive requirement is a constant speed in one direction for a long period of time as is the case here. The dc torquer which can be mounted on the output shaft thus eliminating the gear train is worthy of consideration. Advantages being in control of the acceleration and deceleration phase and in the ability to position the output shaft, once stopped, at a specific location where a holding pin can be engaged to lock the shaft. A brush-type dc torquer would not be preferred. A brushless type dc torquer of sufficient torque rating and capable of operating at the required speed would have to be developed. An accuracy of better than 0.5 percent could be attained using the rate of change of the encoder output as a closed loop control. However, the system complexity required for the dc torquer system indicates that the synchronous motor is preferred.

The selection of the natural binary, optical encoder was primarily based on the beam position accuracy requirement and equipment availability. The beam position accuracy is specified to be 0.3 beamwidth. At 118.7 GHz the beamwidth is 0.115 deg so the encoder accuracy should be 0.0345 deg or about 1 part in 10,000. This is slightly greater than 2^{13}. A search for an encoder showed that none are available with greater than 2^{13} resolution at the speed of operation (324 rpm). Therefore the resolution at 118.7 GHz will be 0.04 deg. A suitable sensor alternative would be a magnetic rather than an optical device. Also considered was the synchro and synchro-to-digital converter, however resolution achievable at this speed seems to be limited to 2^{12} and so were eliminated.

C75-664/034A

4. TEST PLAN CONSIDERATIONS

4.1 ELECTRICAL TESTS

There are several unique characteristics of this antenna which make its RF evaluation somewhat extraordinary. These aspects are discussed below.

4.1.1 Static vs Dynamic Test

Dynamic deflections at the design rotation speed are calculated to be relatively small. Consequently, a static test is sufficient to prove the performance of the antenna, and a system level dynamic test against radiometric point sources would prove the performance does not change with the wheel rotating at its design speed. One way to prove the dynamic antenna performance would be to compare the static antenna patterns to oscilloscope traces which represent the radiometer response as the beam sweeps through a point source. Only static tests will be discussed in this section.

4.1.2 Antenna Range Setup

The range length at 118.7 GHz ($2D^2/\lambda$) should be at least 2027m (6651 feet). Because very accurate boresighting accuracy is required over this range, a laser autocollimation boresighting technique is suggested, as shown in Figure 4-1. An

ANTENNA MOUNT (UPPER AZIMUTH TURNTABLE)
PRECISION ROTARY TABLE
FEED WHEEL
ENCODER

LASER BEAM

OPTICAL FLAT ATTACHED TO REFLECTOR
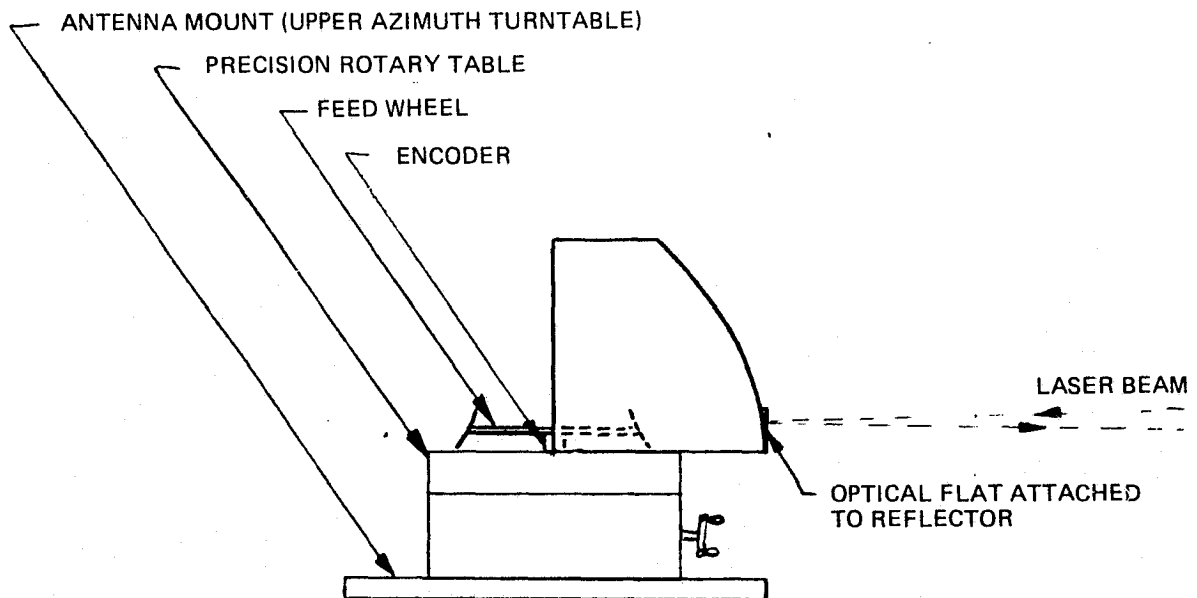
Figure 4-1. Precision Boresighting Method

4-1

optical flat would be permanently mounted to the back of the reflector and parallel to the X - Z plane. When the reflected laser beam is centered on the laser itself, the reflector is positioned properly relative to the range. The precision rotary table (machinist's type) can then be rotated 180 deg, and the pattern can be measured. The precision rotary table can then be re-positioned over the ±60 deg scan range and additional pattern cuts made. The feed wheel shaft encoder gives a precision readout of the angle of the feed wheel relative to the reflector.

This range setup allows precision measurements without any reference to the positioner synchros, except to reset the 0 deg position after each pattern. The rotary table is much more accurate than the synchros. The rotary table can be eliminated, however, if the antenna positioner has an encoder mounted. It appears that useable patterns at 118.7 GHz can be recorded on the 0.5 deg per inch scale provided that the antenna positioner runs smoothly. Patterns with this approximate beamwidth have been measured at Rockwell/Autonetics on a six foot millimeter reflector.

Measurement of main beam efficiency is very difficult, requiring a number of pattern cuts and integration of the measured patterns. It is suggested that these be made only at a few critical frequency channels, with measurements of gain and beamwidths (az and el) for the other channels to verify that performance levels are sufficiently near calculated values. With so many frequency channels, it would be easy to unnecessarily increase the cost and delay the schedule with too much testing.

4.2 MECHANICAL/STRUCTURAL TESTS

4.2.1 Acoustic vs Random Vibrations Test

Several considerations lead to the conclusion that conducting both acoustic and random vibration tests will be redundant, and that the acoustic test is the most appropriate. These are discussed below.

The random vibration levels encountered in the shuttle payload compartment represent the response of the mid fuselage to the acoustic environment. Consequently, testing to the acoustic environment is more related to the cause than a random vibration test.

Because of the large surface area of the SIMS-A antenna, large acoustic pressures will be present to transmit stresses into the structure from the exposed surfaces. The shuttle mid fuselage attach points, on the other hand, are connected to a massive structure with considerable damping, so their response to the acoustic environment will tend to be much lower. One would expect, therefore, that the stresses from the direct acoustic environment will be much larger than the stress from the induced response of the shuttle structure. A cursory investigation of the expected acoustic and random vibration levels in the shuttle payload bay support this conclusion.

Finally, the acoustic test will be less expensive. The reason for this is the cost of a vibration test fixture, which will be very high for an antenna of this size and weight, while only minor fixturing is required for acoustic tests.

4.2.2 Photogrammetric Measurements

Essential to the success of the SIMS-A performance is the surface conformity of the reflector surfaces. Conventional means are convenient to measure the sub-reflectors, however due to its large size it is desirable to measure the surface contour photogrammetrically. This technique was developed primarily for the purpose of accurate measurement of large reflector contours. It is capable of accuracies in excess of 1 part in 100,000 of the antenna aperture ($\simeq$ .0016 in).

Analytical photogrammetric triangulation is a least squares triangulation process. Two or more accurate two dimensional photographic records of an object on which an unlimited number of discrete targets are located provide sufficient data from which to calculate a unique set of three dimensional coordinates for each target (and thus the surface contour).

The reflector surface will be prepared by lightly affixing an array of targets at arbitrary locations. The surface is then photographed by two or more cameras, also at arbitrary locations, and the image is recorded on micro-flat photographic plates. The sets of X, Y coordinates of the target images on the plates is then measured in a coordinatograph. Once these points are known and the focal length of the lens is accurately known, sets of simultaneous equations are developed. More than a sufficient number of knowns exist to permit solutions by the method of least squares. The X, Y, Z coordinates of all of the targets are obtained from these solutions.

The technique is thus an instantaneous record of all data necessary to determine the surface contour. For SIMS-A the following photogrammetric measurements of the surface contour are recommended: the engineering model upon fabrication; the prototype model subsequent to qualification tests; and the flight model upon fabrication.

4.3 RECOMMENDED TEST PLAN

For qualification, the following test program is recommended for the antenna.

1. Limited Functional Test (including photogrammetric measurements of the reflector contour)

2. Acoustic Test (non operating)

3. Limited Functional Test

4. Thermal Vacuum Test (non operating)

5. Complete functional (including photogrammetric measurements of the reflector contour)

For acceptance the same test sequence is used, at reduced levels, except that the reflector contour measurements will only be made prior to testing. The complete functional tests will give confidence that the reflector contour remains accurate after the environmental tests.

5. CONCLUSIONS

This study started with the basic concept of a parabolic torus and a rotating feed assembly with Gregorian subreflector feeds and prime focus type feeds. The performance of both types of feeds was analyzed in a fairly rigorous manner using physical optics methods, leading to the conclusion that these concepts were useable for all channels except 2.695 GHz. A unique seven-beam slot array feed for 2.695 GHz was conceived and optimized. Performance with this aberration correcting feed was more than adequate. A design concept covering all eleven channels with adequate performance levels (>90% beam efficiency and resolution equal to that of a 1.6 m aperture) was therefore worked out.

A preliminary design of the complete antenna system was then defined. It consists of a truss supported graphite/epoxy main reflector with a graphite/epoxy feed wheel assembly having six Gregorian subreflectors, a dual channel concentric feed for each subreflector, and two three-channel prime focus feed assemblies. Preliminary mechanical and structural designs of the parabolic forms, the wheel assembly, and the wheel drive system were executed. Finally, a preliminary design and analysis of a suitable calibration system was performed.

The preliminary design is conservative in the sense that the materials and fabrication concepts have all been used in space. Considering that the shuttle acoustic and vibration environments are generally a decade less severe than those of present launch vehicles, no problems in meeting the environment is foreseen. Thermal environments were identified for the conceptual design, whereas an analytical thermal model will be required for the detailed design. The only item requiring an advancement in the state-of-art is the reflector, which is larger and more precise than those that have been developed in the past. Companies with experience in this area are responsive, however, and very interested in undertaking a development program to meet SIMS-A requirements. This and other risk areas are outlined in Table 5-1. These areas should be monitored carefully during hardware development.

In summary, the conservative preliminary design and thorough performance analysis indicate that the hardware development program will have only normal risks in spite of the large aperture, rapid scan speed, and wide frequency range of the antenna.

Table 5.1 Assessment of Risk Areas

Risk Area	Risk Assessment	Impact	Resolution
Main reflector	See text	Less than 90 percent efficiency in 94 and 118.7 GHz channels due to degraded accuracy	Development and advancement of state-of-art
Availability of graphite/epoxy honeycomb	Low	A new design concept for the feed wheel and Gregorian subreflector will have to be developed	Maintain close observation of product development at Hexcel
Structural failure of feed wheel assembly	Very low (wheel is lightly stressed)	Program delay for re-design or potential safety problems	Thorough structural analysis of design
Plating of Graphite/epoxy	Moderate	Program delay (qual test) Degraded mission (in flight)	Choose vendor with experience or perform extensive process development and testing
Thermal design of calibration cavity	Moderate	Loss of calibration accuracy due to thermal gradients in cavity	Careful thermal design and analysis, or development of broadband absorber with better thermal conductivity
Dual concentric feed for Gregorian	Moderate to high	Higher losses than expected due to spillover, resulting in degraded temperature resolution	Change to design with 8 sub-reflectors (low risk)

6. RECOMMENDATIONS

A program plan for the development, fabrication and test of a flight model of the SIMS-A antenna was developed in the course of this study. This plan, presented in Volume II, constitutes the recommended actions which should follow this conceptual study.

In summary the detailed design and development of the SIMS-A antenna is conceived as consisting of four phases: Phase 1 - Design and Development; Phase 2 - Engineering Model; Phase 3 - Prototype Model; and Phase 4 - Flight Model. Phase 1 will accomplish all of the detailed design, design verification, and interface specification preparation. In Phase 2 the engineering model will be fabricated and tested. Phase 3 will accomplish the fabrication and qualification testing of the prototype model. Phase 4 will consist of fabrication and flight assurance tests of the flight model.

Two areas of required development should be identified specifically. These are:

Feeds
Calibration loads

Performance requirements and design concepts for the feeds and calibration loads were defined in the report, however detailed design parameters are required for proof of design. These parameters require hardware development. This development must be conducted as a distinct development program or as part of the overall antenna development.

7. NEW TECHNOLOGY

The SIMS-A antenna conceptual design study yielded no reportable new technology items.

8. REFERENCES

Section 1

[1]Space Shuttle System, Payload Accommodations document, JSC 07700, Volume XIV, Revision C, Change No. 11

Section 2

[2]"Design of an Offset Fed Scanning Antenna for the Shuttle Imaging Microwave System," J.J. Gustincic, Interim Report No. TR070, JPL Contract No. 954145

[3]Potter, P.D. "A New Horn Antenna with Suppressed Sidelobes and Equal Beamwidths," Microwave Journal, Vol. VI, pp. 71-78, June 1963

[4]Bailey, M.C. "The Development of an L-band Radiometer Dual-Mode Horn," IEEE Trans. Amt. Prop., Vol. AP-23, pp. 439-441, May 1975

[5]"Final Report on Design Study of NIMBUS 'G' SMMR Antenna Subsystem," Microwave Research Corporation report 5525, JPL Contract No. 954092.

[6]Silver, S., "Microwave Antenna Theory and Design"

Section 3

[7]Rush, W.V.T. and Potter, P.D., "Analysis of Reflector Antennas," p. 43.

[8]W.N. Hardy, "Precision Temperature Reference for Microwave Radiometry" IEEE Trans. Microwave Theory Tech., Vol. MTT-21, pp. 149-150, March 1973.

[9]W.N. Hardy, et. al., "An S-Band Radiometer Design with High Absolute Precision", IEEE Trans. Microwave Theory Tech., Vol. MTT 22, pp. 382-390, April 1974.

[10]P.I. Somlo, "Zener Diode Noise Generators", Electron Lett., Vol. 11, p. 290, July 10, 1975.

[11]"Antenna Tolerance Theory - A Review," John Ruze, IEEE Proceedings Vol. 54, April 1966.

[12]Bulletin ANC-23, "Sandwich Construction for Aircraft", Dept. of the Air Force, Air Research and Development Command

[13]R.J. Roark, "Formulas for Stress and Strain", 3rd Edition, McGraw Hill Book Company, New York, Chapter 15, Article 82.

APPENDIX A

GREGORIAN REFLECTOR SYSTEM

1. Main Program to Calculate Subreflector Currents and Two Cuts of Main Reflector Current

2. GEODES Subroutine — Calculates subreflector point given X, Z

3. PRIPAT Subroutine — Calculates primary pattern of feed aperture

4. AMPPHS Subroutine — Plots the output of the main program

5. VCROSS Subroutine — Computes the cross product of two vectors

6. VNORM Subroutine — Normalizes a vector

7. Main Program to Calculate Main Reflector Currents and Far Field Patterns

8. Main Program to Calculate the Directivity of the Feed

REFLECTOR WITH PRIME FOCUS FEED

1. Main Program to calculate the main reflector currents and far field patterns

2. PRIPAT Subroutine — Calculates the feed pattern

3. Main Program to calculate the feed directivity and prepare a radiation distribution printout of the feed pattern. In addition, will calculate the element amplitudes and phases given the amplitudes and phases of the seven beams of the 19 element slot array.

REQUESTED OPTIONS: OPT=2

OPTIONS IN EFFECT: NAME(MAIN) OPTIMIZE(2) LINECOUNT(42) SIZE(MAX) AUTODBL(NONE)
                   SOURCE EBCDIC NOLIST NODECK OBJECT MAP NOFORMAT GOSTMT NOXREF ALC NOANSF NOTERMINAL FLAG(I)

```
                         C****  PARABOLIC TORUS MAIN - GREGORIAN SUBREFLECTOR
                         C****  COMPUTATION OF SUBREFLECTOR CURRENTS AND SCATTER PATTERN
ISN 0002                       REAL*4 RHS(3,700),JS(3,700),PATH(700),VM(350),VPHS(350),HM(350)
                              1 ,HPHS(350),JSDS(3),VRSM(3),AR(3),HI(3),NNS(3),VTEMP(3),STP(4)
ISN 0003                       REAL*8 X,Y,Z,RR(3),NN(3),TF,PF,F,H,S,CT,ST,K,XF(99),DTH,
                              1 TH,PH,XM,ZB,ZM,DRAD,THP,RAD,IH1,TH2,PH1,X1,Z1,XDFL,PI,TWOPI,YYS,
                              2 ZZS,DELX,DELZ,DEL,DELXZ,XZLIM,DPH,XAR(5),ZAR(5),THAR(5),PHAR(5),
                              3 DTEMP,STH,PH2,FY,FZ,C,SC,SS,RRNX,RRNY,RRNZ
ISN 0004                       COMPLEX*8 CTEMP,HP(3),CNX,CNY,CNZ,VPOL,HPOL,CPHS
ISN 0005                       COMMON/REFPRM/F,H,K
ISN 0006                       COMMON/PLTPRM/PXL,PXR,DXDX,NDX,IDX,NXDX,NL,NPL,PX2(350),IX2(350)
ISN 0007                       DATA ETA,DRADS,PI,PIS,TWOPI,CL,DELXZ,XZLIM,DRAD/376.731,
                              1 57.29578,3.141592653589793D0,3.141593,6.283185307179586D0,
                              2 2.997925E-1,1.0D-4,1.0D-4,5.729577951308232D1/
                         C****  READ DATA (MKS UNITS)
ISN 0008              10       READ(5,20,END=200) NTH,NTRL,NAC,F,H,S,THPD,YYS,ZZS,XM,ZB,ZM,PXM,
                              1 PZ,PZB,PZT,DTH,R0,FREQ,A,B,PKGN,FY,FZ,(XF(I),I=1,NTH)
ISN 0009              20       FORMAT(3I4,5F12.0/(6F12.0))
ISN 0010                       WRITE(6,30) NTH,NTRL,NAC,F,H,S,THPD,YYS,ZZS,XM,ZB,ZM,PXM,PZ,
                              1 PZB,PZT,DTH,R0,FREQ,A,B,PKGN,FY,FZ,(XF(I),I=1,NTH)
ISN 0011              30       FORMAT('1',5X,'NO. THETA ON SUBREFLECTOR=',I3,4X,'MAX NO. OF ',
                              1 'ITERATIONS=',I3,8X,'CRT RASTER INCREMENT=',I3/6X,'FEED RADIUS ('
                              2 ,'F) =',F10.6,6X,'FEED DEPRESSION (H) =',F10.6,2X,'SUB. VERTEX ',
                              3 'RADIUS (S) =',F10.6/6X,'FEED POINTING ANGLE=',F10.4,3X,
                              4 'APPROX. CENTER OF SUBREFLECTOR   YYS=',F9.6,2X,'ZZS=',F9.6/
                              5 6X,'XM=',F10.6,20X,'ZB=',F10.6,20X,'ZM=',F10.6/6X,'X MAX IN PLOT'
                              6 ,' 1 =',F10.6,6X,'Z VALUE IN PLOT 1 =',F10.6,4X,'Z MIN IN PLOT ',
                              7 '2 =',F10.6/6X,'Z MAX IN PLOT 2 =',F10.6,6X,'THETA INC. IN SUB.',
                              8 ' =',F10.5,3X,'MAIN REFL RAD=',F10.6/6X,'FREQUENCY=',F10.4,13X,
                              9 'FEED A DIMENSION=',F10.6,6X,'FEED B DIMENSION=',F10.6/6X,'PEAK',
                              1 ' POWER GAIN=',F10.5,7X,'FEED Y OFFSET=',F10.6,9X,'FEED Z OFFSE',
                              2 'T=',F10.6/6X,'INITIAL VALUES OF X FOR EDGE CONTOUR='/(6X,10F10.6
                              3 ))
ISN 0012                       WRITE(6,35)
ISN 0013              35       FORMAT('0',8X,'TH',8X,'PH',3X,'ITRL',3X,'X1',6X,'Z1',5X,'ISP',5X,
```

```
                   1 'RAD)',7X,'DTEMP',7X,'HTOT')
           C****    CALCULATE CONSTANTS
ISN 0014           FS=SNGL(F)
ISN 0015           HS=SNGL(H)
ISN 0016           THP=DBLE(THPD)/DRAD
ISN 0017           ST=DSIN(THP)
ISN 0018           CT=DCOS(THP)
ISN 0019           K=DSQRT(H**2+(F-S)**2)+2.0D0-5
ISN 0020           SP=SNGL(ST)
ISN 0021           CP=SNGL(CT)
ISN 0022           EK=2.*PIS*FREQ/CL
           C****    COMPUTE JS FOR EACH SUBREFLECTOR POINT (TH,PH)
           C****    ANGLES DEFINED RELATIVE TO APPROXIMATE CENTER OF CURVATURE
ISN 0023           ISP=0
ISN 0024           PWR=0.
ISN 0025           DO 120 I=1,NTH
ISN 0026           TH=PI/2.0D0-DTH*(DFLOAT(I)-0.5D0)
ISN 0027           STH=DSIN(TH)
           C****    CALCULATE VALUE OF PHI AT BOTTOM EDGE OF SUBREFLECTOR (ITERATIVE)
ISN 0028           X1=XF(I)
ISN 0029           DO 40 ITRL=1,NTRL
ISN 0030           X=X1-DELXZ
ISN 0031           Z=ZB+(ZM-ZB)*DSQRT(1.0D0-(X/XM)**2)
ISN 0032           CALL GEODES(X,Z,Y,RR,NN)
ISN 0033           RAD=DSQRT(RR(1)**2+(RR(2)+YYS)**2+(RR(3)-ZZS)**2)
ISN 0034           TH1=DARCOS(-RR(1)/RAD)
ISN 0035           X=X1+DELXZ
ISN 0036           Z=ZB+(ZM-ZB)*DSQRT(1.0D0-(X/XM)**2)
ISN 0037           CALL GEODES(X,Z,Y,RR,NN)
ISN 0038           RAD=DSQRT(RR(1)**2+(RR(2)+YYS)**2+(RR(3)-ZZS)**2)
ISN 0039           TH2=DARCOS(-RR(1)/RAD)
ISN 0040           DELX=DELXZ*(TH1+TH2-2.0D0*TH)/(TH2-TH1)
ISN 0041           X1=X1-DELX
ISN 0042           IF(DABS(DELX).LT.XZLIM) GO TO 50
ISN 0044      40   CONTINUE
           C****    CALCULATE PARAMETERS FOR LAST ESTIMATE OF SOLUTION
ISN 0045      50   Z1=ZB+(ZM-ZB)*DSQRT(1.0D0-(X1/XM)**2)
ISN 0046           CALL GEODES(X1,Z1,Y,RR,NN)
ISN 0047           RAD=DSQRT(RR(1)**2+(RR(2)+YYS)**2+(RR(3)-ZZS)**2)
ISN 0048           TH1=DARCOS(-RR(1)/RAD)
```

```
ISN 0049              PH1=DATAN2(RR(3)-ZZS,-RR(2)-YYS)
ISN 0050              WRITE(6,55) TH1,PH1,ITRL,X1,Z1
ISN 0051        55    FORMAT(' ',3X,2F10.6,I3,2F8.4)
ISN 0052              DPH=DTH/STH
ISN 0053              JM=TWOPI/DPH
ISN 0054              DO 116 J=1,JM
ISN 0055              PH=PH1+DPH*(DFLOAT(J)-0.5D0)
              C*****  FIND(X1,Z1) WHICH CORRESPONDS TO DESIRED (TH,PH) ON SUBREFLECTOR
ISN 0056              DO 70 ITRL=1,NTRL
ISN 0057              XAR(1)=X1
ISN 0058              XAR(2)=X1+DELXZ
ISN 0059              XAR(3)=X1
ISN 0060              XAR(4)=X1-DELXZ
ISN 0061              XAR(5)=X1
ISN 0062              ZAR(1)=Z1
ISN 0063              ZAR(2)=Z1
ISN 0064              ZAR(3)=Z1+DELXZ
ISN 0065              ZAR(4)=Z1
ISN 0066              ZAR(5)=Z1-DELXZ
ISN 0067              DO 60 IPT=1,5
ISN 0068              CALL GEODES(XAR(IPT),ZAR(IPT),Y,RR,NN)
ISN 0069              RAD=DSQRT(RR(1)**2+(RR(2)+YYS)**2+(RR(3)-ZZS)**2)
ISN 0070              THAR(IPT)=DARCOS(-RR(1)/RAD)-TH
ISN 0071        60    PHAR(IPT)=DATAN2(RR(3)-ZZS,-RR(2)-YYS)-PH
ISN 0072              DTEMP=(THAR(2)-THAR(4))*(PHAR(3)-PHAR(5))-(THAR(3)-THAR(5))*
                     1 (PHAR(2)-PHAR(4))
ISN 0073              DELX=2.0D0*DELXZ*(PHAR(1)*(THAR(3)-THAR(5))-THAR(1)*(PHAR(3)-
                     1 PHAR(5)))/DTEMP
ISN 0074              DELZ=2.0D0*DELXZ*(THAR(1)*(PHAR(2)-PHAR(4))-PHAR(1)*(THAR(2)-
                     1 THAR(4)))/DTEMP
ISN 0075              DEL=DSQRT(DELX**2+DELZ**2)
ISN 0076              X1=X1+DELX
ISN 0077              Z1=Z1+DELZ
ISN 0078              IF(DEL.LE.XZLIM) GO TO 80
ISN 0080        70    CONTINUE
ISN 0081        80    IF(Z1.GE.ZB) GO TO 90
ISN 0083              IF(DSQRT((X1/XM)**2+((ZB-Z1)/ZB)**2).GT.1.0D0) GO TO 120
ISN 0085              GO TO 100
ISN 0086        90    IF(DSQRT((X1/XM)**2+((Z1-ZB)/(ZM-ZB))**2).GT.1.0D0) GO TO 120
              C*****  CALCULATE PARAMETERS FOR LAST ESTIMATE OF SOLUTION AND INCLUDE
```

```
              C****  EFFECTS OF OFFSETS
ISN 0088      100    CALL GEODES(X1,Z1,Y,RR,NN)
ISN 0089             RAD=DSQRT(RR(1)**2+(RR(2)+YYS)**2+(RR(3)-ZZS)**2)
ISN 0090             TH2=DARCOS(-RR(1)/RAD)
ISN 0091             PH2=DATAN2(RR(3)-ZZS,-RR(2)-YYS)
ISN 0092             DTEMP=(NN(3)*(ZZS-RR(3))-NN(2)*(YYS+RR(2))-NN(1)*RR(1))/RAD
ISN 0093             DS=SNGL(STH*DTH*DPH*RAD**2/DTEMP)*RO**2
ISN 0094             RR(2)=RR(2)+FY
ISN 0095             RR(3)=RR(3)-FZ
ISN 0096             DTEMP=DSQRT(RR(1)**2+RR(2)**2+RR(3)**2)
ISN 0097             TEMP=SNGL(DTEMP)
ISN 0098             RO=TEMP*RO
ISN 0099             TEMP=SNGL(-NN(1)*RR(1)-NN(2)*RR(2)-NN(3)*RR(3))/TEMP
ISN 0100             DOMEG=DS*TEMP/RO**2
ISN 0101             PRNX=RR(1)/DTEMP
ISN 0102             RRNY=RR(2)/DTEMP
ISN 0103             RRNZ=RR(3)/DTEMP
ISN 0104             C=RRNY*CT+RRNZ*ST
ISN 0105             SC=-RRNX
ISN 0106             SS=RRNZ*CT-RRNY*ST
ISN 0107             TF=DATAN2(DSQRT(SC**2+SS**2),C)
ISN 0108             PF=DATAN2(SS,SC)
ISN 0109             STP(1)=SIN(SNGL(TF))
ISN 0110             STP(2)=COS(SNGL(TF))
ISN 0111             STP(3)=SIN(SNGL(PF))
ISN 0112             STP(4)=COS(SNGL(PF))
ISN 0113             CALL PRIPAT(STP,A,B,EK,PKGN,HTP,HPP)
ISN 0114             HTOT=SQRT(HTP**2+HPP**2)
ISN 0115             HI(1)=2.*(HPP*STP(3)-HTP*STP(2)*STP(4))
ISN 0116             HI(2)=-2.*(HPP*SP*STP(4)+HTP*(CP*STP(1)+SP*STP(2)*STP(3)))
ISN 0117             HI(3)=2.*(HPP*CP*STP(4)-HTP*(CP*STP(2)*STP(3)-SP*STP(1)))
ISN 0118             NNS(1)=SNGL(NN(1))*DS/RO
ISN 0119             NNS(2)=SNGL(NN(2))*DS/RO
ISN 0120             NNS(3)=SNGL(NN(3))*DS/RO
ISN 0121             CALL VCROSS(NNS,HI,JSDS)
ISN 0122             ISP=ISP+1
ISN 0123             IF(ISP.GT.700) GO TO 130
ISN 0125             PATH(ISP)=RO
ISN 0126             WRITE(6,105) TH2,PH2,ITRL,X1,Z1,ISP,RAD,DTEMP,HTOT
ISN 0127      105    FORMAT(' ',3X,2F10.6,I3,2F8.4,I6,2F11.7,1PE14.6)
```

```
ISN 0128                DO 110 IC=1,3
ISN 0129                JS(IC,ISP)=JSDS(IC)
ISN 0130        110     RRS(IC,ISP)=SNGL(RR(IC))
ISN 0131                PWR=PWR+ETA*DOMEG*HTOT**2
                C****   IMAGE SIDE OF SUBREFLECTOR, PHI=PI-PHI
ISN 0132                STP(4)=-STP(4)
ISN 0133                CALL PRIPAT(STP,A,B,EK,PKGN,HIP,HPP)
ISN 0134                HI(1)=2.*(HPP*STP(3)-HTP*STP(2)*STP(4))
ISN 0135                HI(2)=-2.*(HPP*SP*STP(4)+HTP*(CP*STP(1)+SP*STP(2)*STP(3)))
ISN 0136                HI(3)=2.*(HPP*CP*STP(4)-HTP*(CP*STP(2)*STP(3)-SP*STP(1)))
ISN 0137                NNS(1)=-NNS(1)
ISN 0138                CALL VCROSS(NNS,HI,JSDS)
ISN 0139                ISP=ISP+1
ISN 0140                IF(ISP.GT.700) GO TO 130
ISN 0142                PATH(ISP)=RO
ISN 0143                DO 113 IC=1,3
ISN 0144        113     JS(IC,ISP)=JSDS(IC)
ISN 0145                RRS(1,ISP)=-SNGL(RR(1))
ISN 0146                RRS(2,ISP)=SNGL(RR(2))
ISN 0147                RRS(3,ISP)=SNGL(RR(3))
ISN 0148        116     PWR=PWR+ETA*DOMEG*(HPP**2+HTP**2)
ISN 0149        120     CONTINUE
ISN 0150        130     NSUB=ISP
ISN 0151                DBSO=10.*ALOG10(1./PWR)
ISN 0152                WRITE(6,135) DBSO,NTH,NTRL,NSUB,F,H,S,THPD,YYS,ZZS,XM,ZB,ZM,DTH,
                       1 RO,FREQ,A,B,PKGN
ISN 0153        135     FORMAT('0',5X,'SPILLOVER LOSS IN DB=',F9.6/'0',5X,'SUBREFLECTOR ',
                       1 'CURRENTS DATA SET LISTING'/'0',1X,3I4,3F12.7,F12.5,F12.7/2X,
                       2 6F12.7/2X,F12.4,2F12.7,F12.6/'0',6X,'RR(1)',9X,'RR(2)',9X,'RR(3)'
                       3 ,8X,'JSDS(1)',7X,'JSDS(2)',7X,'JSDS(3)',9X,'PATH',9X,'ISP'/)
ISN 0154                WRITE(9,140) NTH,NTRL,NSUB,F,H,S,THPD,YYS,ZZS,XM,ZB,ZM,DTH,RO,
                       1 FREQ,A,B,PKGN
ISN 0155        140     FORMAT(3I4,3F12.7,F12.5,F12.7/6F12.7/F12.4,2F12.7,F12.6)
ISN 0156                DO 150 I=1,NSUB
ISN 0157                WRITE(6,155) (RRS(IC,I),IC=1,3),(JS(IC,I),IC=1,3),PATH(I),I
ISN 0158        150     WRITE(9,160) (RRS(IC,I),IC=1,3),(JS(IC,I),IC=1,3),PATH(I),I
ISN 0159        155     FORMAT(' ',1X,1P7E14.6,I8)
ISN 0160        160     FORMAT(1P7E14.6,I8)
                C****   CALCULATE SCATTER PATTERN
ISN 0161                DO 195 ICUTD=1,2
```

```
ISN 0162                IF(ICUTD.EQ.2) GO TO 162
ISN 0164                IF(PXM.LE.0.) GO TO 195
ISN 0166                CALL DXDYV(1.0.,PXM,DXDX,NDX,IDX,NXDX,20.0,IERR)
ISN 0167                PXL=0.
ISN 0168                PXR=PXM
ISN 0169                CALL GRIDIV(1,PXL,PXR,-40.,0.,DXDX,2.,NDX,5,IDX,5,NXDX,3)
ISN 0170                CALL PRINTV(20,'AZIMUTH CUT ALONG Z=',408,1003)
ISN 0171                CALL LABLV(PZ,568,1003,6,1,1)
ISN 0172                GO TO 164
ISN 0173         162    IF(PZT.LE.PZB) GO TO 10
ISN 0175                CALL DXDYV(1,PZB,PZT,DXDX,NDX,IDX,NXDX,20.0,IERR)
ISN 0176                PXL=PZB
ISN 0177                PXR=PZT
ISN 0178                CALL GRIDIV(1,PXL,PXR,-40.,0.,DXDX,2.,NDX,5,IDX,5,NXDX,3)
ISN 0179                CALL PRINTV(28,'ELEVATION CUT ALONG X=0.0000',400,1003)
ISN 0180         164    NL=NXV(PXL)
ISN 0181                NPL=(NXV(PXR)-NL)/NAC+1
ISN 0182                HMAX=0.
ISN 0183                DO 190 I=1,NPL
ISN 0184                IX2(I)=NL+NAC*(I-1)
ISN 0185                IF(ICUTD.EQ.2) GO TO 166
ISN 0187                XS=UXV(IX2(I))
ISN 0188                PX2(I)=XS
ISN 0189                YS=SQRT((1.-PZ**2/2.)**2-XS**2)
ISN 0190                GO TO 168
ISN 0191         166    PZ=UXV(IX2(I))
ISN 0192                PX2(I)=PZ
ISN 0193                XS=0.
ISN 0194                YS=1.-PZ**2/2.
ISN 0195         168    DO 170 IC=1,3
ISN 0196         170    HP(IC)=(0.,0.)
ISN 0197                DO 180 J=1,NSUB
ISN 0198                VRSM(1)=XS-RRS(1,J)
ISN 0199                VRSM(2)=YS-FS-RRS(2,J)
ISN 0200                VRSM(3)=PZ+HS-RRS(3,J)
ISN 0201                CALL VNORM(VRSM,AR,RSM)
ISN 0202                RSM=R0*RSM
ISN 0203                T1=EK*(RSM+PATH(J))
ISN 0204                CTEMP=CMPLX(1./RSM**2,EK/RSM)*CMPLX(COS(T1),-SIN(T1))
ISN 0205                CALL VCROSS(JS(1,J),AR,VTEMP)
```

```
ISN 0206              DO 180 IC=1,3
ISN 0207          180 HP(IC)=HP(IC)+CTEMP*CMPLX(VTEMP(IC),0.)
ISN 0208              T1=SQRT(1.+PZ**2)
ISN 0209              T2=T1*SQRT(XS**2+YS**2)
ISN 0210              CNX=CMPLX(-XS/T2,0.)
ISN 0211              CNY=CMPLX(-YS/T2,0.)
ISN 0212              CNZ=CMPLX(-PZ/T1,0.)
              C****    DETERMINE PHASE AT APERTURE PLANE Y=0, RELATIVE TO GEOMETRIC
              C****     OPTICS PHASE, AND WITH PI PHASE SHIFT REMOVED
ISN 0213              T1=EK*R0*(SNGL(K)-YS)-PIS
ISN 0214              CPHS=CMPLX(COS(T1),SIN(T1))/CMPLX(4.*PIS,0.)
ISN 0215              VPOL=(CNX*HP(2)-CNY*HP(1))*CPHS
ISN 0216              HPOL=(CNY*HP(3)-CNZ*HP(2))*CPHS
ISN 0217              VM(I)=CABS(VPOL)
ISN 0218              IF(VM(I).EQ.0.) GO TO 182
ISN 0220              VPHS(I)=DRADS*ATAN2(AIMAG(VPOL),REAL(VPOL))
ISN 0221              GO TO 184
ISN 0222          182 VPHS(I)=0.
ISN 0223          184 HM(I)=CABS(HPOL)
ISN 0224              IF(HM(I).EQ.0.) GO TO 186
ISN 0226              HPHS(I)=DRADS*ATAN2(AIMAG(HPOL),REAL(HPOL))
ISN 0227              GO TO 188
ISN 0228          186 HPHS(I)=0.
ISN 0229          188 VTM=SQRT(VM(I)**2+HM(I)**2)
ISN 0230              IF(VTM.GT.HMAX) HMAX=VTM
ISN 0232          190 CONTINUE
ISN 0233              CALL AMPPHS(VM,HMAX,VPHS,0)
ISN 0234              CALL AMPPHS(HM,HMAX,HPHS,1)
ISN 0235          195 CONTINUE
ISN 0236              GO TO 10
ISN 0237          200 STOP
ISN 0238              END
```

A-8

C75-664/034A

```
ISN 0002              SUBROUTINE GEODES(X,Z,Y,RR,NN)
ISN 0003              REAL*8 RR(3),NN(3),N(3),M(3),RF(3),X,Z,F,H,Y,TEMP1,TEMP2,C,K,
                     1 RRN(3)
ISN 0004              COMMON/REFPRM/F,H,K
ISN 0005              Y=DSQRT((1.0D0-Z**2/2.0D0)**2-X**2)
ISN 0006              RF(1)=X
ISN 0007              RF(2)=Y-F
ISN 0008              RF(3)=Z+H
ISN 0009              TEMP1=DSQRT(1.0D0+Z**2)
ISN 0010              TEMP2=TEMP1*DSQRT(X**2+Y**2)
ISN 0011              N(1)=-X/TEMP2
ISN 0012              N(2)=-Y/TEMP2
ISN 0013              N(3)=-Z/TEMP1
ISN 0014              M(1)=-2.0D0*N(1)*N(2)
ISN 0015              M(2)=1.0D0-2.0D0*N(2)**2
ISN 0016              M(3)=-2.0D0*N(3)*N(2)
ISN 0017              C=((K-Y)**2-RF(1)**2-RF(2)**2-RF(3)**2)/(2.0D0*(K-Y+M(1)*RF(1)+
                     1 M(2)*RF(2)+M(3)*RF(3)))
ISN 0018              DO 10 I=1,3
ISN 0019       10     RR(I)=RF(I)+C*M(I)
ISN 0020              TEMP1=DSQRT(RR(1)**2+RR(2)**2+RR(3)**2)
ISN 0021              DO 20 I=1,3
ISN 0022       20     RRN(I)=RR(I)/TEMP1
ISN 0023              TEMP1=DSQRT(2.0D0*(1.0D0+RRN(1)*M(1)+RRN(2)*M(2)+RRN(3)*M(3)))
ISN 0024              DO 30 I=1,3
ISN 0025       30     NN(I)=-(RRN(I)+M(I))/TEMP1
ISN 0026              RETURN
ISN 0027              END
```

C75-664/034A

TIONS IN EFFECT: NAME(MAIN) OPTIMIZE(2) LINECOUNT(42) SIZE(MAX) AUTODBL(NONE)
                 SOURCE EBCDIC NOLIST DECK OBJECT MAP NOFORMAT GOSTMT NOXREF ALC NOANSF NOTERMINAL FLAG(I)

```
ISN 0002              SUBROUTINE PRIPAT(STP,A,B,EK,PKGN,HT,HP)
                C****  PATTERN OF RECTANGULAR APERTURE, COSINE TAPER IN BOTH PLANES,
                C****  EQUAL ELECTRIC AND MAGNETIC DIPOLES FOR LOW CROSS-POLARIZATION
ISN 0003              REAL*4 STP(4)
ISN 0004              DATA PI,ETA/3.141593,376.731/
ISN 0005              U1=EK*A*STP(1)*STP(4)/2.
ISN 0006              U2=EK*B*STP(2)/2.
ISN 0007              AF=COS(U1)*COS(U2)*SQRT(STP(1)*STP(3)*PKGN/(4.*PI*ETA))/((1.-(
               1 2.*U1/PI)**2)*(1.-(2.*U2/PI)**2))
ISN 0008              TEMP=SQRT(1.-(STP(1)*STP(4))**2)
ISN 0009              HP=AF*0.5*(1.+STP(3)/TEMP)
ISN 0010              HT=-AF*0.5*STP(2)*STP(4)/TEMP
ISN 0011              RETURN
ISN 0012              END
```

```
ISN 0002              SUBROUTINE AMPPHS(AMP,AMPM,PHS,ICONT)
ISN 0003              REAL*4 AMP(1),PHS(1)
ISN 0004              COMMON/PLTPRM/PXL,PXR,DXDX,NDX,IDX,NXDX,NL,NPL,PX2(350),IX2(350)
             C****    ICONT=0 FOR THE FIRST SET OF GRAPHS AND 1 FOR THE SECOND
ISN 0005              IF(ICONT.EQ.0) GO TO 10
ISN 0007              CALL GRID1V(1,PXL,PXR,-40.,0.,DXDX,2.,NDX,5,IDX,5,NXDX,3)
ISN 0008              CALL PRINTV(28,'CROSS POLARIZATION AMPLITUDE',400,1023)
ISN 0009              GO TO 15
ISN 0010      10      CALL PRINTV(32,'PRINCIPLE POLARIZATION AMPLITUDE',384,1023)
ISN 0011      15      IX1=NL
ISN 0012              IY1=NYV(20.*ALOG10(AMAX1(0.01,AMP(1)/AMPM)))
ISN 0013              DO 20  I=2,NPL
ISN 0014              IY2=NYV(20.*ALOG10(AMAX1(0.01,AMP(I)/AMPM)))
ISN 0015              CALL LINEV(IX1,IY1,IX2(I),IY2)
ISN 0016              CALL LINEV(IX1,IY1,IX2(I),IY2)
ISN 0017              IX1=IX2(I)
ISN 0018      20      IY1=IY2
ISN 0019              CALL GRID1V(1,PXL,PXR,-180.,+180.,DXDX,20.,NDX,5,IDX,5,NXDX,4)
ISN 0020              CALL PRINTV(29,'PHASE RELATIVE TO G. O. PHASE',396,1023)
ISN 0021              IX1=NXV(PX2(1))
ISN 0022              IY1=NYV(PHS(1))
ISN 0023              DO 30  I=2,NPL
ISN 0024              IXP2=NXV(PX2(I))
ISN 0025              IY2=NYV(PHS(I))
ISN 0026              CALL LINEV(IX1,IY1,IXP2,IY2)
ISN 0027              CALL LINEV(IX1,IY1,IXP2,IY2)
ISN 0028              IX1=IXP2
ISN 0029      30      IY1=IY2
ISN 0030              RETURN
ISN 0031              END
```

```
0001                    SUBROUTINE VCROSS(A,B,C)
0002                    REAL*4 A(3),B(3),C(3)
0003                    C(1)=A(2)*B(3)-A(3)*B(2)
0004                    C(2)=A(3)*B(1)-A(1)*B(3)
0005                    C(3)=A(1)*B(2)-A(2)*B(1)
0006                    RETURN
0007                    END
```

A-12

C75-664/034A

```
0001                    SUBROUTINE VNORM(A,B,VM)
0002                    REAL*4 A(3),B(3)
0003                    VM=SQRT(A(1)**2+A(2)**2+A(3)**2)
0004                    B(1)=A(1)/VM
0005                    B(2)=A(2)/VM
0006                    B(3)=A(3)/VM
0007                    RETURN
0008                    END
```

A-13

C75-664/034A

```
             C****   COMPUTE MAIN REFLECTOR CURRENTS AND FAR FIELD PATTERNS OF A
             C****   TORUS/GREGORIAN REFLECTOR SYSTEM
             C****   PROGRAM MAKES USE OF JX = -JX ACROSS SYMMETRY LINE
ISN 0002            INTEGER*4 NX(46)
ISN 0003            REAL*4 RRX(600),RRY(600),RRZ(600),JSX(600),JSY(600),JSZ(600)
                   1 ,PATH(600),JMAG(20,20),PWP(75),PWT(75),Y(46,46),HP(17,75),
                   2 HC(17,75),JMGX,WT(17)
ISN 0004            COMPLEX*8 HPX,HPY,HPZ,HVX,HVY,HVZ,HHX,HHY,HHZ,CNX,CNY,CNZ,CARX,
                   1 CARY,CARZ,TWDS,HFX,HFY,HFZ,CTEMP,JMX(46,46),JMY(46,46),
                   2 JMZ(46,46),CSTB(3142)
ISN 0005            DATA PI,CL,DRAD,ETA/3.141593,2.997925E-1,57.29578,376.731/
ISN 0006            DTH=2.*PI/3142.
ISN 0007            DO 5 I=1,3142
ISN 0008            TP=DTH*(FLOAT(I)-0.5)
ISN 0009        5   CSTB(I)=CMPLX(COS(TP),SIN(TP))
ISN 0010       10   READ(5,20,END=210) NXM,NZ,NPR,NPTS,NCUTS,DX,DZ,DTHD,DPHD,PHIOD,
                   1 TBD,WT
ISN 0011       20   FORMAT(5I4,4X,4F12.0/2F12.0/17F3.0)
ISN 0012            READ(9,30) NTH,NTRL,NSUB,F,H,S,THPD,YYS,ZZS,XM,ZB,ZM,DELTH,RO,
                   1 FREQ,A,B,PKGN
ISN 0013       30   FORMAT(3I4,5F12.0/(6F12.0))
ISN 0014            I=0
ISN 0015       40   I=I+1
ISN 0016            READ(9,50,END=60) RRX(I),RRY(I),RRZ(I),JSX(I),JSY(I),JSZ(I),PATH(
                   1 I),ICRD
ISN 0017       50   FORMAT(7F14.0,I8)
ISN 0018            GO TO 40
ISN 0019       60   I=I-1
ISN 0020            WRITE(6,70) NXM,NZ,NPR,NPTS,NCUTS,DX,DZ,DTHD,DPHD,PHIOD,TBD,WT,
                   1 NTH,NTRL,NSUB,F,H,S,THPD,YYS,ZZS,XM,ZB,ZM,DELTH,RO,FREQ,A,B,PKGN,
                   2 I
ISN 0021       70   FORMAT('1',5X,'CARD INPUT PARAMETERS'/6X,'NXM=',I4,12X,'NZ=',I4,
                   1 13X,'NPR=',I3,13X,'NPTS=',I4,11X,'NCUTS=',I4/6X,'DX=',F8.5,9X,
                   2 'DZ=',F8.5,9X,'DTHD=',F8.5,7X,'DPHD=',F9.4,6X,'PHIOD=',F9.4/6X,
                   3 'TBD=',F9.4/6X,'CUT WEIGHTS=',17F5.1/'0',
```

```
                        4 5X,'STORAGE INPUT PARAMETERS'/6X,'NTH=',I3,13X,'NTRL=',I2,13X,
                        5 'NSUB=',I5,10X,'F=',F9.6,9X,'H=',F9.6/6X,'S=',F9.6,9X,'THPD=',
                        6 F8.4,7X,'YYS=',F9.6,7X,'ZZS=',F9.6,7X,'XM=',F9.6/6X,'ZB=',F9.6,
                        7 8X,'ZM=',F9.6,8X,'DELTH=',F9.6,5X,'R0=',F9.6,8X,'FREQ=',F9.4/6X,
                        8 'A=',F9.6,9X,'B=',F9.6,9X,'PKGN=',F9.5/6X,'NUMBER OF SUBREFLECT',
                        9 'OR POINTS READ=',I4)
              C****   COMPUTE MAIN REFLECTOR CURRENTS * * *   JMX,JMY,JMZ ARE JS*DS
ISN 0022              RECWL=FREQ/CL
ISN 0023              EK=2.*PI*RECWL
ISN 0024              R04PI=R0/(4.*PI)
ISN 0025              THMD=DTHD*FLOAT(NPTS)
ISN 0026              DTH=DTHD/DRAD
ISN 0027              DPH=DPHD/DRAD
ISN 0028              PHIO=PHIOD/DRAD
ISN 0029              TB=TBD/DRAD
ISN 0030              STB=SIN(TB)
ISN 0031              CTB=COS(TB)
ISN 0032              JMGX=0.
ISN 0033              CALL COUNTV
ISN 0034              DO 90 I=1,NZ
ISN 0035              Z=DZ*(FLOAT(I)-0.5)
ISN 0036              XM=1.-Z**2/2.
ISN 0037              NX(I)=2*MINO(NXM,INT(XM/DX))
ISN 0038              JM=NX(I)
ISN 0039              JH=JM/2
ISN 0040              JHP1=JH+1
ISN 0041              DO 85 J=1,JH
ISN 0042              JMH=J-JH
ISN 0043              X=DX*(FLOAT(JMH)-0.5)
ISN 0044              Y(I,J)=SQRT((1.-Z**2/2.)**2-X**2)
ISN 0045              T1=SQRT(1.+Z**2)
ISN 0046              T2=T1*SQRT(X**2+Y(I,J)**2)
ISN 0047              T3=Y(I,J)/T2
ISN 0048              CNX=CMPLX(-X/T2,0.)
ISN 0049              CNY=CMPLX(-T3,0.)
ISN 0050              CNZ=CMPLX(-Z/T1,0.)
ISN 0051              TWDS=CMPLX(2.*DX*DZ*R0**2/T3,0.)
ISN 0052              PX=X
ISN 0053              PY=Y(I,J)-F
ISN 0054              PZ=Z+H
```

```
ISN 0055          HPX=(0.,0.)
ISN 0056          HPY=(0.,0.)
ISN 0057          HPZ=(0.,0.)
ISN 0058          DO 80 K=1,NSUB
ISN 0059          SMX=PX-RRX(K)
ISN 0060          SMY=PY-RRY(K)
ISN 0061          SMZ=PZ-RRZ(K)
ISN 0062          RSM=R0*SQRT(SMX**2+SMY**2+SMZ**2)
ISN 0063          T1=RECWL*(RSM+PATH(K))
ISN 0064          IT1=3143-INT(3142.*(T1-AINT(T1))+1.0)
ISN 0065          T2=R04PI/RSM**2
ISN 0066          CTEMP=CMPLX(T2/RSM,T2*EK)*CSTB(IT1)
ISN 0067          VTX=JSY(K)*SMZ-JSZ(K)*SMY
ISN 0068          VTY=JSZ(K)*SMX-JSX(K)*SMZ
ISN 0069          VTZ=JSX(K)*SMY-JSY(K)*SMX
ISN 0070          HPX=HPX+CTEMP*VTX
ISN 0071          HPY=HPY+CTEMP*VTY
ISN 0072     80   HPZ=HPZ+CTEMP*VTZ
ISN 0073          JMX(I,J)=TWDS*(CNY*HPZ-CNZ*HPY)
ISN 0074          JMY(I,J)=TWDS*(CNZ*HPX-CNX*HPZ)
ISN 0075     85   JMZ(I,J)=TWDS*(CNX*HPY-CNY*HPX)
          C       IF(J.LE.JH) GO TO 90          (REPLACE IF NO SYMMETRY)
ISN 0076          DO 90 J=JHP1,JM
ISN 0077          JMH=J-JH
ISN 0078          JC=JM-J+1
ISN 0079          Y(I,J)=Y(I,JC)
ISN 0080          JMX(I,J)=-JMX(I,JC)
ISN 0081          JMY(I,J)=JMY(I,JC)
ISN 0082          JMZ(I,J)=JMZ(I,JC)
ISN 0083          IPR=I/NPR
ISN 0084          JPR=JMH/NPR
ISN 0085          IF((NPR*IPR.NE.I).OR.(NPR*JPR.NE.JMH)) GO TO 90
ISN 0087          JMAG(IPR,JPR)=SQRT(REAL(JMX(I,J)*CONJG(JMX(I,J))+JMY(I,J)*
         1 CONJG(JMY(I,J))+JMZ(I,J)*CONJG(JMZ(I,J))))
ISN 0088          IF(JMAG(IPR,JPR).GT.JMGX) JMGX=JMAG(IPR,JPR)
ISN 0090     90   CONTINUE
ISN 0091          CALL TIMEV(ELTIME)
ISN 0092          WRITE(6,95) ELTIME
ISN 0093     95   FORMAT('0',5X,'COMPUTATION OF MAIN REFLECTOR CURRENTS IS NOW ',
         1 'COMPLETE. ELAPSED TIME=',F8.3,' SECONDS'/'0',5X,'AMPLITUDE MAP '
```

C75-664./034A

```
                          2 ,'OF MAIN REFLECTOR CURRENT')
ISN 0094              IM=NZ/NPR
ISN 0095              DO 110 I=1,IM
ISN 0096              JM=NX(I)/(2*NPR)
ISN 0097              DO 100 J=1,JM
ISN 0098        100   JMAG(I,J)=20.*ALOG10(AMAX1(0.001,JMAG(I,J)/JMGX))
ISN 0099        110   WRITE(6,120) I,(JMAG(I,J),J=1,JM)
ISN 0100        120   FORMAT(I5,1X,20F5.1/(6X,20F5.1))
                C****   COMPUTE FAR FIELD PATTERN
ISN 0101              HTM=0.
ISN 0102              DO 130 J=1,NPTS
ISN 0103              PWP(J)=0.
ISN 0104        130   PWT(J)=0.
ISN 0105              DO 150 I=1,NCUTS
ISN 0106              PP=PHI0+DPH*FLOAT(I-1)
ISN 0107              SPP=SIN(PP)
ISN 0108              CPP=COS(PP)
ISN 0109              DO 150 J=1,NPTS
ISN 0110              TP=DTH*(FLOAT(J)-0.5)
ISN 0111              STP=SIN(TP)
ISN 0112              CTP=COS(TP)
ISN 0113              ARX=STP*CPP
ISN 0114              CARX=CMPLX(ARX,0.)
ISN 0115              ARY=CTB*STP*SPP-STB*CTP
ISN 0116              CARY=CMPLX(ARY,0.)
ISN 0117              ARZ=STB*STP*SPP+CTB*CTP
ISN 0118              CARZ=CMPLX(ARZ,0.)
ISN 0119              ST=SQRT(ARX**2+ARZ**2)
ISN 0120              CT=-ARY
ISN 0121              SP=ARZ/ST
ISN 0122              CP=ARX/ST
ISN 0123              HVX=CMPLX(-CT*CP**2-SP**2,0.)
ISN 0124              HVY=CMPLX(-ST*CP,0.)
ISN 0125              HVZ=CMPLX(SP*CP*(1.-CT),0.)
ISN 0126              HHX=-HVZ
ISN 0127              HHY=CMPLX(ST*SP,0.)
ISN 0128              HHZ=CMPLX(CP**2+CT*SP**2,0.)
ISN 0129              HFX=(0.,0.)
ISN 0130              HFY=(0.,0.)
ISN 0131              HFZ=(0.,0.)
```

```
ISN 0132            DO 140 II=1,NZ
ISN 0133            Z=DZ*(FLOAT(II)-0.5)
ISN 0134            JM=NX(II)
ISN 0135            JH=JM/2
ISN 0136            DO 140 JJ=1,JM
ISN 0137            X=DX*(FLOAT(JJ-JH)-0.5)
ISN 0138            T1=RECWL*R0*(X*ARX+Y(II,JJ)*ARY+Z*ARZ)
ISN 0139            T2=T1-AINT(T1)
ISN 0140            IF(T2) 133,136,136
ISN 0141      133   T2=T2+1.
ISN 0142      136   IT1=INT(3142.*T2+1.0)
ISN 0143            CTEMP=CSTB(IT1)
ISN 0144            HFX=HFX+CTEMP*(JMY(II,JJ)*CARZ-JMZ(II,JJ)*CARY)
ISN 0145            HFY=HFY+CTEMP*(JMZ(II,JJ)*CARX-JMX(II,JJ)*CARZ)
ISN 0146      140   HFZ=HFZ+CTEMP*(JMX(II,JJ)*CARY-JMY(II,JJ)*CARX)
ISN 0147            HP(I,J)=EK*CABS(HVX*HFX+HVY*HFY+HVZ*HFZ)/(4.*PI)
ISN 0148            HC(I,J)=EK*CABS(HHX*HFX+HHY*HFY+HHZ*HFZ)/(4.*PI)
ISN 0149            HTOT=SQRT(HP(I,J)**2+HC(I,J)**2)
ISN 0150            IF(HTOT.GT.HTM) HTM=HTOT
ISN 0152            PWP(J)=PWP(J)+STP*ETA*WT(I)*HP(I,J)**2
ISN 0153      150   PWT(J)=PWT(J)+STP*ETA*WT(I)*HTOT**2
ISN 0154            GDB=10.*ALOG10(4.*PI*ETA*HTM**2)
ISN 0155            CALL TIMEV(ELTIME)
ISN 0156            WRITE(6,160) GDB,ELTIME
ISN 0157      160   FORMAT('0',5X,'COMPUTATION OF PATTERNS IS NOW COMPLETE'/6X,
                   1 'PEAK GAIN=',F9.5,' DB',10X,'ELAPSED TIME=',F8.3,' SECONDS')
ISN 0158            CALL DXDYV(1,0.,THMD,DXDX,NDX,IDX,NXDX,20.0,IERR)
ISN 0159            DO 190 I=1,NCUTS
ISN 0160            PPD=PHIOD+DPHD*FLOAT(I-1)
ISN 0161            CALL GRID1V(1,0.,THMD,-40.,0.,DXDX,2.,NDX,5,IDX,5,NXDX,3)
ISN 0162            DO 180 J=1,NPTS
ISN 0163            TPD=DTHD*(FLOAT(J)-0.5)
ISN 0164            IX2=NXV(TPD)
ISN 0165            IYP2=NYV(20.*ALOG10(AMAX1(0.01,HP(I,J)/HTM)))
ISN 0166            IYC2=NYV(20.*ALOG10(AMAX1(0.01,HC(I,J)/HTM)))
ISN 0167            IF(J.EQ.1) GO TO 170
ISN 0169            CALL LINEV(IX1,IYP1,IX2,IYP2)
ISN 0170            CALL LINEV(IX1,IYP1,IX2,IYP2)
ISN 0171            CALL LINEV(IX1,IYC1,IX2,IYC2)
ISN 0172            CALL LINEV(IX1,IYC1,IX2,IYC2)
```

C75-664/034A

```
ISN 0173      170    IX1=IX2
ISN 0174             IYP1=IYP2
ISN 0175      180    IYC1=IYC2
ISN 0176             CALL PRINTV(4,'PHI=',10,0)
ISN 0177             CALL LABLV(PPD,42,0,6,1,3)
ISN 0178      190    CALL PRINTV(7,'DEGREES',98,0)
ISN 0179             PWP(1)=PWP(1)*DPH*DTH
ISN 0180             PWT(1)=PWT(1)*DPH*DTH
ISN 0181             DO 193 I=2,NPTS
ISN 0182             PWP(I)=PWP(I)*DPH*DTH+PWP(I-1)
ISN 0183      193    PWT(I)=PWT(I)*DPH*DTH+PWT(I-1)
ISN 0184             WRITE(6,196) (PWP(I),I=1,NPTS)
ISN 0185      196    FORMAT('0',5X,'PRINCIPLE POLARIZED POWER'/(3X,15F7.4))
ISN 0186             WRITE(6,198) (PWT(I),I=1,NPTS)
ISN 0187      198    FORMAT('0',5X,'TOTAL POWER'/(3X,15F7.4))
ISN 0188             CALL GRID1V(1,0.,THMD,0.,1.,DXDX,0.05,NDX,2,IDX,4,NXDX,3)
ISN 0189             IX1=NXV(DTHD)
ISN 0190             IYP1=NYV(PWP(1))
ISN 0191             IYC1=NYV(PWT(1))
ISN 0192             DO 200 J=2,NPTS
ISN 0193             IX2=NXV(DTHD*FLOAT(J))
ISN 0194             IYP2=NYV(PWP(J))
ISN 0195             IYC2=NYV(PWT(J))
ISN 0196             CALL LINEV(IX1,IYP1,IX2,IYP2)
ISN 0197             CALL LINEV(IX1,IYP1,IX2,IYP2)
ISN 0198             CALL LINEV(IX1,IYC1,IX2,IYC2)
ISN 0199             CALL LINEV(IX1,IYC1,IX2,IYC2)
ISN 0200             IX1=IX2
ISN 0201             IYP1=IYP2
ISN 0202      200    IYC1=IYC2
ISN 0203             GO TO 10
ISN 0204      210    STOP
ISN 0205             END
```

```
0001                  REAL*4 STP(4),STM(4)
0002                  DATA PI,CL,ETA,STM/3.141593,2.997925E-1,376.731,1.0,0.0,1.0,0.0/
0003          10      READ(5,20,END=60) NTP,A,B,FREQ
0004          20      FORMAT(I12,3F12.0)
0005                  WRITE(6,30) NTP,A,B,FREQ
0006          30      FORMAT('1',5X,'NTP=',I5,5X,'A=',1PE14.6,5X,'B=',E14.6,5X,'FREQ=',
                     1 E14.6)
0007                  EK=2.*PI*FREQ/CL
0008                  DTP=PI/FLOAT(NTP)
0009                  P=0.
0010                  DO 40 I=1,NTP
0011                  TH=DTP*(FLOAT(I)-0.5)
0012                  STP(1)=SIN(TH)
0013                  STP(2)=COS(TH)
0014                  DO 40 J=1,NTP
0015                  PH=DTP*(FLOAT(J)-0.5)
0016                  STP(3)=SIN(PH)
0017                  STP(4)=COS(PH)
0018                  CALL PRIPAT(STP,A,B,EK,1.,HT,HP)
0019          40      P=P+STP(1)*(HT**2+HP**2)
0020                  P=P*ETA*DTP**2
0021                  CALL PRIPAT(STM,A,B,EK,1.,HT,HP)
0022                  PMAX=ETA*(HT**2+HP**2)
0023                  DIR=4.*PI*PMAX/P
0024                  DBDIR=10.*ALOG10(DIR)
0025                  WRITE(6,50) DIR,DBDIR
0026          50      FORMAT(6X,'DIRECTIVITY=',F10.5,5X,'DB=',F7.3)
0027                  GO TO 10
0028          60      STOP
0029                  END
```

```
            C****   FAR FIELD PATTERN OF A PARABOLIC TORUS REFLECTOR WITH A PRIME
            C            FOCUS FEED
ISN 0002          INTEGER*4 NX(46)
ISN 0003          REAL*4 JMGX,JMAG(20,20),JPHS(20,20),PWP(75),XF(19),YF(19),PWT(75),
                 1 Y(46,46),HP(17,75),HC(17,75),WT(17),SCA(4),DB(75)
ISN 0004          COMPLEX*8 HVX,HVY,HVZ,HHX,HHY,HHZ,CNX,CNY,CNZ,CARX,CARY,CARZ,TWDS,
                 1 HFX,HFY,HFZ,HXF,HYF,HZF,HPX,HPY,HPZ,CTEMP,CSTP,CCTP,CFRA,
                 2 JMX(46,46),JMY(46,46),JMZ(46,46),CSTB(3142),AC(19)
ISN 0005          DATA PI,CL,DRAD,ETA/3.141593,2.997925E-1,57.29578,376.731/
ISN 0006          DTH=PI/1571.
ISN 0007          DO 10 I=1,3142
ISN 0008          TP=DTH*(FLOAT(I)-0.5)
ISN 0009    10    CSTB(I)=CMPLX(COS(TP),SIN(TP))
ISN 0010    20    READ(5,30,END=250) IE,NE,NXM,NZ,NPR,NPTS,NCUTS,FD,HD,TPD,RO,
                 1 FREQ,PD,DX,DZ,DTHD,DPHD,PHIOD,TBD,WT,(XF(I),YF(I),AC(I),I=1,NE)
ISN 0011    30    FORMAT(7I3,3X,4F12.0/6F12.0/2F12.0/17F3.0/(4F15.0))
ISN 0012          WRITE(6,40) IE,NE,NXM,NZ,NPR,NPTS,NCUTS,FD,HD,TPD,RO,FREQ,PD,DX,
                 1 DZ,DTHD,DPHD,PHIOD,TBD,WT,(XF(I),YF(I),AC(I),I=1,NE)
ISN 0013    40    FORMAT('1',5X,'ELEMENT TYPE=',I2,10X,'NUMBER OF ELEMENTS=',I3,3X,
                 1 'MAX REFL X SEGMENTS=',I3,2X,'REFL Z SEGMENTS=',I3/6X,'N INCR F',
                 2 'OR PRINT=',I2,6X,'NO PTS PER CUT=',I3,7X,'NUMBER OF CUTS=',I3,7X
                 3 ,'FEED RADIUS=',F6.4/6X,'FEED DEPRESSION=',F6.4,3X,'FEED ANGLE=',
                 4 F6.2,8X,'REFLECTOR RADIUS=',F6.3,2X,'FREQUENCY=',F8.3/6X,'FEED ',
                 5 'DIRECT.=',F9.5,3X,'X INCREMENT=',F8.5,5X,'Z INCREMENT=',F8.5,
                 6 5X,'TH INCREMENT=',F8.5/6X,'PH INCREMENT=',F8.5,4X,'INITIAL PH=',
                 7 F8.3,6X,'BEAM CL ANGLE=',F8.4/6X,'CUT WEIGHTS=',17F4.1/12X,'XF',
                 8 16X,'YF',14X,'A-REAL',12X,'A-IMAG'/(' ',1P4E18.6))
            C****   CALCULATE CONSTANTS
ISN 0014          RECWL=FREQ/CL
ISN 0015          EK=2.*PI*RECWL
ISN 0016          TP=TPD/DRAD
ISN 0017          STP=SIN(TP)
ISN 0018          CTP=COS(TP)
ISN 0019          CSTP=CMPLX(STP,0.)
ISN 0020          CCTP=CMPLX(CTP,0.)
```

C75-664/034A

```
ISN 0021          THMD=DTHD*FLOAT(NPTS)
ISN 0022          DTH=DTHD/DRAD
ISN 0023          DPH=DPHD/DRAD
ISN 0024          PHIO=PHIOD/DRAD
ISN 0025          TB=TBD/DRAD
ISN 0026          STB=SIN(TB)
ISN 0027          CTB=COS(TB)
          C****   CALCULATE MAIN REFLECTOR CURRENTS * * * JMX,JMY,JMZ ARE JS*DS
ISN 0028          JMGX=0.
ISN 0029          CALL COUNTV
ISN 0030          DO 75 I=1,NZ
ISN 0031          Z=DZ*(FLOAT(I)-0.5)
ISN 0032          XM=1.-Z**2/2.
ISN 0033          NX(I)=2.*MINO(NXM,INT(XM/DX))
ISN 0034          JM=NX(I)
ISN 0035          JH=JM/2
ISN 0036          JHP1=JH+1
ISN 0037          DO 50 J=1,JH
ISN 0038          JMH=J-JH
ISN 0039          X=DX*(FLOAT(JMH)-0.5)
ISN 0040          Y(I,J)=SQRT((1.-Z**2/2.)**2-X**2)
ISN 0041          T1=SQRT(1.+Z**2)
ISN 0042          T2=T1*SQRT(X**2+Y(I,J)**2)
ISN 0043          T3=Y(I,J)/T2
ISN 0044          CNX=CMPLX(-X/T2,0.)
ISN 0045          CNY=CMPLX(-T3,0.)
ISN 0046          CNZ=CMPLX(-Z/T1,0.)
ISN 0047          TWDS=CMPLX(2.*DX*DZ*R0**2/T3,0.)
ISN 0048          FRX=X
ISN 0049          FRY=Y(I,J)-FD
ISN 0050          FRZ=Z+HD
ISN 0051          FRM=SQRT(FRX**2+FRY**2+FRZ**2)
ISN 0052          T1=FRM*R0
ISN 0053          T2=-EK*T1
ISN 0054          CFRA=CMPLX(COS(T2)/T1,SIN(T2)/T1)
ISN 0055          CTF=(FRZ*CTP+FRY*STP)/FRM
ISN 0056          IF(CTF.LE.0.) GO TO 45
ISN 0058          SC=-FRX/FRM
ISN 0059          SS=(FRZ*STP-FRY*CTP)/FRM
ISN 0060          PF=ATAN2(SS,SC)
```

C75-664/034A

```
ISN 0061            STF=SQRT(SS**2+SC**2)
ISN 0062            SCA(1)=STF
ISN 0063            SCA(2)=CTF
ISN 0064            SCA(3)=SIN(PF)
ISN 0065            SCA(4)=COS(PF)
ISN 0066            CALL PRIPAT(SCA,IE,NE,XF,YF,AC,EK,PD,HXF,HYF,HZF)
ISN 0067            HPX=-HXF*CFRA
ISN 0068            HPY=(HZF*CSTP-HYF*CCTP)*CFRA
ISN 0069            HPZ=(HZF*CCTP+HYF*CSTP)*CFRA
ISN 0070            JMX(I,J)=TWDS*(CNY*HPZ-CNZ*HPY)
ISN 0071            JMY(I,J)=TWDS*(CNZ*HPX-CNX*HPZ)
ISN 0072            JMZ(I,J)=TWDS*(CNX*HPY-CNY*HPX)
ISN 0073            GO TO 50
ISN 0074      45    JMX(I,J)=(0.,0.)
ISN 0075            JMY(I,J)=(0.,0.)
ISN 0076            JMZ(I,J)=(0.,0.)
ISN 0077      50    CONTINUE
ISN 0078            DO 75 J=JHP1,JM
ISN 0079            JMH=J-JH
ISN 0080            JC=JM-J+1
ISN 0081            Y(I,J)=Y(I,JC)
ISN 0082            JMX(I,J)=-JMX(I,JC)
ISN 0083            JMY(I,J)=JMY(I,JC)
ISN 0084            JMZ(I,J)=JMZ(I,JC)
ISN 0085            IPR=I/NPR
ISN 0086            JPR=JMH/NPR
ISN 0087            IF((NPR*IPR.NE.I).OR.(NPR*JPR.NE.JMH)) GO TO 75
ISN 0089            JMAG(IPR,JPR)=SQRT(REAL(JMX(I,J)*CONJG(JMX(I,J))+JMY(I,J)*
                   1 CONJG(JMY(I,J))+JMZ(I,J)*CONJG(JMZ(I,J))))
ISN 0090            IF(JMAG(IPR,JPR).GT.JMGX) JMGX=JMAG(IPR,JPR)
ISN 0092            T1=EK*R0*(Z*CTB-Y(I,J)*STB)
ISN 0093            IF(IE.EQ.1 .OR. IE.EQ.3) GO TO 60
ISN 0095            CTEMP=JMX(I,J)*CMPLX(COS(T1),SIN(T1))
ISN 0096            GO TO 70
ISN 0097      60    CTEMP=JMY(I,J)*CMPLX(COS(T1),SIN(T1))
ISN 0098      70    JPHS(IPR,JPR)=ATAN2(AIMAG(CTEMP),REAL(CTEMP))
ISN 0099      75    CONTINUE
ISN 0100            CALL TIMEV(ELTIME)
ISN 0101            WRITE(6,80) ELTIME
ISN 0102      80    FORMAT('0',5X,'COMPUTATION OF MAIN REFLECTOR CURRENTS IS NOW C',
```

```
                          1 'OMPLETE. ELAPSED TIME=',F8.3,' SECONDS'/'0',5X,'AMPLITUDE/PHASE'
                          2 ,' MAP OF MAIN REFLECTOR CURRENT')
ISN 0103                  IM=NZ/NPR
ISN 0104                  DO 100 I=1,IM
ISN 0105                  JM=NX(I)/(2*NPR)
ISN 0106                  DO 90 J=1,JM
ISN 0107        90        JMAG(I,J)=20.*ALOG10(AMAX1(0.001,JMAG(I,J)/JMGX))
ISN 0108                  WRITE(6,95) I,(JMAG(I,J),J=1,JM)
ISN 0109        95        FORMAT('0',I4,1X,20F5.1)
ISN 0110        100       WRITE(6,110) (JPHS(I,J),J=1,JM)
ISN 0111        110       FORMAT(6X,20F5.2)
ISN 0112                  HTM=0.
ISN 0113                  DO 120 J=1,NPTS
ISN 0114                  PWP(J)=0.
ISN 0115        120       PWT(J)=0.
ISN 0116                  DO 160 I=1,NCUTS
ISN 0117                  PP=PHIO+DPH*FLOAT(I-1)
ISN 0118                  SPP=SIN(PP)
ISN 0119                  CPP=COS(PP)
ISN 0120                  DO 160 J=1,NPTS
ISN 0121                  TP=DTH*(FLOAT(J)-0.5)
ISN 0122                  STP=SIN(TP)
ISN 0123                  CTP=COS(TP)
ISN 0124                  ARX=STP*CPP
ISN 0125                  CARX=CMPLX(ARX,0.)
ISN 0126                  ARY=CTB*STP*SPP-STB*CTP
ISN 0127                  CARY=CMPLX(ARY,0.)
ISN 0128                  ARZ=STB*STP*SPP+CTB*CTP
ISN 0129                  CARZ=CMPLX(ARZ,0.)
ISN 0130                  ST=SQRT(ARX**2+ARZ**2)
ISN 0131                  CT=-ARY
ISN 0132                  SP=ARZ/ST
ISN 0133                  CP=ARX/ST
ISN 0134                  HVX=CMPLX(-CT*CP**2-SP**2,0.)
ISN 0135                  HVY=CMPLX(-ST*CP,0.)
ISN 0136                  HVZ=CMPLX(SP*CP*(1.-CT),0.)
ISN 0137                  HHX=-HVZ
ISN 0138                  HHY=CMPLX(ST*SP,0.)
ISN 0139                  HHZ=CMPLX(CP**2+CT*SP**2,0.)
ISN 0140                  HFX=(0.,0.)
```

C75-664/034A

```
ISN 0141          HFY=(0.,0.)
ISN 0142          HFZ=(0.,0.)
ISN 0143          DO 150 II=1,NZ
ISN 0144          Z=DZ*(FLOAT(II)-0.5)
ISN 0145          JM=NX(II)
ISN 0146          JH=JM/2
ISN 0147          DO 150 JJ=1,JM
ISN 0148          X=DX*(FLOAT(JJ-JH)-0.5)
ISN 0149          T1=RECWL*RO*(X*ARX+Y(II,JJ)*ARY+Z*ARZ)
ISN 0150          T2=T1-AINT(T1)
ISN 0151          IF(T2) 130,140,140
ISN 0152      130 T2=T2+1.
ISN 0153      140 IT1=INT(3142.*T2+1.0)
ISN 0154          CTEMP=CSTB(IT1)
ISN 0155          HFX=HFX+CTEMP*(JMY(II,JJ)*CARZ-JMZ(II,JJ)*CARY)
ISN 0156          HFY=HFY+CTEMP*(JMZ(II,JJ)*CARX-JMX(II,JJ)*CARZ)
ISN 0157      150 HFZ=HFZ+CTEMP*(JMX(II,JJ)*CARY-JMY(II,JJ)*CARX)
ISN 0158          HP(I,J)=EK*CABS(HVX*HFX+HVY*HFY+HVZ*HFZ)/(4.*PI)
ISN 0159          HC(I,J)=EK*CABS(HHX*HFX+HHY*HFY+HHZ*HFZ)/(4.*PI)
ISN 0160          HTOT=SQRT(HP(I,J)**2+HC(I,J)**2)
ISN 0161          IF(HTOT.GT.HTM) HTM=HTOT
ISN 0163          PWP(J)=PWP(J)+STP*ETA*WT(I)*HP(I,J)**2
ISN 0164      160 PWT(J)=PWT(J)+STP*ETA*WT(I)*HTOT**2
ISN 0165          GDB=10.*ALOG10(4.*PI*ETA*HTM**2)
ISN 0166          CALL TIMEV(ELTIME)
ISN 0167          WRITE(6,170) GDB,ELTIME
ISN 0168      170 FORMAT('0',5X,'COMPUTATION OF PATTERNS IS NOW COMPLETE'/6X,
                1 'PEAK GAIN=',F9.5,' DB',10X,'ELAPSED TIME=',F8.3,' SECONDS'/'0',
                2 5X,'PATTERN CUTS FOR PRINCIPLE POLARIZATION')
ISN 0169          CALL DXDYV(1,0.,THMD,DXDX,NDX,IDX,NXDX,20.0,IERR)
ISN 0170          DO 200 I=1,NCUTS
ISN 0171          PPD=PHIOD+DPHD*FLOAT(I-1)
ISN 0172          CALL GRID1V(1,0.,THMD,-40.,0.,DXDX,2.,NDX,5,IDX,5,NXDX,3)
ISN 0173          DO 190 J=1,NPTS
ISN 0174          TPD=DTHD*(FLOAT(J)-0.5)
ISN 0175          IX2=NXV(TPD)
ISN 0176          DB(J)=20.*ALOG10(AMAX1(0.01,HP(I,J)/HTM))
ISN 0177          IYP2=NYV(DB(J))
ISN 0178          IYC2=NYV(20.*ALOG10(AMAX1(0.01,HC(I,J)/HTM)))
ISN 0179          IF(J.EQ.1) GO TO 180
```

```
ISN 0181              CALL LINEV(IX1,IYP1,IX2,IYP2)
ISN 0182              CALL LINEV(IX1,IYP1,IX2,IYP2)
ISN 0183              CALL LINEV(IX1,IYC1,IX2,IYC2)
ISN 0184              CALL LINEV(IX1,IYC1,IX2,IYC2)
ISN 0185      180     IX1=IX2
ISN 0186              IYP1=IYP2
ISN 0187      190     IYC1=IYC2
ISN 0188              CALL PRINTV(4,'PHI=',10,0)
ISN 0189              CALL LABLV(PPD,42,0,6,1,3)
ISN 0190              CALL PRINTV(7,'DEGREES',98,0)
ISN 0191      200     WRITE(6,205) I,(DB(J),J=1,NPTS)
ISN 0192      205     FORMAT('0',1X,I2,15F7.2/(4X,15F7.2))
ISN 0193              PWP(1)=PWP(1)*DPH*DTH
ISN 0194              PWT(1)=PWT(1)*DPH*DTH
ISN 0195              DO 210 I=2,NPTS
ISN 0196              PWP(I)=PWP(I)*DPH*DTH+PWP(I-1)
ISN 0197      210     PWT(I)=PWT(I)*DPH*DTH+PWT(I-1)
ISN 0198              WRITE(6,220) (PWP(I),I=1,NPTS)
ISN 0199      220     FORMAT('0',5X,'PRINCIPLE POLARIZED POWER'/(4X,15F7.4))
ISN 0200              WRITE(6,230) (PWT(I),I=1,NPTS)
ISN 0201      230     FORMAT('0',5X,'TOTAL POWER'/(4X,15F7.4))
ISN 0202              CALL GRID1V(1,0.,THMD,9.,1.,DXDX,0.05,NDX,2,IDX,4,NXDX,3)
ISN 0203              IX1=NXV(DTHD)
ISN 0204              IYP1=NYV(PWP(1))
ISN 0205              IYC1=NYV(PWT(1))
ISN 0206              DO 240 J=2,NPTS
ISN 0207              IX2=NXV(DTHD*FLOAT(J))
ISN 0208              IYP2=NYV(PWP(J))
ISN 0209              IYC2=NYV(PWT(J))
ISN 0210              CALL LINEV(IX1,IYP1,IX2,IYP2)
ISN 0211              CALL LINEV(IX1,IYP1,IX2,IYP2)
ISN 0212              CALL LINEV(IX1,IYC1,IX2,IYC2)
ISN 0213              CALL LINEV(IX1,IYC1,IX2,IYC2)
ISN 0214              IX1=IX2
ISN 0215              IYP1=IYP2
ISN 0216      240     IYC1=IYC2
ISN 0217              GO TO 20
ISN 0218      250     STOP
ISN 0219              END
```

```
ISN 0002          SUBROUTINE PRIPAT(STP,IE,NE,X,Y,A,EK,PD,HXF,HYF,HZF)
ISN 0003          REAL*4 X(19),Y(19),STP(4)
ISN 0004          COMPLEX*8 A(19),AF,HXF,HYF,HZF
ISN 0005          DATA PI,ETA/3.141593,376.731/
ISN 0006          AF=(0.,0.)
ISN 0007          DO 10 I=1,NE
ISN 0008          PHS=EK*STP(1)*(X(I)*STP(4)+Y(I)*STP(3))
ISN 0009   10     AF=AF+A(I)*CMPLX(COS(PHS),SIN(PHS))
ISN 0010          AF=AF*CMPLX(STP(2)**0.75*SQRT(PD/(4.*PI*ETA)),0.)
ISN 0011          GO TO (20,30,40,50),IE
           C****  IE=1  VERTICALLY POLARIZED SLOT ELEMENT
ISN 0012   20     STS=STP(1)**2
ISN 0013          CPS=STP(4)**2
ISN 0014          DENOM=SQRT(1.-STS*CPS)
ISN 0015          HNX=(STS*CPS-1.)/DENOM
ISN 0016          HNY=STS*STP(3)*STP(4)/DENOM
ISN 0017          HNZ=STP(1)*STP(2)*STP(4)/DENOM
ISN 0018          GO TO 60
           C****  IE=2  HORIZONTALLY POLARIZED SLOT ELEMENT
ISN 0019   30     STS=STP(1)**2
ISN 0020          SPS=STP(3)**2
ISN 0021          DENOM=SQRT(1.-STS*SPS)
ISN 0022          HNX=-STS*STP(3)*STP(4)/DENOM
ISN 0023          HNY=(1.-STS*SPS)/DENOM
ISN 0024          HNZ=-STP(1)*STP(2)*STP(3)/DENOM
ISN 0025          GO TO 60
           C****  IE=3  VERTICALLY POLARIZED DIPOLE ELEMENT
ISN 0026   40     DENOM=SQRT((STP(1)*STP(4))**2+STP(2)**2)
ISN 0027          HNX=-STP(2)/DENOM
ISN 0028          HNY=0.
ISN 0029          HNZ=STP(1)*STP(4)/DENOM
ISN 0030          GO TO 60
           C****  IE=4  HORIZONTALLY POLARIZED DIPOLE ELEMENT
ISN 0031   50     DENOM=SQRT((STP(1)*STP(3))**2+STP(2)**2)
ISN 0032          HNX=0.
```

C75-664/034A

```
ISN 0033          HNY=STP(2)/DENOM
ISN 0034          HNZ=-STP(1)*STP(3)/DENOM
ISN 0035     60   HXF=AF*CMPLX(HNX,0.)
ISN 0036          HYF=AF*CMPLX(HNY,0.)
ISN 0037          HZF=AF*CMPLX(HNZ,0.)
ISN 0038          RETURN
ISN 0039          END
```

C75-664/034A

```
              C****  EVALUATE PRIMARY PATTERNS AND CALCULATE DIRECTIVITY
ISN 0002             REAL*4 STP(4),DB(26),PP(26),A(19),P(19),X(19),Y(19),D(19)
ISN 0003             COMPLEX*8 AC(19),SUM,HXF,HYF,HZF,CTEMP,EJP
ISN 0004             DATA PI,CL,DRAD,ETA,SQ32,UB,DTH,DPH,DPB,D/3.141593,2.997925E-1,
                    1 57.29578,376.731,8.660254E-1,3.400,8.726646E-2,1.208305E-1,
                    2 1.047198,3.2686E-2,5.0762E-2,3.2686E-2,5.0762E-2,6.7215E-2,
                    3 6.7215E-2,5.0762E-2,3.2686E-2,6.7215E-2,9.6022E-2,6.7215E-2,
                    4 3.2686E-2,5.0762E-2,6.7215E-2,6.7215E-2,5.0762E-2,3.2686E-2,
                    5 5.0762E-2,3.2686E-2/
ISN 0005       10    READ(5,20,END=270) IE,NE,NTP,NC,FREQ,DE,(A(I),P(I),X(I),Y(I),I=1,
                    1 NC)
ISN 0006       20    FORMAT(4I3,2F12.0/(4F12.0))
ISN 0007             WRITE(6,30) IE,NE,NTP,NC,FREQ,DE,(A(I),P(I),X(I),Y(I),I=1,NC)
ISN 0008       30    FORMAT('1',5X,'IE=',I2,5X,'NE=',I3,4X,'NTP=',I2,4X,'NC=',I3,4X,
                    1 'FREQ=',F9.4,6X,'DE=',1PE14.6/13X,'A',19X,'P',19X,'X',19X,'Y'/
                    2 (' ',1P4E20.6))
ISN 0009             EK=2.*PI*FREQ/CL
ISN 0010             R=2.32*DE
ISN 0011             GO TO (40,70,100),NTP
ISN 0012       40    WRITE(6,50)
ISN 0013       50    FORMAT(6X,'AMPLITUDE AND PHASE OF ELEMENTS SPECIFIED'/'0',12X,
                    1 'X',19X,'Y',17X,'A-REAL',14X,'A-IMAG')
ISN 0014             DO 60 I=1,NE
ISN 0015       60    AC(I)=CMPLX(A(I)*COS(P(I)),A(I)*SIN(P(I)))
ISN 0016             GO TO 180
ISN 0017       70    WRITE(6,80)
ISN 0018       80    FORMAT(6X,'COMPLEX AMPLITUDE OF ELEMENTS SPECIFIED'/'0',12X,'X',
                    1 19X,'Y',17X,'A-REAL',14X,'A-IMAG')
ISN 0019             DO 90 I=1,NE
ISN 0020       90    AC(I)=CMPLX(A(I),P(I))
ISN 0021             GO TO 180
ISN 0022      100    WRITE(6,110)
ISN 0023      110    FORMAT(6X,'AMPLITUDE AND PHASE OF BEAMS SPECIFIED'/'0',12X,'X',
                    1 19X,'Y',17X,'A-REAL',14X,'A-IMAG')
ISN 0024             EJP=CMPLX(COS(P(1)),SIN(P(1)))
```

```
ISN 0025                DO 120 I=1,3
ISN 0026                X(I)=DE*FLOAT(I-2)
ISN 0027                Y(I)=-2.*DE*SQ32
ISN 0028         120    AC(I)=EJP*CMPLX(D(I)*A(1),0.)
ISN 0029                DO 130 I=4,7
ISN 0030                X(I)=DE*(FLOAT(I)-5.5)
ISN 0031                Y(I)=-DE*SQ32
ISN 0032         130    AC(I)=EJP*CMPLX(D(I)*A(1),0.)
ISN 0033                DO 140 I=8,12
ISN 0034                X(I)=DE*FLOAT(I-10)
ISN 0035                Y(I)=0.
ISN 0036         140    AC(I)=EJP*CMPLX(D(I)*A(1),0.)
ISN 0037                DO 150 I=13,16
ISN 0038                X(I)=DE*(FLOAT(I)-14.5)
ISN 0039                Y(I)=DE*SQ32
ISN 0040         150    AC(I)=EJP*CMPLX(D(I)*A(1),0.)
ISN 0041                DO 160 I=17,19
ISN 0042                X(I)=DE*FLOAT(I-18)
ISN 0043                Y(I)=2.*DE*SQ32
ISN 0044         160    AC(I)=EJP*CMPLX(D(I)*A(1),0.)
ISN 0045                DO 170 I=1,6
ISN 0046                IB=I+1
ISN 0047                PB=DPB*(FLOAT(I)-0.5)
ISN 0048                SP=SIN(PB)
ISN 0049                CP=COS(PB)
ISN 0050                DO 170 J=1,19
ISN 0051                PS=P(IB)-U6*(X(J)*CP+Y(J)*SP)/R
ISN 0052                CTEMP=CMPLX(D(J)*A(IB),0.)
ISN 0053         170    AC(J)=AC(J)+CTEMP*CMPLX(COS(PS),SIN(PS))
ISN 0054         180    SUM=(0.,0.)
ISN 0055                DO 190 I=1,NE
ISN 0056         190    SUM=SUM+AC(I)
ISN 0057                DO 200 I=1,NE
ISN 0058                AC(I)=AC(I)/SUM
ISN 0059                WRITE(6,195) X(I),Y(I),AC(I)
ISN 0060         195    FORMAT(' ',1P4E20.6)
ISN 0061         200    WRITE(14,210) X(I),Y(I),AC(I)
ISN 0062         210    FORMAT(1P4E15.6)
ISN 0063                PWR=0.
ISN 0064                DO 240 I=1,18
```

```
SN 0065                  TF=DTH*(FLOAT(I)-0.5)
SN 0066                  STP(1)=SIN(TF)
SN 0067                  STP(2)=COS(TF)
SN 0068                  DO 230 J=1,26
SN 0069                  PF=DPH*(FLOAT(J)-0.5)-PI/2.
SN 0070                  STP(3)=SIN(PF)
SN 0071                  STP(4)=COS(PF)
SN 0072                  CALL PRIPAT(STP,IE,NE,X,Y,AC,EK,1.,HXF,HYF,HZF)
SN 0073                  PINC=ETA*REAL(HXF*CONJG(HXF)+HYF*CONJG(HYF)+HZF*CONJG(HZF))
SN 0074                  PWR=PWR+STP(1)*PINC
SN 0075                  IF(IE.EQ.1 .OR. IE.EQ.3) GO TO 220
SN 0077                  PP(J)=ATAN2(AIMAG(HYF),REAL(HYF))
SN 0078                  GO TO 230
SN 0079            220   PP(J)=ATAN2(AIMAG(HXF),REAL(HXF))
SN 0080            230   DB(J)=10.*ALOG10(4.*PI*PINC)
SN 0081            240   WRITE(6,250) DB,PP
SN 0082            250   FORMAT('0',1X,26F5.1/2X,26F5.2)
SN 0083                  PD=0.5/(PWR*DTH*DPH)
SN 0084                  PDDB=10.*ALOG10(PD)
SN 0085                  WRITE(6,260) PD,PDDB
SN 0086            260   FORMAT(6X,'DIRECTIVITY=',F9.5,5X,'DB=',F7.3)
SN 0087                  GO TO 10
SN 0088            270   STOP
SN 0089                  END
```

3.50 (88²) DIA TBD

3.250 (82²⁵) DIA

4.200 (106⁴⁸) TBD SPH DIA

25° TBD

TBD

1.750 (44⁴⁵)

CLEAR

5.375 DIA (136²⁸)

2.000 (50 ⁸⁰)

TBD 0.50 (12²)

4.50 (114³)

MAX MOM ARM

DESIGN TO INTERFACE

FIELD JT

TRUNNION DETAILS

48 (219⁵)   60 (1524⁸)

35 (FOR "1"²) (889)

20 (508)

X 1307 (33197⁹)

X 1292 (32816⁸) {FOR "1, "2, "3}

X 1303 (33096⁸)

39°

34 (863⁵)

SYMM ABOUT ₵ (FOR "1, "2, "3)

Z 448 (11379⁵)   STAB SUPPORT
X 1303 (33096⁸)
Z 409 (10388⁴)

PRIM. SUPPORT   } (FOR "1, "2, "3)
X 1202.73 (30549³)
Z 414 (10515⁴)

X 1194 (30327⁹)
180 (4572) P/L DIA

42 (1067)

74 (1879⁶)

Z 414 (10515⁶)

Z 372.5 (9461⁵)

148 (3759⁵) (FOR "1 & "2)

Z 428 (10871⁴)

"1 (ONE KIT)   "2 (TWO KITS)   "3 (THREE KITS)

OMS KIT INSTALL / P/L OVERHANG DETAIL NO SCALE

NOTE: - P/L CLEARANCE NOT INCLUDED
- ATTACH LOCATION X 1187 (30149⁸) AVAILABLE
  FOR P/L USE WITH OMS KITS INSTALLED

SPECIAL AFT ATTACH LOCATION— TRUNNION ON BOLT-DOWN PLATE

LONGERON

LONG. BRIDGE

AFT LONGERON BRIDGE

BLKHD ADAPTIVE STRUCTURE

AFT BLKHD STRUCTURE

TRACE - FUSELAGE FRAME STA X 1249 (31724⁶)
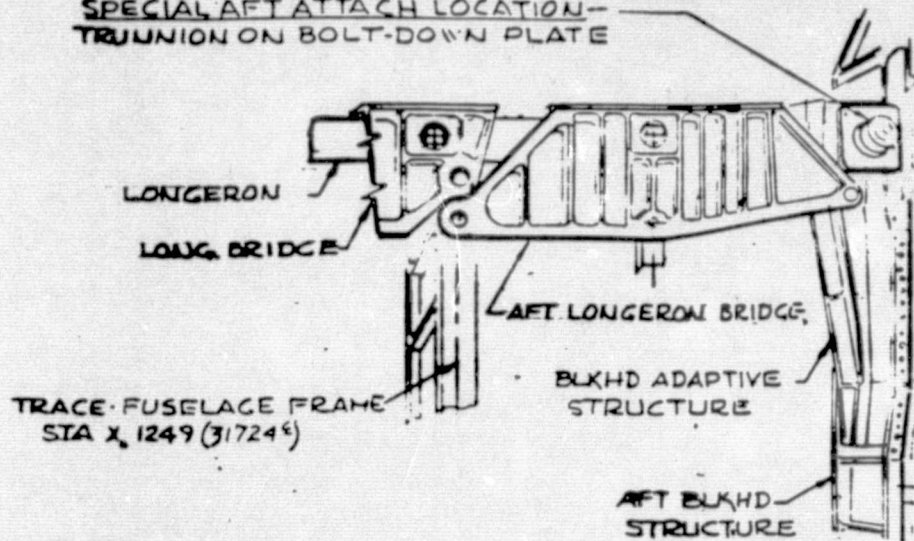
VIEW DD - NO SCALE

INSTALL DETAILS • AFT LONGERON
• AFT ATTACH LO
X 1303 (33197⁹) Z
& Y ± 91.4 (232
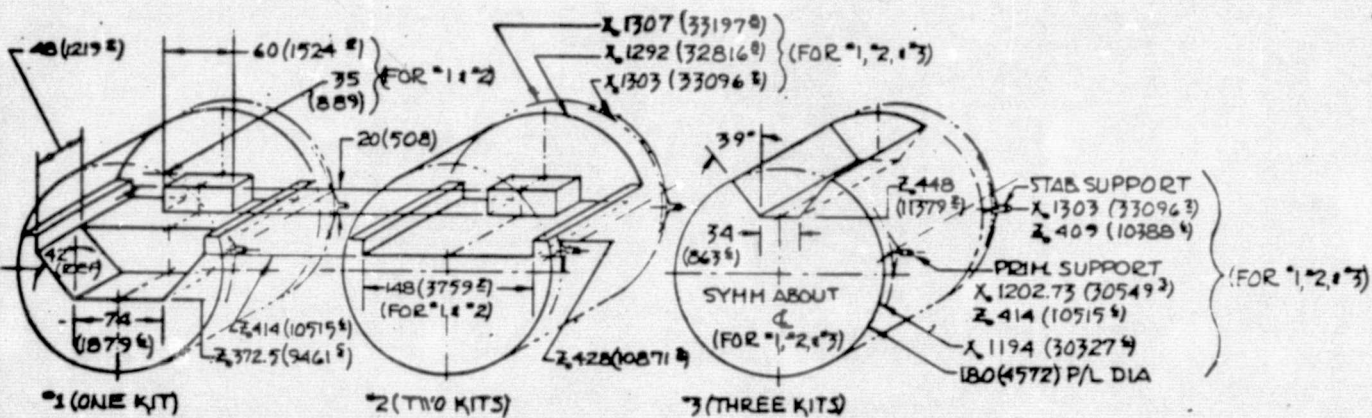
(2286) 90 R

P/L TRUNNION CONCEPT

Y 94 (2387⁶)

SURFACE FOR MGSE ATTACHMENT

JOURNAL

LONGERON

LONG BRIDGE ASSY

X 1249 (31724⁶)

93 R (2362⁴)

90 P/L R (2286⁶)

Y 26 (660⁴)

WING BOX

P/L TONGUE
Y/W LOADS

Y 0

VIEW E-SCALE 1/8 - 6
KEEL BRIDGE ASSY.
OVER WING BOX

Z 308.4 (7833⁴)

Z 310 (7874²)

BRIDGE
ATION AT
09 (10388 9)

REFERENCE ATTACH
LOCATION STATION FOR
DEPLOYABLE P/L

GUIDE STOWED
(LATCH CLOSED)

LATCH-OPEN
POSITION

P/L DEPLOY/DOCK
GUIDE-ERECTED
(LATCH OPENED)

LATCH-CLOSED POSITION

Z_0 414 (10515)

Z_0 410 (10414)

LONGERON

SIDE BRIDGE FTG

TYPICAL DEPLOYABLE P/L ATTACH SCALE $\frac{1}{2}$

VIEW LOOKING AT RH SIDE

RETAINED JOURNAL CAP
SWINGS AFT

P/L FRAME

TYPICAL ATTACH
LOCATION

Z_0 414 (10515)

Z_0 410 (10414)

Z_0 408.25
(10369 5)

LONGERON
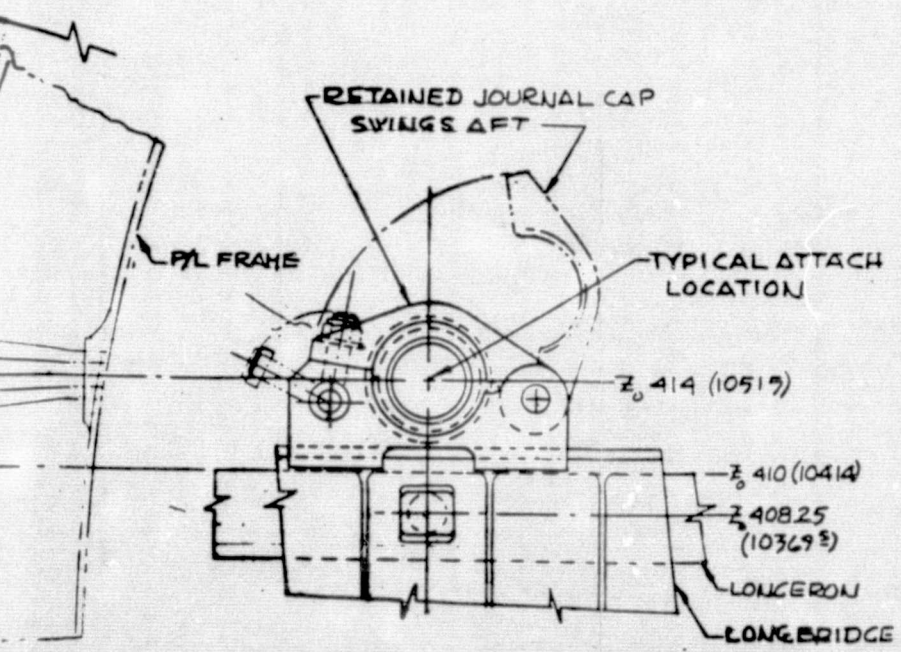
LONG BRIDGE

TYPICAL NONDEPLOYABLE P/L ATTACH SCALE $\frac{1}{4}$

VIEW LOOKING OUTBD · R H SIDE

P/L OMITTED THIS VIEW

P/L SEGMENT

P/L FIXED ATTACH FTG

P/L TRUNNION

ATTACH

ATTACH HDWR VERT

TYPICAL LONG BRIDGE A

ATTACH LOCATION

Z_{7752}
$(24079 \, X)$

NOTE: ATTACH LOCATIONS OVER FRAMES MAY BE
AVAILABLE THROUGH SPECIAL CUSTOM-DESIGNED
LONG BRIDGE FITTINGS

Z_{414}
(10515)

$Z_{410} \, (10414)$

LONGERON

LONG. BRIDGE CAN BE SPECIALLY
DESIGNED FOR A SPECIFIC PAYLOAD

FUSELAGE PRIMARY FRAME (2 PLACES)

FUSELAGE STUB
FRAME

X_{919}
(23342)

X_{9422}
(24110)

X_{9736}
(24079)
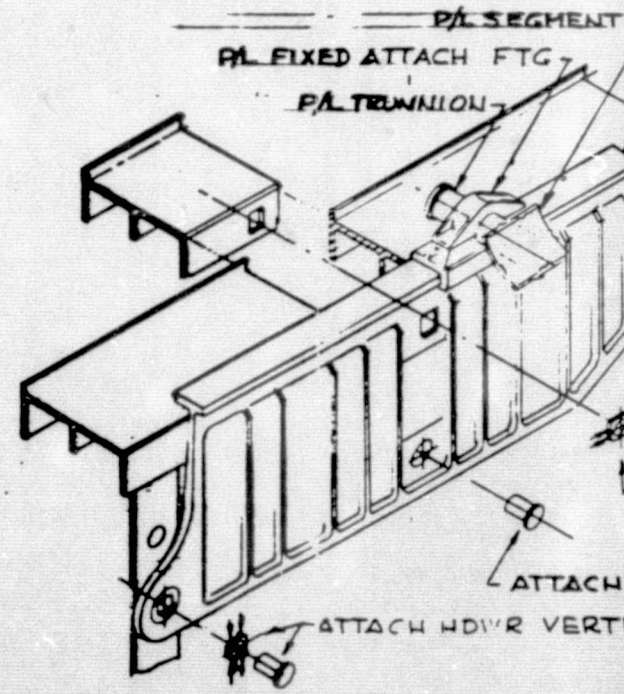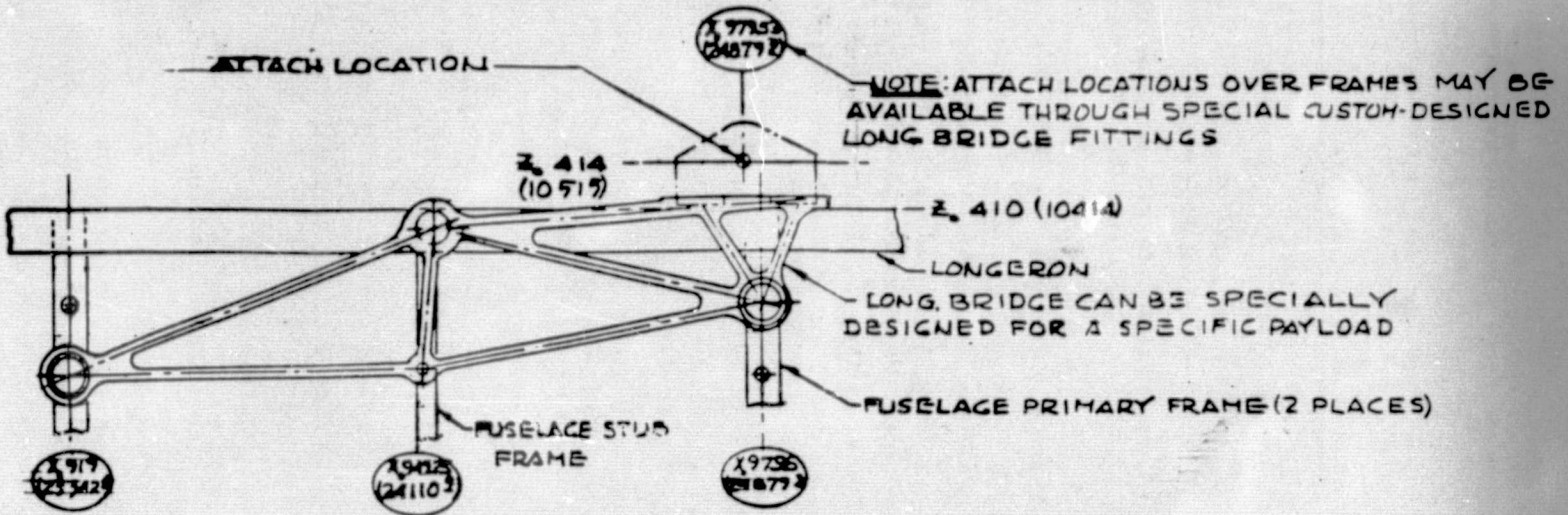
VIEW B-B SCALE $\frac{1}{8} - 8$

CUSTOM-DESIGN LONG. BRIDGE ASSY. CONCEPT

NOTE: NOT ORBITER-SUPPLIED

LONG. BRIDGE
(R H SIDE SHOWN)

SILL LONGERON

PRIMARY FUS. FRAME

ATTACH HDWR
VERTICAL (Z) LOADS

TTACH HDWR
LONGITUDINAL (X) LOADS
LATERAL (Y) FRICTION LOAD
HDWR-LATERAL STABILITY
L (Z) LOADS

INSTALL NO SCALE

REFERENCE ATTACH LOCATION

SHEAR KEEL FTG

LOADED ATTACH LOCATION (REF)

LOADED KEEL FITTING

KEEL BRIDGE

STAB

YA

X_{919}
(23342)

X_{957}
(24133)

X_{9735}
(24079)

P/L YAW TONGUE ENVELOPE TB

STABILIZING STRUT
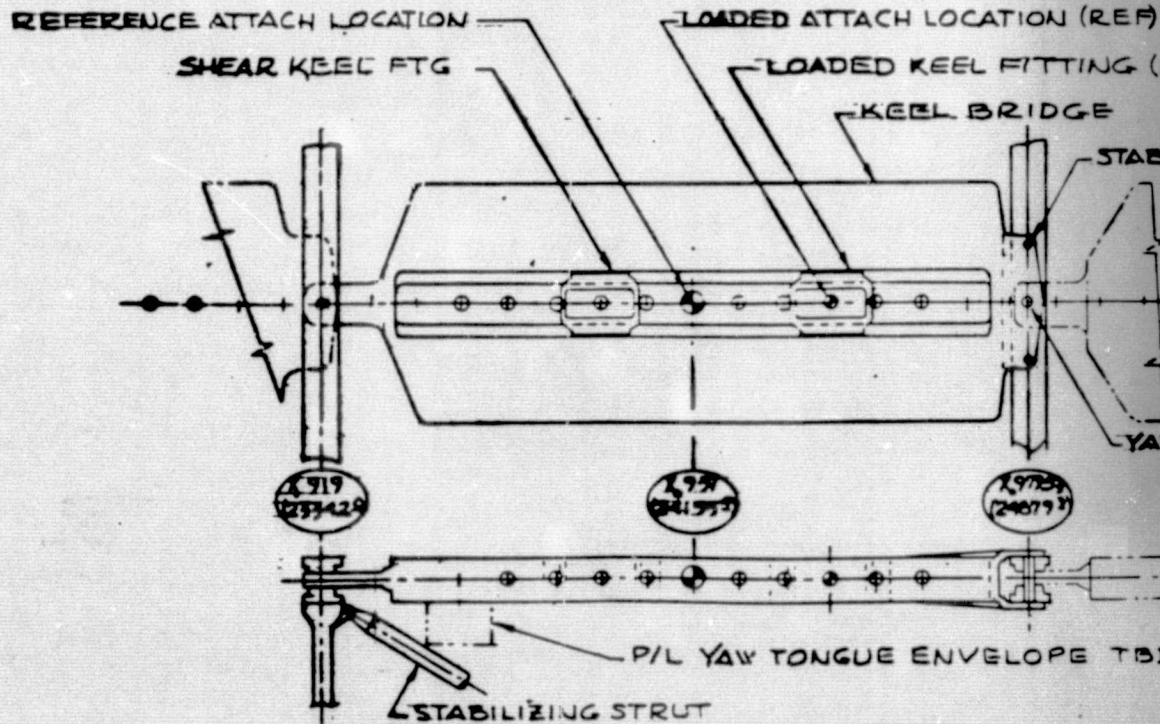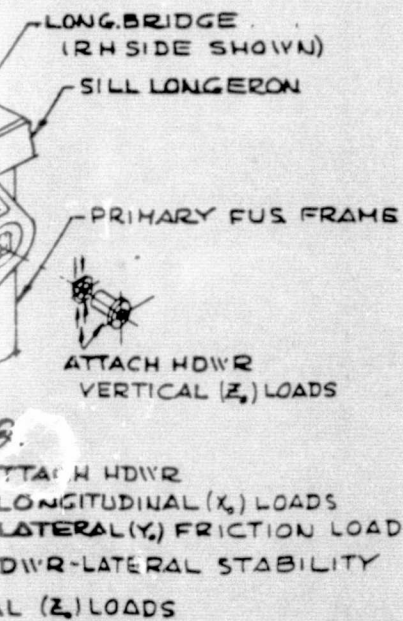
VIEW C-C SCALE $\frac{1}{8} - 8$

TYPICAL KEEL BRIDGE ASSY INSTALL

VC70-004105

DOUT FRAME 3

REFERENCE POINT

TYPICAL ATTACH LOCATIONS

LOCATIONS DESIGNATED 'B' NOT AVAILABLE BESIDE P/L BAY DOOR DRIVE

LOCATIONS DESIGNATED 'C' NOT AVAILABLE BESIDE MANIPULATOR MECHANISM

NOTE: WITH MANIPULATOR REMOVED (WITH PROGRAM APPROVAL) THESE LOCATIONS ARE AVAILABLE

REFERENCE POINT

THESE LOCATIONS DESIGNATED AVAILABLE OVER BRIDGE-BRIDGE EXCEPT AS NOTED IN VIEW

B A   C   A

$Z_o 414$ (10515)

$Z_o 410$ (10414)

LONGERON

LONGERON BRIDGE B-B, FOR CUSTOM LOAD

$L 1128$ 766518

$L 1157$ 730479

59 (1498) REFERENCE ATTACH SPACING

NOTE: ATTACH LOCATIONS AT REFERENCE SPACING = 3.933 (999)

VIEW A·A SCALE $\frac{1}{8}$

ATTACH LOCATION DETAIL

IZING ATTACH T (2 PLACES)

$\phi Y_o 0$

LOAD ATTACH PT

$Z_o 305$ (7747)

SILL LONGERON

LONGERON BRIDGE

STABILIZING (FWD) FITTING

PRIMARY FUS. FRAME

PRIMARY (AFT) FITTING

CG (OVER KEEL BRID

$\pm Z_o$ LOADS

$\pm X_o$ LOADS

$\pm Z$ LOADS

$\pm Z_o$ LOAD

NOTE: EXCEP

$\pm Z$ LOADS

NOTE: THIS (OR OPPOSIT NOT BE UTIL DETERMINAT

KEEL BRIDGE (IN PLANE OF

TYPICAL 3-PT P/L INSTALLATION   NO SCALE

NOTE: C.G. LOCATION OVER KEEL FTG NOT MANDATO STAB & PRIMARY INSTALL REVERSIBLE

MAJOR FUSELAGE FRAME X, STA

FWD BLKHD X, STA

REFERENCE ATTACH LOCATIONS X, STATION

(582 / 14782 #) (636 / 16154 #) (693 / 17602 #) (750 / 19050 #) (807 / 20497 #) (863 / 21920 #)

(576 / 14630 #)

(619 / 15722 #) (649 / 16484 #) (715 / 18161 #) (774 / 19659 #) (833 / 21158 #) (8? / 226?)

A   B A   A   A

OFFICE

A NOT
G JOINT
V B-B,

186 (4724 #) DIA
MIN ORBITER STATIC
ENVELOPE

180 (4572) DIA
MAX P/L DYNAMIC
ENVELOPE

(SEE VIEW
NG. BRIDGE)

TYPICAL 3 IN (76.2)
STATIC CLEARANCE

(X.579 / 14712.9)

720 (18288) MAX P/

726 (18440 #) MIN OR

GE ASSY)

LOADS

ADS

THIS DIM. NOT CONSTRAINED
T FOR INTERFERENCES AS
NOTED IN VIEW A-A & ATTACH
LOCATIONS TABLE

ATTACH LOCATION
E LOCATION) WOULD
LIZED FOR 4-PT
E INSTALLATION

MANIPULATOR
SUPPORTED AS SHOWN

KEEL B
REACT

(X.673.5 / 17259.9)

(X.717 / 18361)

ASSY · Y₀ LOADS
P/L C G)

ORY

VC70-004105

FOLDOUT

SEE VIEW A-A.; FOR CODE DETAILS

D1 — 3.933 (999)

LONGERON BR
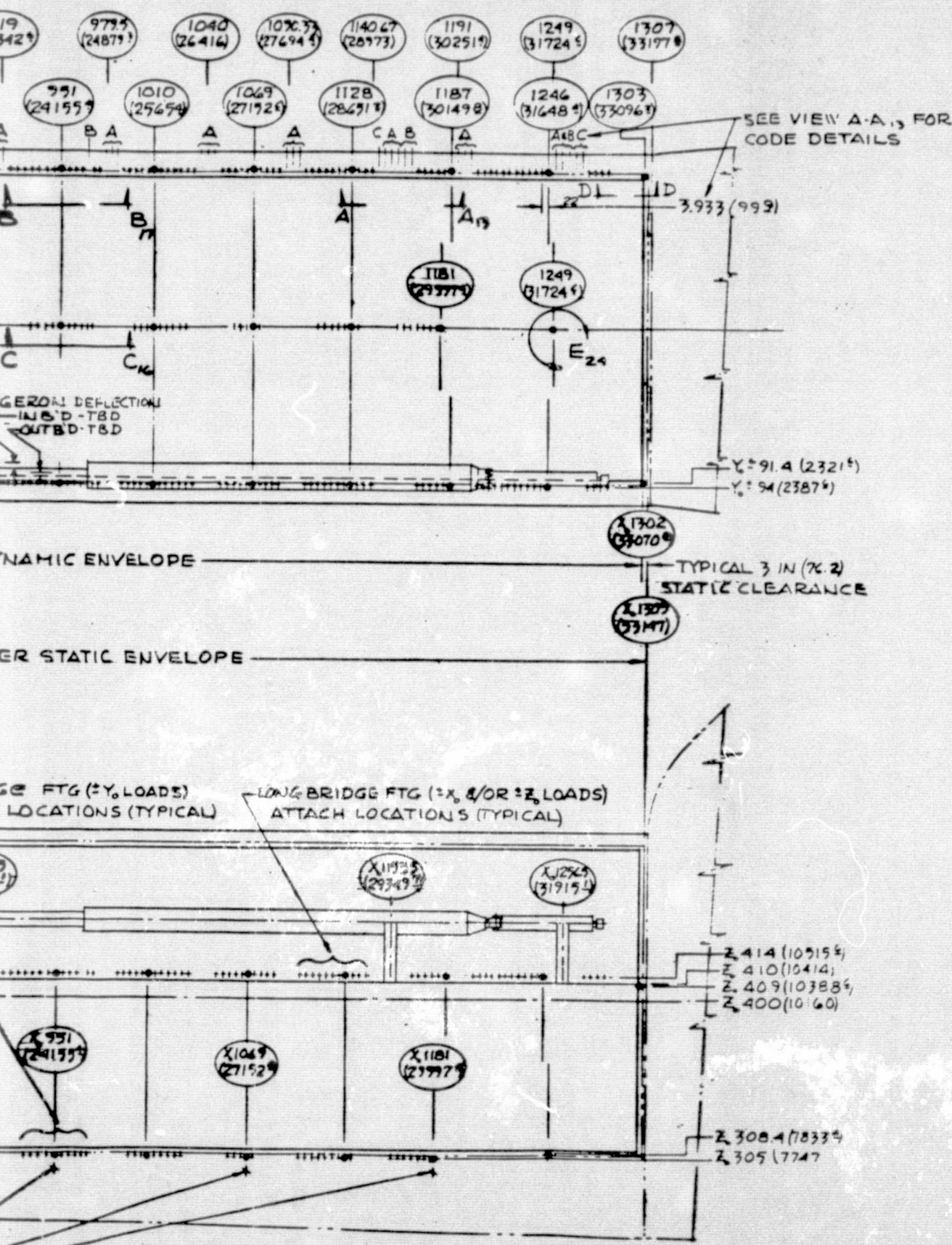
X LOCATION/CO

- 619.00 (17729) D R
- 645.00 (16484) D R
- 703.20 (17861) F
- 707.13 (17761) F
- 711.07 (18061) F
- 715.00 (18161) D-E
- 718.93 (18260) F
- 722.87 (18360) F
- 726.80 (18460) F
- 730.73 (18560) F
- 734.67 (18660) F
- 738.60 (18760) B R
- 742.73 (18860) F
- 746.47 (18960) A
- 750.40 (19060) A
- 754.33 (19160) A
- 758.27 (19260) F
- 762.20 (19359) F
- 766.13 (19459) F
- 770.07 (19559) F
- 774.00 (19659) D-E
- 777.93 (19759) F
- 781.87 (19859) F
- 785.80 (19959) F
- 789.73 (20059) F
- 793.67 (20159) F
- 797.60 (20259) F
- 801.73 (20359) F
- 805.47 (20459) A
- 809.40 (20559) A
- 813.33 (20659) A
- 817.27 (20759) F
- 821.20 (20859) F
- 825.13 (20959) F
- 829.07 (21059) F
- 833.00 (21159) D-E
- 836.93 (21259) F
- 840.87 (21359) F
- 844.80 (21459) F
- 848.73 (21559) F
- 852.67 (21659) F
- 856.60 (21759) F
- 860.53 (21859) A
- 864.47 (21959) A
- 868.40 (22059) A
- 872.33 (22159) F
- 876.27 (22259) F
- 880.20 (22359) F
- 884.13 (22459) F
- 888.07 (22559) F

ATTACH LOCATION COD

A — INDICATES
B — BRIDGE FTG-TO-
  FOR SPECIAL
B — INTERFERENCE
C — INTERFERENCE
  FOR SPECIAL
D — ORIGINAL REFE
E — DEPLOYABLE
NOTE: NONDEPLOY
  EXCEPT
F — COPLANAR KE
G — ORIGINAL KEE

DYNAMIC ENVELOPE

TYPICAL 3 IN (76.2) STATIC CLEARANCE

ER STATIC ENVELOPE

$Y = 91.4$ (2321)
$Y = 94$ (2387)

GERON DEFLECTION
—IN B'D - TBD
—OUTB'D - TBD

FTG (±Y_o LOADS)
LOCATIONS (TYPICAL)

LONG BRIDGE FTG (±X_o &/OR ±Z_o LOADS) ATTACH LOCATIONS (TYPICAL)

Z 414 (10515)
Z 410 (10414)
Z 409 (10388)
Z 400 (10160)

Z 308.4 (7833)
Z 305 (7747)

IAL KEEL LOCATIONS FOR
RYING X_o AXIS LOADS

FTG ATTACH LOCATIONS

LOCATION/CODE	X LOCATION/CODE
92.00 (2265.8) D·E·F	1088.67 (27652) A
95.93 (2275.2) A	1092.60 (27752) A
99.87 (2285.6) F	1096.53 (27851.7) A
97.80 (2295.6) B·C·F	1100.47 (27951.2) F
07.73 (2305.4) C·F	1104.40 (28051) F
11.67 (2315.6) A·C·F	1108.33 (28151) F
15.60 (2325.6) A·C	1112.27 (28251) F
19.53 (2335.6) A·C	1116.20 (28351) F
23.47 (2345.6)	1120.13 (28451) F
27.40 (2355.6)	1124.07 (28551) F
31.33 (2365.5) F	1128.00 (28651.5) D·E·F
35.27 (2375.5) F	1131.93 (28751) F
39.20 (2385.5) F	1135.87 (28851) F
43.13 (2395.5) F	1139.80 (28950)
47.07 (2405.5) F	1143.73 (29050) A·B
51.00 (2415.5) D·E·F	1147.67 (29150) A·C
54.93 (2425.7) F	1151.60 (29250) A·C
58.87 (2435.5) C	1155.53 (29350) C·F
62.80 (2445.5)	1159.47 (29460.5) C·F
66.73 (2455.5) B·F	1163.40 (29550) C·F
70.67 (2465.4) F	1167.33 (29650) F
74.60 (2475.1)	1171.27 (29750) F
78.53 (2485.4) A	1175.20 (29850) F
82.47 (2495.4) A	1179.13 (29950) F
86.40 (2505.4) A	1183.07 (30049) *
90.33 (2515.4) F	1187.00 (30149.2) D·E
94.27 (2525.4) F	1190.93 (30249) A
98.20 (2535.4) F	1194.87 (30349) A
02.13 (2545.4) F	1198.80 (30449) A
06.07 (2555.4) F	1202.73 (30549)
10.00 (2565.4) D·E·F	1206.67 (30649)
13.93 (2575.3) F	1210.60 (30749)
17.87 (2585.3) F	1214.53 (30849)
21.80 (2595.3) F	1218.47 (30947)
25.73 (2605.3) F	1222.40 (31049)
29.67 (2615.3) F	1226.33 (31148)
33.60 (2625.3)	1230.27 (31248)
37.53 (2635.3) A	1234.20 (31348)
41.47 (2645.3) A	1238.13 (31448)
45.40 (2655.3) A	1242.07 (31548)
49.33 (2665.3)	1246.00 (31648) D·E *
53.27 (2675.3) F	1249.93 (31748) C
57.20 (2685.2) F	1253.87 (31848) C
61.13 (2695.2) F	1257.80 (31948) C
65.07 (2705.2)	1261.73 (32048) B·C
69.00 (2715.2) D·E·F	1265.67 (32147) B·C
72.93 (2725.2)	1269.60 (32247)
76.87 (2735.2) F	1273.53 (32347)
80.80 (2745.2) F	1277.47 (32447)
84.73 (2755.2)	1281.40 (32547)
	1303.00 (33096) D

REFERENCE DRAWINGS
(USE LATEST REVISION)

VC 70·000002 DESIGN GEOMETRY·SHUTTLE
VC 72·000003 DESIGN CONFIGURATION CONTR
VC 70·004001 MIDFUSELAGE DESIGN CONTRO
VL 70·008417 OMS CARGO BAY KIT·HORIZ TANK
VL 70·004190 P/L ACCOMM·GROUND HANDLIN
VC 70·009011 │ │ AFT FUSELAGE F
VC 70·004107 │ │ MIDFUSELAGE SY
VC 70·003002 │ │ FWD FUSELAGE P
VL 70·004145 P/L ACCOMM P/L HANDLING &
VL 70·003344 KIT *1 DOCK. MODULE ASSY·INST
VL 70·003345 KIT *2 │ │ │
VL 70·003346 KIT *3 DOCK MODULE ASSY·INST
HC 621·0052 MANIPULATOR INSTALL (PROCUR

GENERAL NOTES

1. THIS DWG IS BASELINE PER HCR 0200 R7 0·17·7
   - REMOTE CONTROL TRUNNION RELEASE AT STATION
   - 59 (1498) SPACING OF REFERENCE ATTACH LOC
   - P/L-TO-ORBITER FIELD JOINT AT BEARING OU
   - 4-PT DETERMINATE P/L INSTALL
   - P/L MAX DYNAMIC ENVELOPE
   - REMOTE MANIPULATOR
   - SPECIAL KEEL LOCATIONS FOR X. LOADS
   - SPECIAL AFT LONGERON BRIDGE
   - 3.933 INCH VERNIER ATTACH LOCATIONS

2. IF CUSTOM DESIGN BRIDGE (VIEW B·B) OVER B2 DG
   ADJACENT BRIDGE FTG CANNOT BE INSTALLE
3. WHEN THE SPECIAL AFT BRIDGE FTG (VIEW D·D)
   (a) THE ADJACENT FWD FTG MUST ALSO BE
   (b) THE X, 1303 (33096) ATTACH LOCATION FTG C
4. THIS DWG REPLACES DWG *VL 70·004105 (SA
5. WITH THE SLIDING (FORWARD) P/L ATTACH, THE
   THE STATIONARY ATTACH IS NOT CONSTRAI

R SYSTEMS INTERFERENCE PER A.B.C CODE
INT OVER PRIMARY FRAME (SEE VIEW B·B)
BRIDGE FTG) DESIGNATED 'A'
P/L BAY DOOR DRIVE MECHANISM SHOWN BY 'B'
MANIPULATOR LATCH (SEE VIEW A·A)
IDERATION) INDICATED BY 'C'
E ATTACH LOCATIONS NOTED AS 'D'
OAD MECHANISM AVAILABLE THESE LOCATIONS, E
P/L ATTACH AVAILABLE AT ALL LOCATIONS
OTED BY CODE A, B, & C.
PPORT FTG AVAILABLE AS SHOWN THUSLY 'F'
ATION @ X, 1181 (29997) & @ X, 1249 (31724)

APPENDIX B. SPACE DIVISION BASELINE DRAWING

REFERENCE DRAWINGS
(USE LATEST REVISION)

VC 70-000002	DESIGN GEOMETRY SHUTTLE
VC 72-000003	DESIGN CONFIGURATION CONTROL
VC 70-004001	MIDFUSELAGE DESIGN CONTROL
VL 70-008417	OMS CARGO BAY KIT-HORIZ TANKS STUDY
VL 70-004150	P/L ACCOMM·GROUND HANDLING PROV
VC 70-009011	AFT FUSELAGE PROV.
VC 70-004107	MIDFUSELAGE SYS INTERFACE
VC 70-003002	FWD FUSELAGE PROV.
VL 70-004145	P/L ACCOMM P/L HANDLING & VIEWING
VL 70-003344	KIT #1 DOCK. MODULE ASSY·INSTALL INTERFACE
VL 70-003345	KIT #2
VL 70-003346	KIT #3 DOCK. MODULE ASSY·INSTALL INTERFACE
HC 621-0052	MANIPULATOR INSTALL (PROCUREMENT)

GENERAL NOTES

1. THIS DWG IS BASELINE PER HCR 0200 R7 0-17-74 FOR THE FOLLOWING ITEMS:
   - REMOTE CONTROL TRUNNION RELEASE AT STATIONS INDICATED
   - 59 (1498.5) SPACING OF REFERENCE ATTACH LOCATIONS
   - P/L-TO-ORBITER FIELD JOINT AT BEARING OUTER RACE
   - 4-PT DETERMINATE P/L INSTALL
   - P/L MAX DYNAMIC ENVELOPE
   - REMOTE MANIPULATOR
   - SPECIAL KEEL LOCATIONS FOR X. LOADS
   - SPECIAL AFT LONGERON BRIDGE
   - 3.933 INCH VERNIER ATTACH LOCATIONS

2. IF CUSTOM DESIGN BRIDGE (VIEW B-B) OVER 32 DGE-BRIDGE JT IS USED, THE ADJACENT BRIDGE FTG CANNOT BE INSTALLED

3. WHEN THE SPECIAL AFT BRIDGE FTG (VIEW D-D) IS USED
   (a) THE ADJACENT FWD FTG MUST ALSO BE USED 1
   (b) THE X. 1303 (33096.2) ATTACH LOCATION FTG CANNOT BE USED

4. THIS DWG REPLACES DWG #VL 70-004105 (SAME TITLE)

5. WITH THE SLIDING (FORWARD) P/L ATTACH, THE SPAN BETWEEN THIS AND THE STATIONARY ATTACH IS NOT CONSTRAINED EXCEPT AS NOTED

C75-664/034A

APPENDIX C. REPORT NO. GDC CM75-2393
SHUTTLE IMAGING MICROWAVE SYSTEM (SIMS)
MAIN REFLECTOR
A REPORT TO ROCKWELL INTERNATIONAL
29 OCTOBER 1975

INTRODUCTION

General Dynamics Convair Division is pleased to submit this brief technical report to Rockwell International for the Shuttle Imaging Microwave System (SIMS). In this proposed approach, a reflector configuration is discussed that incorporates only those design concepts and manufacturing methods with proven, successful performance at Convair.

The Convair design concept consist of a surface-adjustable parabolic-torus reflector of thin-gage, pseudoisotropic graphite/epoxy, reinforced by radial truss members and outside closure skins of similar material. Contour adjustment points along each radial truss allow the reflector to be "tuned" during final assembly. This low-risk assembly approach has been used extensively at Convair for large, precision reflectors and has resulted in acceptance of 100% of the composite antennas produced. The reflector will mount to a "L" shaped torque box which also serves as the drive mechanism housing. Arms extending from this torque box provide for additional support for the rotating feed disc. The torque box and arms will consist of laminated graphite/epoxy channel side members spanned by graphite/epoxy honeycomb skin panels. The lower portion of this torque box will be reinforced with rib members where Y-load shuttle attach fittings are located. Similar attach fittings are located at the reflector ends to react X and Z loads for the entire system.

Convair experience with lightweight graphite/epoxy antennas is typified by the eight-foot-diameter technology antenna shown in Figure 1. This 45-pound structure had a natural frequency of more than 50 Hz. Contour accuracy at fabrication was 2.5 mils rms. During solar-thermal-vacuum testing, using a 300-point photogrammetic measurement, with the worst-case side-on-sun condition, only a 0.5-mil rms increase was experienced on the reflector surface with a +200 to -200° F thermal differential.

The SIMS reflector study was organized within and managed by the Convair Composite Structures Programs group. This project-oriented organization consists of key technical specialists from Structures, RF Design, Materials Research, Manufacturing Development, Tooling, and Design-to-Cost functional departments. All group members are located within the project area.

Composite Structures Programs, managed by Mr. D. R. Dunbar, has been an established group with Convair since 1967. Over the years, Convair has become a recognized leader in composite structures technology and has been in the forefront of development of composite antennas and other thermally stable composite systems.

LARGE PRECISION GRAPHITE/ EPOXY SYSTEMS HAVE BEEN BUILT

C-BAND TO 300 GHz FREQUENCY COMMUNICATION ANTENNAS ARE FEASIBLE WITH GAIN CAPABILITY TO 70 dB

	SPEC	MEASURED
● RF PERFORMANCE		
GAIN (CAPABILITY), dB	70	—
1st SIDELOBE, dB	<13	<19
AXIAL RATIO, dB	<1.5	<0.5
VSWR	<1.1:1.0	<1.1:1.0
BORESIGHT SHIFT, DEG.	<0.05	<0.02
TRACKING NULL, dB	>25	>35
● AUTOTRACK CAPABILITY		
MAX. ERROR, DEG.	<0.0138	0.0071
● MECHANICAL PERFORMANCE		
NATURAL FREQ., Hz	>50	55
INERTIA LOADING, g	30	30
SURFACE CONTOUR:		
MFG., IN.	0.0035	0.0025
ORBITAL, IN.	0.007	0.0031
WEIGHT, LB.	52	45
ACOUSTICS, dB	147	147
● THERMAL COATINGS		
ABSORPTANCE/EMITTANCE	0.6-0.9	0.7
SOFT X-RAY, CAL/CM^2	>0.1	0.5
HARD X-RAY, CAL/CM^2	>1	2.5
LIFE, YR.	5-7	7
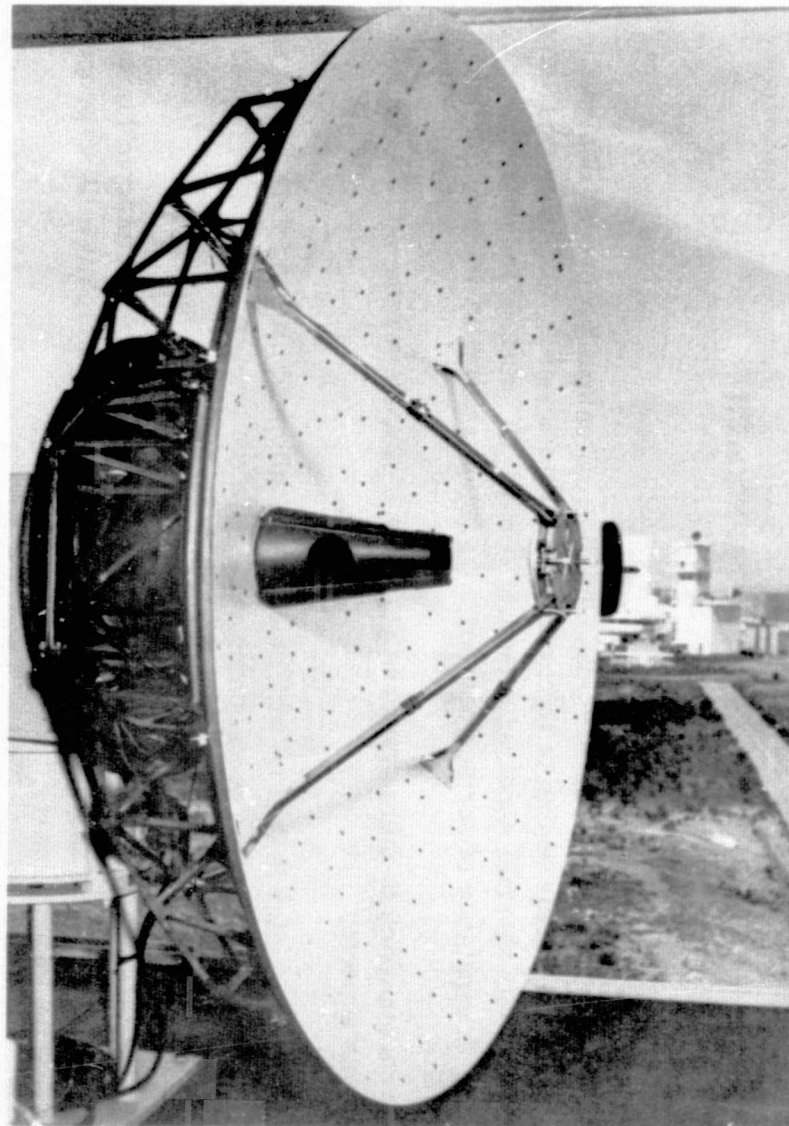
Figure 1.

14104CVE5193B

TECHNICAL APPROACH

GENERAL

DESIGN PHILOSOPHY — Convair proposes to use a unique but proven design for the main reflector. This design is lightweight, easily inspected, and immune from problems associated with thermal shock or pressure decay. Of greatest importance, however, is the built in capability of surface contour adjustment as part of antenna assembly.

Convair's approach to minimizing the reflector's distortion from optimum shape has six unique aspects.

1. The reflector is laid up with computer-configured prepreg tiles. This ensures that the properties at any point on the surface are the same as any other within the tolerances equivalent to a flat plate layup.

2. The use of the GY-70/X-30 graphite/epoxy system is an isotropic laminate for all thermal expansion and minimal deformations due to dissimilar properties of the graphite parts.

3. Thermal cycling will increase the dimensional stability of the graphite parts.

4. The adjustment capability of the shell concept ensures optimum shaping and minimizes or eliminates differences in the reflector coming off the tool due to small inherent variations in composite properties and cure cycles eliminating risk of losing a shell due to not meeting specified surface tolerances.

5. A profilometer system and accompaning software will be used that measures thousands of points on the reflector and draws a contour map of the best fit parabola and focal position.

6. Thermally controlled factory assembly area with 70 ±3F and 20% humidity (control for graphite).

Convair will use the technology developed in more than $5.5 million worth of similar composite experience as typified by our eight-foot technology antenna shown in Figure 1. The extensive qualification testing (Figure 2) done on that antenna gives Convair confidence that the design philosophy proposed for the SIMS reflector is one that will ensure success.

DESIGN DESCRIPTION — The SIMS reflector assembly is shown in Figure 3. It is a section of a parabolic torus and must fulfill the primary requirements listed in Table I.

SOLAR THERMAL/VACUUM TEST (72 HOURS)
PHOTOGRAMMETRIC CONTOUR CONDITIONS

CONTOUR CHECK

ONE -g CONTOUR (3) PHOTOGRAMMETRIC

RF GAIN/ PATTERN

NO SUN: AMBIENT TEMPERATURE & PRESSURE

AMBIENT TEMP. 10^{-8} TORR 24-HR. HOLD

SUN 10^{-8} TORR SIXTH CYCLE

AMBIENT TEMP. 10^{-8} TORR

30g (2 MIN.) CENTRIFUGE

30g (2 MIN.) CENTRIFUGE

RF GAIN/ PATTERN

CONTOUR CHECK

MODAL VIBRATION 55 CPS, FIRST MODE

CONTOUR CHECK

ACOUSTIC 136 db 141 db

CONTOUR CHECK

ACOUSTIC 147 db (3 MIN.)

CONTOUR CHECK

147 db (6 MIN.)

Figure 2. Test Program Successfully Completed on Convair's 8-foot Graphite Antenna

C-5

C75-664/034A

C75-664/034A

CANDIDATE RETENTION FITTING LOCATIONS

RETENTION FITTINGS - LONGERON

RETENTION FITTINGS - KEEL

TRUSS STRUCTURE ENVELOPE

DRIVE MECHANISM HOUSING

TRUSS STRUCTURE ENVELOPE

-Y

FWD (-X)

+Y

SCALE : 1 INCH = 1 METER

FEED ASSY (TYPICAL 6 PLACES)

SUB-REFLECTOR (6 IDENTICAL)

RADIOMETER CLUSTER
(30 RADIOMETERS TOTAL)

PAYLOAD BAY CLEARANCE ENVELOPE

55.5 cm (tentative)

1,413 GHz FEED

ROTATING FEED DISC

PARABOLIC TORUS REFLECTOR SURFACE

DRIVE MECHANISM HOUSING

PARABOLA CONTOUR

24 cm

STA 1305

STA 1246   STA 1187

22.8 cm

45 cm

50.8 cm

35.56 cm

CENTERLINE - PAYLOAD BAY

G. M. OP DISC
AND DRIVE ASSY
200 Kg MAX.

2 m R

TRUSS ENVELOPE - TBD

228.6 cm RADIUS

232.7 cm

+Z

SIMS-A

PRELIMINARY LAYOUT

MAXIMUM ENVELOPE

61 cm

241.3 cm

-Z

.61 & 2.695 GHz
FEED

4 m

22.8 cm TYPICAL

STA 1249

STA 1181

2 m

30.5 cm

PAYLOAD BAY FLOOR

Figure 3

1 m

3 m

+X

Table I. Primary Design Requirements

Reflector surface accuracy (full range of frequencies)	±.001 rms	.0035 peak
Reflector surface accuracy (reduced range of frequencies)	±.0013 rms ±.002 rms	.0035 peak .0045 peak
Reflector geometry	section of parabolic-torus 2 meters × 4 meters	
RF frequency (99% reflectivity)	0.610 GHz to 118.7 GHz	
CTE reflector material	$\approx .01 \times 10^{-6}$ in/in° F	
Weight	< 1000 Kg	
Interface	Mount to Space Shuttle payload retention devices	

The general structural arrangement shown in Figure 4 depicts the basic parabolic-torus section and the "L-shaped" drive mechanism housing and support arms. The basic parabolic-torus section (reflector) consist of a .065-inch thick shell of pseudo-isotropic 10-ply graphite/epoxy (GY-70/X-30). A coating of vapor deposited aluminum 0.04 mils thick with a protective overcoat of SiO_2 will provide the high gain desired.

Convair chose a open isogrid radial rib system to support the reflector shell because of its extremely low weight and cost and its adaptability to "tuning" the reflector surface. Convair has demonstrated the low cost of isogrid structural panels (cocured out of graphite/epoxy) during its 1973-1975 IRAD programs. Figure 5 depicts the isogrid (truss) rib design. The clips at the top of the rib interface with the backside of the reflector shell. These clips will be prefitted to the various ribs (13) and reflector backside. The first bond operation will be at the clip/reflector interface. The clip/rib interface will be clamped until "tuning" has been completed. Proper position of each clip is finally secured by bonding the clip to the rib. All backup structure for the reflector skin was to be previously bonded together prior to the "tuning" of the reflector surface. The removable back panel provides access for this "tuning" operation. The back panel will then be bonded in place to close out the structure. It is expected that all panels (i.e., back, forward and aft panels) will be similar in construction and thickness to the reflector shell.

Convair chose (graphite/epoxy) honeycomb for the basic panel construction of the Drive Mechanism Housing and support arms structure because of its low weight and cost, especially when large, flat clean panels are required. Convair has built and tested

RIBS - ISOGRID (TRUSS)
LOCATE ON 15°
RADIALS

FORWARD PANEL

SUPPORT ARMS

REFLECTOR SKIN

BACK PANEL
(TYP)

DRIVE MECHANISM
HOUSING

AFT PANEL
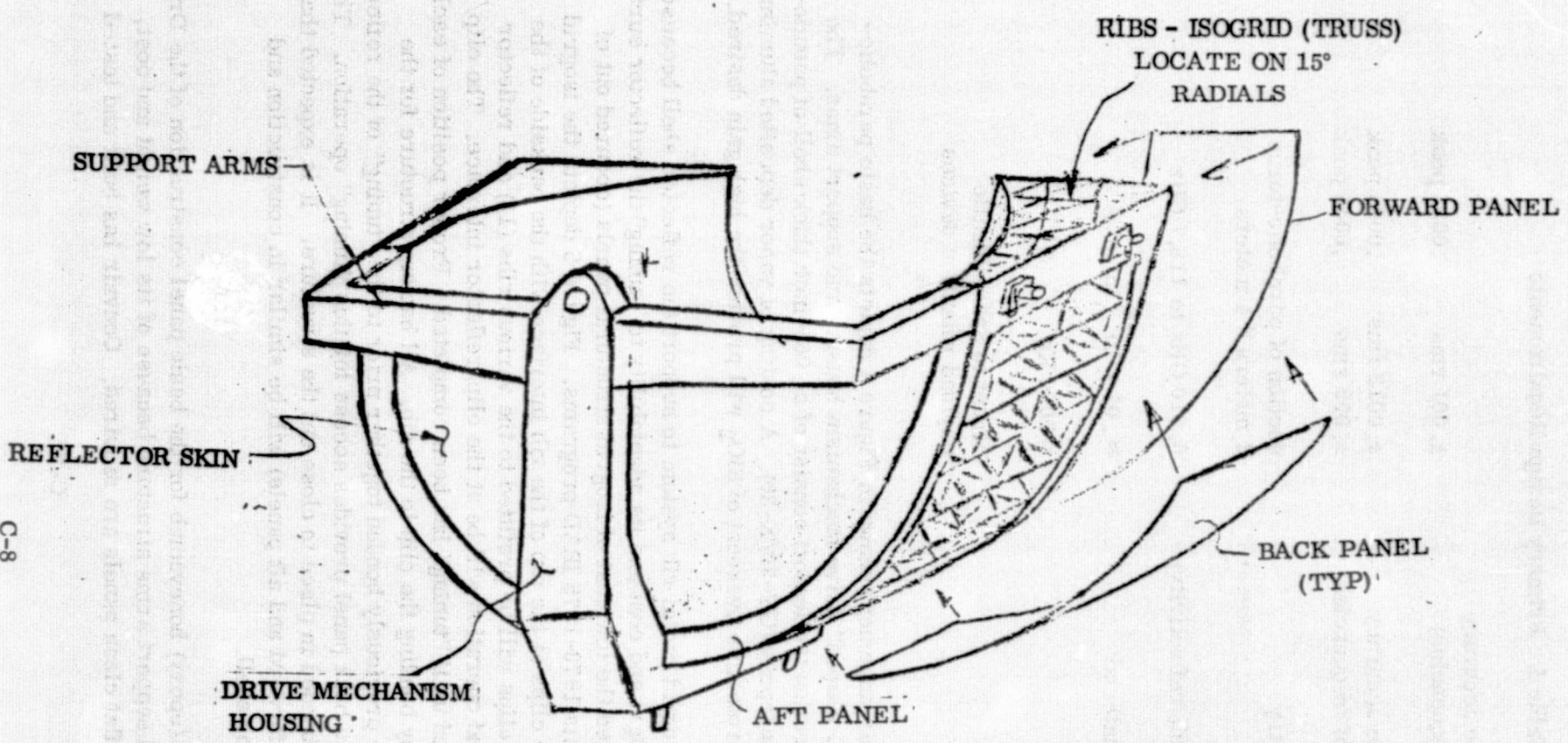
Figure 4. Sketch SIMS Parabolia-Torus Reflector

"T" SECTION
(TYP CONSTR)

BOND SURFACE
(REFLECTOR BACKSIDE)
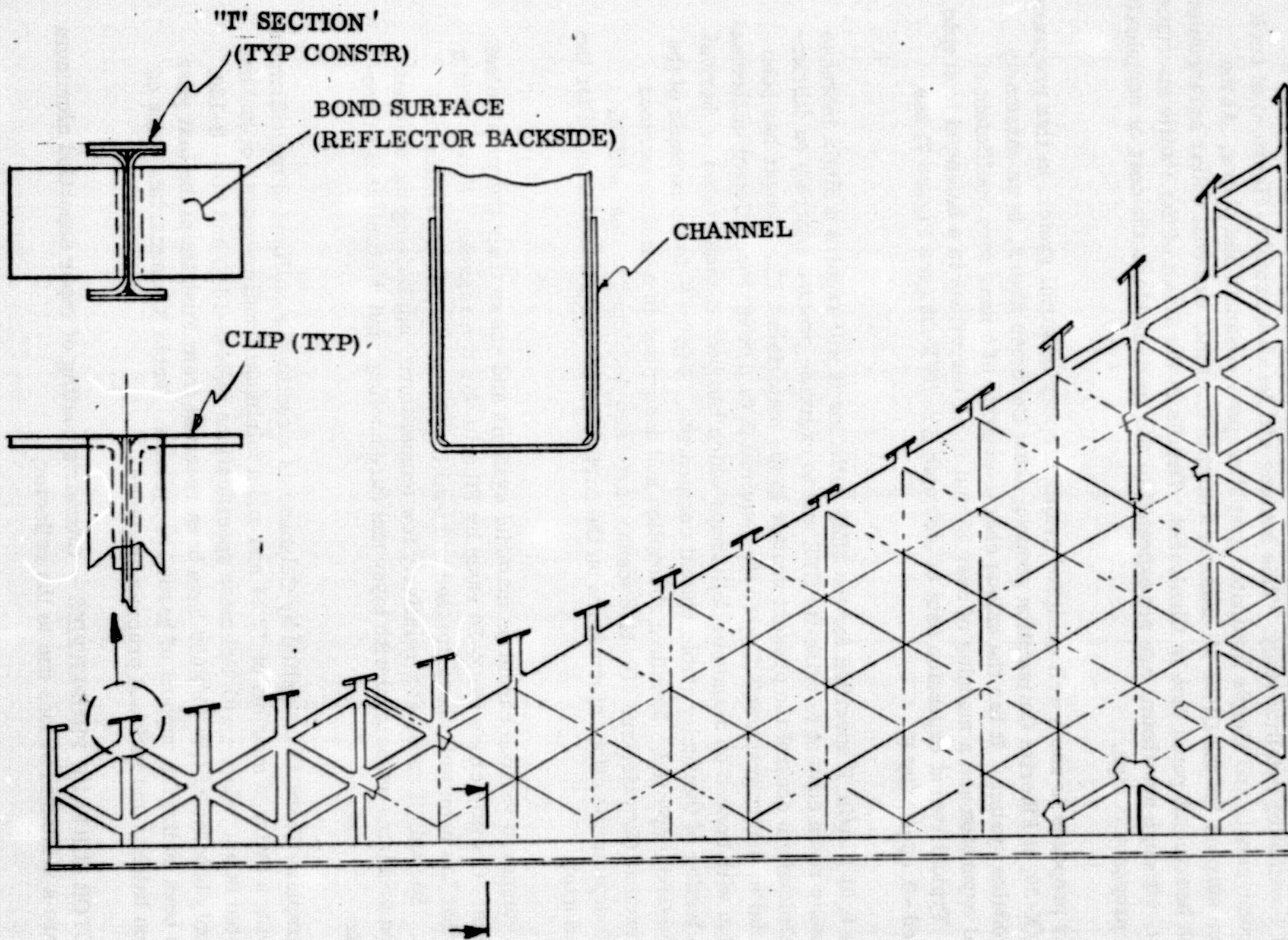
CHANNEL

CLIP (TYP)

Figure 5. Sketch - Rib Open Isogrid (truss)

many small sandwich panels and test beams having ultra-thin graphite/epoxy facings and has built a large flat demonstration panel having 0.010-inch-thick facings for a Global Positioning Satellite study. This housing will be an assembly (Figure 6) of such honeycomb panels and simple laminated graphite/epoxy channels and plates. At the trunnion support for the Drive Mechanism a simple internal, external collar arrangement on each honeycomb panel face is illustrated. Details in the areas of the shuttle interface fittings, although not shown, are not expected to add appreciable to the cost or complexity of this proposed design.

Convair proposes to use a well qualified graphite/epoxy material system in this program. GY-70/X-30, a Fiberite Corporation prepreg using Celanese fibers, is an extremely high modulus system. It has the unique characteristics of a near zero coefficient of thermal expansion and a modulus of over 15 msi in all directions in a balanced isotropic layup. Typical recent expansion data of isotropic GY-70/X-30 (see Figure 7) has averaged -0.03 μin/in° F.

For the 0.01 μin/in° F specified for the SIMS reflector it will require a slight increase in the basic resin content to raise its CTE and to exercise precise controls on fabrication techniques to control the present scatter in the materials CTE. Convar has been successful in tuning graphite/epoxy to the required 0.01 μin/in° F coefficient of thermal expansion with bonded on aluminum foil strips which has been demonstrated in thermal vacuum testing of thermally stable optical components. Figure 8 is an example of the tuning method employed. Moisture absorption and desorption is a well understood phenomenon at Convair, and effective means have been developed to deal with it. Figure 9 depicts the effect of moisture on the particular laminate recommended for the SIMS reflector.

Table 2 compares various candidate material systems and shows their thermophysical properties. Convair chose the X-30 resin by Fiberite for two reasons. First, it is a system that has been well characterized and qualified for space optical systems at Convair. Second, it cures at a relatively low temperature, minimizing the thermal expansion problems associated with layup and cure cooling, and it eliminates micro-cracking.

GY-70 graphite fibers are supplied by Celanese as a continuous collimated multifilament yarn having a average modulus of 77 ±4 msi and a minimum tensile strength of 220 ksi when tested in accordance with Celanese specifications SUM-S-108G and SUM-S-130. Over twenty batches of GY-70/X039 have been received from Fiberite in the last year and have been utilized in support of hardware systems. Table 3 summarizes tests on production batches and included prepreg properties.

REFLECTOR SURFACE PROPERTIES — Convair's coating of vapor depostied aluminum will ensure a minimum of loss due to the reflector.
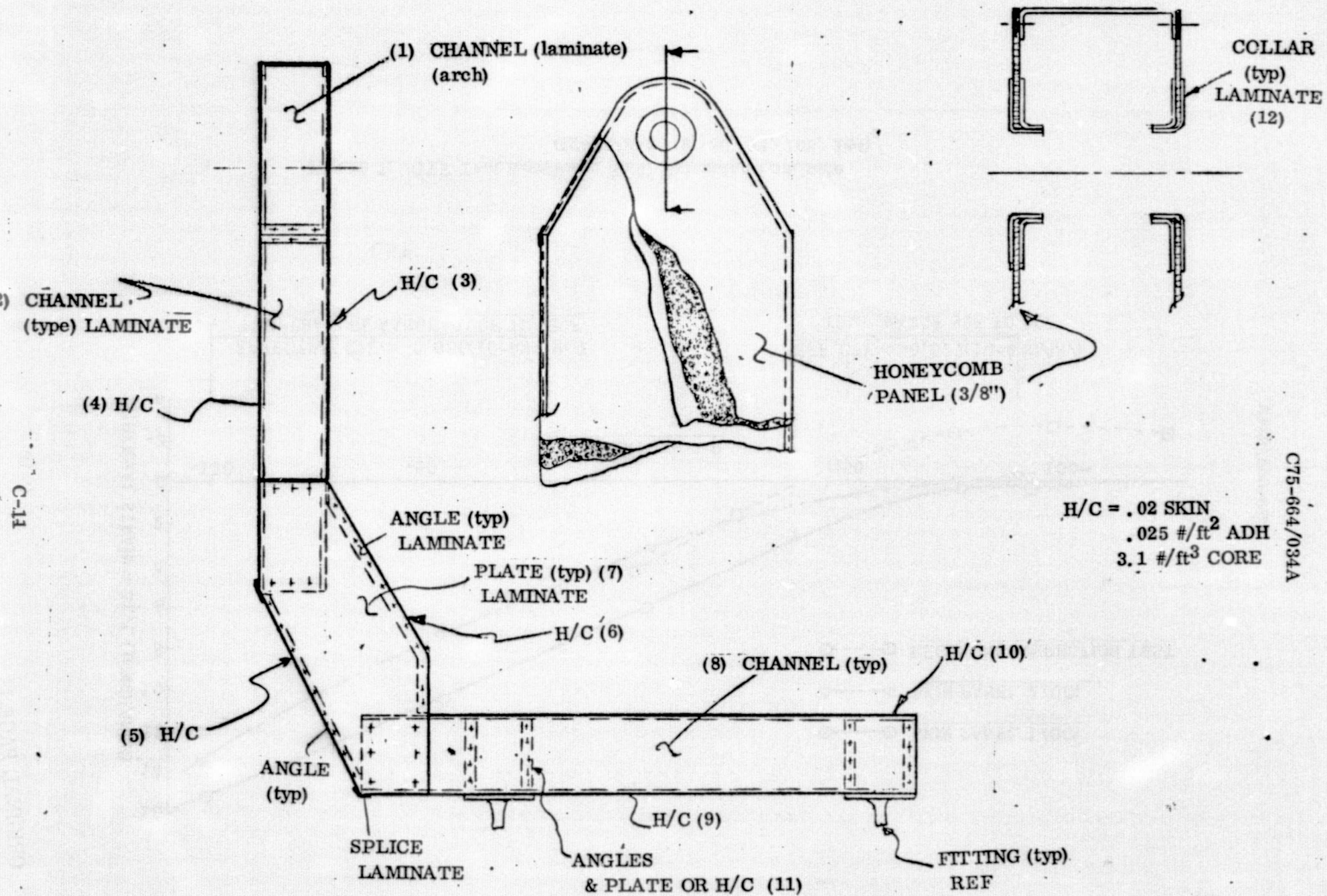
Figure 6. Sketch – Drive Mechanism Housing
(typical construction for support)

(1) CHANNEL (laminate) (arch)

CHANNEL (type) LAMINATE

H/C (3)

(4) H/C

COLLAR (typ) LAMINATE (12)

HONEYCOMB PANEL (3/8")

ANGLE (typ) LAMINATE

PLATE (typ) (7) LAMINATE

H/C (6)

(5) H/C

ANGLE (typ)

SPLICE LAMINATE

ANGLES & PLATE OR H/C (11)

H/C (9)

(8) CHANNEL (typ)

H/C (10)

FITTING (typ) REF

H/C = .02 SKIN
.025 #/ft^2 ADH
3.1 #/ft^3 CORE

C75-664/034A

C-11
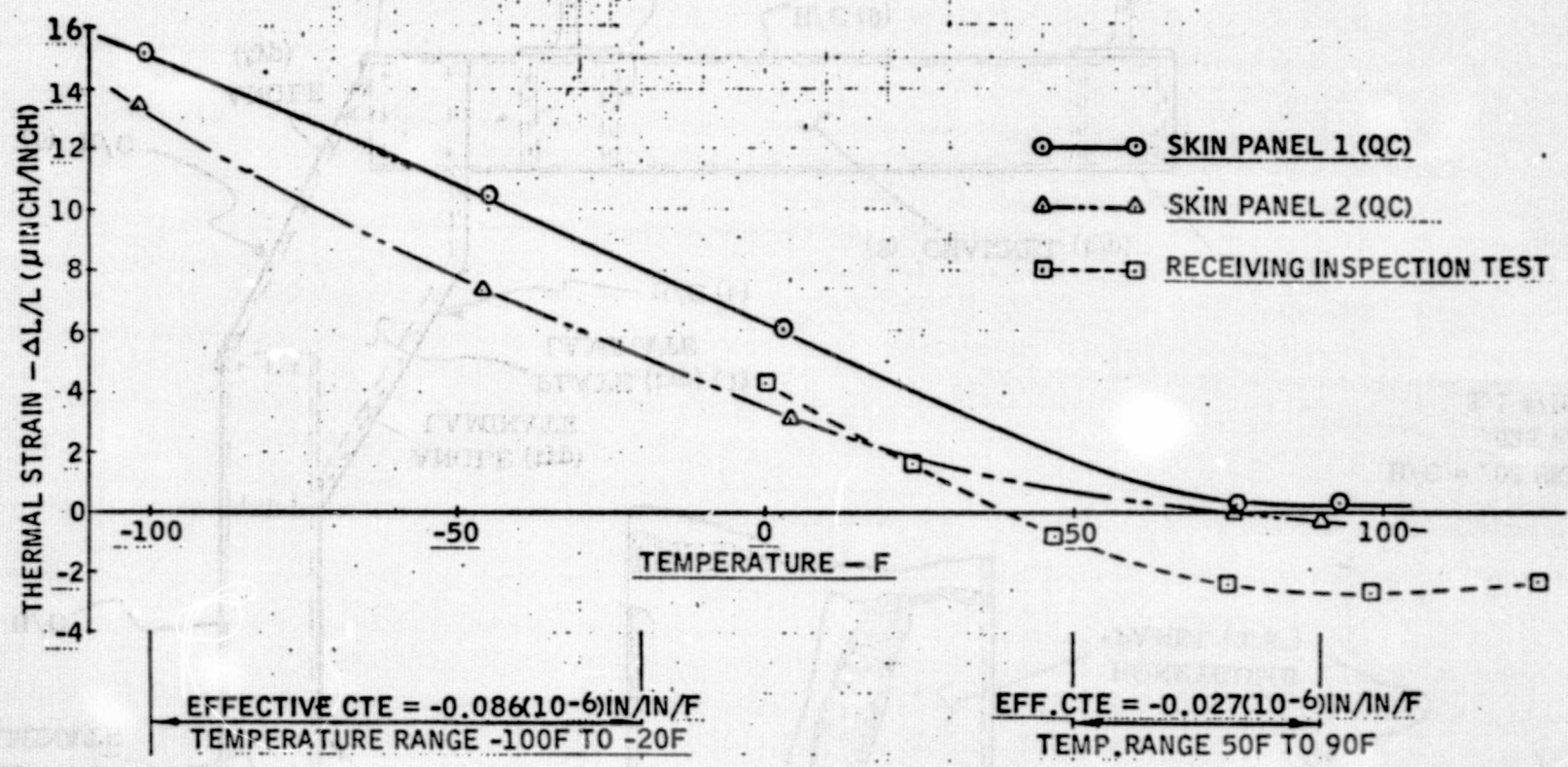
Figure 7. CTE Test Results of Shell Extension Laminate
GY-70/X-30 (0, 36, 72, 108, 144)$_s$

2.26 IN.

26.2 IN.

0.01 ALUMINUM

1,400

1,200

UNTUNED
a = 0.4 μ IN./IN. °F

TEST
RESULTS

800

EXPANSION
(μ IN.)

400

TUNED
a = 0.01 μ IN./IN. °F
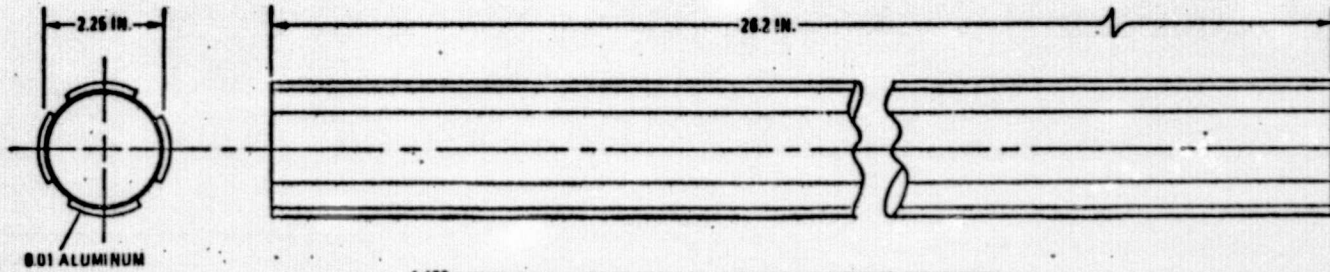
TUBE MATERIAL:
18-PLY GRAPHITE/EPOXY
HM-S/3501
$(0, \pm 45, 0_6)_s$
THEORETICAL
a = 0.5 μ IN./IN. °F

-80   -40   0   40   80

SPECIMEN TEMPERATURE (F)

Figure 8. Structural Tuning Experiment

LENGTH CHANGE AS A FUNCTION OF EXPOSURE TIME TO 75F, 50% RH FOR
GY-70/X-30 (0,45,90,135)s 2 (16ply)
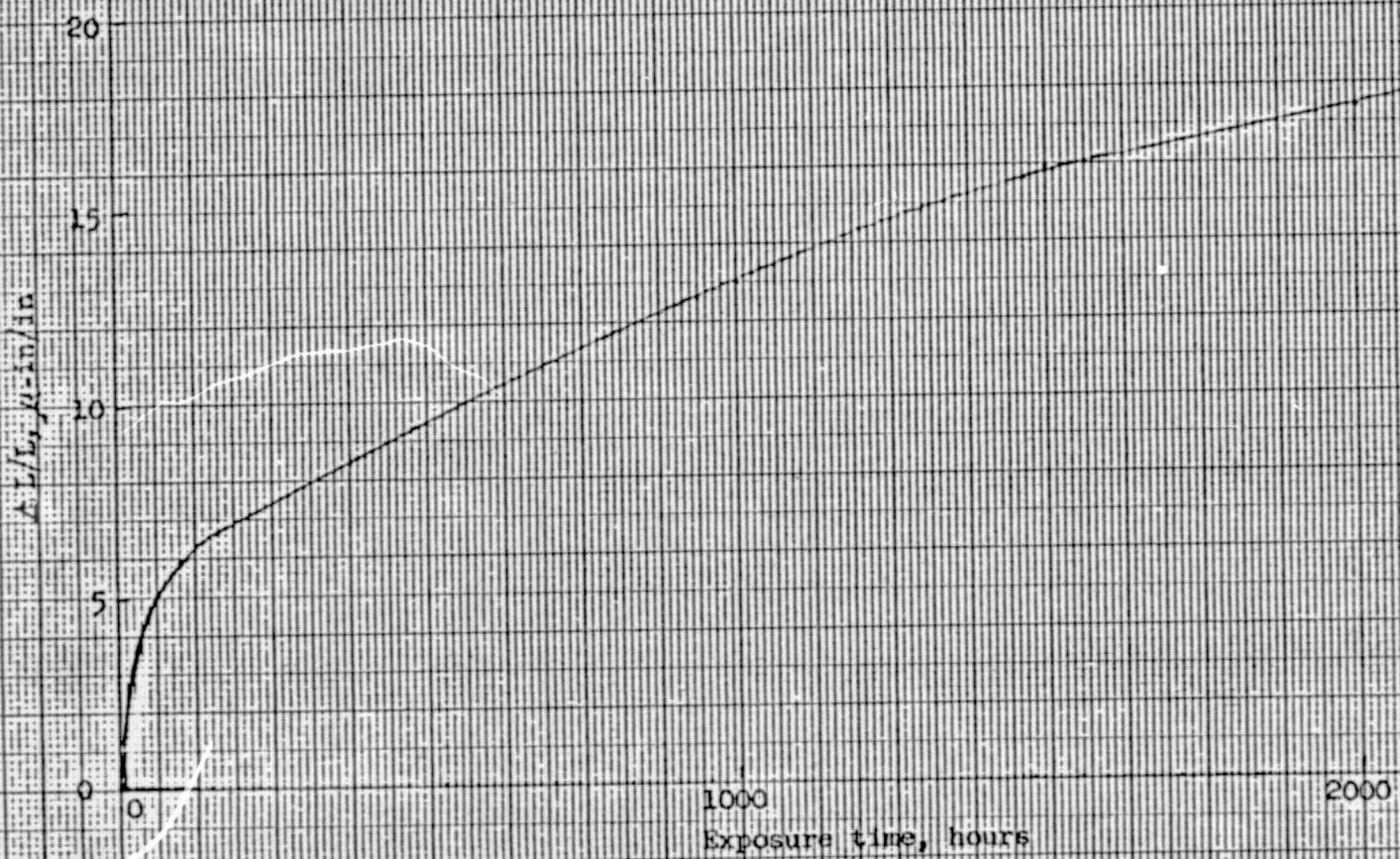
Figure 9

C75-664/034A

Table 2. Candidate Material Systems

Material System	E (MSI)	FTU (ksi)	α in./in./F x 10^{-6}	ρ (lb/in.^{3})	K $-(Btu/ft\text{-}hr/F)$
Graphite/Epoxy (GY-70/X-30 Uni.)	42.5	79.8	-0.6	0.063	0.8, 6
Graphite/Epoxy (GY-70/X-30 Iso.)	14.9	28.1	-0.03	0.063	0.8, 6
Graphite/Epoxy (HM-S/934 Iso.)	12.1	36.9	0.2	0.063	0.8, 6
Beryllium	42.5	44.0	6.4	0.066	87.0
Invar	20.5	65.0	0.7	0.291	6.05
Titanium	16.0	160.0	5.8	0.16	4.2
Aluminum	10.5	70.0	13.0	0.10	76.0

Table 3. Quality Control Tests on Production Batches of GY-70/X-30

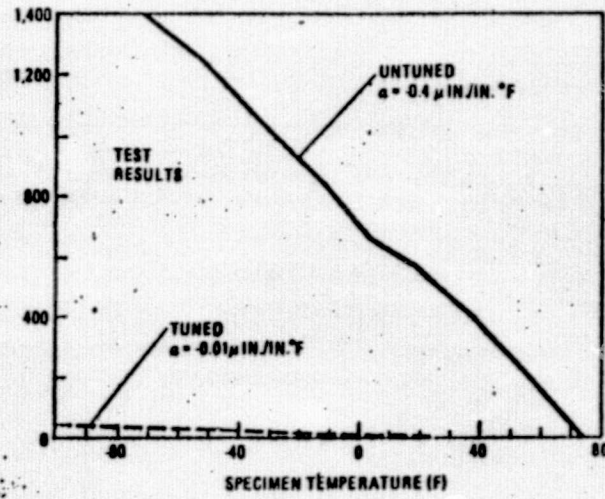|	Prepreg Properties					Fiber Properties			Composite Properties	
Lot No.	Resin Solids (%)	Volatiles (%)	Flow % at 100	Tack	Drape	Tensile Strength (ksi)	Tensile Modulus (msi)	Density gm/cc	Horizontal Beam Shear (ksi)	Flexure Strength (ksi)
4A-13	41.3	4.6	26.4	Pass	Pass	228/227	73/76	1.92		138.3
4A-37	41.0	5.0	26.9	Pass	Pass	228/227	73/76	1.92	9.9	137.5
4A-40	39.5	5.0	24.4	Pass	Pass	230/244/239	76/74/73	1.94	9.0	121.4
4A-61	40.2	4.0	22.9	Pass	Pass	229/246/228	74/79/77	1.94	8.9	132.4
4A-56	44.0	4.3	28.3	Pass	Pass	230/244/236	74/73/76	1.94	8.7	143.5
4A-64	40.9	4.9	25.8	Pass	Pass	228	77	1.94	10.0	146.4
4A-65	42.1	4.7	25.5	Pass	Pass	234/229	73/74	1.94	9.6	112.0
4A-68	41.6	4.9	25.2	Pass	Pass	234/228	73/77	1.94	9.9	146.6
4A-71	40.7	5.0	22.4	Pass	Pass	236/236/228	74/76/77	1.94	9.7	114.0
4A-75	41.9	4.7	24.2	Pass	Pass	236/278/228	74/77/77	1.94	9.1	144.9
4A-82	40.7	4.8	24.1	Pass	Pass	247/230/236/ 234/278	76/77/78/ 77/77	1.94	8.6	112.9
4A-83	42.0	5.0	24.9	Pass	Pass	247/230/228	76/77/79	1.94	9.5	122.4
4A-86	39.5	4.8	23.6	Pass	Pass	247/230/260/ 249/262	76/77/78.2/ 76.9/76.1	1.94	9.9	117.0
4A-87	41.8	4.9	22.4	Pass	Pass	262/246/258	79/76.1/78.7	1.94	10.6	114.5
4A-90	44.4	5.0	25.9	Pass	Pass	257/279/254	75/76/79	1.93/ 1.96/ 1.94	10.7	151.7
4A-99	39.1	4.7	25.2	Pass	Pass	249/246/261/ 254/256	81/78.7/79/ 79/76	1.93/ 1.94	9.5	130.2
4B-98A	43.1	2.7	23.2	Pass	Pass	278/278/264	76/76/76	1.95/ 1.94		
4B-98B	43.2	3.6	25.0	Pass	Pass	254/260/278/ 264	77/76/76/76	1.96/ 1.95/ 1.94		
4B-98C	45.0	1.4	24.8	Pass	Pass	254/260/278/ 264	77/76/76/76	1.96/ 1.95/ 1.94		
4B-98D	42.3	1.7	23.0	Pass	Pass	243/262/269/ 254/260/264/ 264		1.92/ 1.94/ 1.96		

As revealed by photomicrograph techniques, graphite fibers inbedded in an epoxy matrix form an essentially continuous semi-conductive plane. The resistivity of carbon fibers varies from 775×10^{-6} ohm-cm to 1500×10^{-6} ohm-cm, depending upon the type of fiber.

Measurements of reflectivity at 12 and 18 GHz conducted at Convair on polished copper and aluminum and bare HM-S/epoxy graphite/epoxy verify the theoretical plot of reflectivity shown in Figure 10 within a few hundredths of a decibel. Measurements conducted on HM-S/epoxy cured shell samples indicate a loss of approximately 0.02 to 0.04 dB relative to a polished copper sample.

OUTGASSING CHARACTERISTICS — Outgassing of materials in vacuum are of concern for two reasons:

1.   Outgassed products cause a secondary system malfunction such as deposition of coating on mirrors which alters the mirror's optical properties or deposition of an insulating coating on electrical conteacts which prevents electrical continuity during system operation.

2.   Materials being outgassed can suffer a change in mechanical or physical properties that may be detrimental to the function of the material.

Stanford Research Institute (SRI) in its work for Jet Propulsion Laboratory (JPL) defines volatile condensable material (VCM) as the weight of condensate obtainable at 77F (25C) in a given interval of time from a given weight of material (1/8 inch thick) maintained at 257F (125C) in a vacuum of at least 5×10^{-6} torr. JPL and SRI selected 125C in 1962 as the upper limit that might be encountered in spacecraft operations in space.

A number of test methods exists for determining the applicability of various nonmetallic materials for use in space. Most methods determine total weight loss and VCM for a given time period, and most are modifications of the SRI technique. SRI used thermal-vacuum analytical procedures to determine loss in weight, maximum VCM content, and the character of the VCM released by the polymeric products. SRI used infrared spectro-photometry to identify VCM and mass spectrometry to identify the noncondensable substances. From a historical standpoint, it was assumed that polymeric substances that lose less than 1% of their weight in a thermal-vacuum environment are suitable for spacecraft applications. It is very important that the nature of the materials lost is known, and a value of $\leq 0.1\%$ VCM was set up as an additional standard. Many materials that exceed the 1% total weight loss will still meet the more important 0.1% maximum VCM.

SRI developed a technique known as "micro-VCM" determination for rapid screening of candidate polymeric materials. This method has been correlated with macro-VCM determinations. SRI's system can accommodate and test 24 samples simultaneously. The candidate polymeric materials are cut into small pieces of about 1/16 by 1/16 inch
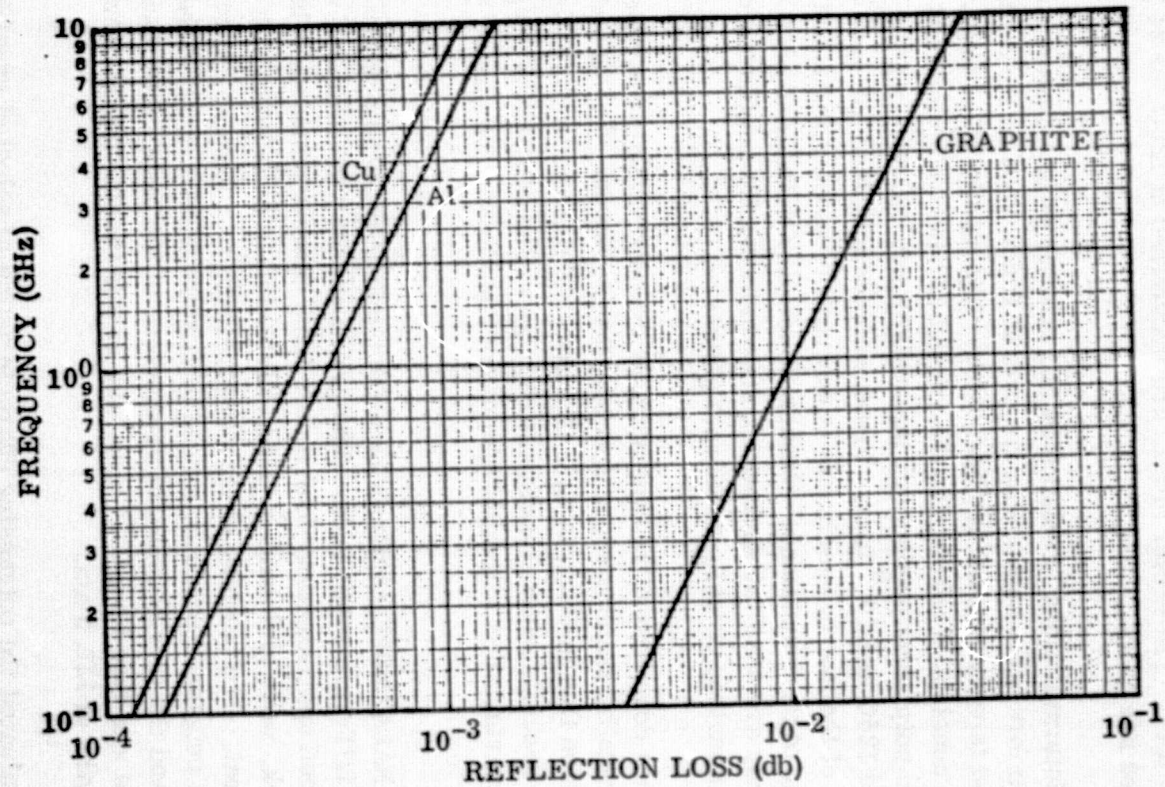
Figure 10. Reflector Surface Reflectivity Loss

and postcured as required. Coatings are evaluated after application to stainless steel screens, while oils or viscous liquids are taken up in ignited asbestos. Samples of 100 to 200 milligrams are placed in preweighed microaluminum boats and stored for a minimum of 24 hours at room temperature and 50% RH. The samples are weighed on a microbalance and placed in compartments in heatable copper blocks. Preweighed copper or salt flat collector plates are also attached to copper cooling blocks. The whole system is assembled in a vacuum system, which is then evacuated to a pressure less than 10^{-6} torr. The heater blocks are maintained at 125C for 24 hours while the collector plates are at 25C.

Macro-VCM determinations developed by SRI utilizes 4- to 10-gram samples, and this test provides information concerning the rate at which VCM is re-evaporated. The equipment used is very similar for both micro- and macro-VCM tests. A macro-VCM determination consists of measuring the amount of VCM collected (and weight loss incurred) from polymeric products at intervals of 24, 48, 96, and 336 hours in an environment of 125C and 10^{-6} torr. Fresh samples are used for each time period. The thickness of the macro specimens is no greater than 1/3 inch, and there is no preconditioning of the specimens. Results obtained with the macro-VCM apparatus are definitive. They are used for spacecraft material selection, whereas the micro-VCM is used for eliminating grossly inadequate polymers.

NASA/MSFC has done extensive evaluation of the outgassing properties of both non-metallic and metallic materials per Specification 50M02442, "ATM Material Control for Contamination Due to Outgassing", in support of the Apollo Telescope Mount (ATM) Program, and recently several facilities throughout the country have evaluated the outgassing characteristics of graphite/epoxy composites. The data is summarized in Table 4 .

The testing at NASA/MSFC of HM-S/X-904 and HT-S/E-350 was specifically conducted to support the LST-type application. The graphite/epoxy was mounted on an electrical heater and placed approximately four inches from sample mirrors. These mirrors, provided by Itek, were aluminum-coated, first-surface reflectors with a magnesium fluoride overcoat. The purpose of the overcoat was to minimize the reflectance at 121.6 nm. All outgassed products moved toward the mirrors due to the pumping action of the system and the thermodynamic parameters of the tests. The vacuum maintained during the tests was less than 10^{-6} torr, and no significant optical damage was observed above wavelengths of 121.6 nm.

Convair has evaluated the outgassing characteristics of selected graphite/epoxy composites under AFML Contract F33615-72C-1388. The device consists basically of an ultra-clean, oil-free vacuum system equipped with a quartz crystal microbalance (QCM) which measure the mass deposeted 8 inches from the line perpendicular to the 4-inch-diameter specimen, a residual gas analyzer (RGS), and optical surfaces for collecting outgassing products. The RGS monitors residual gases in the 0 to 250 atomic mass unit range to identify outgassing products within this range. The optical collection

Table 4. Outgassing Data on Graphite/Epoxy and Boron/Epoxy Composites

Material	Panel Fabricator	Testing Agency	Test Method	Total Weight Loss (%)	VCM (%)
Type I/5208	Lockheed	NASA/Goddard	SRI type	0.093	0.014
HM-S/BP-907	Hercules, Inc.	Ball Bros	ATM type	0.079	None
A-S/3501	Hercules, Inc.	Ball Bros	ATM type	0.159	None
HM-S/X-904	Convair	NASA/MSFC	ATM	—	None
HT-S/E-350	Convair	NASA/MSFC	ATM	—	None
A-S/3501	Rockwell Int	Sandia Corp	SRI type	0.77	None
Modmor II/1004	Rockwell Int	Sandia Corp	SRI type	0.49	0.009
Epoxy/Carbon	Goodyear	NASA/GSFC	SRI type	0.55	0.04
Rigidite 5505	Whittaker	JPL	SRI type	0.46	0.01
Boron/828, 1031	Shell Chemical	JPL	SRI type	0.25	0.02
HY-E-1002	Fiberite Co	JPL	SRI type	0.32	0.04
HY-E-1001	Fiberite Co	JPL	SRI type	0.53	0.04
HM-S/4617	—	NR-NASA	SRI type	0.63	0.03
HM-S/4617 with Al coat	—	NR-NASA	SRI type	0.55	0.02
GY-70/X-30	Convair	NASA/MSFC	ATM	Passed	

surfaces can be moved into a section of the vacuum chamber, where it is irradiated by UV radiation at either 1,236 Å or 1,849 Å while the specular reflectance or hemispherical scattered radiation is measured. This information tells how the outgassing products would affect the performance of optical surfaces upon which the products could deposit. The QCM and the optical collection surfaces are cooled with circulating water to about 60F, while the outgassing sample can be heated to +150F. The QCM is capable of detecting 3.5×19^{-9} gm/cm^2.

A specimen of GY-70/X-904 was tested for 30 days and no outgassing was detected during this period. At the end of the 30-day period, the specimen was heated to 104F for a 12-hour period with no outgassing detected. Additional exposures with a GY-70/X-904-faced sandwich panel heated to 150F shoed no outgassing products detected at masses greater than 43 atomic mass units. No changes in specular or diffuse reflectance was noted at either 1,848 Å or 1,236 Å of test mirrors held at 70F in the vacuum system during the test. Similar testing has recently been conducted at Convair on HM-S/X-30 with identical results. (See Table 5).

Since in outgassing the resin is the prime contributer, the latter data is a confirmation of the ATM type data obtained at NASA/MSFC. None of the boron or graphite reinforced epoxies evaluated to date to either SRI or ATM tests have failed to pass the respective requirements.

DIMENSIONAL STABILITY — One of the prime material requisites for this program is a predictable and repeatable coefficient of thermal expansion. Convair has evaluated numerous graphite/epoxy composites in the past from -320 to 375F. This work was

Table 5. Outgassing of HM-S/X-30 Composite

Test Duration	10 days
Specimen Temperature	150F
QCM Temperature	75F
Sample Reflector Temperature:	75F
Average Pressure:	2 x 10⁻⁷ Torr
QCM Change (0 Hz)	No Change
RGA:	No AMU above 44 Detected
Change in Reflectance Ratio:	

1848A		1236A	
Specular	Diffuse	Specular	Diffuse
No Change -0-	No Change -0-	No Change -0-	No Change -0-

Note: Test performed under AFML Contract F33615-72-C-1388

extensively conducted under Air Force Contracts F33615-70-C-1442 and F33615-72-C-1388, and Convair IRAD programs. The data includes the effect of fiber modulus, resin content, voids and microcracks, layup orientation, and batch-to-batch variation. It has been found in many of the thermal expansion runs that several temperature cycles are required until stabilization occurs and the test points can be repeated time after time. This has also been found to be true in large bonded graphite/epoxy structures. Generally, five thermal cycles are more than adequate to thermally stabilize the graphite/epoxy. The stabilization mechanism has never been pin-pointed although many theories exist. Convair believes that for antenna applications, it is good practice to thermally cycle all graphite/epoxy parts before final use.

The repeatability of thermal expansion characteristics from part to part is of utmost importance for the proposed antenna and associated hardware. In order to assure stability of the thermal expansion characteristics of the hardware, Convair proposes to expose it to ten thermal cycles from -10 to 50C before final usage.

RESISTANCE TO MICROCRACKING — Microcracking, sometimes known as translaminar stress relief cracking, occurs with many graphite/epoxy composites. The primary cause is the difference in the elastic and thermal properties of the graphite reinforcement and the epoxy. In many cases, the microcracking can be analytically predicted. Composites containing higher modulus fibers are more likely to encounter microcracking because of more negative thermal expansion coefficients and because they are generally more difficult to adhere to, resulting in lower shear strengths. Therefore, one would expect GY-70 and Thornel 75 laminates to be more prone to cracking than HM-S and Modmor I systems, which in turn would be more likely to crack than HT-S, A-S, or Thornel 300 systems. Layup orientations also affect the occurrence of microcracking. Generally, in crossplied layups it is desirable to minimize the angle between successive plies and to minimize large numbers of plies in one direction sandwiched between angled plies. Selection of resin is of extreme importance, it being desirable to have a tough resin with a high modulus and high strain capacity. A resin that cures at relatively low temperature (250 to 275F) will also minimize microcracking since it results in lower built-in thermal stresses.

Microcracking is not a concern from a structural standpoint, at least with respect to low cycle fatigue criteria. Testing of microcracked laminates under Air Force Contract F33615-70-C1442 showed no adverse effects as a result of low cycle fatigue.

Convair has recently shown that GY-70/X-904 isotropic laminates almost always crack in cooldown after curing at 375F. Cracks generally parallel the fibers in each lamina. In some cases where the panels at RT have not microcracked, subsequent cooling to -320F causes cracking. By going to the Fiberite X-30 resin that cures at 250 to 275F, isotropic GY-70 laminates have been prepared which survive cycling to -320F without cracking. Using the most sensitive thermal expansion measuring equipment available (laser precision dilatometer), the temperature at which microcracking occurs can be accurately pinpointed.

Figure 10 shows GY-70/X-30 that has been cycled from 300F to -320F. Thermal cracking to a very minor extent was encountered at approximately -170F. The photomicrograph taken at 50X shows the normal void-free appearance of GY-70/X-30. In contrast, the best 350F curing GY-70/ep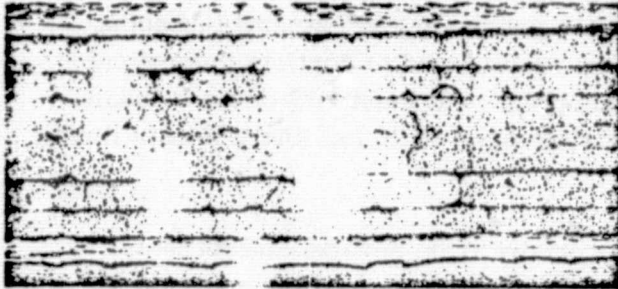oxy from a thermal stability standpoint will have many more microcracks. Generally, higher temperature curing systems will have more lamina affected and the crack spacing will be about half that of the GY-70/X-30.

Figure 10. Montage of Photomicrographs of Thermally Cycled (0/45/90/135)$_s$ GY-70/X-30. Note occasional microcracks.

MOISTURE EFFECTS — Graphite/epoxy composites are affected by moisture absorption. The effects, which have been the subject of considerable experimental efforts by Convair, are manifested in two forms: (1) loss in high temperature, matrix-dominated strength properties and (2) changes in physical dimensions. The effects are reversible in that either heat and/or vacuum will drive off the moisture and return the composites to their dry control properties and dimensions. The cause of the problem is the plasticization of the epoxy resin by moisture which subsequently lowers the glass transition temperature of the resin. This is true for all epoxy resins, and the effects on reinforced epoxies have been noted with boron, graphite, fiberglass, and Kevlar reinforced systems.

Under Contract NAS8-27435, it was shown that water boil is a good accelerated aging test technique and correlates well with three- and six-week exposures to 120F and 95 to 100% RH. It also correlates well with exposures to 20 weeks at 65 to 75F and 52% RH. Ambient exposures in vacuum (10^{-3} torr) dry the composites, and testing specimens after such exposure shows slight improvement in strength over initial control tests. Testing to date with high modulus or ultra-high modulus (HM-S or GY-70) reinforced epoxies shows less effect due to moisture exposure than that obtained with the higher strength, lower modulus graphite-reinforced epoxies. Convair has shown that vacuum drying of graphite/epoxy is possible at RT and 10^{-3} torr. Recent testing

at Convair of a 26-inch-long by 2-inch-diameter graphite/epoxy tube after ambient aging showed that length stabilization occurred after approximately six hours in vacuum.

PRECISION STRAIN (MICROYIELD) CHARACTERISTICS — The microyield strength of a material is defined as the tensile stress level at which one part per million of permanent plastic strain is detectable. Recently graphite/epoxy systems have been measured for the first time. Itek Corporation, using an Instron test machine in a controlled temperature environment, measured the microstrain behavior of unidirectional and crossplied panels of GY-70/X-904, HM-S/4617, and GY-70/X-30 panels prepared by Convair. The technique consisted of loading to a stress level, unloading, and measuring residual strain with large precision strain gages. This was repeated at higher and higher stress levels until the residual strain exceeded 0.5 microinch. Figure 11 3-19 shows plots of the precision strain characteristics of both GY-70/X-904 and GY-70/X-30. Testing of the GY-70 unidirectional and pseudoisotropic laminates was stopped at 20,000 psi (which is far in excess of the precision yield strength of some metals) because of equipment limitations. These results tend to confirm theoretical considerations, which suggest the precision yield point is at least 90% of the breaking strength. For this program, however, a microyield point of 20 ksi (the test data limit) wall be conservatively assumed.

RESISTANCE TO RADIATION — Radiation is a concern from several standpoints: (1) possible loss in strength or change in elastic moduli and (2) possible scission of polymers into lower molecular weight species, which will increase outgassing rates and thereby increase potential for changes in optical properties of mirror systems.

The effects of radiation on reinforced plastics as well as other polymeric materials are dependent on the environments to which the material is exposed, such as elevated temperatures and vacuum or air atmospheres. As a rule, the effects of penetrating radiation and elevated temperature on a polymer in air are more severe than the effects of the same dose of radiation and elevated temperature in vacuum or inert atmosphere.

Ultraviolet radiation can produce photochemical reations in the polymeric resin binder of reinforced plastics that are similar to the reactions taking place during exposure to penetrating radiation (i.e., cross-linking and chanin scission). Because of the high absorptivity of the resins in the ultra-violet region of the spectrum, however, most of the energy is deposited near the exposed surfaces, and damage effects are limited to changes in spectral properties such as darkening or an increase in solar absorptivity. The bulk of the material is not affected, and mechanical properties of typical cross-sectional thicknesses used for structural applications on the external surfaces of a spacecraft are not significantly changed. The damage effects noted by various investigators appear to have been due principally to the elevated temperature produced by energy absorption during the accelerated ultraviolet irradiation rather than to the ultra-violet photolysis itself.
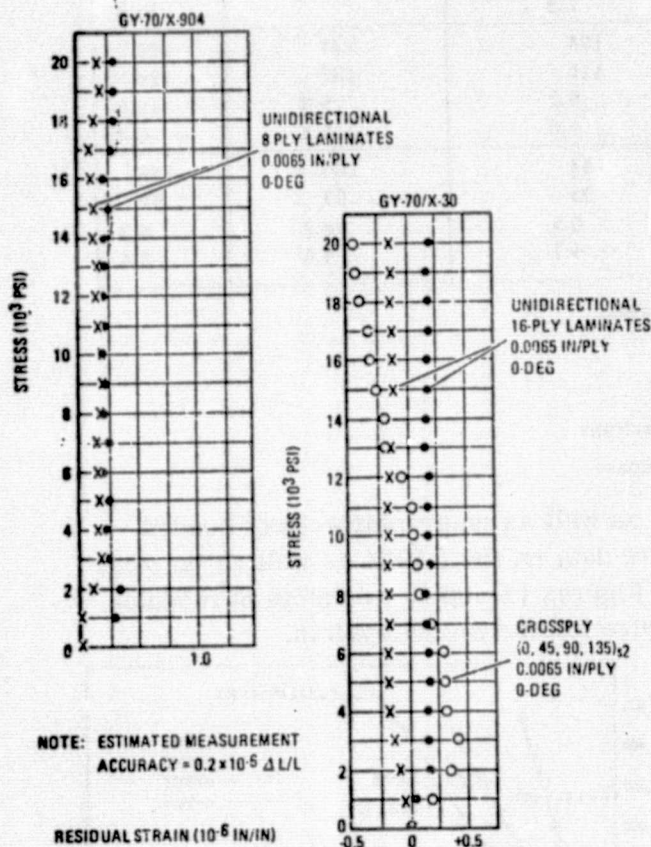
Under Air Force Contract F33615-70-C-1422, Convair conducted extensive exposures of graphite/epoxy composites to space environments using the guidelines established in SAMSO-TR-70-218, "Space Environmental Testing of Advanced Composite Materials," dated April 1970. It was recognized that planned spacecraft will have active lifetimes in the space environment of from two years to as long as fifteen years.

Specimens of epoxy matrix composites were subjected to UV exposure in vacuum, electron, and proton radiation. Dimensions, flexure strength, and shear strength were checked.

All the samples were exposed to 756 hours of vacuum (10^{-6} torr) and equivalent four-sun UV exposure. None of the specimens showed any change in width or length as a result of this exposure, and none showed any visible discoloration or surface change of any kind. Therefore, the irradiated specimens were subjected to 1 Mev particle radiation for 10 minutes. The results of this testing also indicate no strength loss at room temperature. The loss in strength at 350F was attributed to moisture effects since there was more than six months of ambient storage between exposure and testing. A summary of the data is given in Table 6.

Figure 11. Precision Yield Characteristics for Graphite/Epoxy Composite Materials

EPOXY ADHESIVE — Convair proposed to join the structural details by adhesive bonding. The adhesive selected is Hysol Corporation's EA934. This system is a filled modified epoxy that cures at room temperature. Originally developed by Shell Chemical Corporation, it has been used extensively at Convair for Atlas and Centaur applications at temperatures from -320F to 450F. This system was used in the assembly of a large OV1 graphite/epoxy adapter section, which was successfully built and tested under Air Force Contract F33615-70-C-1442 and also on the GEMS (half-scale graphite/epoxy shell version of the large space telescope), the HEAO-B, and the 8-foot composite antenna.

Table 6 . Radiation Exposure Data (unidirectional layups)

System	Test	Temperature	Vacuum/UV	Vac/UV/Electrons	Vac/UV/Protons	Control
SP272 Boron/ Epoxy	Flexure	RT	286	265	—	280
		350F	70	69.5	—	217*
	Shear	RT	13.5	13.8	—	15.7
		350F	8.3	7.3	—	11.4*
HT-S/X-904	Flexure	RT	—	198	227	226
		350F	—	119	137	120
	Shear	RT	—	8.7	9.3	12.2
		350F	—	4.6	5.3	6.4
GY-70/X-904	Flexure	RT	—	141	106	118
		350F	—	98	97	92
	Shear	RT	—	6.5	6.2	6.3
		350F	—	4.7	4.6	3.6

*Strength at 350F after water boil was 23.7 ksi flex & 5.7 ksi shear

1. All values in ksi

2. Vacuum/UV is 756 hours 10^{-6} torr at 4 suns UV

3. Vac/UV/electrons same as note 2 plus 10 minutes 1 Mev electrons

4. Vac/UV/protons same as note 2 plus 10 minutes 1 Mev protons

Extensive test data exists on the basic adhesive as well as on graphite/epoxy bonded joints. Table 7 summarizes some bulk adhesive data on the EA934 as well as on other adhesive candidates for space optics systems. Figures 12 and 13 are plots of modulus and thermal expansion as a function of temperature for the EA934 system.

Table 7 . Structural Properties of Candidate Adhesives (cast bulk tensile specimens - room temperature)

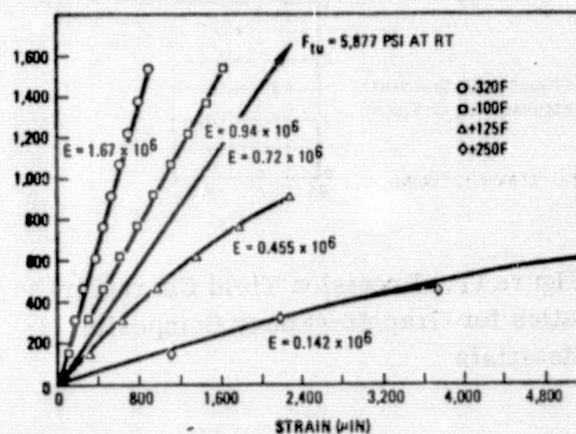| Adhesive	F_{tu} (psi)	E(msi)
EA-9309	3,242	0.35
	3,493	0.28
	3,542	0.28
Avg	3,426	0.30
EA-9320	5,582	0.39
	5,865	0.40
	6,016	0.40
Avg	5,821	0.40
EA-934	5,597	0.71
	5,209	0.73
	6,825	0.71
Avg	5,877	0.72
ADX-394.1	3,920	0.49
	5,427	0.58
	4,810	0.55
Avg	4,719	0.53

Figure 12. Stress-Strain Data for Cast Hysol EA-934 Adhesive

In all graphite/epoxy joint testing, failure has occurred in the graphite/epoxy adherends rather than the adhesive. Joint strength is, therefore, dependent on the specific graphite/epoxy, the joint geometry, and test conditions. Table 8 shows some
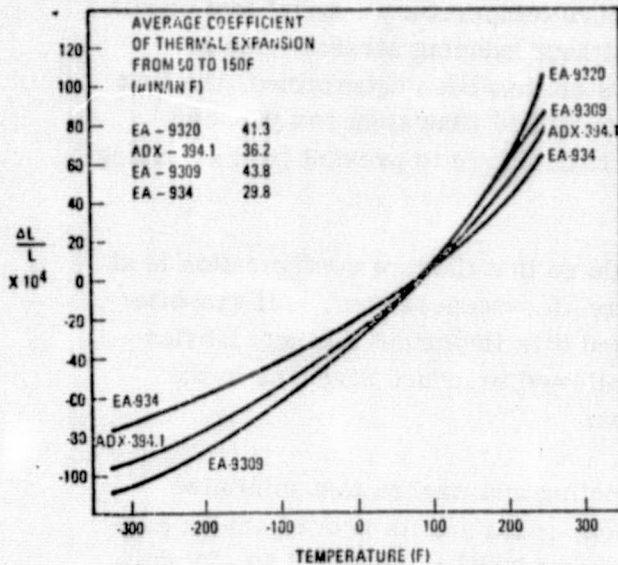
AVERAGE COEFFICIENT OF THERMAL EXPANSION FROM 50 TO 150F (µIN/IN F)

EA – 9320	41.3
ADX – 394.1	36.2
EA – 9309	43.8
EA – 934	29.8

Figure 13. Total Linear Thermal Expansion of Candidate Bonding Adhesives

Table 8. Cure Time Versus Tensile Shear (etched 2024-T3 Clad, MMM-A-132).

Time (at end of pot. life)	Strength (psi)
3-4 hr at 75F	300
8 hr at 75F	700
12 hr at 75F	1,000
24 hr at 75F	2,200
5-7 days at 75F	3,000
3 hr at 160F	3,000
90 min at 180F	3,000
60 min at 200F	3,000
2 hr at 200F	3,500

Table 9. Summary of Outgassing Data on EA-934

Cure Conditions	Data Source	Test Method	Total Wt. Loss (%)	VCM (%)
16 hr at 52C (126F)	JPL	SRI	0.42	0.02
7 days at RT	GSFC	SRI	0.28	0.01
1 hr at 82C (180F)	SRI	SRI	0.10	0.08
16 hr at 65C (149F)	NAR	SRI	0.42	0.02
16 hr at 65C (149F)	NAR	SRI	0.17	0.01
4 hr at 66C (150F) plus 2 hr at 100C (212F) in vacuum)	MSFC	ATM	Passed	

Hysol data on EA934 bonded aluminum joints as a function of cure time and temperature. It shows that the reaction is completed at room temperature in less than one week. This is important from an outgassing standpoint.

Extensive outgassing tests have been conducted on EA934 using both the ATM and the more stringent SRI conditions. A summary of the data is given in Table 9. The data supports the selection of the EA934 as the adhesive. In addition, the GEMS structure has just completed extensive thermal/vacuum testing. This large bonded graphite/epoxy structure was subjected to 36 days at approximately 10^{-6} torr, during which time extensive measurements were made on its optics using a Hewlett Packard 5526A laser measurement system. Visual examination of the mirrors after 36 days of exposure showed no outgassed products. In fact, the very sensitive laser system showed no power losses that could be attributed to outgassed products. Since the GEMS shell was bonded with EA934, this fine performance supports Convair's material selections.

FABRICATION AND ASSEMBLY

FABRICATION AND ASSEMBLY PHILOSOPHY – The antenna manufacturing philosophy is based on minimizing all stress and tolerance buildup during the fabrication and assembly sequence.

An aid in fabricating graphite/epoxy components is Convair's proprietary dielectric monitor which can be used during each heat cure cycle. The monitor visually indicates the "static gel point," a phase during a heat cure cycle where the resin system and any type of tooling material is thermally compatible.

The monitor is used initially to determine at what cure temperature a metal tool should be designed to for curing a specific resin system without inducing stresses due to thermal expansion differences between the resin system has been determined, the heat cure temperature is held at that point until a predetermined time span has passed. Pressure and vacuum are released during cure cycle cooldown to prevent part stressing during that phase of the cure cycle.

All metal cure cycle tools will be designed and made so that the tool configuration is at the required shape when the static gel point of the resin system occurs. All graphite/epoxy parts remain thermally stable at this point and it is important that any fabrication tool, other than a graphite/epoxy tool, is not allowed to induce stresses in the parts due to heatup or cooldown thermal differences.

Assembly distortions will be minimized by using tooling approaches that minimize bondline pressures. The hydroscopic nature of epoxy resin and its accompanying geometric growth will be reduced by maintaining a constant 20% humidity and 70 ±5F during assembly and profilometer tests.

FABRICATION AND ASSEMBLY SEQUENCE

Reflector Shell

The reflector shell will be laid up on a male bulk graphite tool. Graphite is chosen due to its stability and machinability. The tool will be machined to a ±1-mil tolerance by using a trace template and machining in a controlled temperature machine shop. The surface RMS will be initially determined by use of a ±1-mil tolerance check template. The reflector tool will be made with thermal differences determined to produce a graphite/epoxy reflector dish having the desired shape acceptance criteria.

A computer program is used to plot patterns for graphite prepreg tiles for the isotropic paraboloid shell. The primary advantage of this approach is that the tiles are shaped so that fibers are oriented along the major axis of the panels, reducing waste, while the fibers are "clocked" tile-to-tile to achieve isotropic characteristics over the compound surface. The full-size computer generated patterns are transferred photographically to template stock, reducing drafting time.

An "ideal" fiber in the surface of the paraboloid at a vertex centered point (r, θ, z) makes an angle $(\theta + \phi)$ to the tangent radial vector at the point where ϕ is the ply angle. This simple algorithm is used as a basic for pattern generation.

There are two steps in generating a panel: (1) constructing a fiber that runs longitudinally through the center of the panel, and (2) constructing a flat panel around the fiber which has the proper shape and dimensions so that when worked down on the surface of the paraboloid, the central fiber follows its correct path and the boundaries of the panel

fit adjacent panels. The first step is solution by numerical methods of the equations governing the ideal fiber. The second step is an empirical solution based upon observed characteristics of unidirectional graphite fibers in an uncured resin matrix when worked into a three-dimensional shape.

Preliminary patterns for a single lamination are generated and taped together over the master tool to verify the pattern fit. Another set is generated to layout the cutting procedure from graphite stock. When the pattern set meets requirements of engineering and fabrication, it drawn finally on dimensionally stable pattern material. This flexibility provided by the computer yields near optimum patterns for the isotropic shell.

Each shell layup ply will be vacuum compacted to ensure intimate contact with the tool and with each succeeding ply. The reflector dish will then be vacuum bagged and heat cured. Figure 14 shows typical tiles for one-quarter of a prepreg laminae.

Thermal Cycling

It is recommended that the main reflector be thermal cycled to increase the composite material's dimensional stability. Tests at Convair indicate that for those structures, where holding a shape is critical, thermal cycling materially reduces creep or permanent set. A typical truss assembly was thermally cycled 15 times and its shape measured before and after each five cycles. The results are shown in Figure 15 . It is clear that most stability is achieved after only five cycles.

Reflector Dish Surface Preparation

The reflector assembly will be abraded with a fine 35μ grit. The surface will then be cleaned by a water/oil-free solvent and a 0.04-mil-thick vapor deposited aluminum coating and overcoat applied.

Reflector Shape Adjustment

The reflector assembly will be positioned under Convair's computerized dish measurement device and adjusted to the specified tolerances by use of micrometer adjustors.

The reflector assembly will then be inverted and positioned from the same points as experienced under the dish measurement device. The truss ribs will then be locked-out by bonded-on clips.

The reflector assembly will then be placed in a holding fixture which also picks up the same positioning points as used on previous assembly operations. The remaining angle clips will be located and bonded in position.
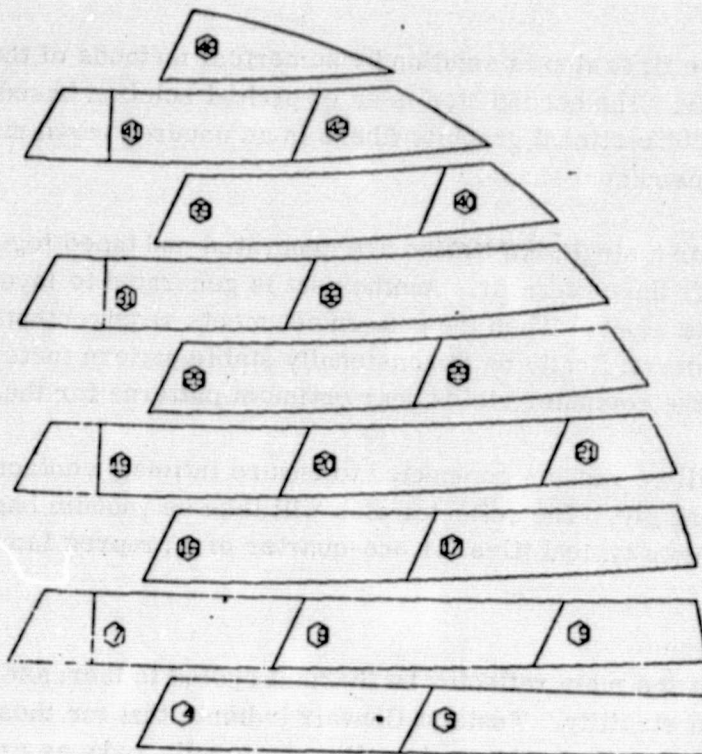
Figure 14. Typical Computer-Generated Tiles for Reflector Prepreg
Laminae
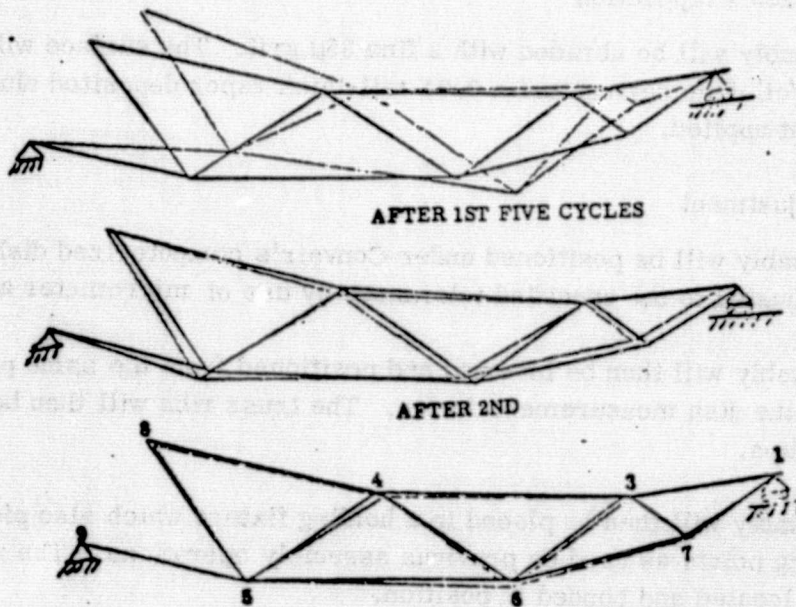

AFTER 1ST FIVE CYCLES

AFTER 2ND

Figure 15. Exaggerated Plot of Permanent Set Due to Thermal Cycling
(scale - 0.15, set exaggerated 1000X)

SURFACE CONTOUR MEASUREMENT DEVICE — Facilities for precision reflector surface measurement (to 0.0001 inch) consist of an adjustable (two angular coordinates) sweep arm and an electronic sensor head (shown in Figure 16). Data is recorded digitally and immediately processed for contour evaluation, as shown in Figure 17 . Output parameters are surface rms, focal length, rotation about x and y axes, vertex displacement, and deviation of each sample point from the best fitting paraboloid. A detailed contour plot of the overall surface is also produced.

On the basis of this plot, the sensor arm is positioned over high and low areas of the contour; micrometer adjustments force the surface toward the best-fit parabola-torus.

Figure 16 . Surface Contour Measurement Apparatus

The major advantage of this proposed design is that it allows fine surface contour adjustment after the reflector dish is cured, thus minimizing the impact of manufacturing and material variations inherent in the layup and cure conditions. This is accomplished as shown in Figure 18 for a typical antenna.

ACCEPTANCE TESTING

Acceptance testing will consist of a modal search on the test model (or engineering model) plus a thermal environment test on each antenna.

MODAL SURVEY — To verify the math model analysis, Convair will conduct a low level sinusoidal vibration and modal survey test. The antenna assembly will be evaluated using the same techniques developed in the Viking modal survey tests. It will be mounted in our 15 by 15 by 25-ft dynamic test tower and hard mounted by its interface fittings to the tower base reaction mass. This mass is a plate, 12 by 12 ft by 6 in., weighing 35,000 pounds.

Two 50-pound-force electrodynamic exciters will be attached to the antenna structure using "sting" bars. The attack locations will be varied to assure excitations of fundamental torsional and bending modes. We will install ten Endevco 2200 series accelerometers on the structure in locations designated by Convair personnel. A low force survey sweep between 5 and 150 Hz will be made to determine the maximum response frequencies. The input and response data will be recorded on real-time direct write recorders. This data will be used to identify the modal frequencies by the relative responses of the accelerometer
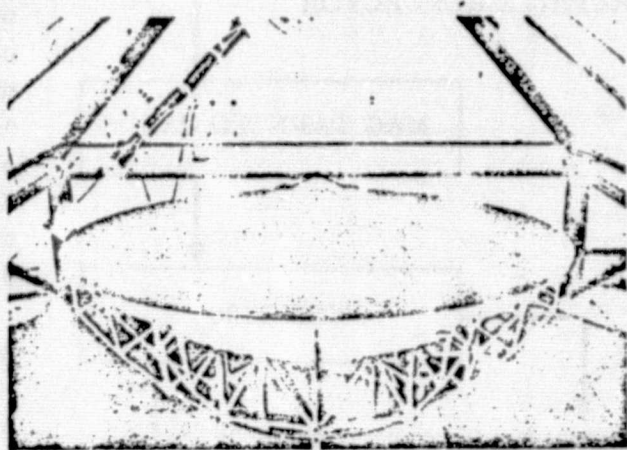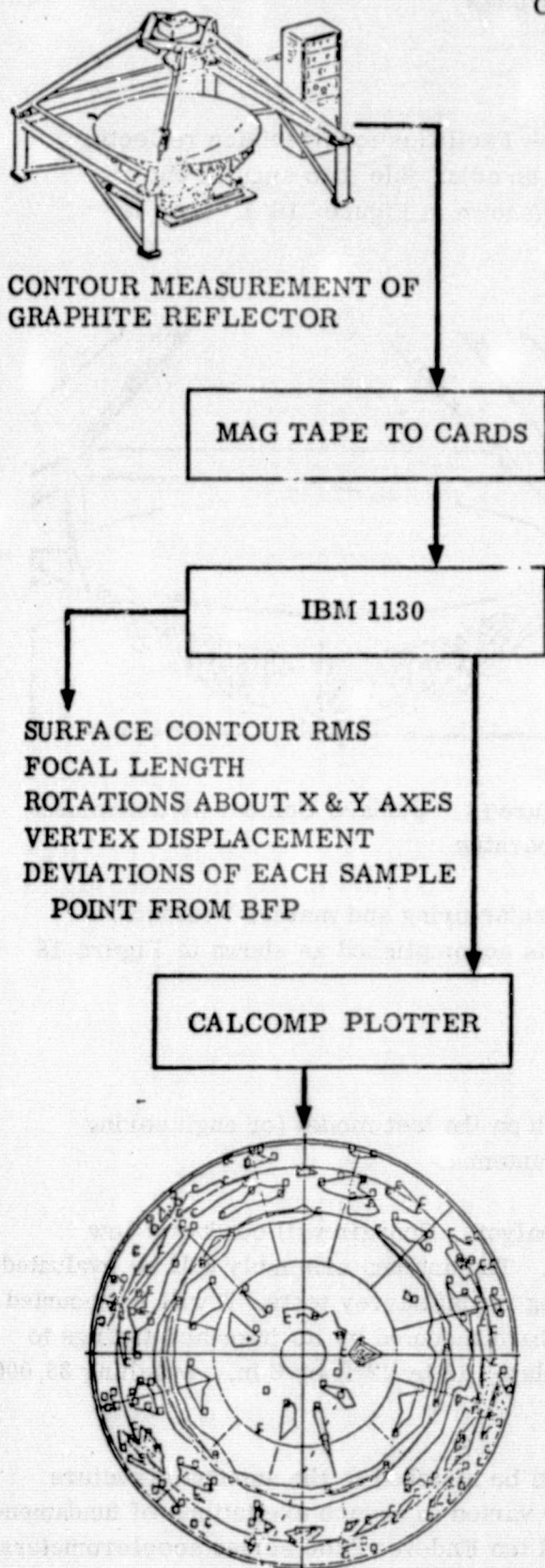
CONTOUR MEASUREMENT OF
GRAPHITE REFLECTOR

MAG TAPE TO CARDS

IBM 1130

SURFACE CONTOUR RMS
FOCAL LENGTH
ROTATIONS ABOUT X & Y AXES
VERTEX DISPLACEMENT
DEVIATIONS OF EACH SAMPLE
   POINT FROM BFP

CALCOMP PLOTTER

ANTENNA SURFACE CONTOUR PLOT

Figure 17. Contour Data Software

We will also use a roving accelerometer to refine the mode shape data. We will derive this steady state response using the co-quad analyzer. The accelerometer outputs are fed to a co-quad analyzer to produce the resulting mode shape. The co-quad output is in turn fed to the digital computer system and stored on digital magnetic tape. When sufficient data is accumulated at each frequency the mode shape will be printed in tabular form. A Tektronics Model 4010 computer display terminal will be used for real time display of the mode shape data.

MASS PROPERTIES

Mass properties for the reflector, Drive Mechanism Housing and Support Arms is shown in Table 10. These are very rough figures of the graphite/epoxy material components that have been identified and exclude the attach fittings, fasteners, aluminum foil and adhesives that would be utilized in the completed structure.

1) The barrel assembly is bonded to the cured reflector shell.
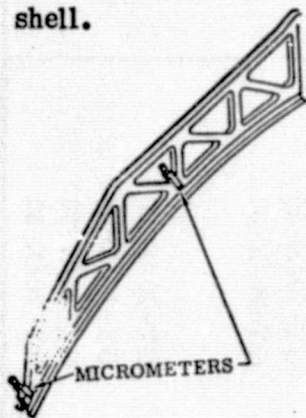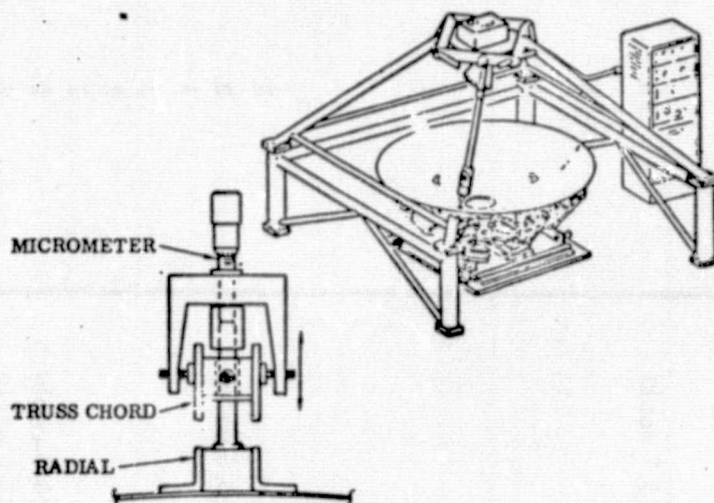
2) The trusses are then attached to the barrel and micrometer adjustment devices installed between the truss and the dish at twelve points (2 × 6 trusses)

3) This rigid assembly is then put under the profilometer (GDCA's contour measuring device) and the micrometers are used to push or pull the thin shell from the rigid truss until the optimum shape is obtained. This is done in a humidity (20% RH) and temperature controlled environment.
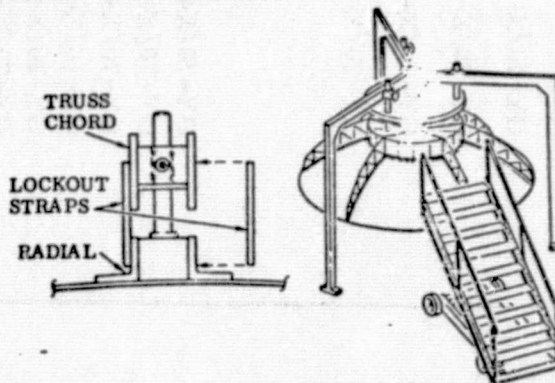
4) The adjustment pins are then locked out and the assembly is removed from the profilometer and placed on the assembly fixture where straps are bonded to the truss chord member and the shell's radial angles, thus locking the trusses and the shell in the optimum position. The adjusting pin and set screw are then removed.

Figure 18. Contour Adjustment Process for a Typical Large Antenna

Table 10. Part Breakdown

Part	Material	Weight (lbs)	Number of Parts
Reflector			
Truss	GY-70/X-30	74 (5.7 each)	13
Skin (reflector)	GY-70/X-30	65	1
Back Panel	GY-70/X-30	81	1
Fwd Panel	GY-70/X-30	33	1
Aft Panel	GY-70/X-30	5	1
Drive Mechanism			
Housing & Support			
1) Channel (arch)	GY-70/X-30	7	1
2) Channel	GY-70/X-30	13 (6.5 each)	2
3) H/C Panel	GY-70/X-30	16	1
4) H/C Panel	GY-70/X-30	16	1
5) H/C Panel	GY-70/X-30	8	1
6) H/C Panel	GY-70/X-30	8	1
7) Plate	GY-70/X-30	16 (8.0 each)	2
8) Channel	GY-70/X-30	16 (8.0 each)	2
9) H/C Panel	GY-70/X-30	16	1
10) H/C Panel	GY-70/X-30	16	1
11) Plate	GY-70/X-30	26 (6.5 each)	4
12) Collar	GY-70/X-30	1 (.5 each)	2
13) Misc. Angles & Clips	GY-70/X-30	8	-
Support Arms			
Channels (LH)	GY-70/X-30	13 (6.5 each)	2
Channels (RH)	GY-70/X-30	13 (6.5 each)	2
H/C (LH)	GY-70/X-30	8	1
H/C (RH)	GY-70/X-30	8	1

Total 467 lbs.

APPENDIX D. TECHNICAL DESCRIPTION OF A SIMS-A ANTENNA —
TULSA DIVISION OF ROCKWELL INTERNATIONAL,
OCTOBER 1975
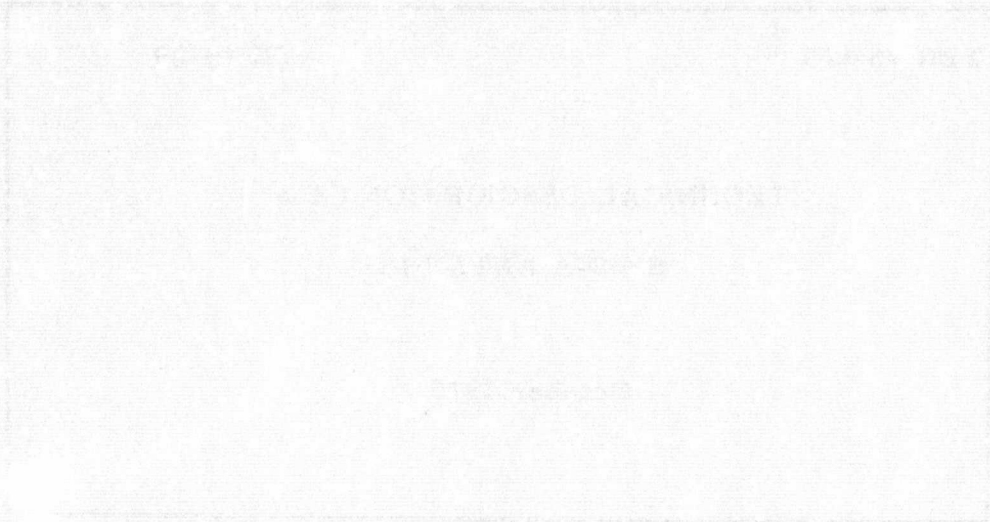
Accession No. T-026678

TDN 76-008   TD 75-39

TECHNICAL DESCRIPTION OF A

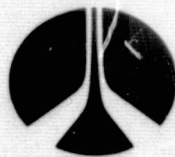# SIMS-A ANTENNA

October 1975

Rockwell International

49-0732

TABLE OF CONTENTS

TABLE OF CONTENTS (Continued)

LIST OF FIGURES

LIST OF TABLES

SHUTTLE IMAGING MICROWAVE SYSTEM ANTENNA

(SIMS-A ANTENNA)

INTRODUCTION

The Missile Systems Division of Rockwell International has requested from the Tulsa Division a Rough Order of Magnitude (ROM) cost and a technical description to design and fabricate the SIMS-A Antenna. Tulsa Division has been making glass composite parts for twelve years and advanced composite parts for six years. The Division is currently under contract to design and fabricate the Payload Bay Doors for the Space Shuttle. These are graphite/epoxy, 60-foot long doors made from 15 foot by 12-1/2 foot individual panels. A photograph of a panel and other photographs of a layup and bond tool, and a manufacturing demonstration panel are attached. The proposed SIMS-A Antenna is similar in overall size to the pictured 15 foot by 12-1/2 foot graphite/epoxy panel.

SUMMARY

The SIMS-A Antenna requires a graphite/epoxy material that is very rigid and that has a coefficient of expansion of approximately $.01 \times 10^{-6}$ inch/inch $^{\circ}$F. This is a lower coefficient of expansion than materials used on current programs. A development program will be conducted by Tulsa Laboratories using cross ply layups of graphite/epoxy tape to select a combination of a specific modulus graphite with its epoxy matrix that will as near as possible have a coefficient of expansion of $.01 \times 10^{-6}$ inch/inch $^{\circ}$F. The coefficient of expansion will be checked over the range of +220 F to -170 F. The preferred material will then be subjected to water absorption to measure dimensional stability.

The proposed antenna design uses a honeycomb structure for the shell with an eggcrate backing to provide maximum rigidity. Analysis techniques using the ASKA program will confirm the structural integrity of the antenna.

Graphite/epoxy structure is cured in an autoclave at 350 F. Gelation occurs at about 280 F to 300 F. To eliminate tool expansion a graphite/epoxy tool will be developed. In fabrication of the part, layers of .005 inch tape in 3 inch strips will be layed up on the tool. The cross ply technique will be used in a repeating manner to reach the desired thickness for the skin. Experience has shown that there is some spring back of parts so the antenna will be brought into final tolerance by grinding. The reflector surface will then be nickel plated followed by a final polishing operation.

The antenna final dimensional accuracy will be verified at the grinding vendor's facility.

The program schedule shows the time span for major activities. In order to complete the effort in 24 months, an overlap of job tasks is required. For example the design can be in work at the same time that the optimization of the low coefficient of expansion material is being done.

DESCRIPTION OF STRUCTURAL CONFIGURATION

The SIMS-A Antenna structure consists of the following.

Antenna Shell

The shell is a graphite/epoxy composite approximately one inch thick. The inner precured moldline skin is approximately .15 inches thick, the outer cocured skin is approximately .06 inch thick. The core material is one inch Nomex flex core.

The composite shell is closed out by the core being chamfered 30 degrees.

Antenna Support Truss

The truss work is comprised of approximately four bulkhead frames, six longitudinal frames and four partial longitudinal frames. The frames are graphite/epoxy composites of approximately .50 inch thick with .016 inch skins using Nomex core. The framework has an "eggcrate" design being attached to each other and the shell by graphite/epoxy angles. The truss has exterior skins making the structure torsionally rigid.

Cruciform

The cruciform at the aft end is a graphite/epoxy layup. There are two sections, horizontal and vertical. Each layup has a hat section major layup and a skin to close out the structure. There is allowance made in design for adjustment to the antenna shell in the cruciform. The adjustments are in both vertical and horizontal directions and are of the eccentric pin design.

Forward Beam

The forward beam is adjustable in the horizontal direction and is also a graphite/epoxy layup similar to the cruciform. The adjustment is also an eccentric pin. Pin material will be either stainless or titanium.

PROGRAM SCHEDULE

SYSTEM (Project) NUMBER: SIMS-A ANTENNA

SUBSYSTEM:

TYPE OF SCHEDULE:

AS OF DATE:

LINE		PRIOR SCHEDULE DATES			FY 19 — CY 1976	FY 19	FY 19 — CY 1977	19	19	19	COMPLETION DATES			LINE
		MO	YR	SYS	J F M A M J	J A S O N D	J F M A M J	J A S O N D	1 2 3 4	1 2 3 4	1 2 3 4			
1	FAB TEST SAMPLES				———									1
2	TEST COEFFICIENT OF EXPANSION				———									2
3	TEST STRUCTURAL PROPERTIES				———									3
4	DESIGN ANALYSIS				————————									4
5	DESIGN													5
6	TOOLING				——————									6
7	FABRICATION UNIT 1					——————								7
8	FABRICATION UNIT 2					—————								8
9	GRIND & POLISH UNIT 1					————————								9
10	GRIND & POLISH UNIT 2					——								10
11	PROJECT MANAGEMENT				———————————————————————									11
12														12
13														13
14														14
15														15
16														16
17														17
18														18
19														19
20														20
21														21
22														22
23														23
24														24
25														25
26														26
27														27
28														28
29														29
30														30
31														31
32														32
33														33
34														34
35														35
36														36

AUTHENTICATION

J F M A M J | J A S O N D | J F M A M J | J A S O N D | 1 2 3 4 | 1 2 3 4 | 1 2 3 4

Antenna Retention

There will be six retention locations on the structure to attach to the shuttle. These fittings are expected to be titanium.

Conceptual Sketches

Conceptual sketches of the antenna configuration are shown in Figures 1 through 5. The weight of this structure is less than 1000 Kg.
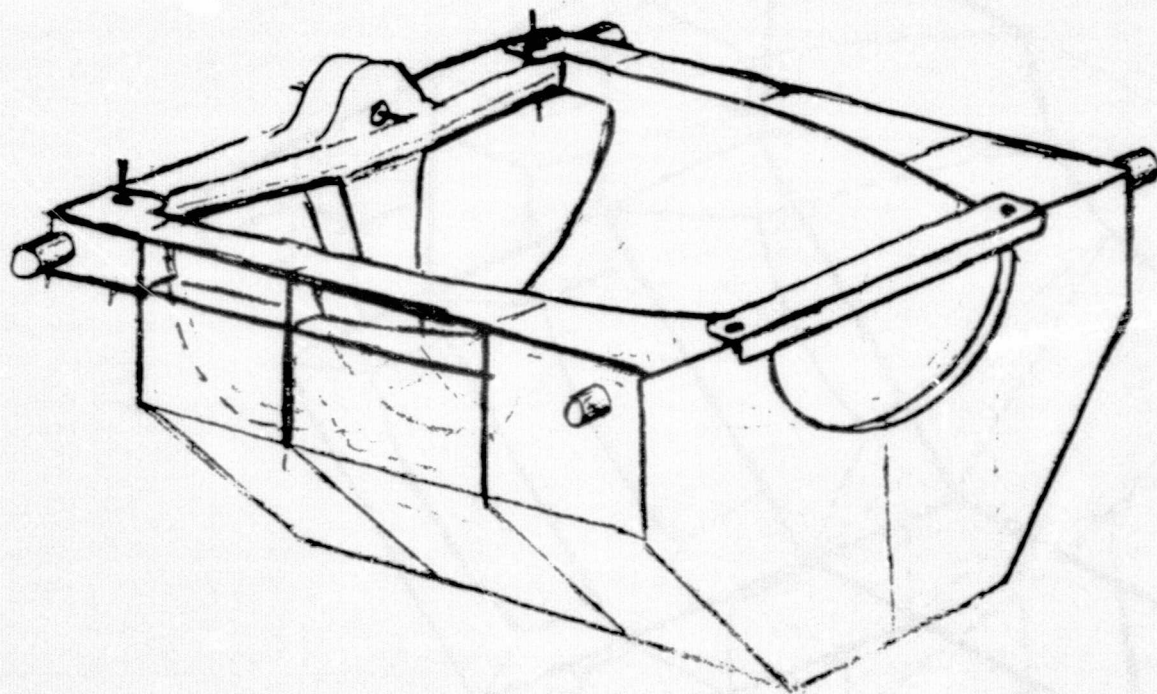
FIGURE 1   ANTENNA ASSY

FIGURE 2
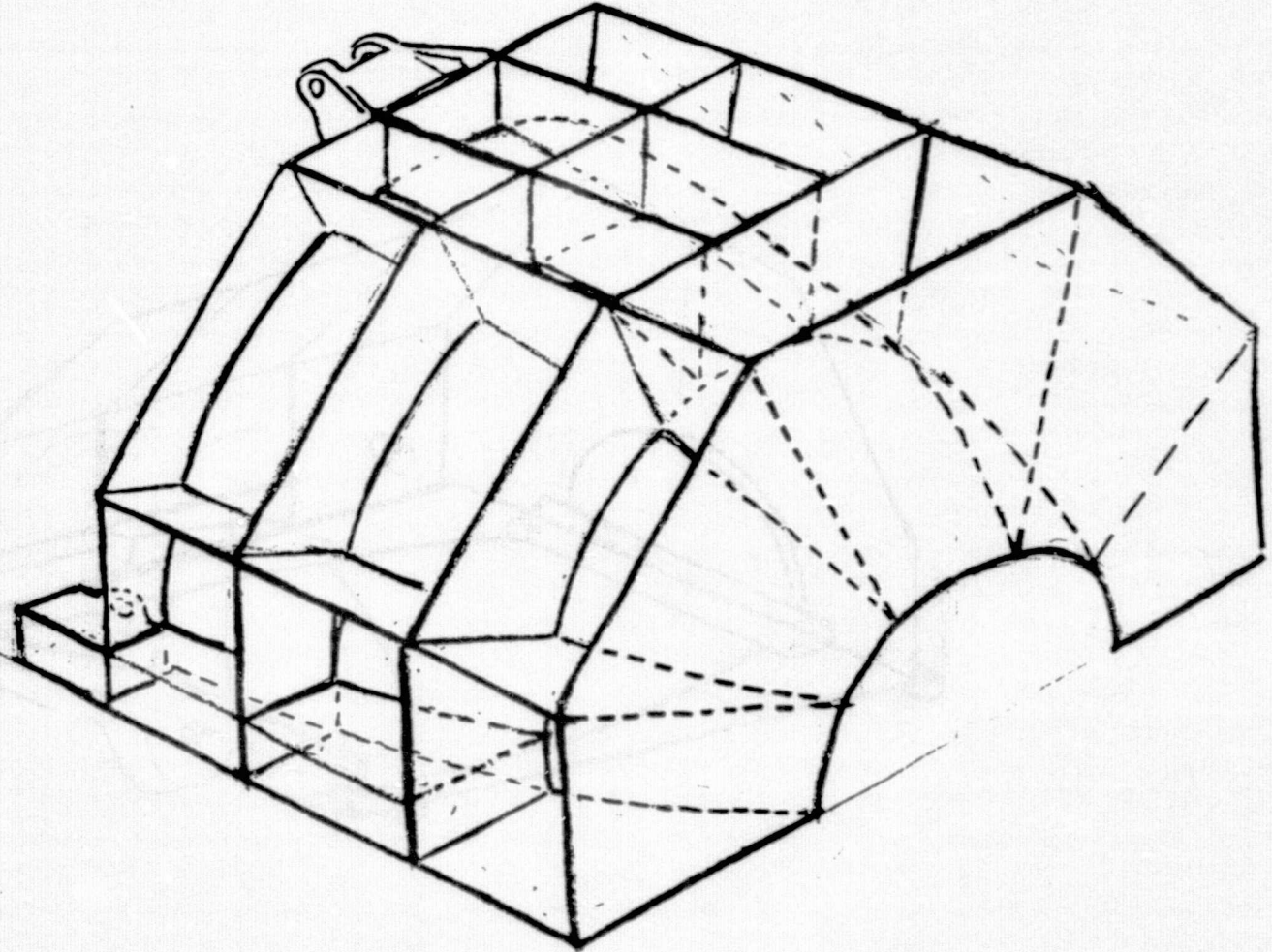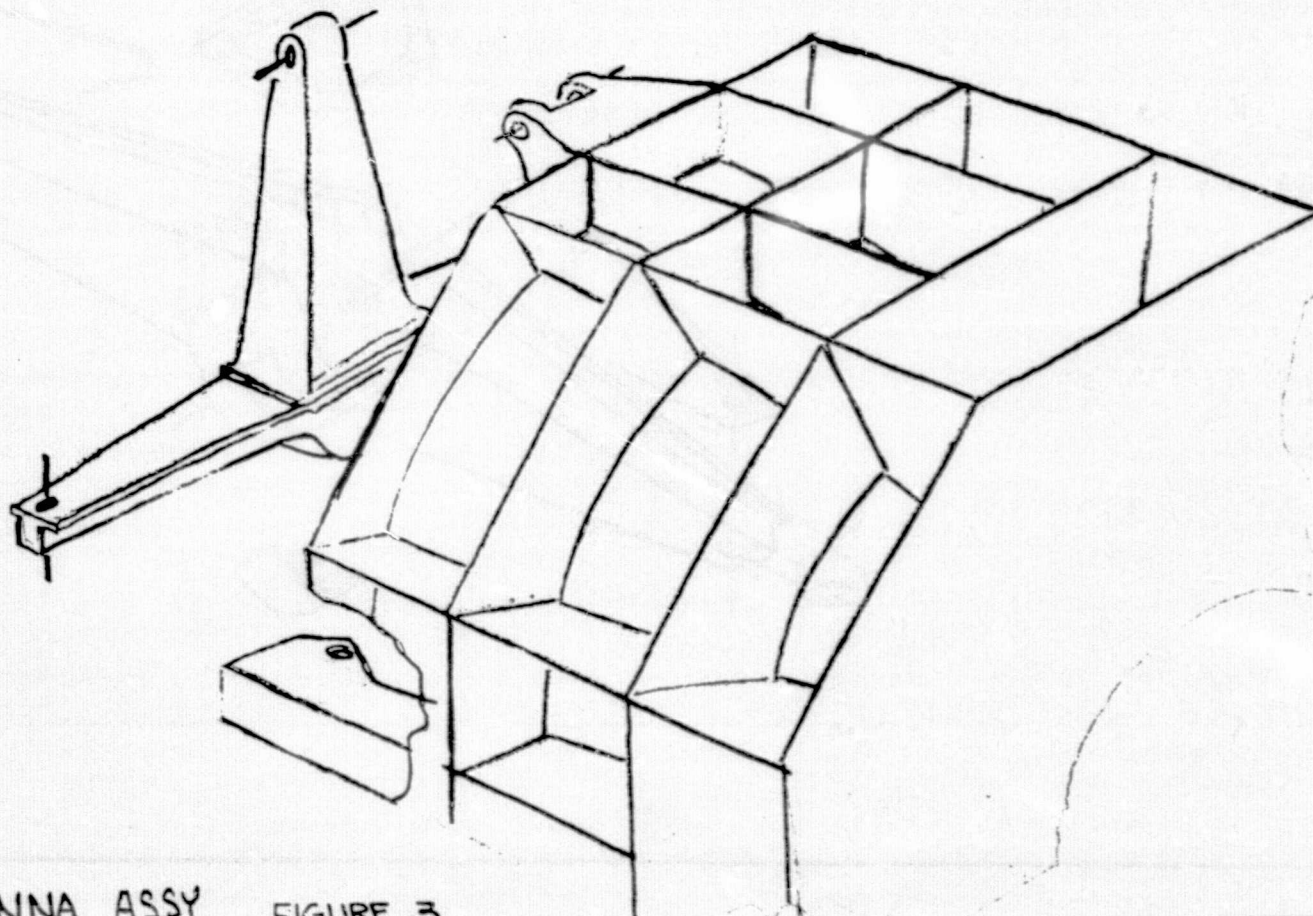
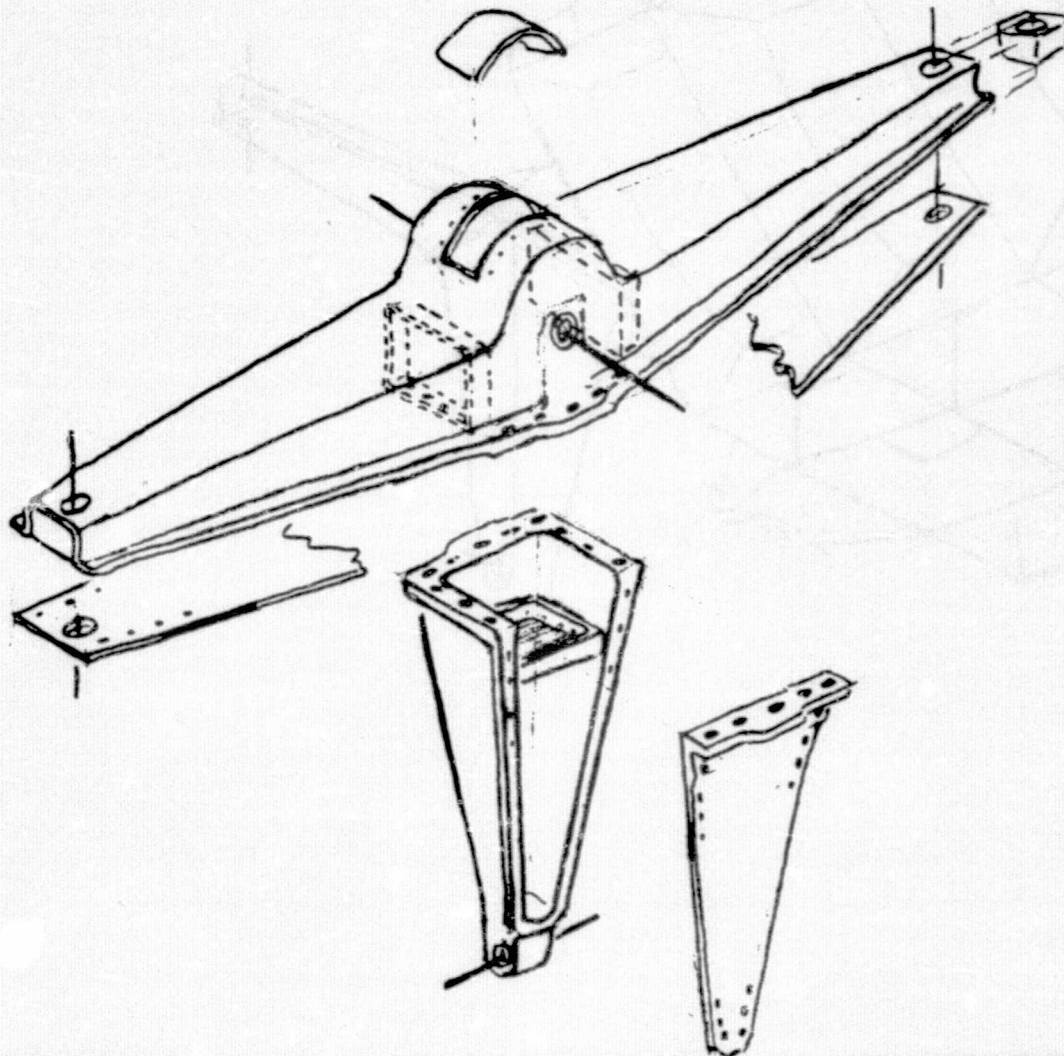ANTENNA ASSY-DF

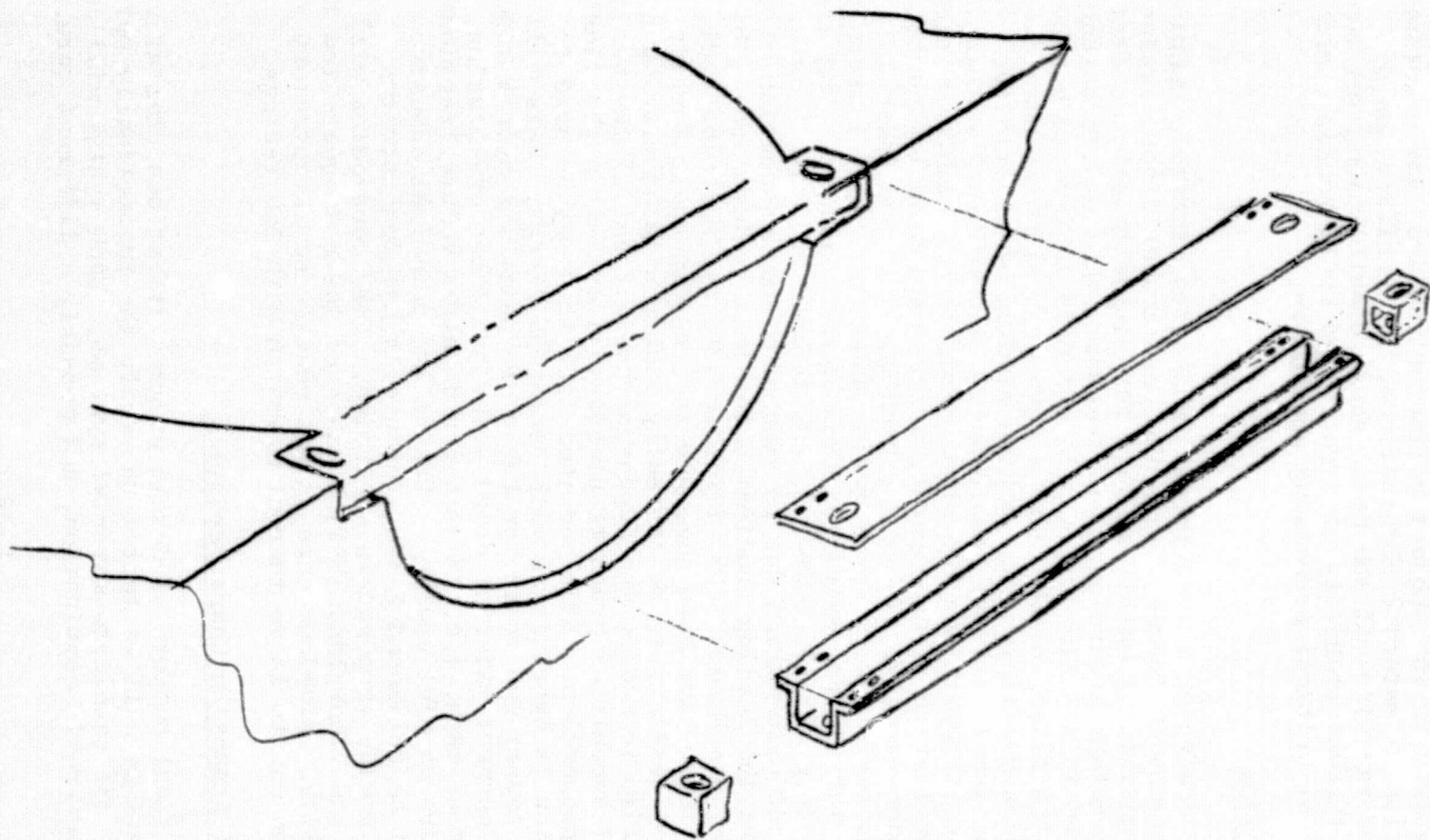CRUCIFORM-TO-ANTENNA ASSY   FIGURE 3

FIGURE 4

CRUCIFORM ASSY

FIGURE 5

FWD BEAM

GRAPHITE/EPOXY MATERIAL DEVELOPMENT

Successful design and fabrication of a zero expansion shell of the
dimensions involved in the subject reflector requires (a) exacting
care in selection of material combinations, (b) verification of
expansion characteristics of the basic shell construction, (c) verifi-
cation of the thermal stability of a contoured shell section, and
(d) generation of critical processing procedures.

MATERIAL SELECTION

Fundamentally, designing a zero thermal expansion structure consists
of balancing expansion forces within the constituent fibers against
those in the constituent matrix so that the composite remains static
over wide temperature excursions. Furthermore, this static balance
must be achieved in all directions. In order to achieve such a balance,
one material (the fiber) must have a very low, slightly negative,
thermal expansion coefficient and a high modulus of elasticity. The
second material (resin matrix) should have a low modulus of elasticity.
Its expansion coefficient, on the other hand, is not highly critical.
Through the application of a computer, a zero-expansion laminate can
be designed theoretically. Table I presents moduli and thermal
expansion characteristics of epoxy resin, adhesive, typical graphite
fibers, and Kevlar fibers, extracted from various sources. The higher
modulus fibers (e.g. GY-70, Modmor I, and Thornel 75) have greater
ability to resist deformation due to expansion and contraction of the
resin, hence are the leading candidates for this application. The
resin candidates are Narmco 5208, Fiberite 934, and Hercules 3501,
because all of these have been demonstrated, during Space Shuttle
Payload Bay Door testing, to be thermally stable without crazing down
to -270F. Ability to modify the expansion coefficient of the resin
by adding small amounts of graphite powder will assist in the final
adjustment of properties. Still another tool that may be used to
control expansion is hybridizing with Kevlar 49 fibers. This will be
used as a last resort due to the probable necessity for hybrid tapes.
Along with the correct material combination and fiber orientation, the
relative amount of each, i.e. the fiber and matrix volume fractions,
will also require careful control. One of the principal adhesive
candidates will be Reliabond R-398, because it has demonstrated
stability over a wide temperature excursion. Core candidates will be
Nomex (HRH-10) and fiberglass (HRP) because of their adequate low tem-
perature stability. Aluminum core is not considered satisfactory for
this application due to large thermal mismatch with the facings.

Verification of Expansion Characteristics

Based upon the final outputs of design program iterations, tentatively
three configurations will be tested to verify the theoretically optimi-
zed designs for (3) candidate material systems. Each system will involve
a different fiber/resin combination, and possibly a different core.

TABLE I
MODULI AND THERMAL EXPANSION COEFFICIENTS OF TYPICAL COMPOSITE MATERIALS

Material	Fiber Orientation	Modulus of Elasticity (MSI)	Test Temperature (Range) °F	Measurement Direction	Expansion Coefficient (μ in/in/°F)
Epoxy Resin (unfilled)		~ 0.5			+25 to +45
Epoxy Resin +15% Graphite Particles					+17
Celion GY-70/X-904	0°	43	-300 to +350	0°	-0.56
	0°	0.8	" "	90°	+18.0
	+45°		" "	45°	-0.43
GY 70 Fiber		77			
Modmor I/Epoxy	0°	40			-0.41
Modmor I Fiber		60			
Thornel 75 Fiber		79	-459 to +932		-0.2 (ave.)
Thornel T-300/5208	0°	~ 20	0 to +200		+0.02
HTS/X904	0°	~ 23	-300 to +500	0°	-0.25
	0°		" "	90°	+15.5
Modmor I/X-30*	$[0_3/\pm45.5/90]_s$		-75 to +75		-.005 to +.014
Kevlar 49 Fiber		19	+32 to +212		-3.6
Reliabond R-398 Adhesive			-270 to +400		+24

*Reported by General Dynamics, Convair Division

The physical measurement test matrix is presented as Table II. Flat
sandwich panels approximately 36" x 36" square will be provided for
testing. Specimens will be tested in sandwich form. Panels will be
fabricated according to optimized procedures established as described
in a subsequent paragraph.

TABLE II
EXPANSION COEFFICIENT TEST MATRIX

Resin System	Fiber	Measurement Angles	No. of Temp. Points	Ply Angle	Total Number of Measurements
1,2,3	A,B,C	2	3	Parallel	18
1	A	3	3	Crossply	9
2	B	3	3	Crossply	9
1,2,3	A,B,C	5	5	Crossply	25
Total					61

Verification of Stability of Curved Shell Sub-Component

A typical section of curved shell will be produced prior to full scale
part manufacture, and thermally tested to demonstrate stability. The
part will be produced in the identical manner planned for the full
scale part, i.e. the reflective surface precured as a thin laminate,
followed by cocuring of the back surface skin over the assembled core.
The subscale shell will represent about one-quarter of the periphery
and full length of the full scale part. Stability will be demonstrated
by (a) accurately measuring the contour of the shell in two planes
normal to each other while the shell rests unrestrained on a supporting
base, (b) raising the temperature of the back surface to about 200F
by suitable means, as with an electric blanket, and (c) remeasuring
the contour at temperature. The test can be performed inexpensively
as: (a) highly accurate contours are not required to confirm stability,
i.e. measurements are relative, and (b) temperature stabilization in
the test panel is not necessary to demonstrate shape stability of an
essentially "zero-expansion" material. Figure 6 illustrates the
simplicity of the test setup. Only relative change in position of
discrete measurement points is involved. The contour template is
made of low expanding material, and is not allowed to become heated
during measurement since only brief point contact is made with the
part. Through use of accurate height gages, changes in contour as
small as .001 inch will be detectable.

Subsequent to thermal stability demonstration, approximately one percent
moisture will be introduced into the structure and any change in contour
determined. In the event moisture absorption causes dimensional instability,
the reflector will be sealed by bonding foil over all exposed areas.
It is assumed that the polished, metal plated reflective surface will in
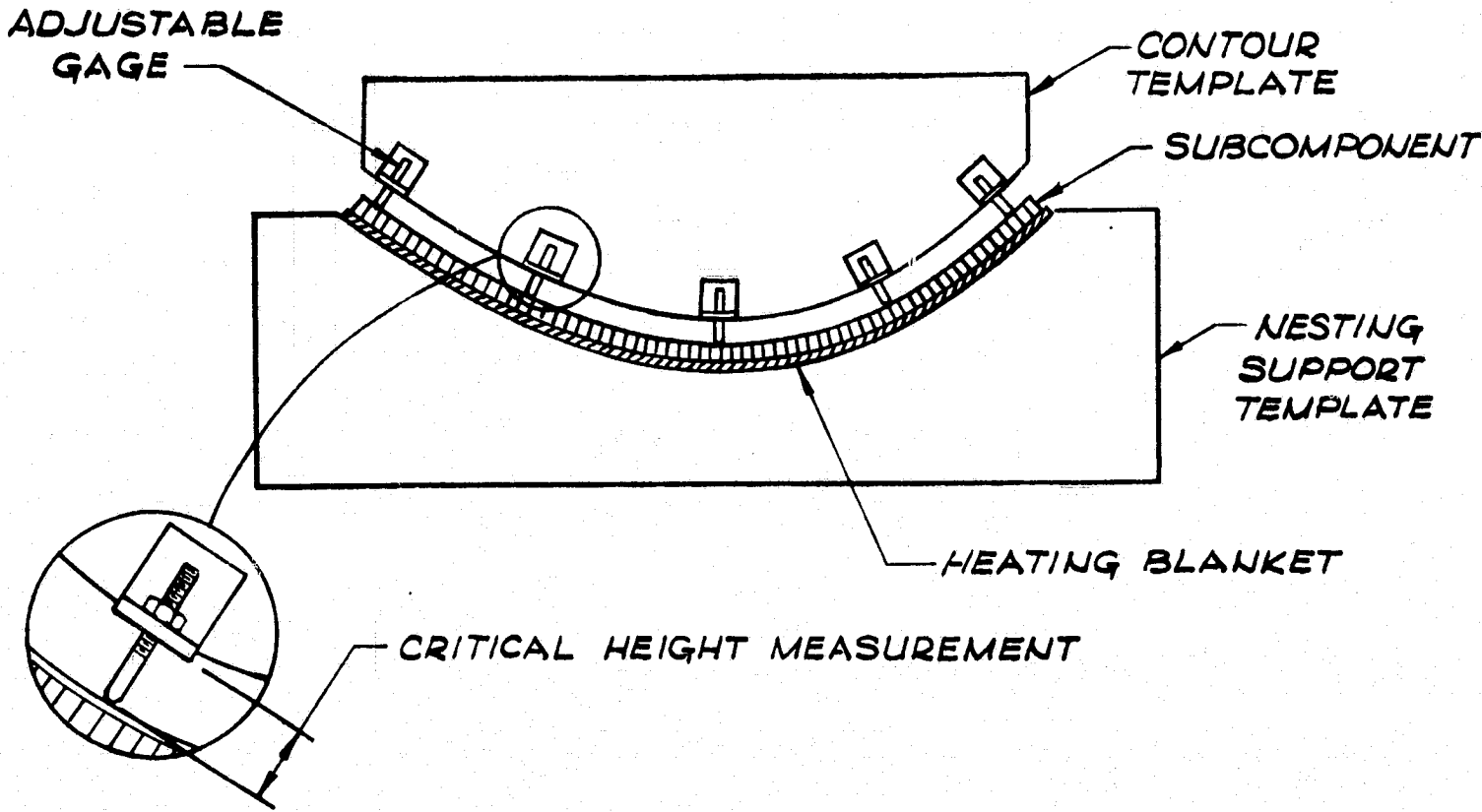itself provide an effective moisture barrier over the plated area.

FIGURE 6 – CONTOUR STABILITY MEASUREMENT FIXTURE
SCHEMATICALLY SHOWN

Establishment of Processing Procedures

Processing of the parabolic reflector will be highly critical in order
to achieve required stability. Precise controls will start with the
pre-impregnated graphite tape materials which will be permitted little
variation in resin content, and which will have imposed on them rigid
uniformity and quality requirements. Layup techniques will emphasize
accurate alignment of fibers. Bleeding and bagging sequences will
stress precise and uniform control of the resin fraction throughout
the molded part. The required bleeder plies will be accurately cal-
culated and resin bleed controlled through use of an essentially
sealed system employing a semi-permeable membrane (see Figure 7).
The semi-permeable membrane permits passage of air and volatile resin
components, while blocking the flow of liquid components. Curing and
postcuring schedules will be designed to: (a) minimize residual
stresses in the cured part, (b) produce void-free skins, and (c) elim-
inate possible residual curing/outgassing in service. Excessive
residual stress may cause distortion during machining of the front
face necessary to bring it into contour. Voids are likely to affect
thermal stability adversely, and will enhance moisture absorption.
Residual curing (with associated resin shrinkage) in service may
significantly distort the contour. Cocuring of the back skin over
honeycomb core poses a special problem in void elimination. Normal
cocuring procedures result in laminates containing voids. Thinner
laminates, and those molded over large sized cells, contain higher
void contents. Void content can be minimized in such cases by using
1/8 inch cell honeycomb and by precuring a ply of adhesive film over
the honeycomb surface prior to molding the skin.

To establish the optimized processing procedure, approximately ten flat
sandwich panels will be fabricated. These panels will be approximately
36 inches square. The criteria for suitability will be visually ob-
served uniformity and quality, resin and fiber fractions in the molded
parts, and flatness after cure and postcure. Flatness will be deter-
mined on a surface table.

Mechanical testing described in the next section will be performed on
specimens from process development panels fabricated during the time
period approaching establishment of the final processing procedure.

Verification of Structural and Physical Properties

Loads to be experienced by the reflector and supporting structure will
be relatively light. Therefore an extensive structural testing program
is not required. Accurate knowledge of stiffness is expected to be
more important than strength. Hence, strain gaging of specimens will
be required. The mechanical test matrix shown in Table III is con-
sidered adequate. All tests are to be performed as sandwich beams.
Moduli and Poisson's ratios will be required to confirm theoretical
design predictions. Test materials will be derived from flat sandwich

SEMI-PERMEABLE MEMBRANE

VACUUM BAG

BREATHER

DOUBLE BACKED TAPE

COROPRENE DAM

VACUUM

REQUIRED RESIN LOSS PER PLY OF PREPREG TAPE:

$$\approx W_f \left(\frac{1}{1-W_{rp}} - \frac{1}{1-W_{rl}} \right)$$

WHERE W_f IS FIBER AREAL WT. $(g/m.^2)$

W_{rp} IS PREPREG RESIN WT. FRACTION

W_{rl} IS LAMINATE RESIN WT. FRACTION

BLEEDER ABSORPTIVITY:

181 FIBERGLASS FABRIC ~ 130 $g/m.^2$ PER PLY

120 FIBERGLASS FABRIC ~ 60 $g/m.^2$ PER PLY

BLEEDER PLIES

PREPREG LAYUP

MOLDING TOOL

FIGURE 7 - BAGGING ARRANGEMENT FOR PRECISE CONTROL OF
RESIN AND FIBER VOLUME FRACTIONS

panels generated during process optimization.

In addition to verifying structural properties for design purposes, it will also be necessary to perform acceptance and process control tests on materials used in hardware for engineering test and delivery. Acceptance tests will consist of the following:

Thermal expansion) (3 temperatures and 3 directions in
& molded flatness) test sandwich)

Sandwich flatwise tension (adhesive)

Resin, fiber, and void volume fractions of test
laminates (skins)

Prepreg physical properties (resin content, flow,
gelation time, volatile content)

Visual examination

Ultrasonic examination of cured panels.

Process control tests will be the same as acceptance tests, excepting for prepreg physical properties.

TABLE III
MECHANICAL TESTING MATRIX

Test or Property	No. of Temp. (°F)	No. of Loading Directions	No. of Tests Per Condition	Total No. of Specimens
Tensile Strength	3	3	5	45
Tensile Modulus	3	3	5	--
Compression Strength	3	3	5	45
Compression Modulus	3	3	5	--
Poisson's Ratio	3	3x2	3	--
Beam (core) Shear	3	2	5	30
Flatwise Tension	3	1	5	15
Thermal Cycle	2	1	5	10
			Total	145

Acceptance and process control tests will be designed to assure attainment of required characteristics in full scale parts, i.e. to assure there has been no significant change in materials after design properties are established.

After establishment of tentative design characteristics and optimized processing procedures, preliminary material and process specifications and detailed processing procedures will be prepared to assure compliance with requirements.

Cycling Tests: Specimens of crossplied sandwich panel described in Table II will be plated with metallic reflective coating, then cycled (100) times between -170F and +210F. The coating will be optically examined for evidence of cracking, blistering, and delamination. Short beam shear tests will then be performed at R.T. and elevated temperature to verify adequacy of the sandwich adhesive bond.

GRINDING AND POLISHING

The SIMS reflector tolerance requirement (conformity to contour) is much tighter than can ordinarily be obtained in graphite/epoxy structures. To get the needed tolerance will require a grinding operation.

The grinding and polishing will be accomplished at Tinsley Laboratory, Inc., Berkeley, California. The grinding and polishing will provide a reflector surface which conforms to the contour defined by the data points to an accuracy of ±.001 inch rms, ±.0025 inch peak. The grinding machine and measurement apparatus are attached to a computer which compares the actual surface contour to the theoretical contour and provides a print-out of contour error. The depth to the surface of the SIMS-A Antenna requires a tooling modification change. Some of this tooling expense could be saved if the 180 degree torus could be reduced to 120 degrees.

SURFACE REFLECTIVITY

To obtain the 99% reflectivity the surface must be a good conductor. The percent reflective ρ is calculated as follows:

$$\rho = \left| \frac{Z_s - Z_o}{Z_s + Z_o} \right| 100$$

where Zo is the free space impedance 377 ohms.

Zs is the surface impedance and may be determined by:

$$|Z_s| = \sqrt{\frac{2\pi f \mu}{\sigma}}$$

where f = frequency in Hz

μ = permeability in henry/meter

σ = conductivity in mhos/meter

The conductive surface skin depth required is determined as follows:

$$\delta = \frac{1}{\sqrt{\pi f \mu \sigma}}$$

This skin depth is the depth at which current density has decreased to 1/e (about 36.8 percent) of its value at the surface. The values obtained for the reflectivity calculations will be valid as long as the material thickness is greater than δ.

Materials considered as possible reflector surfaces and the reflectivity, thickness, and coefficient of expansion are given in the table below.

Material	Min % Reflection	Min δ Skin Depth (inch)	Thermal Expansion Per ^{o}F $(\times 10^{-6})$
Nickel 99.9%	99.75	.00012	7.4
Rhodium	99.88	.000182	4.5
Gold	99.92	.000126	7.9
Silver	99.93	.000103	10.5
Chromium	99.92	.00013	3.4
Solid Graphite	81.2	.0030	.01

After considering the above variables as well as cost and availability it was decided to use nickel on the reflective surface.

The required metal coating for the reflector surface will be applied after the surface has been ground to contour. This metal will be applied by brush electroplating nickel onto the graphite/epoxy to a thickness of 0.00035 inch. This surface would then be ground to remove 0.0002 surface thickness to provide the final contour with a surface finish of 64 microinches.

Thermocycling test will be conducted on graphite/epoxy specimens with the metal plating to insure that the metal used and the plating process will hold up to the required operating temperature range.

PROJECT ENGINEERING

The project engineer will coordinate all technical tasks with the customer and Tulsa Division technical personnel. He will work with Engineering and Laboratory personnel in development of a graphite/epoxy layup that meets design requirements. The project engineer will coordinate with Design, Tooling, and Manufacturing people to insure a part that will comply with specifications. He will interface with subcontractors for measuring thermal coefficient of expansion and for grinding of the reflector surface.

STRUCTURAL DESIGN

The Structural Design support for the SIMS-A Antenna will consist of locating one engineer at Missile Systems Division for approximately two days to establish interfacing at engineering go-ahead, preparing layouts and concepts for design of the antenna from graphite/epoxy, preparing drawings for test evaluation, engineering assistance to the Tulsa Laboratories, technical assistance to the Tulsa Tooling and Manufacturing departments, and Engineering Material Review support for the manufacturing effort.

Drawing Support

The drawing support at Tulsa will consist of preparing various concepts and layouts of the cruciform, forward beam shell, payload retention system and truss support - approximately 100 production drawings and approximately 3 joint test development drawings.

Interface Support

The interface support will require approximately two layouts and two, two-day trips to MSD. One trip will be planned for interfacing and one trip for coordination review.

Technical Assistance

The design support for technical assistance will consist of coordinating engineering information with Tulsa Laboratories, Planning, Manufacturing, and Tooling Departments.

Manufacturing Support

The Manufacturing support will consist of Engineering working directly with Manufacturing effort in material review action, drawing interpretation and drawing change support.

ANALYSIS - STRESS, THERMAL, AND WEIGHTS

Assumptions

1. The general criteria for the Space Shuttle will be used, such as safety factors, etc.

2. The reflector will be designed to react the loads imposed by its own mass and by the drive and control systems housing when acted upon by the accelerations shown in the informal specification for the SIMS main reflector.

3. The antenna and its support structure will be analyzed for the thermal loads which are to be provided to Rockwell-Tulsa at a later date.

4. The material will have a thermal coefficient capable of maintaining the expansion requirements.

5. A dynamic analysis will not be made. The accelerations (G's) listed in the informal specification (Figures 6 and 7) will be used with the idealized static model.

Computer Analysis Justification

o   Finite element analyses will be used to determine SIMS antenna surface distortions induced by thermal gradients.

o   Finite element techniques will also be utilized to obtain stress and strain data from loads resulting from design accelerations.

o   The Automatic Systems Kinematic Analysis (ASKA) finite element program is the program currently best suited for the accomplishment of the analyses listed above because:

    a)   ASKA contains a large family of sophisticated anisotropic finite elements.

b) ASKA has been used extensively for the static analyses of structures composed of advanced composite materials.

c) ASKA has superior multilevel substructuring capabilities.

d) Both mechanical and thermal loading are easily accommodated in ASKA.

e) Dynamic response analyses are provided for in the ASKA-DYNAN system.

f) A high confidence level in the validity of ASKA results has been acquired as a consequence of extensive ASKA usage for the internal loads analyses of the Air Force B-1 Bomber and the NASA Space Shuttle.

g) ASKA was used by the Tulsa Division for the internal loads analyses of the Space Shuttle graphite/epoxy Payload Bay Doors.

The following tasks are necessary to meet the requirement and ensure the structural integrity of the SIMS Antenna system.

Preliminary Review

Become familiar with the system requirements.

Determine general operational requirements.

Computer Analysis

Review and define a method to impose the load criteria, and the thermal requirements on the idealized structure.

Determine nodal point coordinates

Coding topology data.

Run CRT plots.

Geometric data determined.

Material layup determined.

Check of data, boundaries, and checkout runs.

Design Support

Assist the Design section on the structural configuration studies.

Assist in material selections.

Review and approve drawings (approximately 100).

Review and approve material specifications.

Load Analysis

Idealize the structure for a refined finite element analysis and distribute the external loads in a manner which will simulate the actual structure and its loads.

Determine the deflections and thermal stresses due to the environment.

Post-process.

Specimen Testing

Review the different proposed materials and determine if tests are required to determine material properties and thermal-physical properties.

Assist in defining tests.

Monitor tests.

Assist in evaluation of test results.

Stress Analysis

Conduct a stress analysis of the antenna system based on the design criteria and the loads.

Documentation

Prepare a formal stress report which contains the external loads, internal loads, deflections, thermal stresses and deflections, and stress calculations necessary to analytically verify the strength of the structure.

Weight Control

A comprehensive weight control program will be conducted during the design and production phases of the contracted equipment with emphasis placed on the following tasks:

    Weight trade-off studies.
    Establishing target weights.
    Weight and C.G. calculations of the detail components as the
        design progresses.
    Final weight calculations of all components prior to the
        release of drawings.
    Preparation of weight status reports.
    Maintaining up-to-date records.
    Obtaining actual weights during fabrication.

Reports and Coordination Meetings

Time required to attend coordination meetings and prepare weekly and/or monthly reports to assist in project evaluation.

CHECKING AND STANDARDS

The Checking and Standards function will check each drawing to assure conformance with MIL-D-1000 and MIL-STD-100 and will assure that drawings are consistent with each other. Material and standard callouts will be compared with approved listings. Assistance in obtaining standards for use will be provided.

MASTER DIMENSIONS

The master dimensions group will receive and document master dimensions data in the form of basic definition and contour generators. The group will develop and document contour points as definition to support production of design aids and manufacturing tools. They will coordinate with the authorizing division and quality assurance to insure part accuracy.

NASA DOCUMENTATION

Based on recent experience on the Shuttle Payload Bay Doors and interface with the Space Division, the following is estimated to be the documentation required by NASA for the SIMS Antenna.

Material

All material selected for use in manufacture of the antenna will be from an approved list such as Space Division Specification MC999-0096. Material required but not on the approved list will be documented in an IL request to the buyer with rationale as to need and desirability of non-approved material.

All material, including fasteners, material reviews, material substitutions, etc., will be documented on a material usage form for transmittal to the buyer.

Drawings and Specifications

Engineering drawings and specifications shall be prepared to the requirements in MIL-D-1000 and MIL-STD-100. Changes and/or updating of drawings for the deliverable item shall be accomplished by the seller's internal system. Drawings shall be submitted to the buyer upon release. Specifications referenced on drawings will be available upon request.

Analyses

Design analyses associated with structural integrity and thermal stability will be conducted. Results will be documented in the seller's format and transmitted to the buyer.

Test Data

Test procedures for both coefficient of thermal expansion and structural properties as well as test results will be documented in the seller's format and transmitted to the buyer.

Quality Engineering

Inspection and verification procedures will be developed and will be available to the buyer upon request.

Test results which cover surface adequacy, thermal stability, and reflective characteristics will be transmitted to the buyer. An acceptance data package will be assembled for delivery with the hardware which will consist of the following:

1. Drawings
2. Acceptance Test Data
3. DD250
4. Identification of Age Sensitive Items
5. Replacement Record
6. Weight Record
7. Waiver Record
8. Record of Material Review Actions
9. Notes and Comments
10. As Built Configuration

Reports

A monthly status report will be prepared. In addition to general activities the report will contain:

1. Documentation Status/Schedule
2. Mass Property Status.

FACILITIES PLAN

The Tulsa Division, Rockwell International Corporation is located on two major sites adjacent to the Tulsa International Airport, Air Force Plant No. 3, in which Rockwell-Tulsa occupies 706,000 square feet, and the Mingo Facility which consists of 242,000 square feet. In addition, the Tulsa Division has a facility at McAlester, Oklahoma, which consists of 92,000 square feet.

Facility requirements required for fabrication of the SIMS-A Antenna are within existing capabilities at Tulsa with minor modification and rearrangement of bonding operations. Tooling fabrication, detail parts fabrication, bonding and processing will be accomplished within existing area, utilizing available production flows and equipment.

Area will be made available in Air Force Plant No. 3 where the NASA 20 ft. x 40 ft. autoclave is located, and will be activated for bonding the reflector shell structure. Special layup areas and trim areas will be installed to support the autoclave bonding. Non-destructive test, ultrasonic systems and x-ray, are available in Air Force Plant No. 3, and will support the program by adding special holding fixtures and attachments peculiar to the end items.

The Mingo Facility, Building 605 bonding will support the layup, bond and trim of other panels and structure elements by using the existing 9 ft. x 30 ft. autoclave, layup area, and trim area.

Some modifications and rearrangements will be required without impact to ongoing programs.

INSPECTION

The reflector will be inspected prior to grinding, using standard optical equipment templates.

Source inspection will verify the contour and surface requirements at the grinding and plating vendor's facility. The vendor, Tinsley Laboratories, uses a laser measuring system that is a part of their grinding setup to confirm that surface data points are to contour.